NASA/CR–2014-218276

Simulating Wake Vortex Detection with the Sensivu Doppler Wind Lidar Simulator

Dan Ramsey and Chi Nguyen
Aerospace Innovations, LLC, Yorktown, Virginia

June 2014

NASA STI Program . . . in Profile

Since its founding, NASA has been dedicated to the advancement of aeronautics and space science. The NASA scientific and technical information (STI) program plays a key part in helping NASA maintain this important role.

The NASA STI program operates under the auspices of the Agency Chief Information Officer. It collects, organizes, provides for archiving, and disseminates NASA's STI. The NASA STI program provides access to the NASA Aeronautics and Space Database and its public interface, the NASA Technical Report Server, thus providing one of the largest collections of aeronautical and space science STI in the world. Results are published in both non-NASA channels and by NASA in the NASA STI Report Series, which includes the following report types:

- TECHNICAL PUBLICATION. Reports of completed research or a major significant phase of research that present the results of NASA Programs and include extensive data or theoretical analysis. Includes compilations of significant scientific and technical data and information deemed to be of continuing reference value. NASA counterpart of peer-reviewed formal professional papers, but having less stringent limitations on manuscript length and extent of graphic presentations.

- TECHNICAL MEMORANDUM. Scientific and technical findings that are preliminary or of specialized interest, e.g., quick release reports, working papers, and bibliographies that contain minimal annotation. Does not contain extensive analysis.

- CONTRACTOR REPORT. Scientific and technical findings by NASA-sponsored contractors and grantees.

- CONFERENCE PUBLICATION. Collected papers from scientific and technical conferences, symposia, seminars, or other meetings sponsored or co-sponsored by NASA.

- SPECIAL PUBLICATION. Scientific, technical, or historical information from NASA programs, projects, and missions, often concerned with subjects having substantial public interest.

- TECHNICAL TRANSLATION. English-language translations of foreign scientific and technical material pertinent to NASA's mission.

Specialized services also include organizing and publishing research results, distributing specialized research announcements and feeds, providing information desk and personal search support, and enabling data exchange services.

For more information about the NASA STI program, see the following:

- Access the NASA STI program home page at *http://www.sti.nasa.gov*

- E-mail your question to help@sti.nasa.gov

- Fax your question to the NASA STI Information Desk at 443-757-5803

- Phone the NASA STI Information Desk at 443-757-5802

- Write to:
  STI Information Desk
  NASA Center for AeroSpace Information
  7115 Standard Drive
  Hanover, MD 21076-1320

NASA/CR–2014-218276

Simulating Wake Vortex Detection with the Sensivu Doppler Wind Lidar Simulator

Dan Ramsey and Chi Nguyen
Aerospace Innovations, LLC, Yorktown, Virginia

National Aeronautics and
Space Administration

Langley Research Center
Hampton, Virginia 23681-2199

Prepared for Langley Research Center
under Contract NNL12AA24C

June 2014

Available from:

NASA Center for AeroSpace Information
7115 Standard Drive
Hanover, MD 21076-1320
443-757-5802

NASA Atmospheric Environment Safety Technologies NRA

Wake Vortex Hazard Investigation

Simulating Wake Vortex Detection with the Sensivu Doppler Wind Lidar Simulator

Dan Ramsey and Chi Nguyen

Aerospace Innovations LLC

Yorktown, VA

April 21, 2014

In support of NASA's Atmospheric Environment Safety Technologies NRA research topic on Wake Vortex Hazard Investigation, Aerospace Innovations (AI) investigated a set of techniques for detecting wake vortex hazards from arbitrary viewing angles, including axial perspectives. This technical report describes an approach to this problem and presents results from its implementation in a virtual lidar simulator developed at AI. Three-dimensional data volumes from NASA's Terminal Area Simulation System (TASS) containing strong turbulent vortices were used as the atmospheric domain for these studies, in addition to an analytical vortex model in 3-D space. By incorporating a third-party radiative transfer code (BACKSCAT 4), user-defined aerosol layers can be incorporated into atmospheric models, simulating attenuation and backscatter in different environmental conditions and altitudes. A hazard detection algorithm is described that uses a two-component spectral model to identify vortex signatures observable from arbitrary angles.

1 Introduction

Over the past few decades, researchers have successfully measured and characterized aircraft wake vortices with several types of sensors, perhaps most effectively with the pulsed coherent Doppler wind lidar. A typical measurement strategy involves scanning transverse cross-sections of the aircraft flight path to detect the relatively large tangential velocities present in the vortex pair (Figure 1).

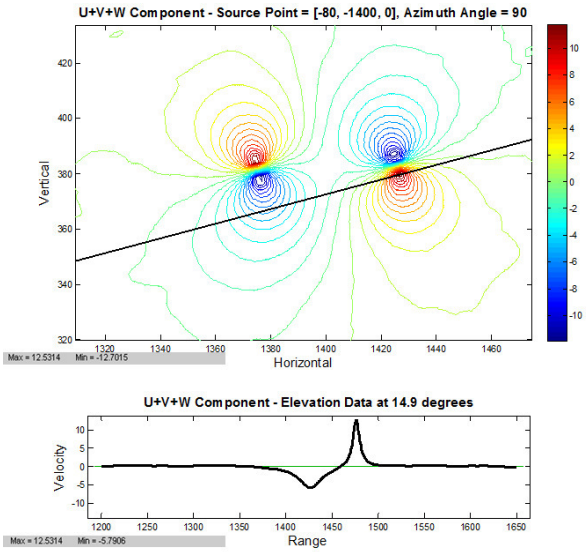

Figure 1.Visualization of vortex tangential velocities viewable from a transverse scan. From this perspective, line-of-sight Doppler instruments can observe the easily detectable tangential velocities. The axial perspective, however, is what poses a unique risk to aircraft during encounter, and it poses a particularly difficult detection challenge.

The axial perspective of the vortex hazard, however, has the potential to induce a severe rolling moment during an aircraft encounter, and this unique risk has motivated a renewed interest in axial detection of wake vortices.

Using novel approaches developed recently in this field [2,3], this simulation study aims to demonstrate the feasibility of identifying vortex signatures observable from arbitrary viewing angles, particularly those substantially parallel to the flight path.

2 Simulation of Heterodyne Detection Lidar

Sensivu is the name of AI's virtual wind lidar instrument. In the present application, it models the heterodyne detection method, whereby the received laser pulse is optically mixed with a local oscillator beam to produce a modulated signal with known frequency. The detector measures the energy reflected by aerosols suspended in the atmosphere, and the Doppler

frequency shift of this return signal can be used to infer line-of-sight characteristics of the atmosphere (Figure 2).

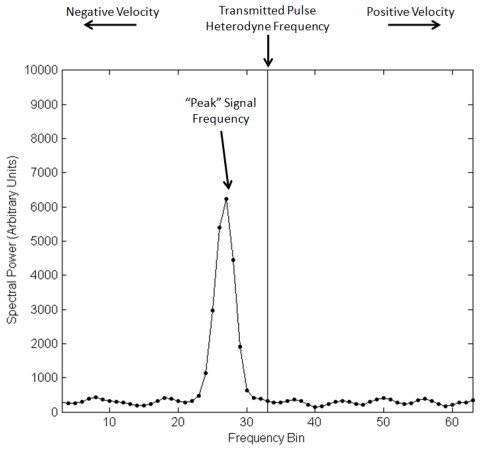

Figure 2.Lidar frequency spectrum schematic. Bulk characteristics of the sampling volume can be inferred from the lidar spectrum, and line-of-sight velocities will appear as shifts in the peak of the spectral curve. Vortex velocities, however, comprise a relatively small fraction of the sampling volume, and measuring them requires a different approach.

2.1 Signal Simulation

Preconfigured lidar system parameters are used to simulate a Gaussian laser pulse, which propagates through a medium of uniformly distributed random scatterers. Each excited scatterer emits a Huygens wavelet with random amplitude and phase. The combined backscattered signal from all scatterers in the field results in an alternating photocurrent from the detector plane, which is digitized in discrete samples and recorded as individual raw signals for each transmitted pulse.[1]

To simulate the raw signal, Sensivu uses one of three user-selected lidar models: Constant CNR, Lisim6, and Radiometric.

Constant CNR. This model uses a signal with constant carrier-to-noise ratio (CNR) specified by the user. Individual signals will vary from the specified value, but the simulation is designed such that bulk statistics will exhibit the user-specified CNR. We expect that this model may be useful to tailor the simulation to field lidar data.

Here, we define wideband CNR in as the average ratio of signal power to noise power:

$$CNR(t) = \frac{\langle i_h^2(t) \rangle}{\langle i_n^2(t) \rangle}$$

Where i_h is the heterodyne signal current and i_n is the receiver noise current. In the estimated power spectrum, we measure wideband CNR using an estimate of the signal and noise

power. We first establish a mean (P_{ns})and standard deviation of the noise level by measuring the magnitude of the power spectrum spectrum well outside of the signal bandwidth ($sigBW$).[1]

We establish a noise threshold four standard deviations above the mean noise level, and we consider any adjacent spectral lines $f_{sig}(k)$within the signal bandwidth that rise above this threshold to comprise our signal spectrum. Summing these lines yields an estimate for signal power:

$$P_{sig} = \sum_{k \in sigBW} f_{sig}(k)$$

The wideband CNR is then estimated as

$$CNR = \frac{P_{sig} - N_{sigBW} P_{ns}}{N_{wb} P_{ns}}$$

where N_{sigBW} is the number of bins in the signal bandwidth, and N_{wb} is the total number of bins in the spectrum.[6]

Lisim-6. Lisim-6 is a model with a fixed transmission and backscatter characteristics based on previous work in this field. This model incorporates an atmosphere with constant transmission coefficients and specified profiles for backscatter coefficient and refractive turbulence that vary with altitude.

Radiometric. Similar to Lisim-6, this model incorporates a user-specified model atmosphere to simulate transmission and backscatter based on the lidar wavelength.

The transmission and backscatter data used in this model are products of the radiative transfer code BACKSCAT 4.0[2]. From user-configured atmospheric layers and setup parameters, the code uses the LOWTRAN7/FASCODE aerosol models and atmospheric model to produce a table of table of aerosol and Rayleigh backscatter and attenuation coefficients as a function of altitude.[7,8]

The radiometric model interpolates coefficients from this table based on the arbitrary beam path and incorporates them into the signal simulation algorithm.

---

[1]Alternatively, we could use the mean level of the power spectrum from a range gate beyond the effective range of the lidar.

[2]BACKSCAT 4.0 (circa 1994) was developed by Sparta, Inc. [8], and is currently distributed by Ontar Corporation (ontar.com), packaged with a lidar simulation program called Betaspec 2.0, a lidar simulator developed by the University of South Florida [7]. BACKSCAT 4.0 is included with the Sensivu 2.0 installation as an executable file. Because it is a 16-bit application, it cannot be run directly from 64-bit windows systems. To accommodate this program, we have included the open-source DOS emulator, DosBOX (dosbox.com), which is called from within Sensivu whenever atmospheric parameters must be generated from BACKSCAT 4.0.

2.2 Scatterer Velocity Simulation

The signal contribution from each scatterer exhibits a Doppler shift from the particle's velocity relative to the sensor line-of-sight (LOS) axis. Hence, each scatterer must be assigned a LOS velocity representative of the atmospheric volume that is reflecting the lidar pulse.

Sensivu gets velocity information from one of two sources: an analytical vortex model or a TASS dataset.

2.2.1 Analytical Vortex Model

The Burnham-Hallock vortex model [9] specifies tangential velocities $v(r)$ for a single vortex as a function of distance from the vortex core r, fixed core radius r_c, and total circulation Γ.

$$v(r) = \frac{\Gamma}{2\pi} \frac{r}{r_c^2 + r^2}$$

In Sensivu, the user specifies parameters for a pair of Burnham-Hallock vortices with independent circulation values and core radii, plus separation distance and tilt angle to determine their relative position. The velocities of the pair are superimposed, and the resulting velocity cross-section is treated as constant along the vortex axis (x), with zero vortex velocity in the x-direction.

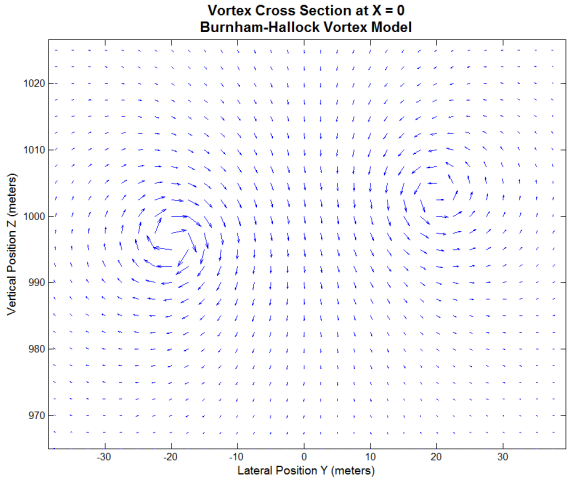

Figure 3.Vector plot of a sample Burnham-Hallock vortex pair used in Sensivu. (Separation = 40m, tilt angle=10°, Γ_1=565m²/s, Γ_2=500m²/s, r_{c_1}=2m, r_{c_2}=3m.) This cross section is constant along the x-axis, with zero vortex velocity in the x-direction.

During simulation, a 2-D velocity is calculated for each scatterer along the beam axis depending on its position. Each of these values is then projected on the lidar LOS vector to obtain the lidar-viewable Doppler velocities for each scatterer.

2.2.2 TASS Data Sets

The other source used to simulate vortex velocities is a static 3-D data set generated by NASA's Terminal Area Simulation System (TASS). Figure 4 shows a sample dataset generated by TASS. The data set shown here models a Boeing 747 wake after 97.5 seconds, part of a simulation effort intended to simulate a wake encounter environment suspected in the American Airlines Flight 587 accident in 2001. [4]

The data set for this time slice consists of three *.faa files, containing orthogonal u, v, and w velocity components in a regular grid. The domain size is 960m by 648m by 360m in the along-track (x), cross-track (y), and vertical directions (z), respectively. Spatial resolution is 1.5m in y and z, and 2m in the x-direction. [4]

Sensivu can also process single *.faa files, which contain all three velocity components in a single file.

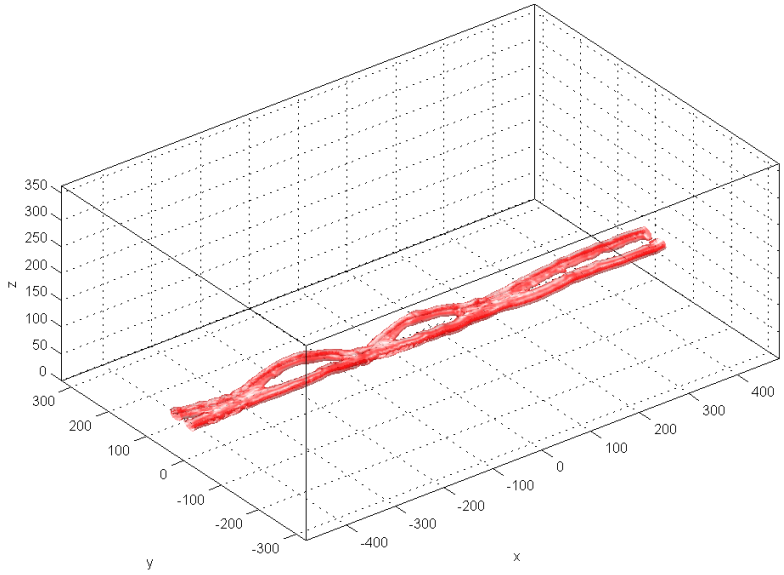

Figure 4.Visualization of the 3-D TASS volume used in the development of Sensivu. The velocity magnitude isosurface (7 m/s) is plotted to visualize the vortex pair. Velocities of the simulation "scatterers" are interpolated from regularly spaced velocity data in this domain.

For each pulse propagating through the simulation domain, Sensivu generates uniformly distributed scatterer positions along the beam axis. It then treats these locations as interpolation points within the regular grid. An interpolated u, v, and w value is assigned for each scatterer, and each of these vectors is then projected onto the beam axis to obtain a line-of-sight velocity for each particle.

2.3 Frequency Spectrum Estimation

To resolve the lidar signal along the beam axis, the return signal is sampled in overlapping range gates. Each range gate is then weighted with a window function, and a zero-padded Fast

Fourier Transform is performed to estimate a power spectrum in the frequency domain. Each spectrum therefore corresponds to a range window whose resolution in space varies depending on the number of samples in each range gate and the length of the laser pulse.

The spectra exhibit significant variation from pulse to pulse, owing to a number of random factors. For this reason, spectra from several pulses are usually averaged to obtain a representative spectrum for each measurement point.

2.4 Scan Pattern

To detect spectral signatures from axial perspectives, we followed the sinusoidal scanning strategy employed in Ref. 3, where a single mirror scans horizontally while a pair of rotating prisms creates a controlled, rapid vertical oscillation (Figure 5).

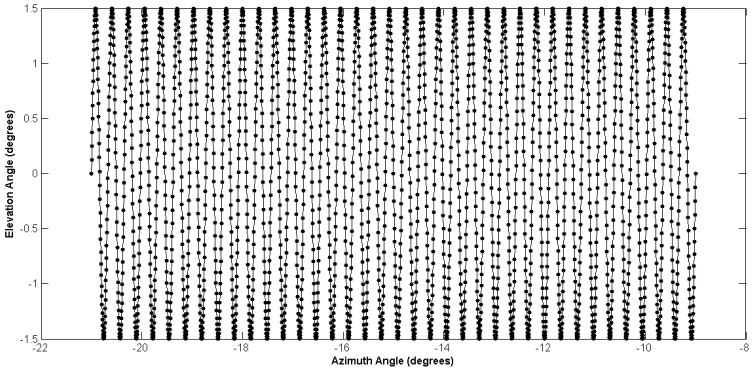

Figure 5. The scan pattern employed in this study. Rapid vertical oscillation combined with slower horizontal sweeps yields a dense sinusoidal scan pattern. One scan frame is shown here, and each dot in the figure above represents an individual pulse.

With this method, we obtain a series of pulses distributed across a horizontal and vertical angular window. The sensing volume therefore takes the shape of an ever widening rectangular wedge (Figure 6).

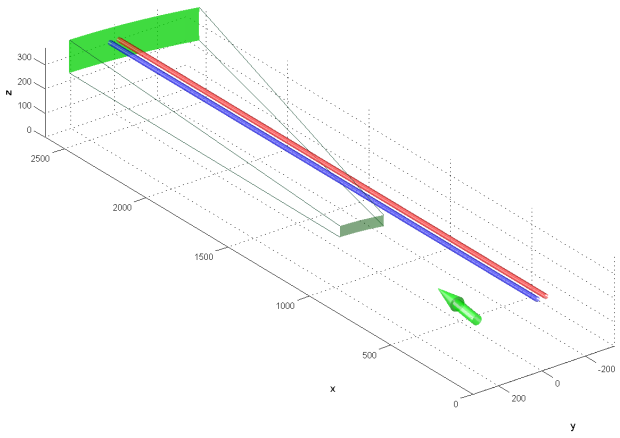

Figure 6.Illustration of scan volume intersecting a Burnham-Hallock vortex pair. For a static sensor, the sampling volume will grow wider up to the range limit. Sampling the signal in overlapping range gates allows us to resolve the spectral data into "planes" or "frames" that exhibit the characteristics of the atmosphere at a given range.

2.5 Moving Sensor Simulation

To explore the special requirements of airborne forward-looking sensors, Sensivu incorporates an option for forward airspeed. This affects the minimum required digital sampling rate, requires modification of the return signal, and can require expanding the data set if the scanning volume exceeds the TASS data limits.

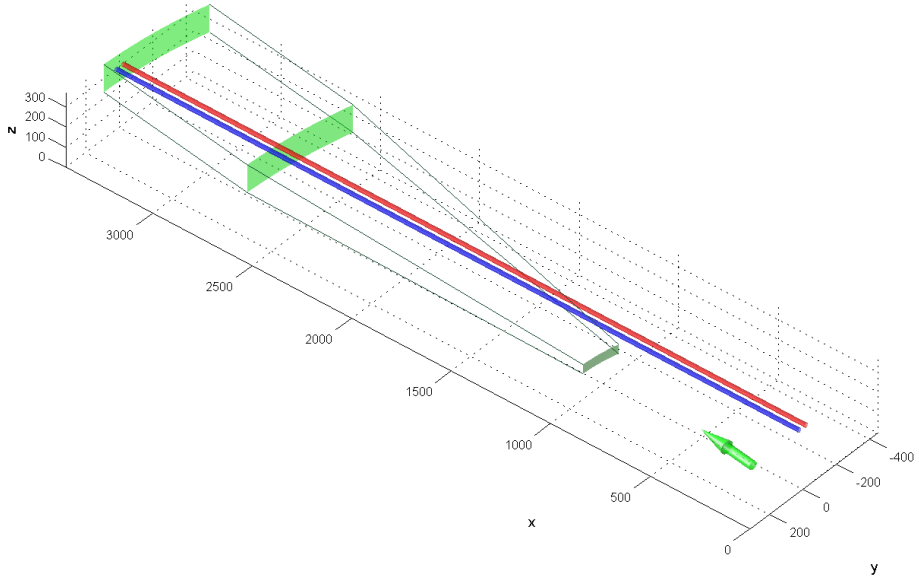

Figure 7.To accommodate the additional distance traveled during the scan, the scanning volume must be extended beyond the region shown in Figure 6.

2.5.1 Increased Sampling Rate

The detectable frequency range estimated by discrete sampling is limited by the sampling rate. Beyond the Nyquist rate (1/2 the sampling rate), it is not possible to discern the frequency components of the signal.

If the sensor is moving forward, this creates a Doppler shift in the return signal. At a forward airspeed of 150m/s, a 2-μm signal transmitting at 25MHz will be shifted to 173MHz. A system sampling at 256MHz (with a Nyquist limit of 128MHz) will not measure this signal adequately. A higher frequency rate, say 500MHz, is required to capture the spectrum at this speed (Figure 8).

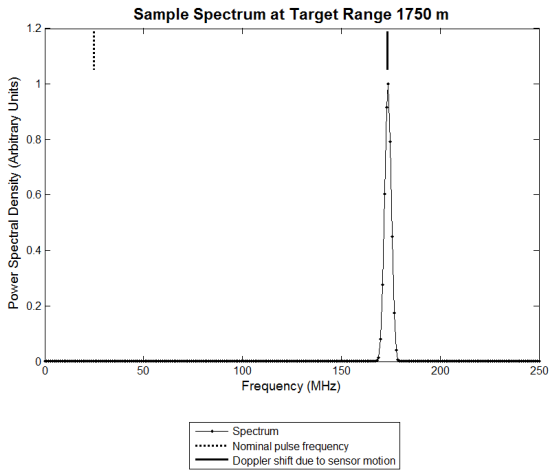

Figure 8.Illustration of Doppler shift at 150m/s airspeed. Here, forward motion of the sensor causes the transmitted pulse at 25MHz (heterodyne frequency) to be shifted to 173MHz when the aerosol return is detected at the receiver.

2.5.2 Sampling Volume Geometry with a Moving Signal

Because the sensor is moving, each pulse is transmitted from a different location. In earlier versions of Sensivu, each individual pulse/signal was trimmed to fit within a coherent volume in space. To encourage compatibility with existing sensor systems, however, this system was modified. Spectral data is collected using fixed range gating parameters: number of samples in each range gate, overlap between gates, number of gates, and so on.

If the aircraft speed is known, each range gate spectrum can be assigned a position in space, and the spectra themselves can be further binned into a predefined number of longitudinally-distributed volumes. During spectral averaging, spectra from each of these volumes are added together to obtain a spectral estimate for that space.

2.5.3 Misalignment Error due to Sensor Motion

Because the sensor head is both rotating and translating in space, pulses are transmitted in a different orientation and position than when they are received. As a result, the receiver is misaligned by some angle when the signal is received at time 2R/c.

To account for this misalignment during simulation, the effective angular misalignment is calculated for each signal sample (Figure 9).

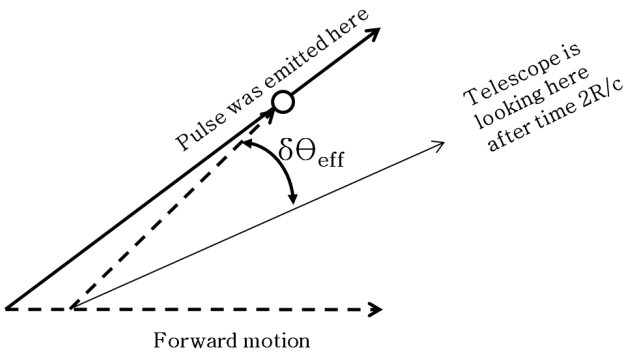

Figure 9.Illustration of effective angular misalignment. Because the sensor has rotated and translated since transmitting the pulse, there is an angular offset to the target in question.

With an angular offset, we are able to use an expression for CNR loss in heterodyne systems related to this offset angle and the diffraction angle at the lidar wavelength[1].

$$\eta = exp\left(\frac{-\delta\theta^2}{{\theta_d}^2}\right)$$

Here, θ_d is the diffraction angle,

$$\theta_d = \frac{\lambda}{\pi\omega}$$

ω is the Gaussian beam waist, and λ is the lidar wavelength. To illustrate the order of magnitude of this error: a 2-μm lidar with 5-cm beam waist, scanning at 20 deg/s, might exhibit a 3.5 dB loss due to this alignment error.

2.5.4 Data Set Expansion

The TASS data sets are fixed size (Figure 4). If using the TASS dataset for a simulation where the scatterers are sampled outside of this volume, the TASS dataset must be expanded to fit the simulation envelope.

At runtime, Sensivu determines the limits of the simulation envelope and mirrors the TASS data along the boundaries in three dimensions until the simulation space can be accommodated. Although it is resource intensive, this method ensures that the dataset is adequately sized for the simulation. Figure 10 demonstrates the expanded dataset.

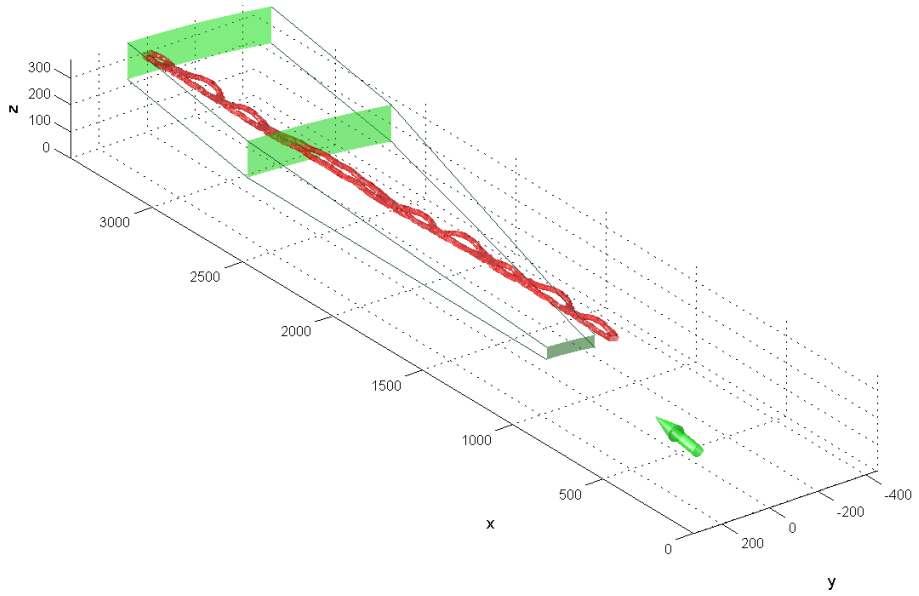

Figure 10. When using the TASS dataset to simulate vortex velocities, the dataset is mirrored along its boundaries until expanded to the required size.

3 Axial Detection Algorithm

The Doppler spectrum contains an estimate of the signal power for each frequency bin measurable at a given sampling rate. The median peak of the distribution can be interpreted as dominant frequency of the return signal. Therefore, the shift of this peak from the heterodyne frequency of the transmitted pulse can be used to estimate the expected line-of-sight velocity for the bulk of the sampled volume (Figure 2).

In classic transverse scanning, vortex tangential velocities typically appear as a minor perturbation at the base of the spectral curve rather than a shift in the bulk peak. As the lidar look angle shifts toward the vortex axis, these perturbations become even more indistinct, and we look to other methods to discern vortex signatures in the lidar signal.

3.1 Zone-Based Spectrum Averaging

In planar scanning patterns, the simplest way to reduce random effects in the spectrum is to average the spectra from a fixed number of sequential pulses. Because of the different scanning pattern described here, however, we employ a zone-based resampling and averaging scheme.

First, the peak values of all spectra are centered in the frequency band to reduce variation when averaging, and each spectrum is assigned a weight based on signal quality in CNR terms.

Next, the angular scan window is divided into a uniform grid, with the center of each cell represented by an azimuth and elevation angle from the sensor reference frame. For each cell, the averaged spectrum includes the accumulation of all pulses within a solid-angle “radius” of the cell center.

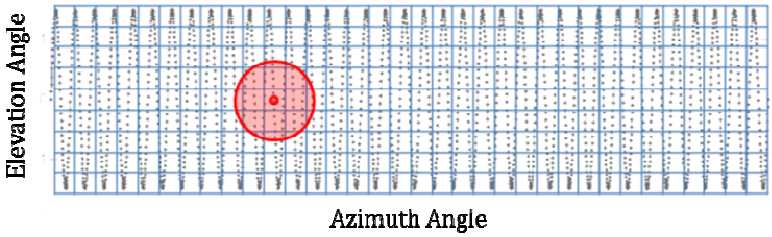

Figure 11.Illustration of zone-based averaging. Any pulse within a solid angle from the center of each cell is accumulated to generate the average spectrum for that cell. This 2-D averaging method is repeated at each resampled range gate to generate a 3-D spatial matrix of averaged spectra.

The result is a series of range gate "planes" with averaged spectral data spaced on a Cartesian grid that becomes larger with increasing range (Figures 7, 8).

3.2 Bi-Gaussian Model Parameter Estimation

We then fit the averaged spectrum for each measurement cell(i,j)to a spectral model, thereby reducing the spectral data to a limited set of model parameters for each point.

The model consists of the superposition of two Gaussian curves, each with a peak frequency (f_n), amplitude (s_n), and standard deviation (σ_n). The noise floor N(f) is modeled as a constant value at each frequency(f) multiplied by a gain value(n). After normalizing the expression further to reduce the degrees of freedom, the model takes the following form: [3]

$$M_2(f) = \frac{e^{-(f_1-f)^2/\sigma_1^2} + s_2 e^{-(f_2-f)^2/\sigma_2^2} + nN(f)}{1 + s_2 e^{-(f_2-f_1)^2/\sigma_2^2} + nN(f_1)}$$

For each spectrum, the six model parameters are varied within specified limits and fitted to the data in a least-squares sense using an iterative optimization routine (Figure 12).

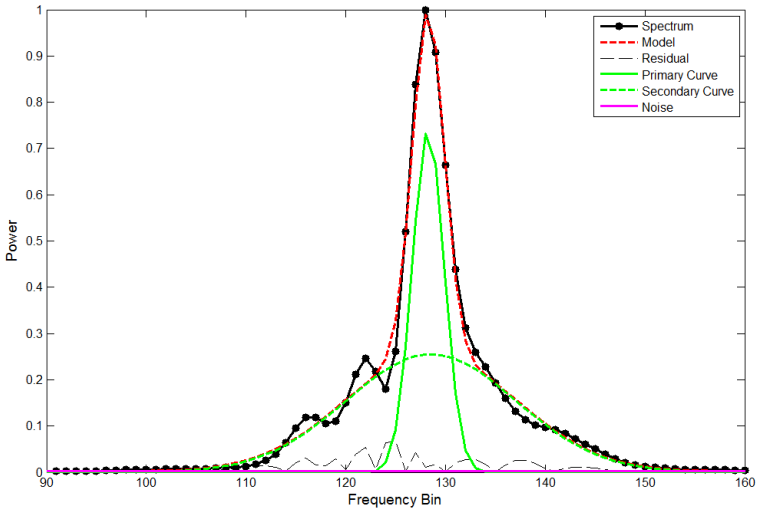

Figure 12.Illustration of bi-Gaussian spectral model. The model curve (M_2) is the sum of the first and second Gaussian curves. The six model parameters are varied within predefined limits until a least squares convergence is reached. The detection field $D(i,j)$ for each range gate is based on the relative magnitude of the 2nd Gaussian curve.

4 Vortex Signatures in the Model Parameters

4.1 S_2 Model Parameter

Since the secondary Gaussian curve is intended to model the vortex-induced spectral broadening, the model parameters that describe it are good candidates for identifying vortex signatures. Indeed, the clearest vortex signatures are visible in the s_2 parameter, which is the amplitude of the secondary curve relative to the amplitude of the primary curve. Figure 13 is an example of a vortex pair signature visible in the s_2 data.

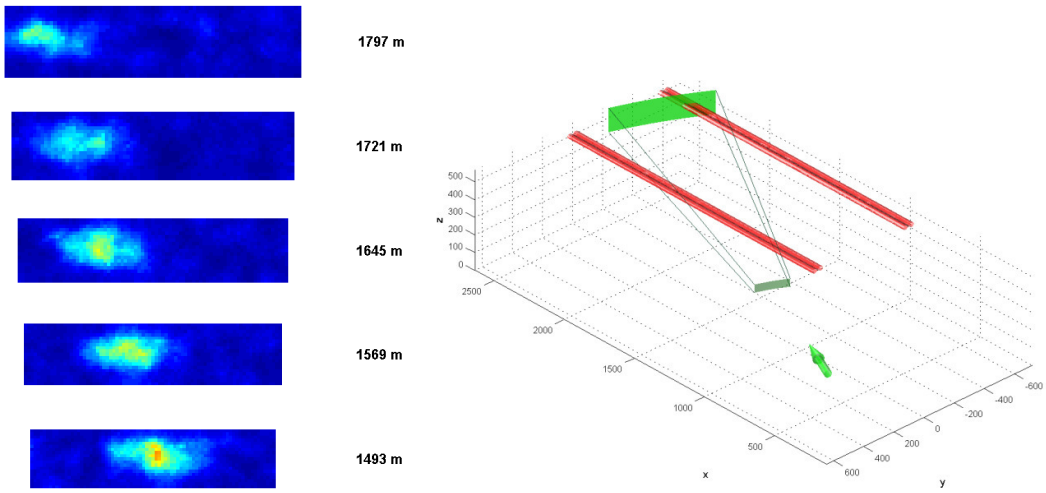

Figure 13. Example of the vortex signatures present in the s_2 model parameter. Five selected range gates are shown on the left. On the right, a schematic shows the overall scanning orientation. An azimuth offset of 25° from the vortex axis makes the signature appear to drift from right to left across the field of view with increasing range.

Other parameters, such as the width of the secondary Gaussian or the area captured under the secondary curve, seem to be more prone to spurious results that do not correlate with vortex signatures. Hence, we use the s_2 parameter as the clearest indicator of the vortex hazard.

5 Hazard Magnitude and Position Estimates

To estimate the vortex hazard, peaks in the s_2 parameter are measured in relation to the background statistics. First, speckle noise is filtered in each range plane using a 3x3 median filter. Next, the characteristics of the background data are estimated (mean and standard deviation), and the peaks in s_2 attributable to vortices are expressed in terms of multiples of standard deviations above the background mean.

5.1 Position Accuracy

In the simulation space, the vortex pair is a linear feature along the X-direction. Any given "hit" in a scan plane has an x coordinate that corresponds to a nearest "slice" in the TASS data. Using this slice, the y and z coordinates corresponding to the vortex positions were read from truth data supplied by NASA with the simulation cases.

Because the algorithm only identifies a single peak in a given frame, we use the average of the two vortex positions as a reference from which to estimate the positional accuracy of the Sensivu hazard algorithm.[3]

[3] In the absence of a hard threshold for false alarm filtering, the track hits were manually filtered. Therefore, any algorithm track hits that identified a spurious peak not associated with the vortex

	Y	Z
Mean Error	-5.8m	-10.4m
Standard Deviation	9.5m	8.4m
(N=87)		

The results show a nominal bias, however it is well within the separation distance between the vortices (approximately 50m).

Figure 14 shows how, for small angles offset from the vortex axis, the algorithm often picks the larger of the two vortex signatures as the single peak. For larger angles, the peak is typically more centrally located in the vortex pair.

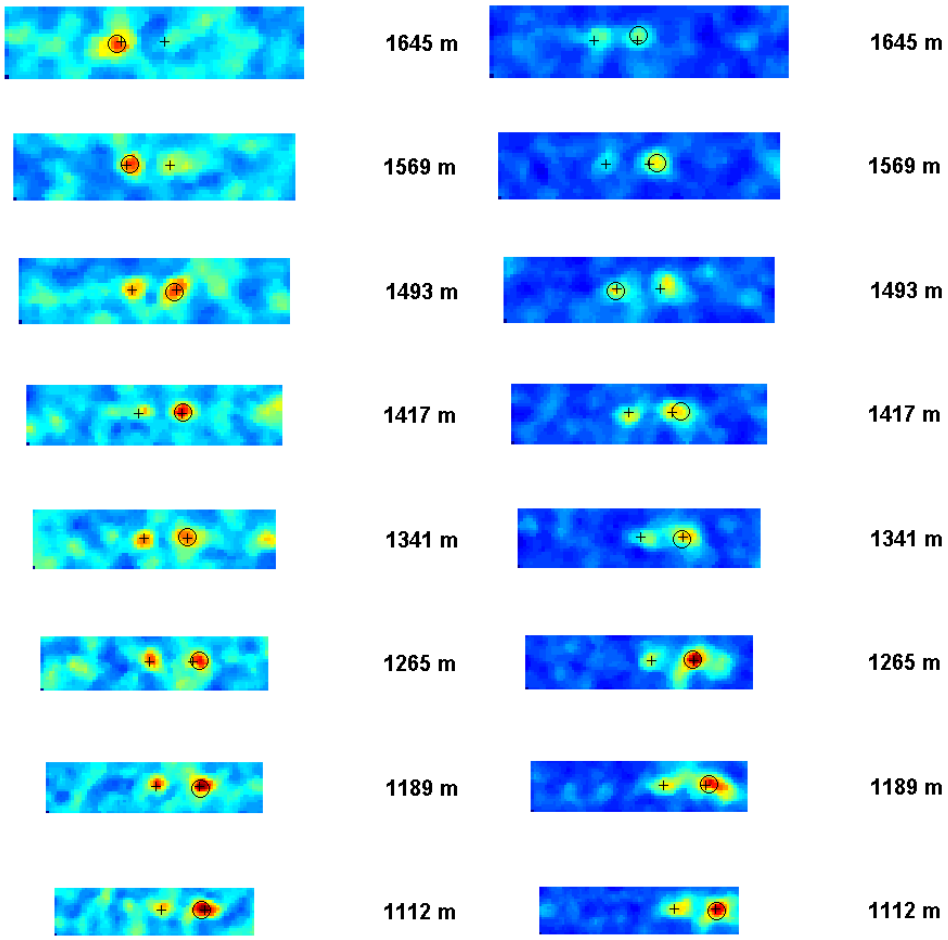

Figure 14. Simulation truth positions (+) compared with algorithm peak detection position results (O). The left image is a 5˚ observation angle, and the right image is the same TASS data viewed from a 10˚ angle. The Sensivu algorithm picks up the largest peak in the scan frame and treats it as the vortex hazard. For small viewing angles such as this, two peaks are usually visible, but only one is chosen as the primary hazard. For larger viewing angles, the

signature was discarded. As a result, the accuracy of the position estimates reflects a human-in-the-loop outlier screening.

peak is typically more centrally located. On average, the error places the position within the vortex pair ellipse, however these results incorporate human-in-the-loop screening of spurious hits for marginal data.

5.2 Dependence of Apparent Hazard Magnitude on Viewing Angle

Since the tangential components of the vortex flow become more dominant as the line-of-sight approaches a perpendicular viewing angle, we expected the apparent strength of the vortex to follow a similar pattern. Indeed, with all other variables held approximately equal, there appears to be a linear relationship between viewing angle and apparent strength.

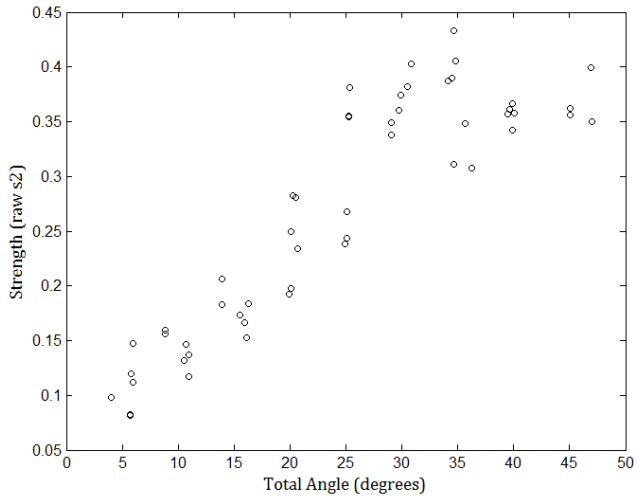

Figure 15. Measured s_2 parameter peak value at various viewing angles to a simulated vortex pair. Azimuth was varied from 5 degrees to 45 degrees relative to the vortex axis. All strength measurements are from a single range gate centered at a distance of 1493m from the lidar. Wind field was NASA's TASS Case 18 (Ref. 10), which simulates a B747 "out of ground effect" wake vortex embedded within a low turbulence atmosphere (eddy dissipation rate = $4x10^{-5}$ m^2s^{-3}). N = 52, circulation truth values: $\mu = 550m^2s^{-1}$, $\sigma = 7.6m^2s^{-1}$ (15-20m average); $\mu = 499m^2s^{-1}$, $\sigma = 20.4m^2s^{-1}$ (10-15m average).

Qualitatively, a few things change as the viewing angle changes from an axial perspective to a more oblique perspective. First, as we observed quantitatively, the vortex signature is more prominent relative to the background. Second, the footprint of the vortex pair signature becomes "smeared" along the direction of the angular offset. Each range gate samples a 3-D volume, and the depth of this volume is responsible for this measurement artifact. Third, the characteristic shape of the vortex signature changes. From an axial perspective, individual vortices can often be discerned, but as the viewing angle becomes wider, the signature takes on the shape of the vortex pair ellipse, with the central "downwash" zone exhibiting the peak signature. Figure 16 illustrates some examples of these qualitative differences.

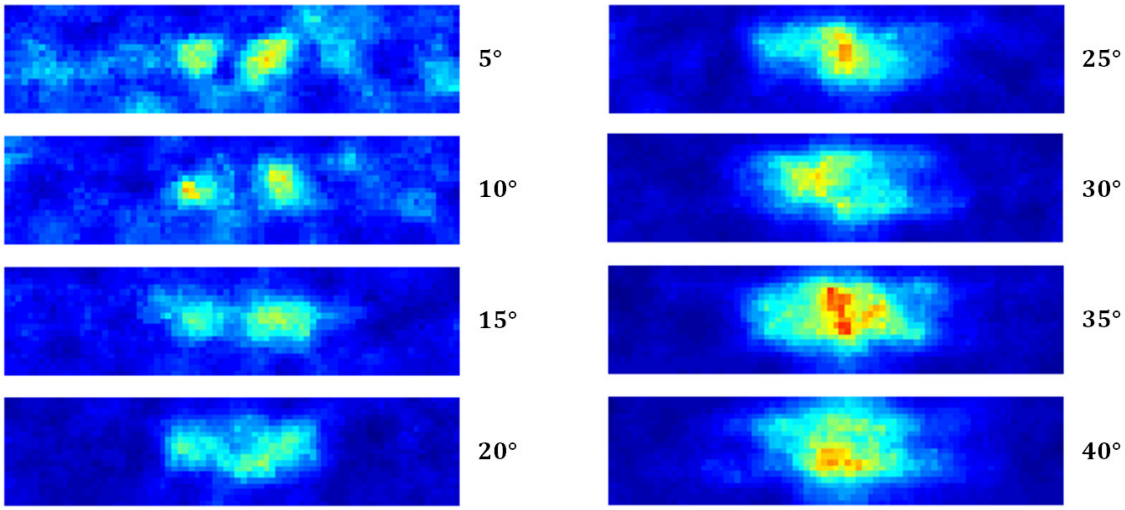

Figure 16. Qualitative comparison of vortex signatures at different viewing angles. Azimuth angle was varied from 5° to 40°, but each image above is taken from the range gate centered at 1493m, which in turn is centered on the same location in the 3-D TASS volume (Case 18, 0s). Note that the pseudocolor scaling changes dynamically between simulation runs, so no absolute comparisons of magnitude can be made between images. One can, however, observe that the background topography appears to diminish relative to the vortex signature as the viewing angle becomes greater.

5.3 CNR and Range Considerations

The lidar equation for coherent detection lidar reveals the R^{-2} relationship between CNR and target range. Put in a different way, a more distant target will result in a weaker spectral peak relative to the noise floor. As the noise floor rises in relation to the signal portion of the spectrum, it will occlude more of the secondary Gaussian curve, which signals the vortex presence. Therefore, it is reasonable to expect a weaker vortex signature at longer range.

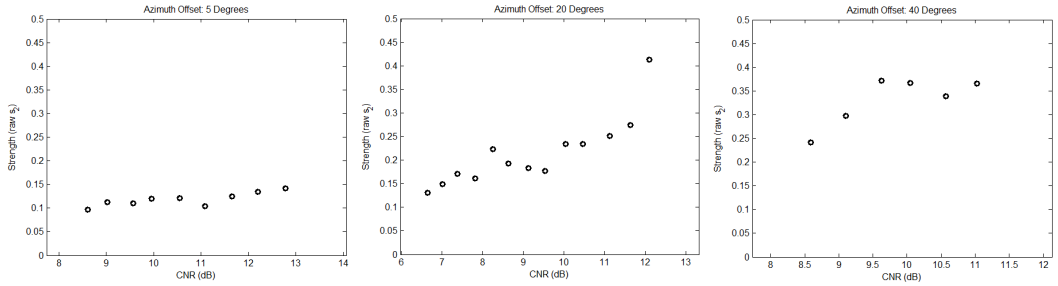

Figure 17. Track hits for three individual simulation runs at 5, 20, and 40 degrees offset from the vortex pair axis. All else equal, apparent strength is correlated positively with CNR.

Indeed, if all other parameters are held constant, a track hit in higher CNR conditions will appear stronger than one in lower CNR conditions.

5.4 Performance Envelope

Because this detection algorithm relies heavily on the aerosol return, this simulation can be expected to apply to coherent lidar systems operating in wavelengths from 1μm to approximately 10μm. At these wavelengths, the atmospheric conditions of the sensing volume must also support a minimum aerosol density in order to detect vortex signatures in the spectra. Although the aerosol density is dependent upon local conditions, our trade studies indicate that this algorithm is generally successful in the atmospheric boundary layer, typically below a ceiling of approximately 2km to 3km AGL.

6 Opportunities for Future Work

6.1 Sensor Application

A natural extension of this work would be applying this algorithm to offline post-processing of data from real-world sensors. Most existing data would likely not suffice, as ground-based measurement campaigns have typically involved two-dimensional planar scanning of transverse wake cross-sections. Implementing this algorithm would require hardware capable of rapidly scanning in a 3-D pattern.

While some integration and modification would certainly be required, the general architecture implemented in Sensivu would make the transition to real-world systems a matter of data conversion and processing.

The nonlinear model fitting approach is computationally intensive, and this system is not currently a candidate for real-time processing. On a PC workstation, processing one simulation run (one scan) takes up to 30 minutes. Although Moore's Law and parallel processing hardware may lead to a scenario where a real-time application is feasible, this algorithm is perhaps best classified as a candidate technology for future sensors rather than an immediately applicable solution.

6.2 Direct Detection Application

The core assumption underlying the development of the processing algorithms described here is that the tell-tale vortex signatures are manifested in the lidar returns as distortions or excursions from the typical signals returned by the bulk atmosphere volumes.

During this study, an investigation into visible and UV wavelengths revealed that this principle might be applied to direct detection lidar as well, albeit in a radically different way. Although a detailed investigation quickly outgrew the scope of this work, there may be an opportunity to investigate model fitting approaches to direct detection Doppler lidars that incorporate fringe imaging. By investigating distortions in the characteristic Airy shape function, a similar approach would fit an analogous model to the data, expecting a set of parameters to reveal vortex signatures.

7 Conclusions

This work was undertaken to "support and facilitate NASA's efforts to link wake vortex behavior and hazard indicators to factors that are detectable by sensors from arbitrary viewing angles and at sufficient range to allow for hazard mitigation or avoidance by an aircraft." [12] To accomplish this objective, a simulation tool was developed that can use NASA's TASS data sets with embedded vortices as sensing volumes. Leveraging existing atmospheric transmission codes, a multispectral simulation tool was developed that simulates coherent detection lidar systems with wavelengths ranging from 1μm to approximately 10μm. To test concepts related to airborne platforms, the simulation also provides for forward motion with optional settings.

Encouraged by a method described in references 2 and 3, an algorithm was developed that can identify vortex signatures from arbitrary viewing angles by fitting a two-component spectral model to the simulated data. The feasibility of this method was demonstrated for a range of acceptable local sampling conditions in the atmospheric boundary layer.

While positional accuracy appears sufficient for avoidance purposes, the current implementation of the hazard identification algorithm falls short of an ability to discern wake characteristics that would drive hazard mitigation technologies. Circulation, a basic measure of the vortex hazard, cannot be estimated with sufficient precision, as the observable variables do not sufficiently explain the variability in the estimated hazard strength observed in the TASS volumes, at least for a single hazard "hit". By identifying the vortex pair as a linear feature, however, the observation angle can be inferred, which is a primary driver of the apparent strength.

In this work, characteristics of 3-D wake vortices were linked to sensor measurables for a wide class of sensors likely to be employed in future systems. While the method seems promising, it should be noted with the caveat that the approach is limited to a narrow section of the atmosphere, and the computational intensity of the approach precludes it from a simple real-time implementation.

The authors' aim is that the results will generate knowledge used by decision makers to steer the development of either airborne or ground-based sensors for vortices, which would provide the information necessary for optimum safe and efficient operations in the NextGen environment as well as supporting evaluation of formation flight concepts.

8 References

1] T. Fujii and T. Fukuchi, ed., *Laser Remote Sensing,* Ch.7. Taylor and Francis, 2005.

2] S. Lugan, L. Bricteux, B. Macq, P. Sobieski, G. Winckelmans and D. Douxchamps, "Simulation of LIDAR-Based Aircraft Wake Vortex Detection Using a Bi-Gaussian Spectral Model,"*IEEE International Geoscience and Remote Sensing Symposium (IGARSS 2007)*, Barcelona, Spain, Jul. 23-27, 2007.

3] D. Douxchamps, Y. Verschueren, S. Lugan, S. Mutuel, B. Macq, and K. Chihara, "On-Board Axial Detection of Wake Vortices using a 2-μm LiDAR,"*IEEE Transactions on Aerospace and Electronic Systems,* Vol. 44, No. 4, October 2008, p. 1276-1290.

4] G. Switzer, "Documentation for Three Wake Vortex Model Data Sets from Simulation of Flight 587 Wake Vortex Encounter Accident Case," Final Report, RTI/8438/006-02F, January 2003.

5] C. Nguyen, D. Ramsey, "Sensivu 3.0 User Guide,"*unpublished* (included with Sensivu 3.0 documentation), April 2014.

6] S. Tucker, M. Hardesty, A. Brewer, "Optical Remote Sensing with Coherent Doppler Lidar," University of Colorado Lecture, April 4, 2011.

7] "Betaspec 2.0 User Manual," September 2009, University of South Florida.

8] D. Longtin, M. Cheifetz, J. Jones, J. Hummel, "Backscat Lidar Simulation Version 4.0: Technical Documentation and Users Guide," Sparta, Inc., June 1994. (DTIC Report AD-A285 851)

9] D. Burnham, and J. Hallock, "Chicago Monostatic Acoustic Vortex Sensing System," Report No. DOT-TSC-FAA-79-103. IV, July 1982.

10] G. Switzer, and F. Duparcmeur, "Wake Vortex Data Set #18 for Sensor Development," *unpublished*, December 2010.

11] J. Vaughan, "The Fabry-Perot Interferometer—History, Theory, Practice, and Applications," Adam Hilger/IOP Publishing, 1989.

12] Amendment No. 8 to the NASA Research Announcement (NRA), "Research Opportunities in Aeronautics – 2010 (ROA-2010)," NNH10ZEA001N, Released June 2, 2010.

9 Appendix: Sample Data Set

Included here are data from a trade study which varied the azimuth angle from 5 degrees to 45 degrees (relative to the vortex axis) in 5-degree increments. This parametric study was performed on the Case 18 data set at six time slices (0s, 12s, 24s, 36s, 48s, 60s).

Each of the simulations consisted of one scan frame, and the results shown here are a series of 2-D maps of the s_2 parameter fitted to the spectral data.

The physical location of the lidar and data set were oriented such that the range gate at 1493m was centered on the same TASS data region for each simulation run. For wider viewing angles, the vortex pair may appear multiple times due to the reflection of the original data set in order to accommodate the entire sensing volume.

Other than the lidar position and orientation, all other simulation and processing parameters were held constant for this study. The following parameters are a selection of those used as initial conditions for the simulation:

Simulation or Processing Parameter	**Value**
Altitude	1000 m
Azimuth angle scan range	12 degrees
Azimuth center	[From 5 degrees to 45 degrees]
Elevation angle scan range	3 degrees
Elevation angle center	0 degrees (horizontal)
Period for one scan sweep	.55 s
Wind data source	TASS Case 18 (B747; EDR=4e-5) [0, 12, 24, 36, 48, and 60 sec]
First signal sample range	1000 m
Last signal sample range	2500 m
Lidar wavelength	2.02 µm
Pulse repetition rate	5k pulses/s
Pulse energy	5 mJ
Pulse width	400 ns
Pulse to pulse frequency fluctuation (standard deviation)	1 MHz
Nominal heterodyne frequency	25 MHz
Sampling rate	128 MHz
Pulse width fluctuation (std. dev.)	20 ns
Pulse timing jitter (std. dev.)	50 ns
Transmitter optical efficiency)	.99
Antenna efficiency (truncation * heterodyne efficiency)	.41
Receiver optical efficiency	.99
Beam splitter optical efficiency	.80
Quantum efficiency	.1
Heterodyne receiver excess noise ratio	1.1
Receiver bandwidth	8e7
Receiver aperture diameter	10 cm
Beam quality (M^2)	1
Season	Spring/Summer
Atmosphere model	US Standard (1976)
Boundary layer height	2 km
Aerosol type	Maritime
Relative humidity	70%
Surface visibility	23 km
Wind speed at 10m	10 m/s
FFT size	512
Samples per range gate	192
Overlap between gates	2/3
Resampling 'radius' solid angle	.5 degrees

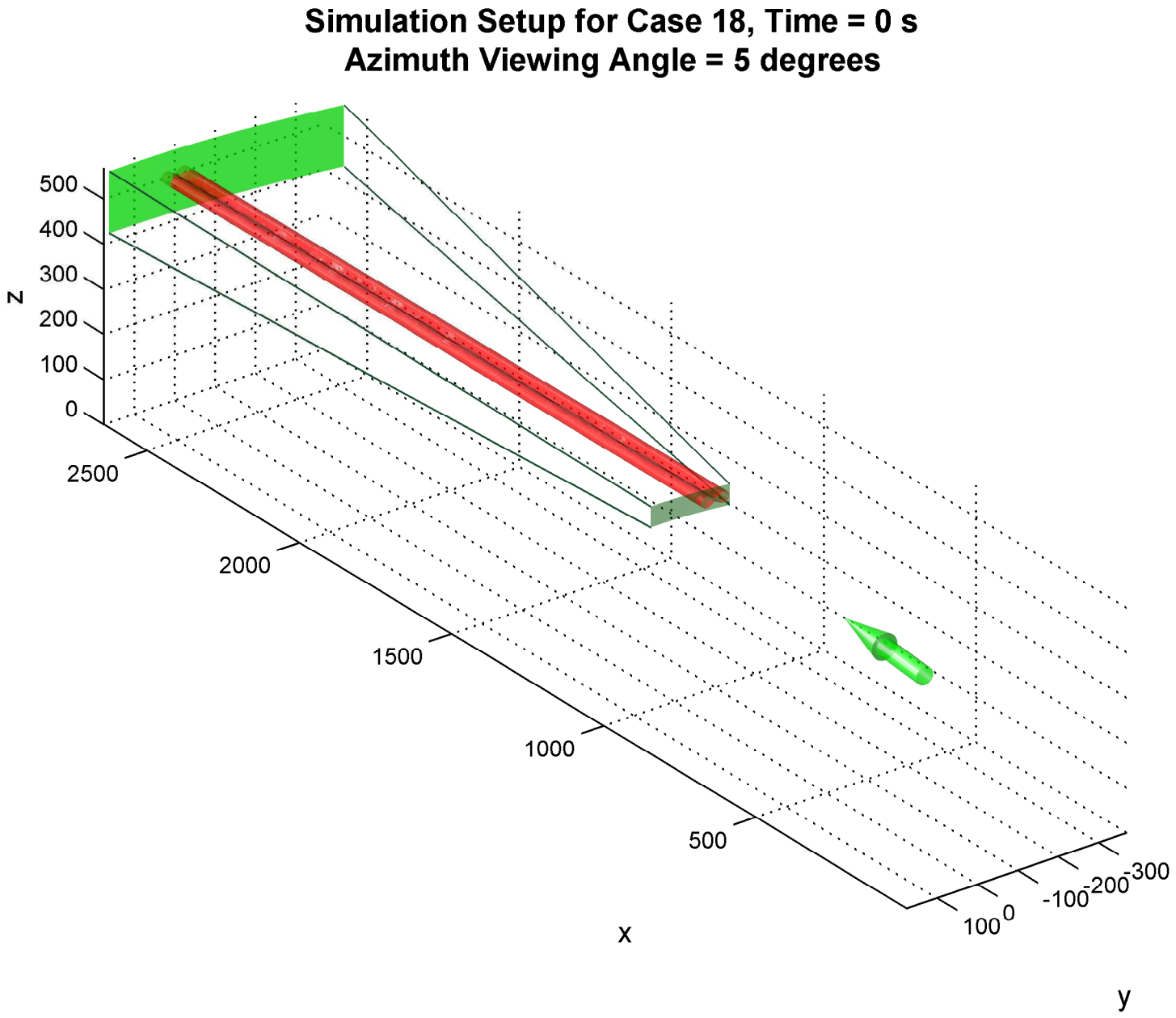
Simulation Setup for Case 18, Time = 0 s
Azimuth Viewing Angle = 5 degrees
z
500
400
300
200
100
0
2500
2000
1500
1000
500
x
100
0
-100
-200
-300
y

Simulation Results for Case 18, Time = 0 s
Azimuth Viewing Angle = 5 degrees

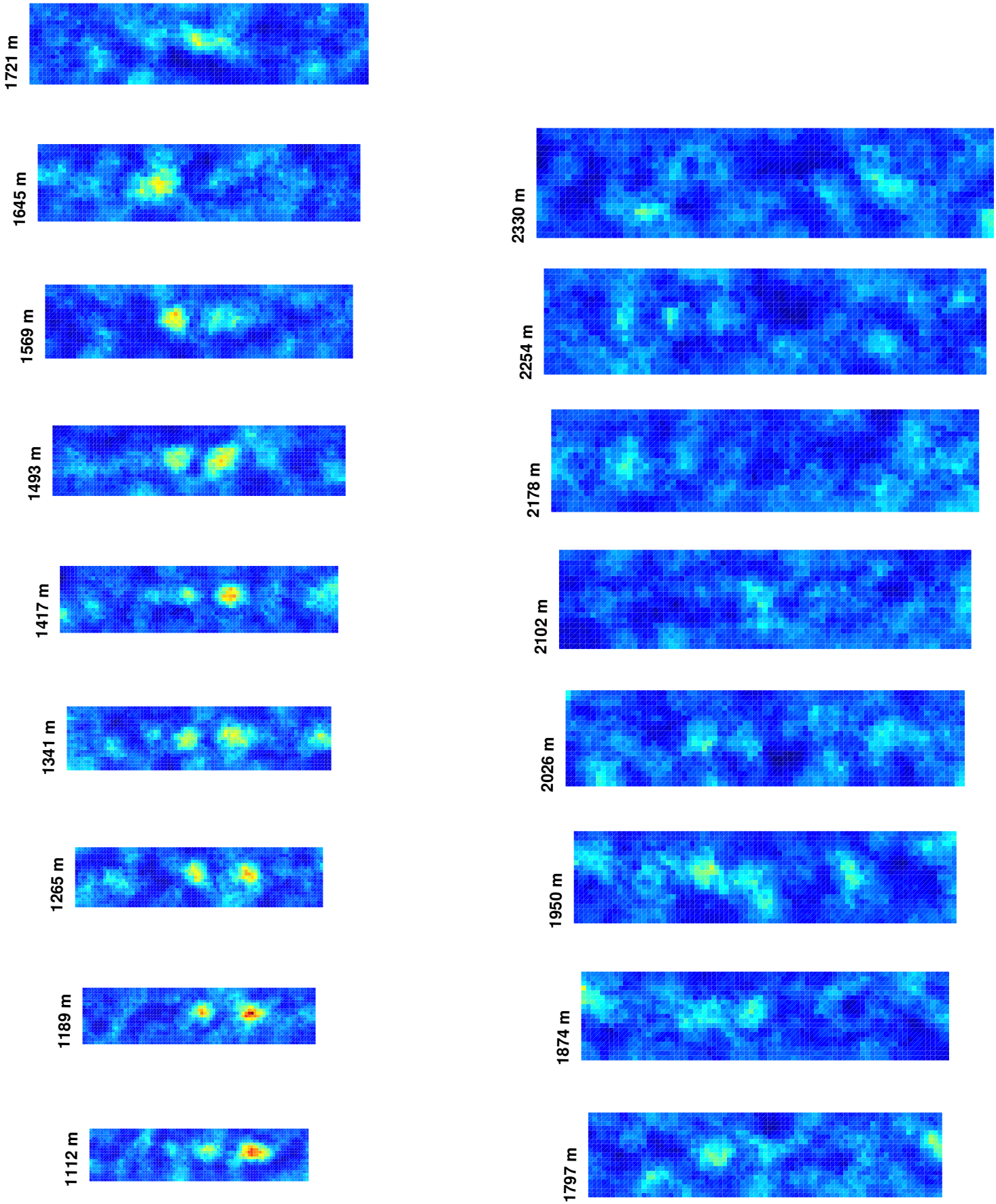

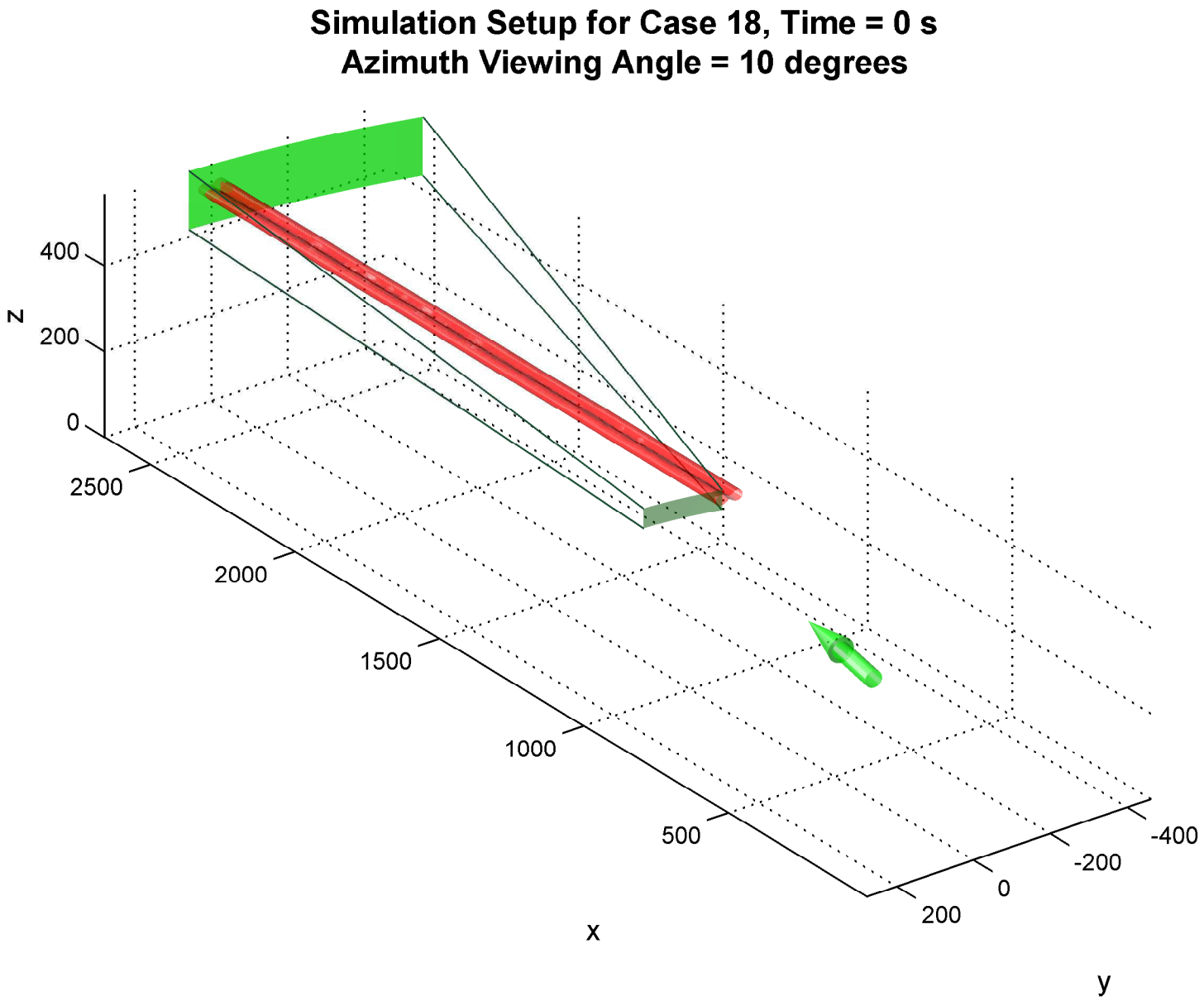
Simulation Setup for Case 18, Time = 0 s
Azimuth Viewing Angle = 10 degrees
400
200
0
z
2500
2000
1500
1000
500
x
200
0
-200
-400
y

Simulation Results for Case 18, Time = 0 s
Azimuth Viewing Angle = 10 degrees

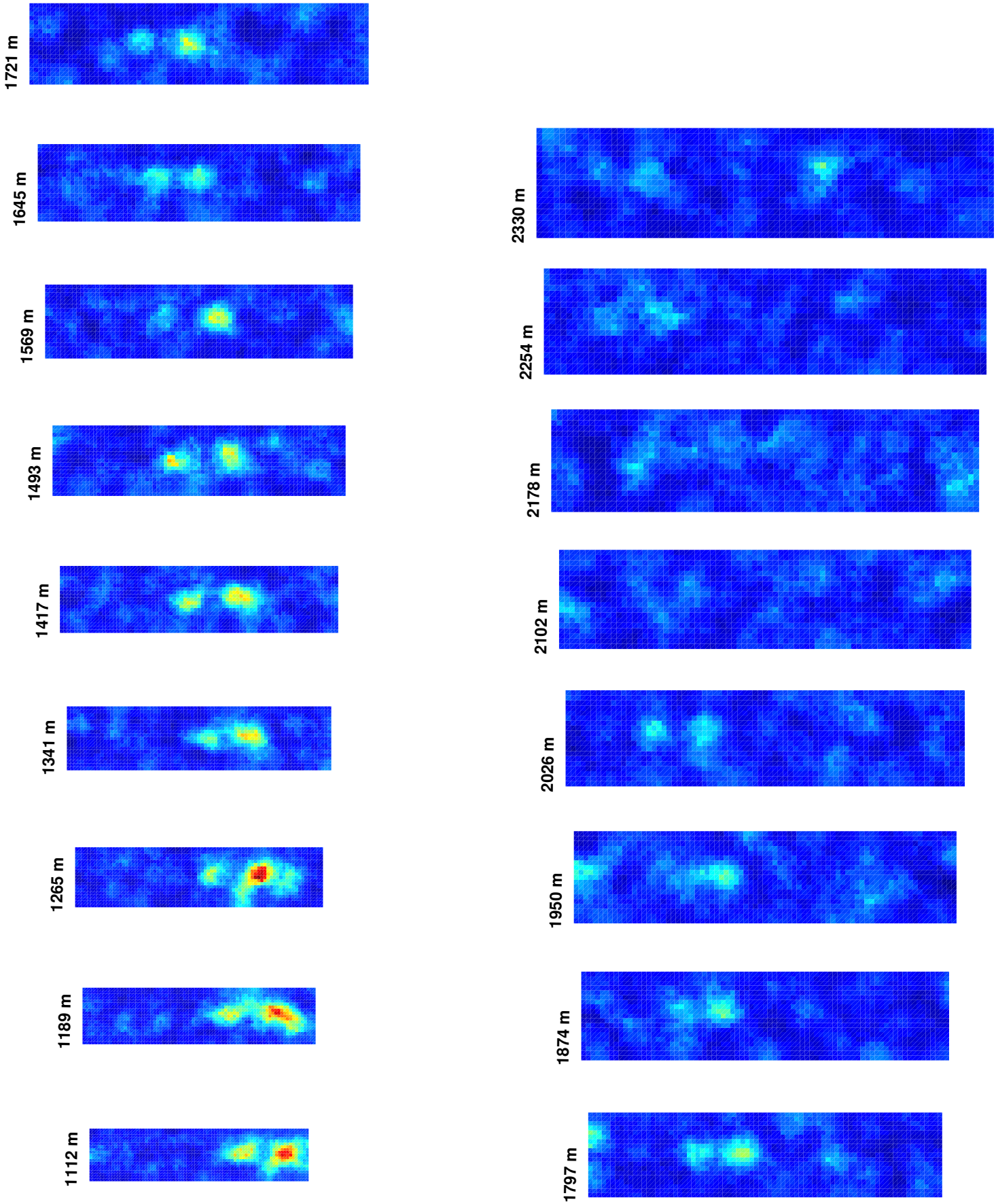

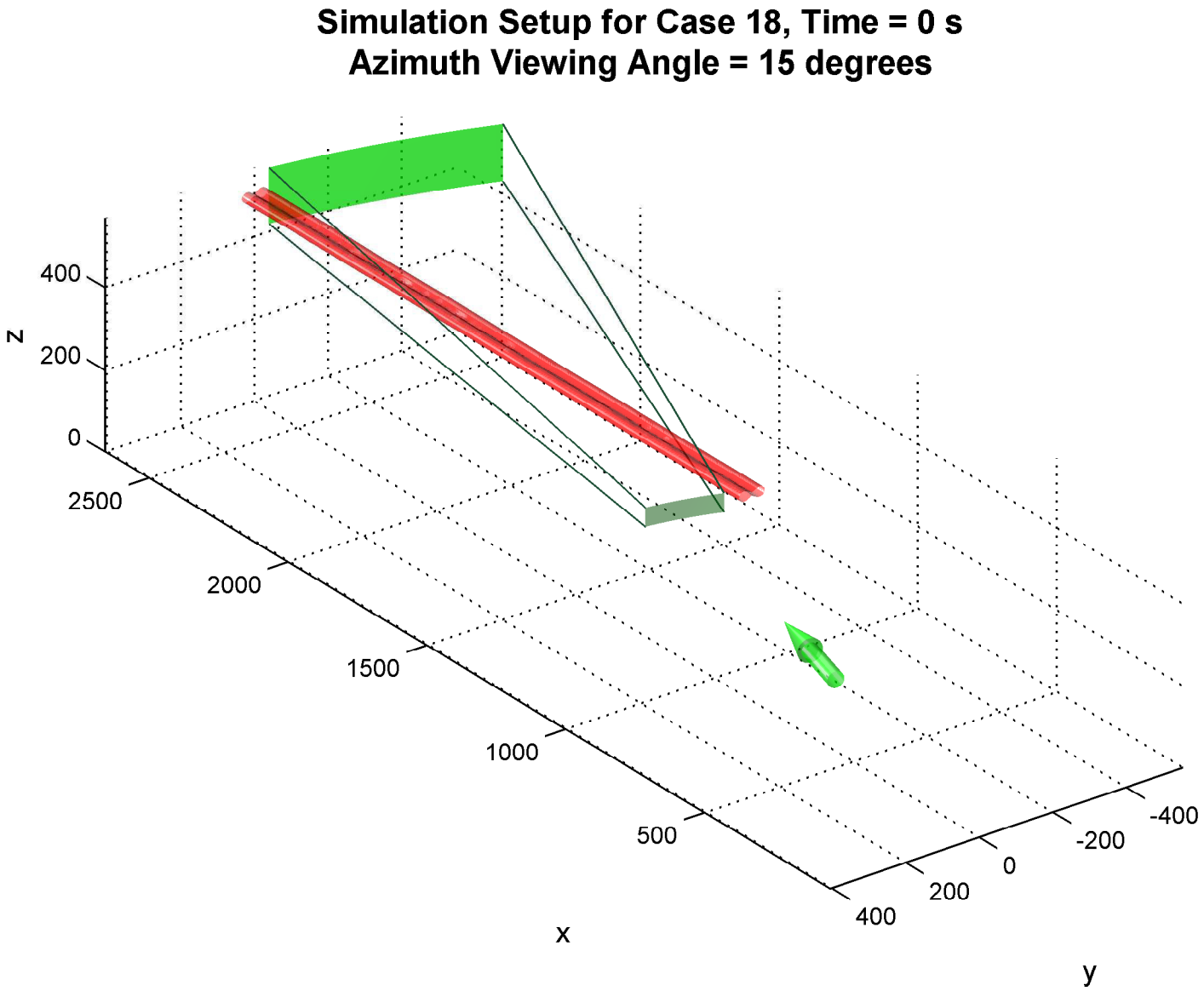
Simulation Setup for Case 18, Time = 0 s
Azimuth Viewing Angle = 15 degrees
z
400
200
0
2500
2000
1500
1000
500
x
400
200
0
-200
-400
y

Simulation Results for Case 18, Time = 0 s
Azimuth Viewing Angle = 15 degrees

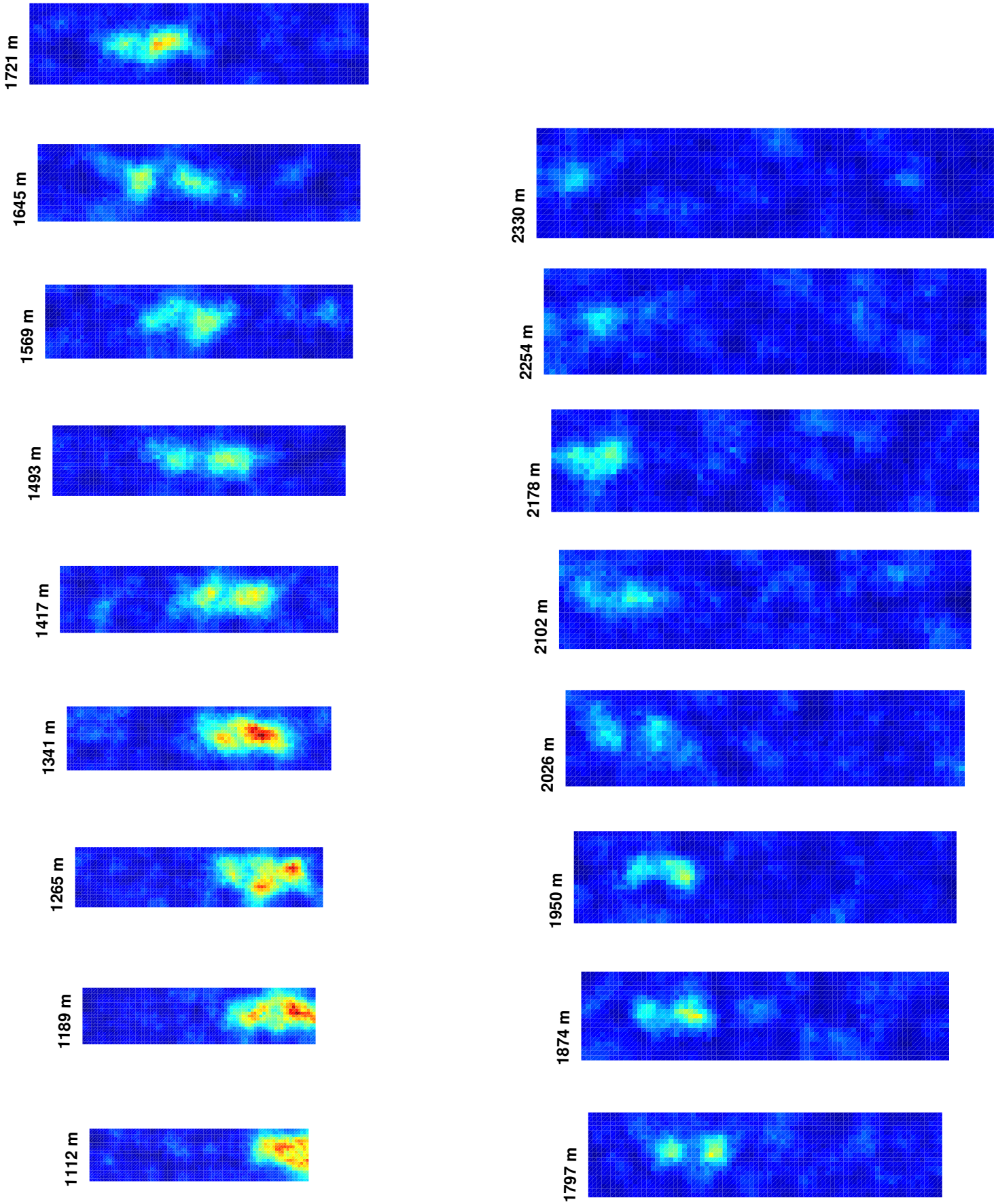

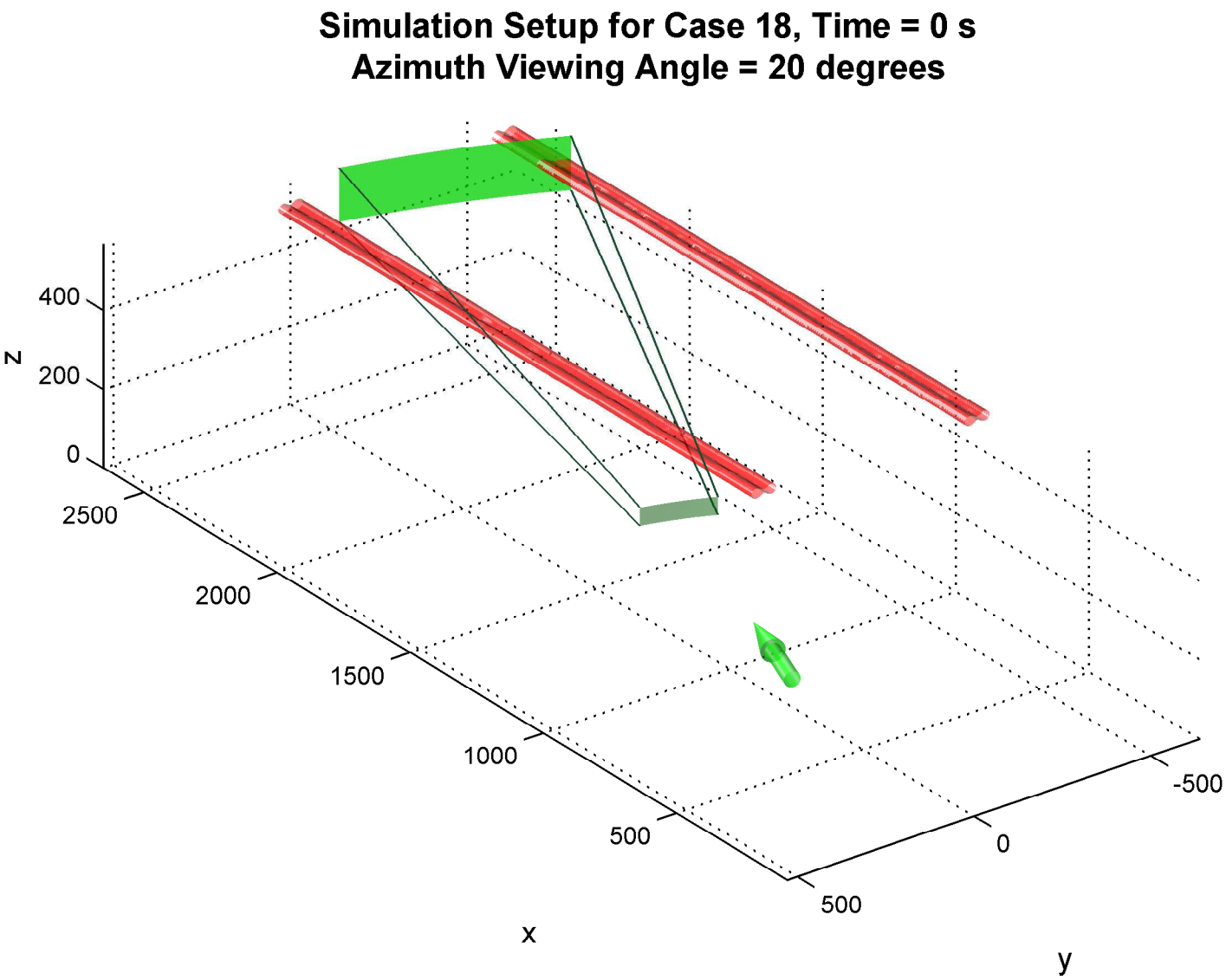
Simulation Setup for Case 18, Time = 0 s
Azimuth Viewing Angle = 20 degrees
z
400
200
0
2500
2000
1500
1000
500
x
500
0
-500
y

Simulation Results for Case 18, Time = 0 s
Azimuth Viewing Angle = 20 degrees

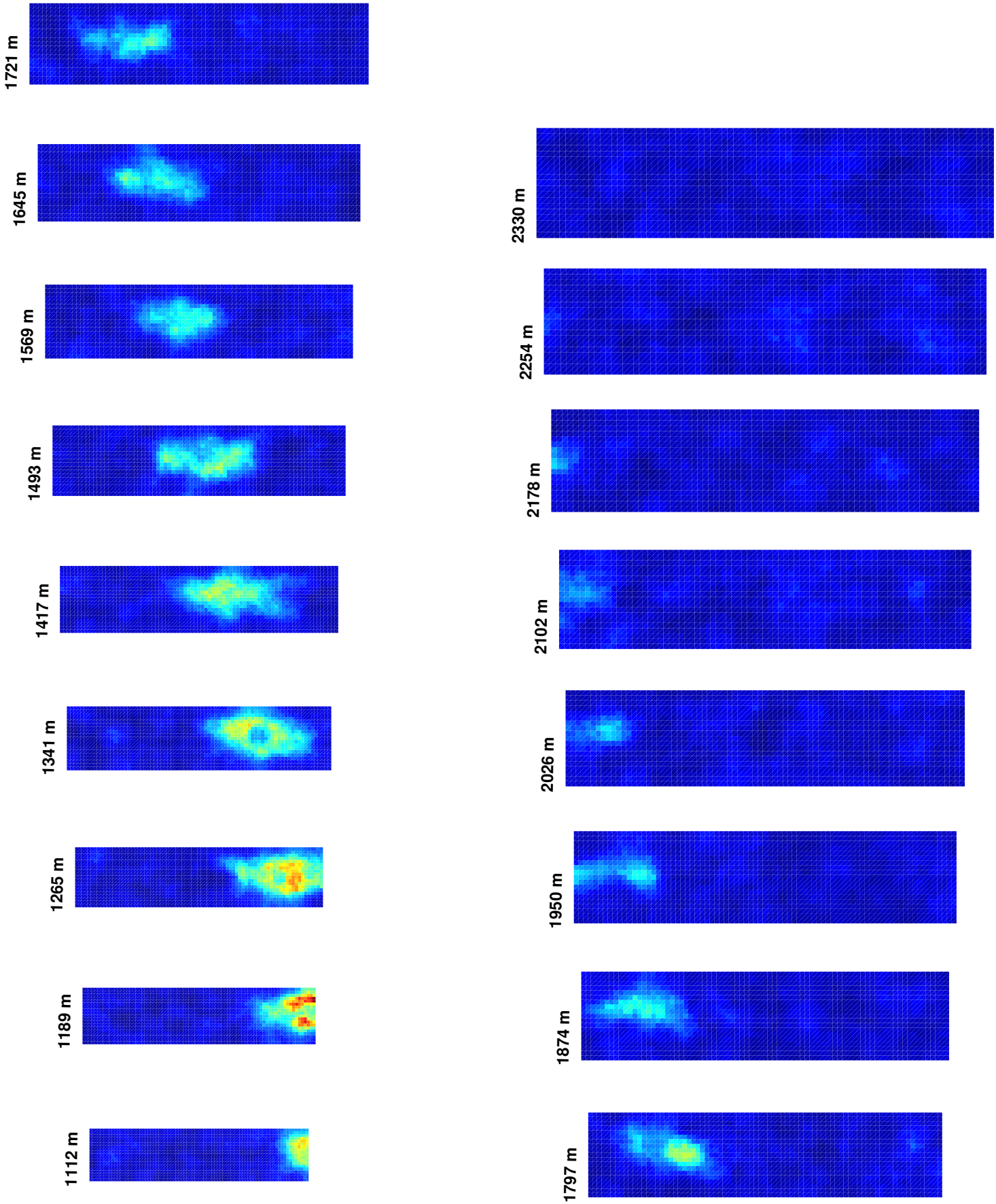

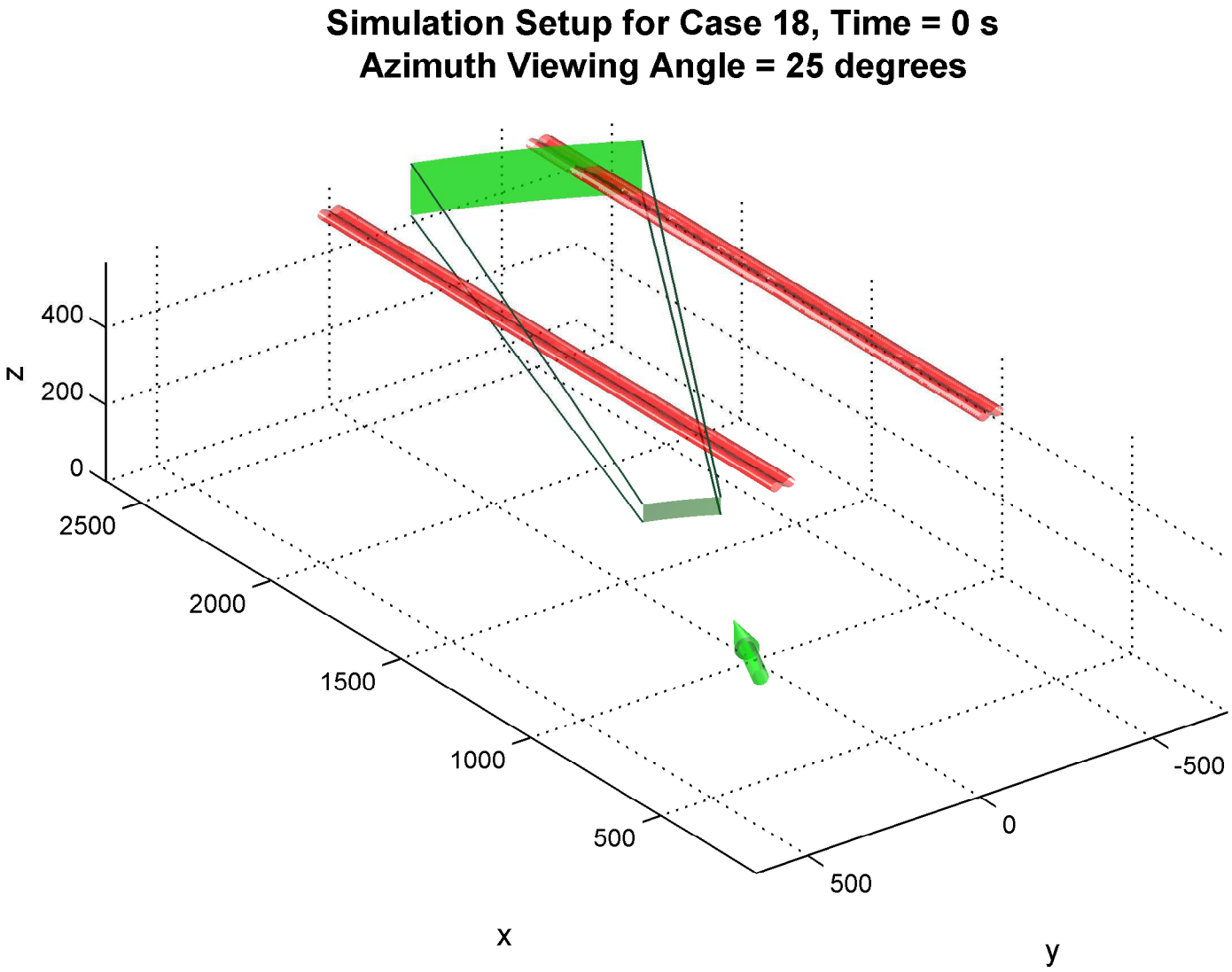
Simulation Setup for Case 18, Time = 0 s
Azimuth Viewing Angle = 25 degrees
z
400
200
0
2500
2000
1500
1000
500
x
500
0
-500
y

Simulation Results for Case 18, Time = 0 s
Azimuth Viewing Angle = 25 degrees

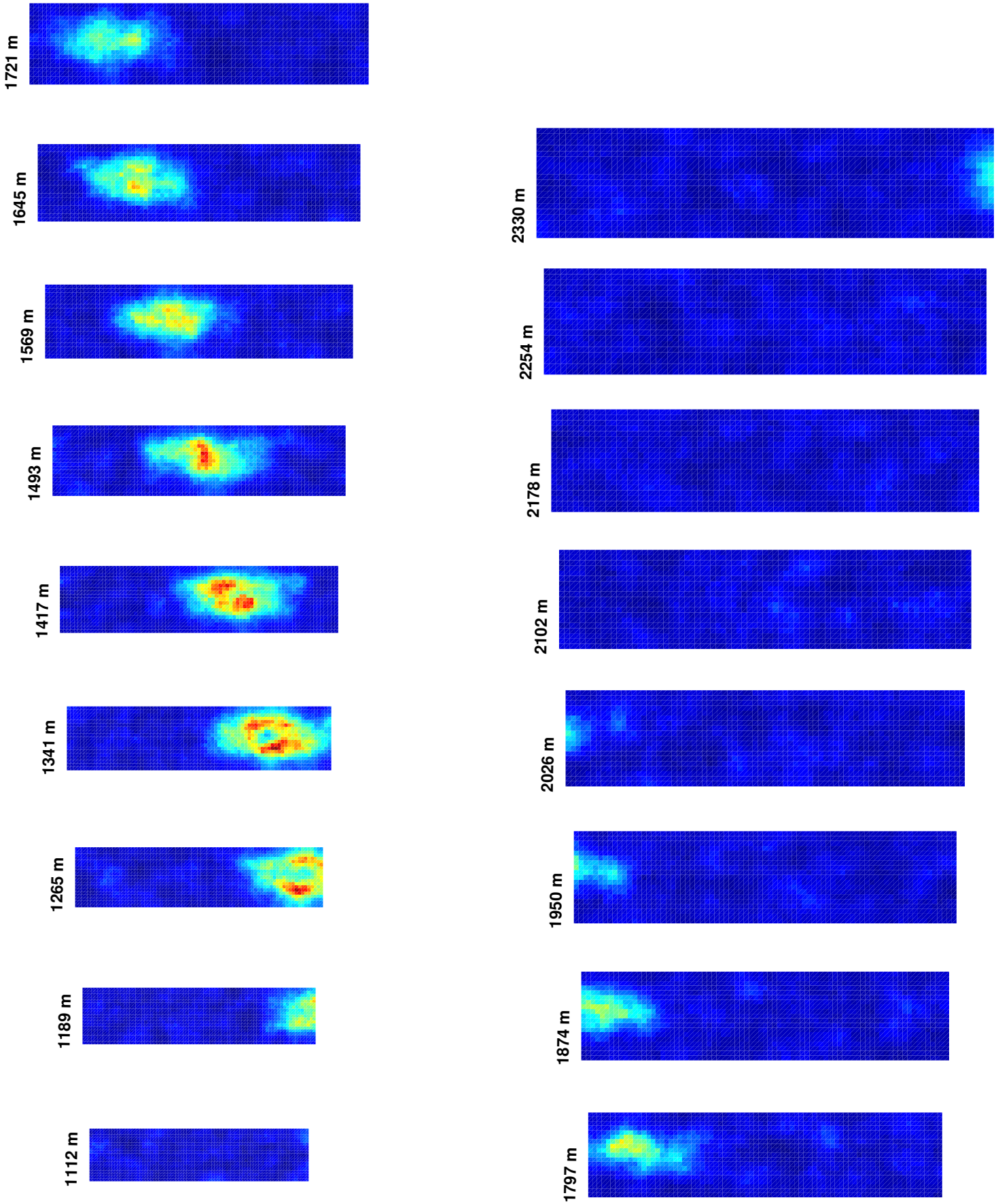

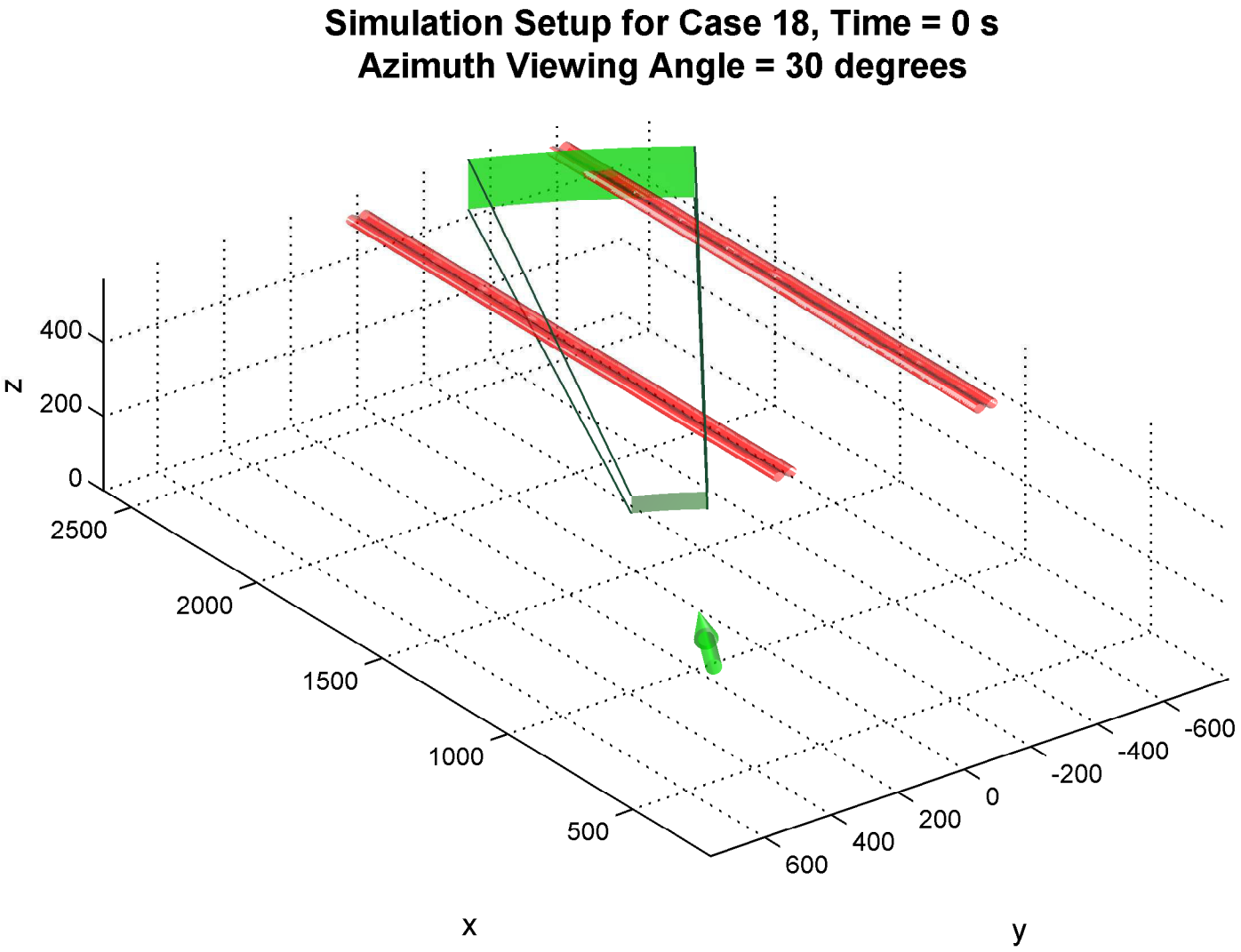
Simulation Setup for Case 18, Time = 0 s
Azimuth Viewing Angle = 30 degrees
z
400
200
0
2500
2000
1500
1000
500
x
600
400
200
0
-200
-400
-600
y

Simulation Results for Case 18, Time = 0 s
Azimuth Viewing Angle = 30 degrees

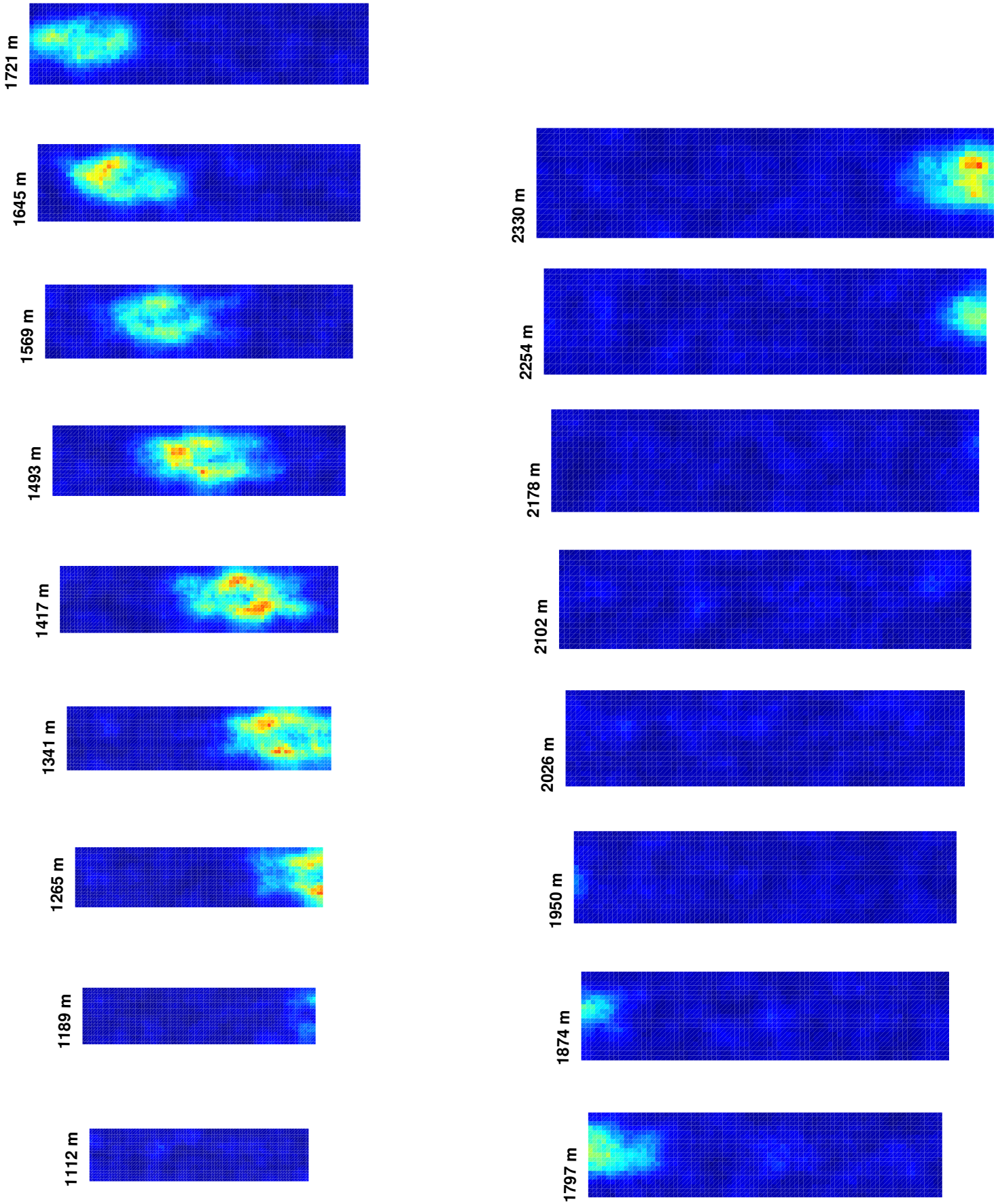

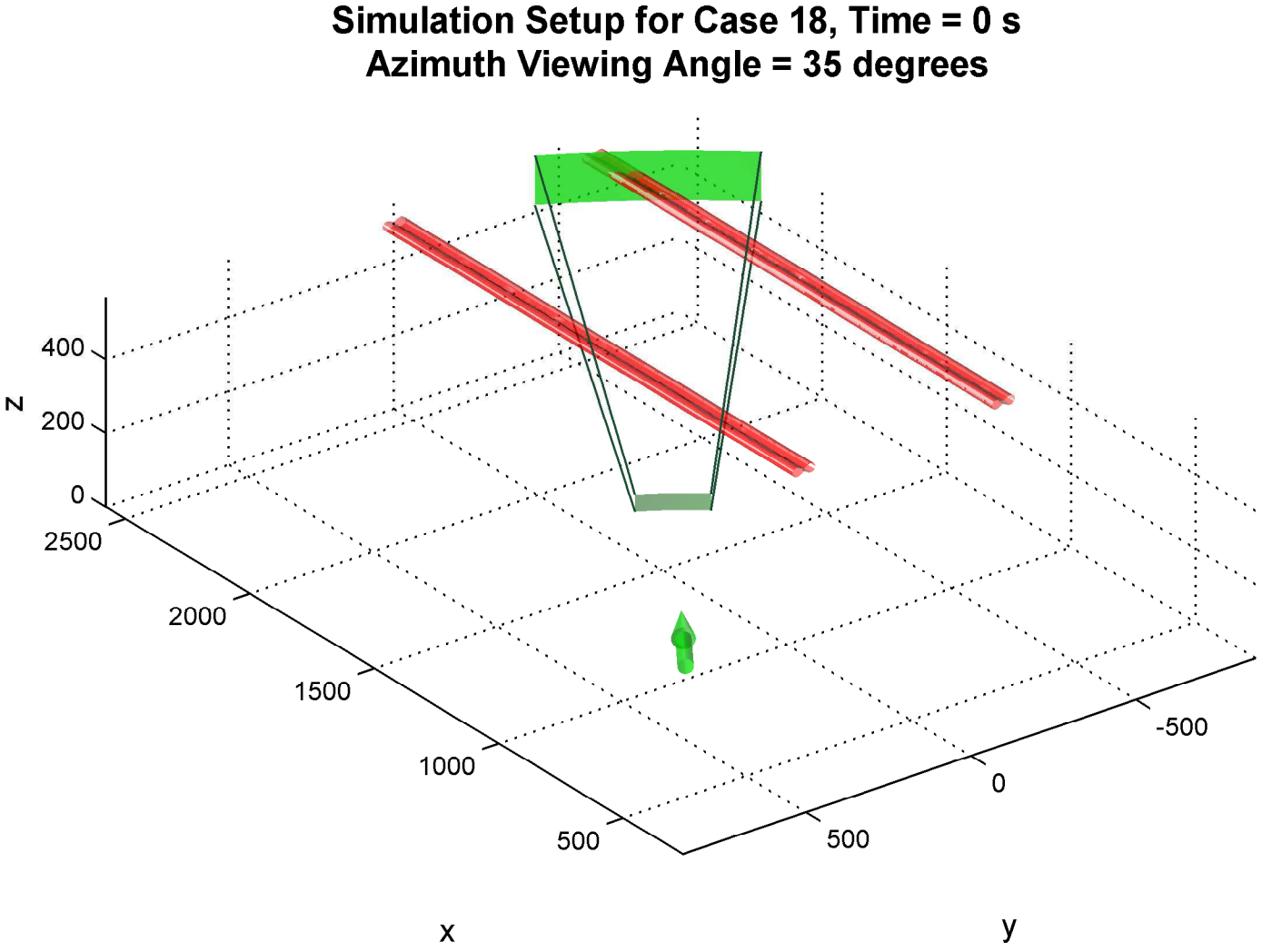
Simulation Setup for Case 18, Time = 0 s
Azimuth Viewing Angle = 35 degrees
z
400
200
0
2500
2000
1500
1000
500
x
500
0
-500
y

Simulation Results for Case 18, Time = 0 s
Azimuth Viewing Angle = 35 degrees

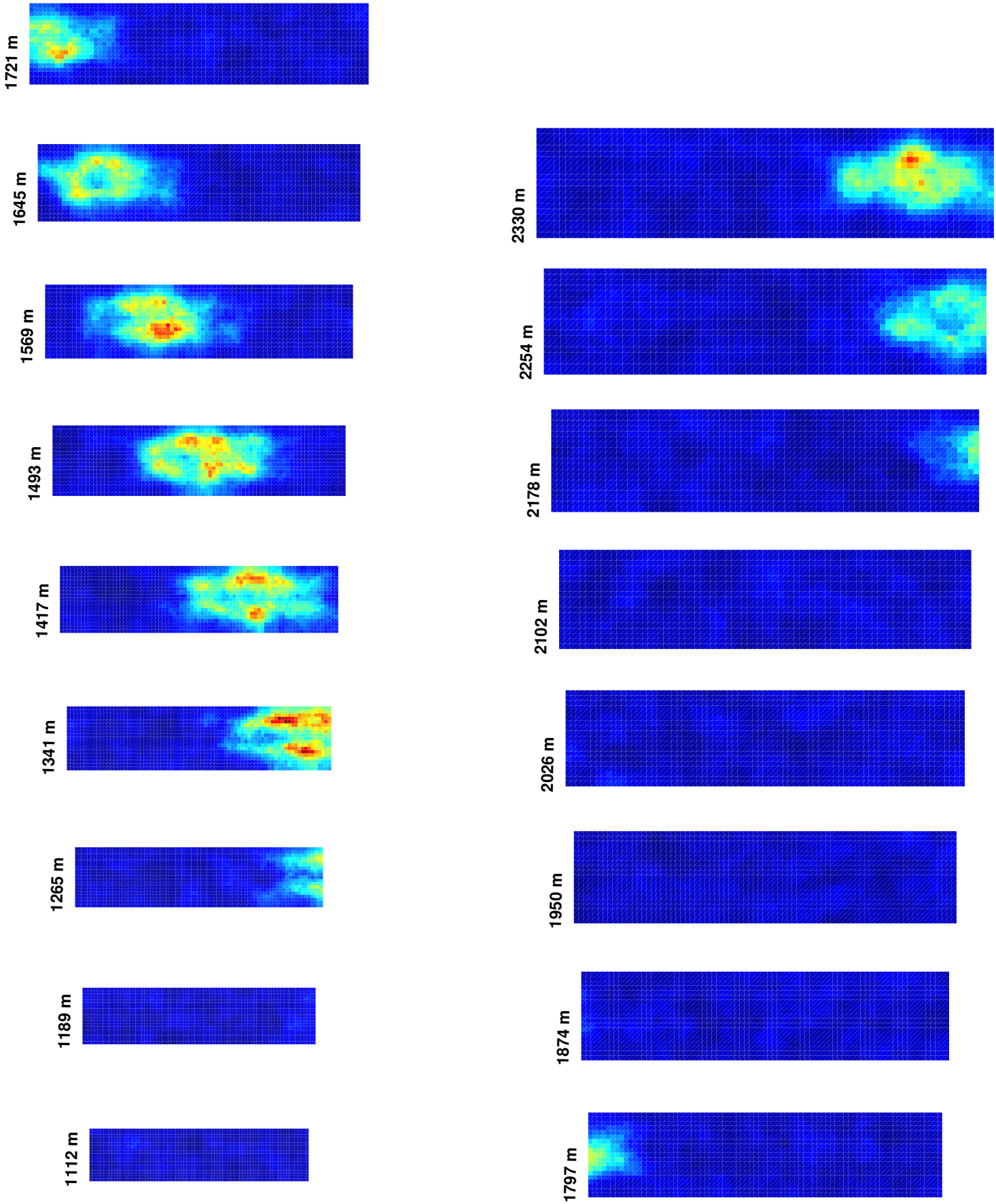

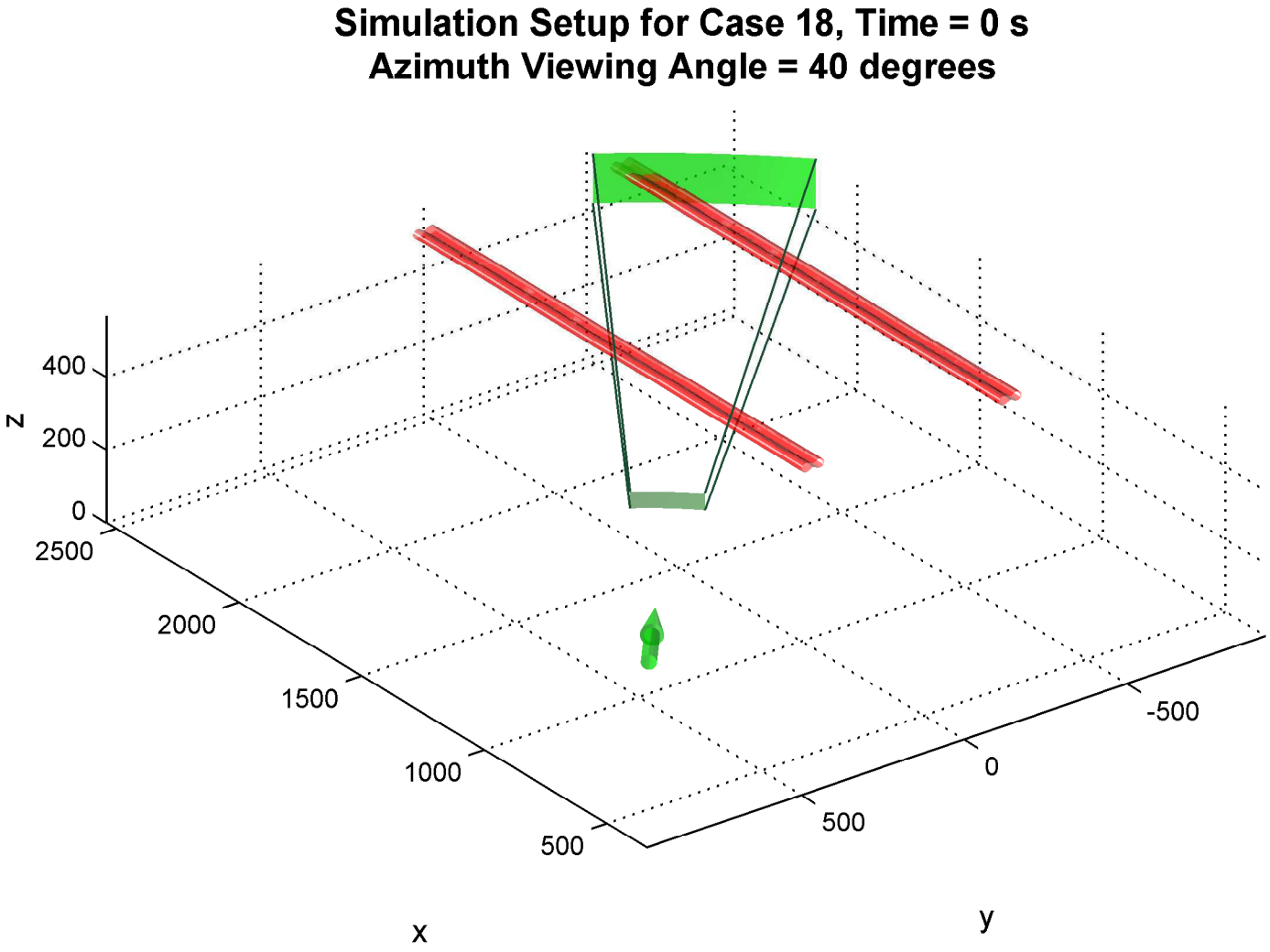
Simulation Setup for Case 18, Time = 0 s
Azimuth Viewing Angle = 40 degrees
z
400
200
0
2500
2000
1500
1000
500
x
-500
0
500
y

Simulation Results for Case 18, Time = 0 s
Azimuth Viewing Angle = 40 degrees

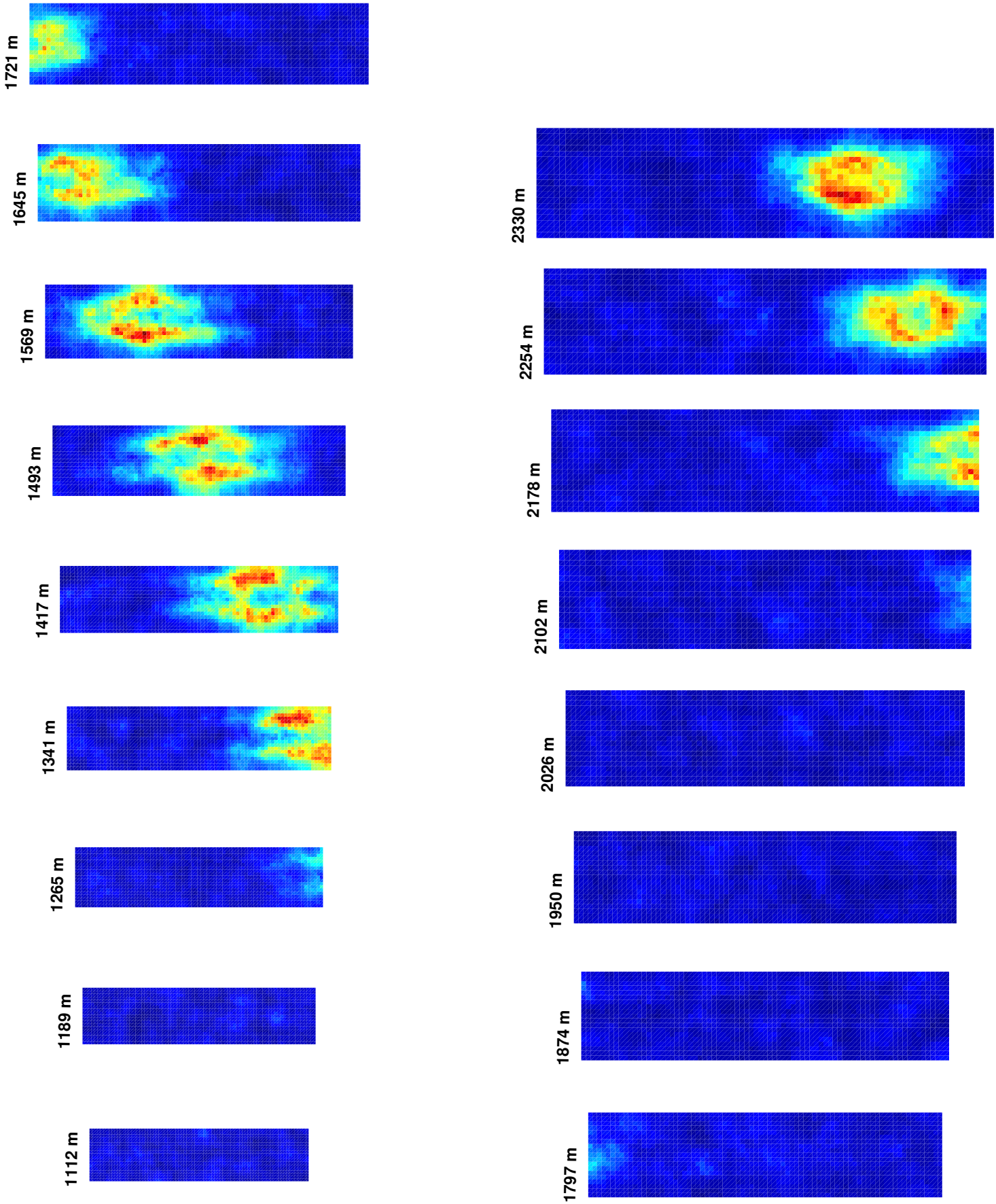

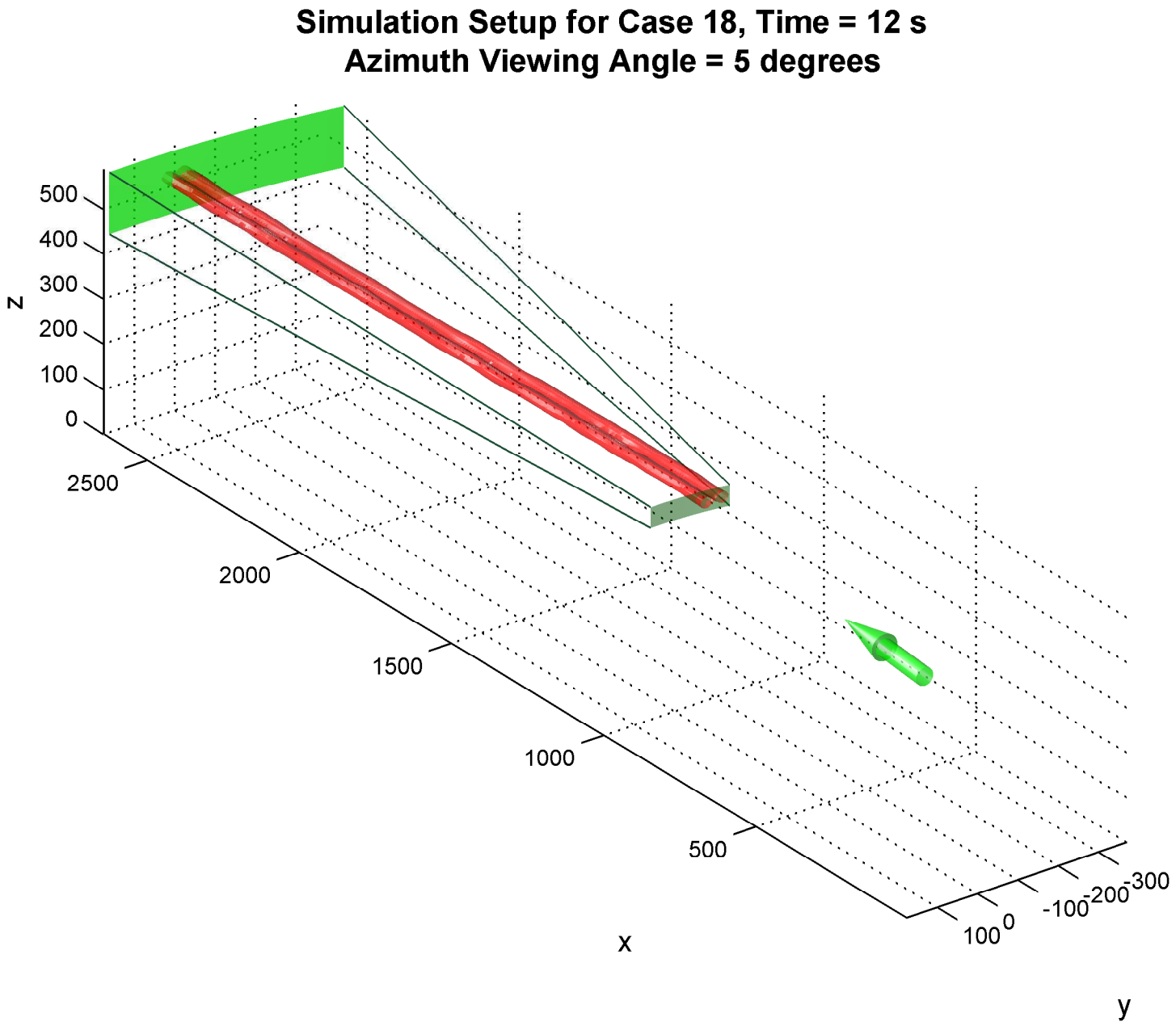
Simulation Setup for Case 18, Time = 12 s
Azimuth Viewing Angle = 5 degrees
z
500
400
300
200
100
0
2500
2000
1500
1000
500
x
100
0
-100
-200
-300
y

Simulation Results for Case 18, Time = 12 s
Azimuth Viewing Angle = 5 degrees

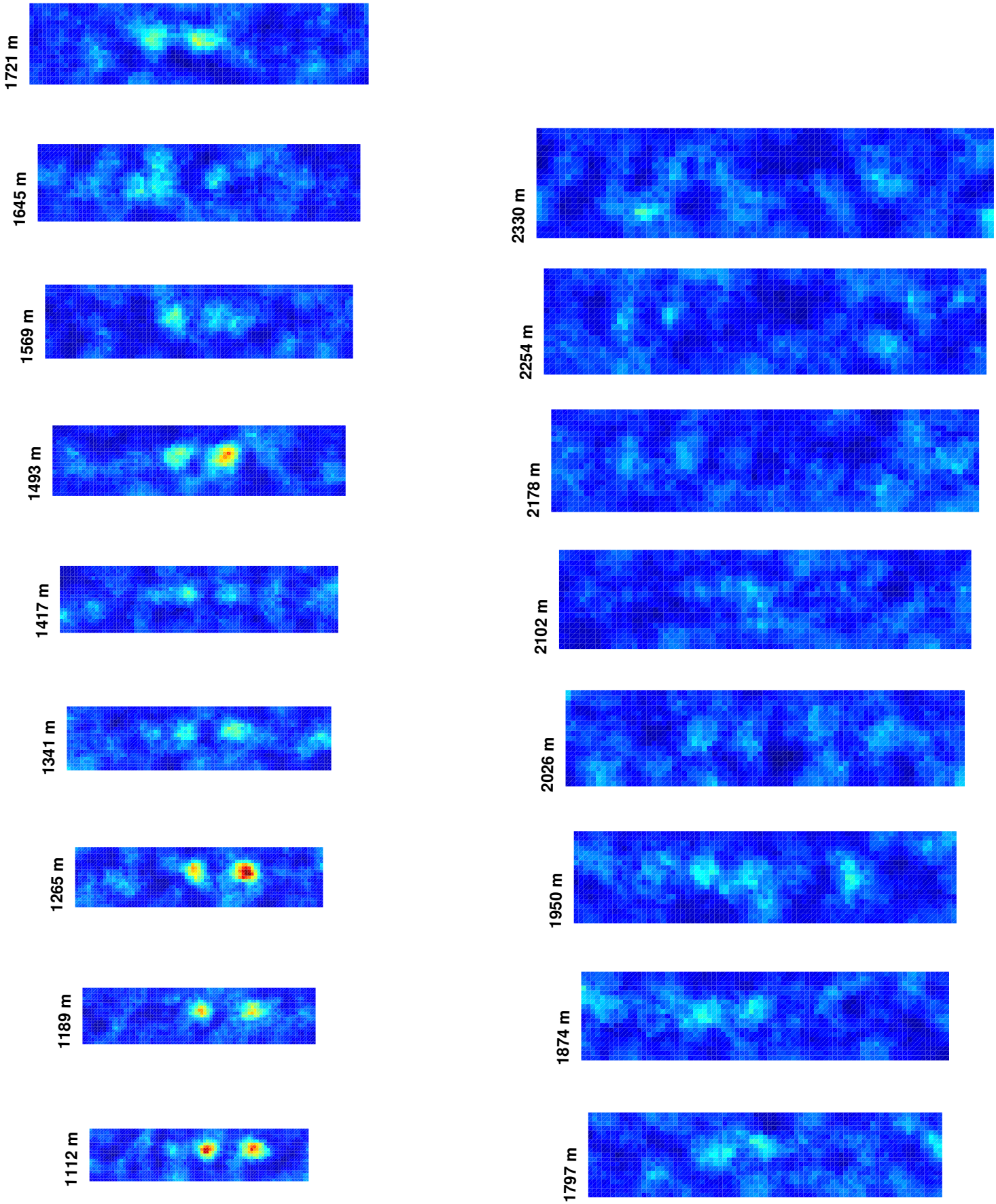

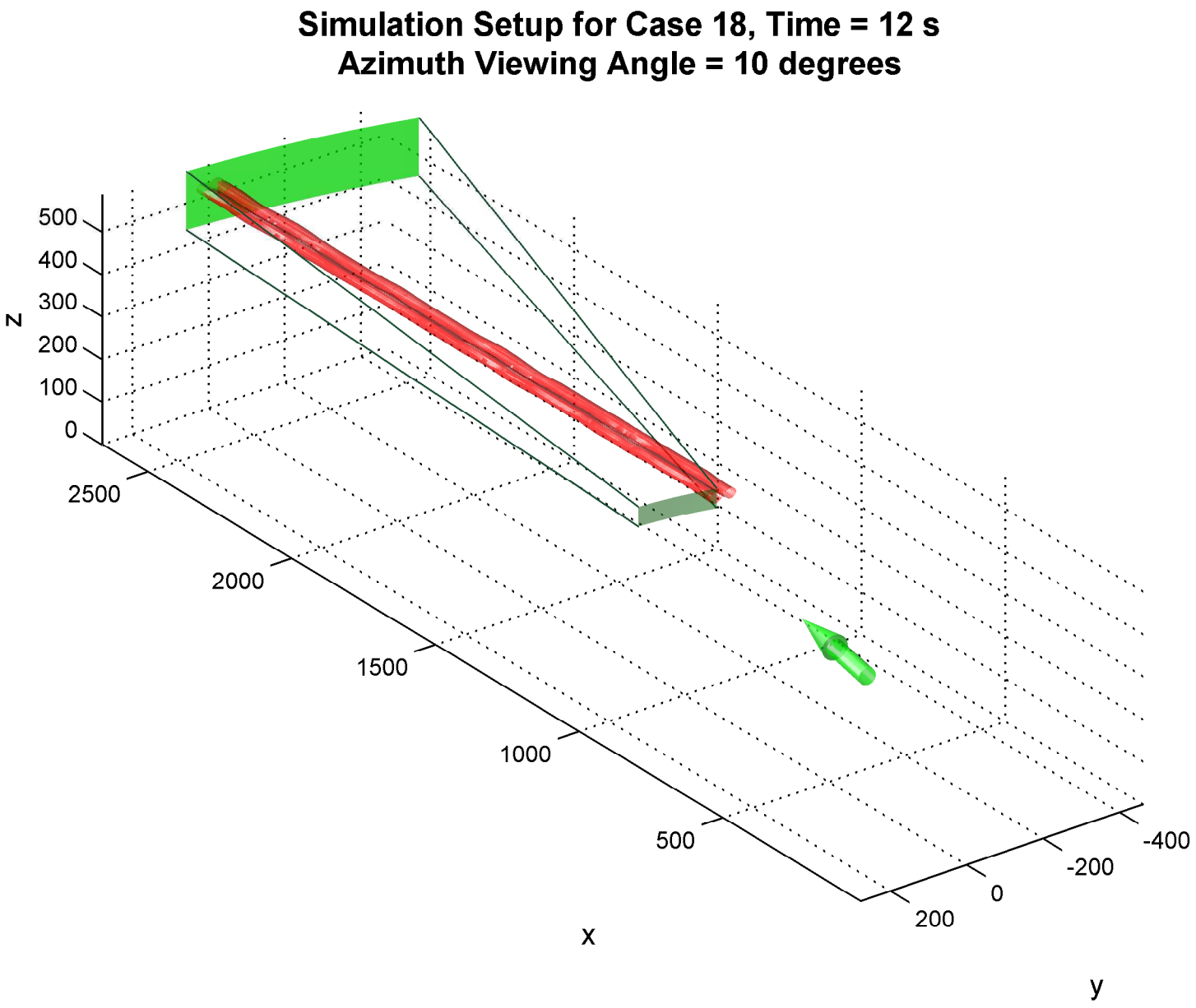
Simulation Setup for Case 18, Time = 12 s
Azimuth Viewing Angle = 10 degrees
z
500
400
300
200
100
0
2500
2000
1500
1000
500
x
200
0
-200
-400
y

Simulation Results for Case 18, Time = 12 s
Azimuth Viewing Angle = 10 degrees

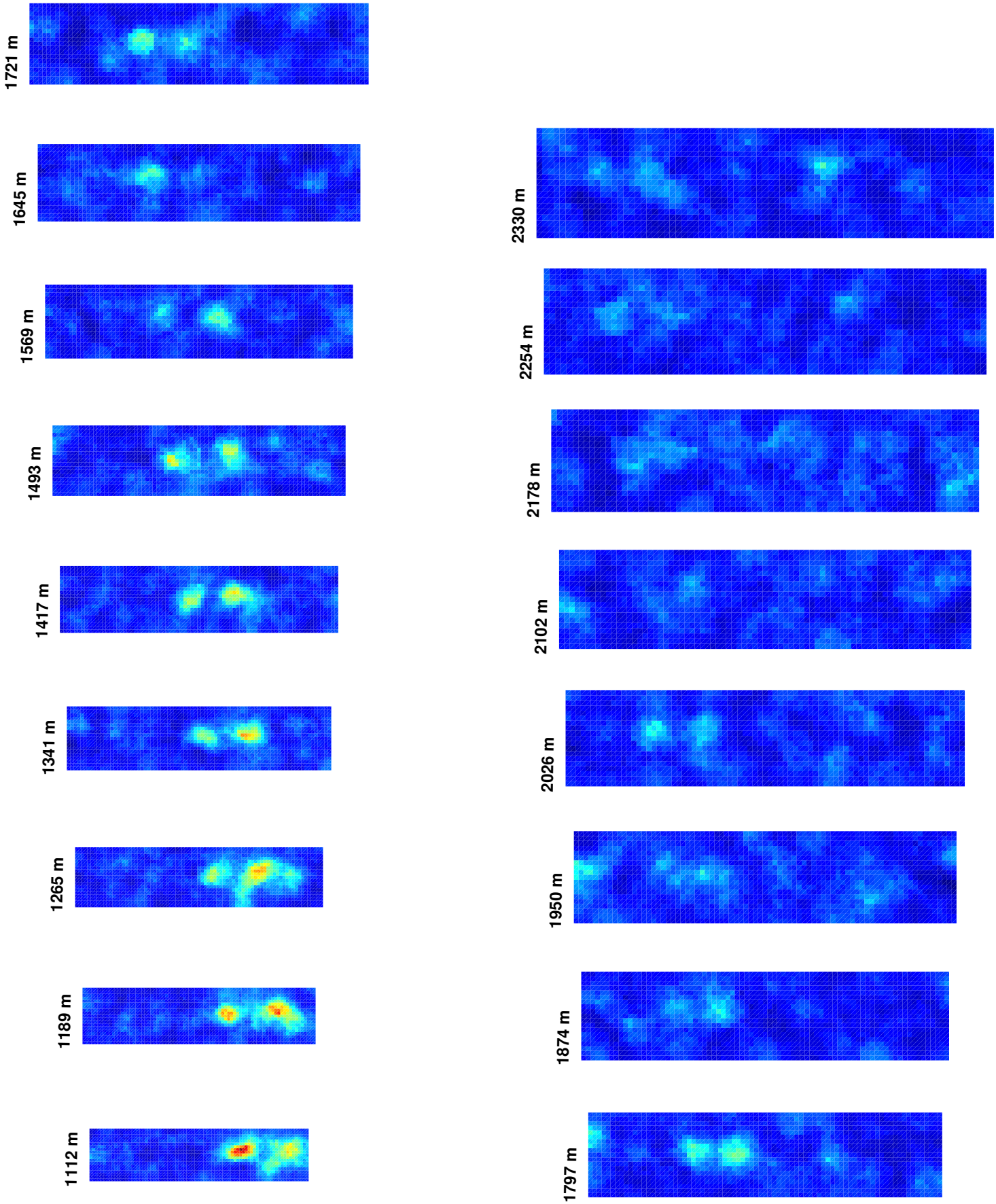

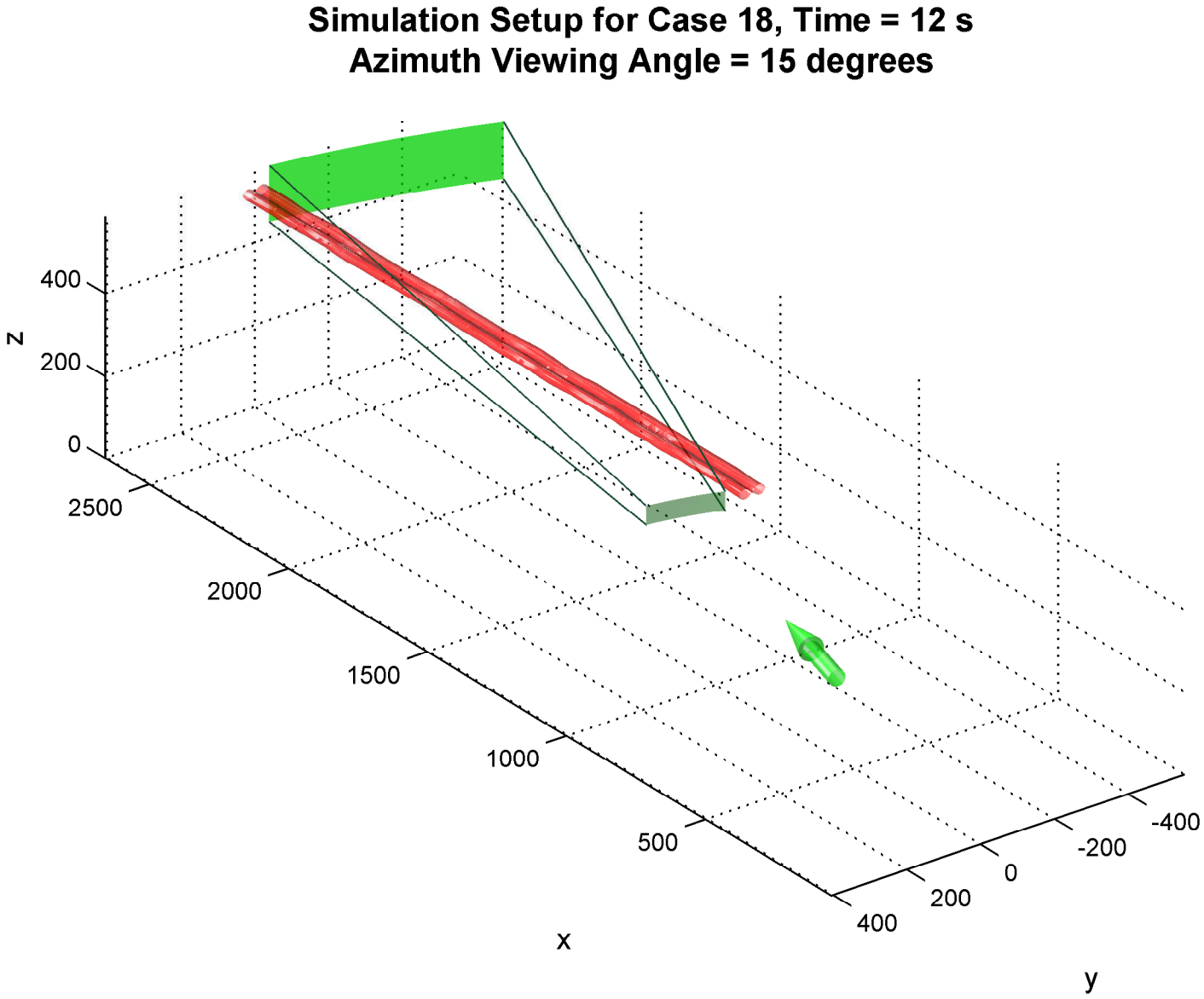
Simulation Setup for Case 18, Time = 12 s
Azimuth Viewing Angle = 15 degrees
z
400
200
0
2500
2000
1500
1000
500
x
400
200
0
-200
-400
y

Simulation Results for Case 18, Time = 12 s
Azimuth Viewing Angle = 15 degrees

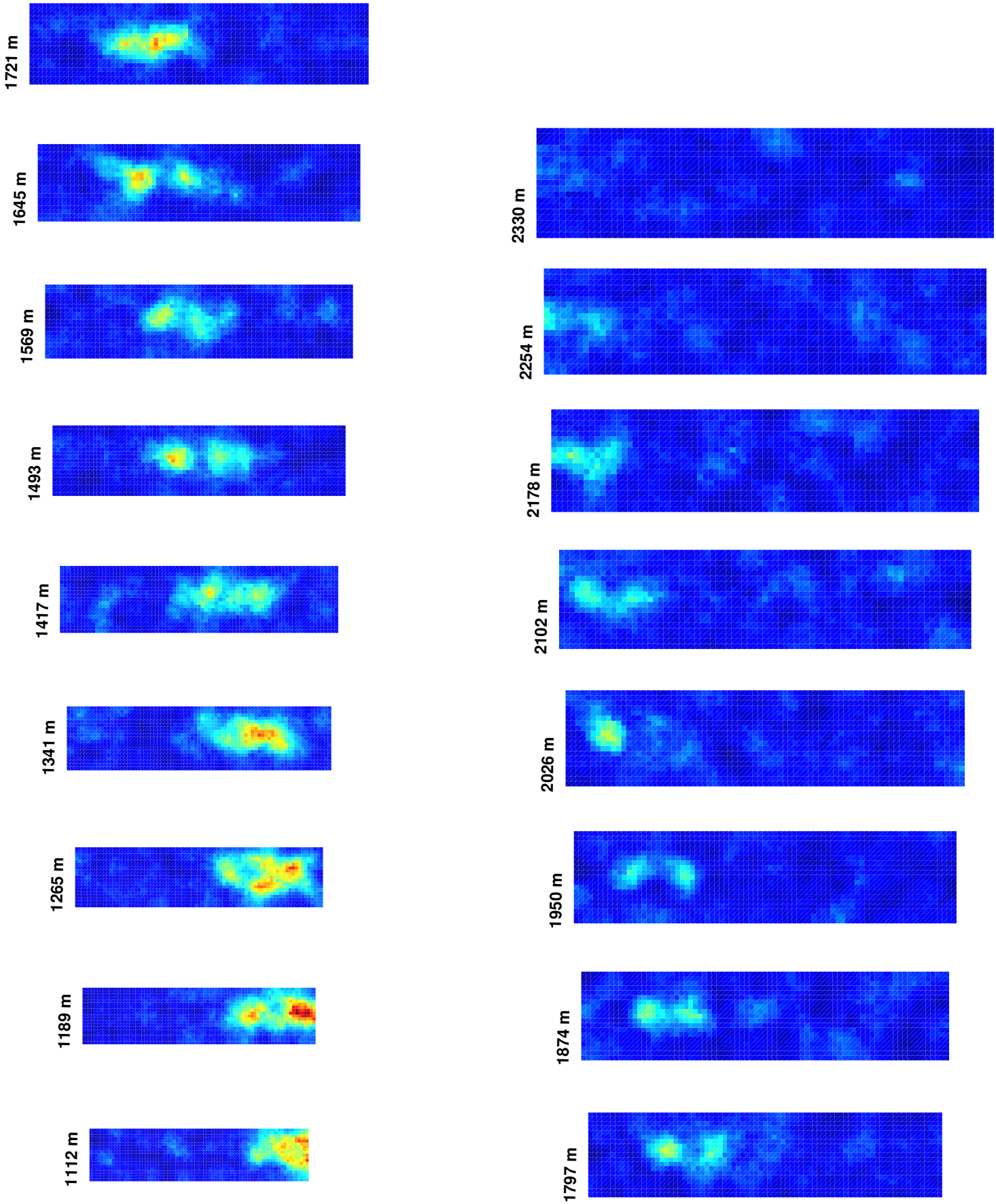

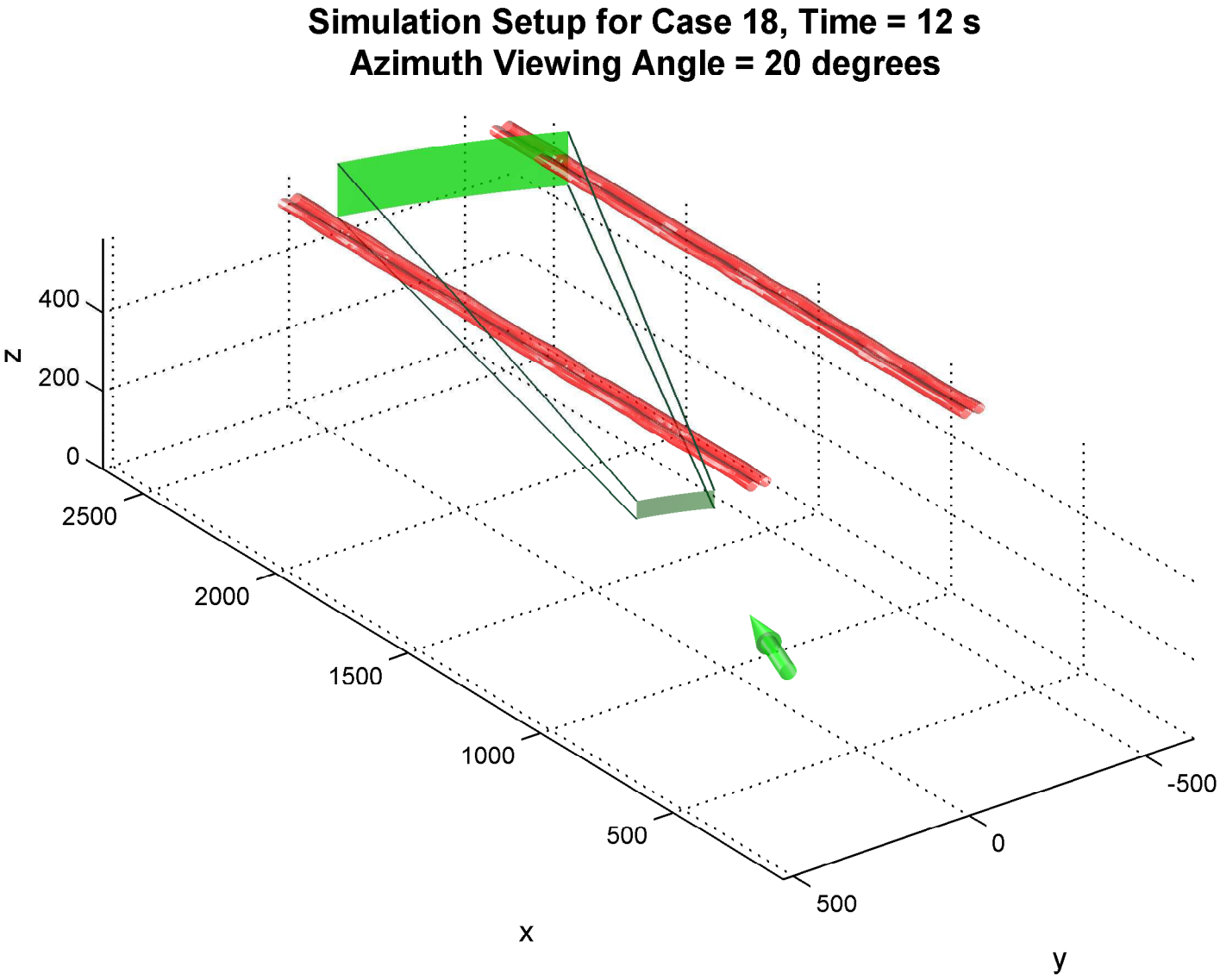
Simulation Setup for Case 18, Time = 12 s
Azimuth Viewing Angle = 20 degrees
z
400
200
0
2500
2000
1500
1000
500
x
500
0
-500
y

Simulation Results for Case 18, Time = 12 s
Azimuth Viewing Angle = 20 degrees

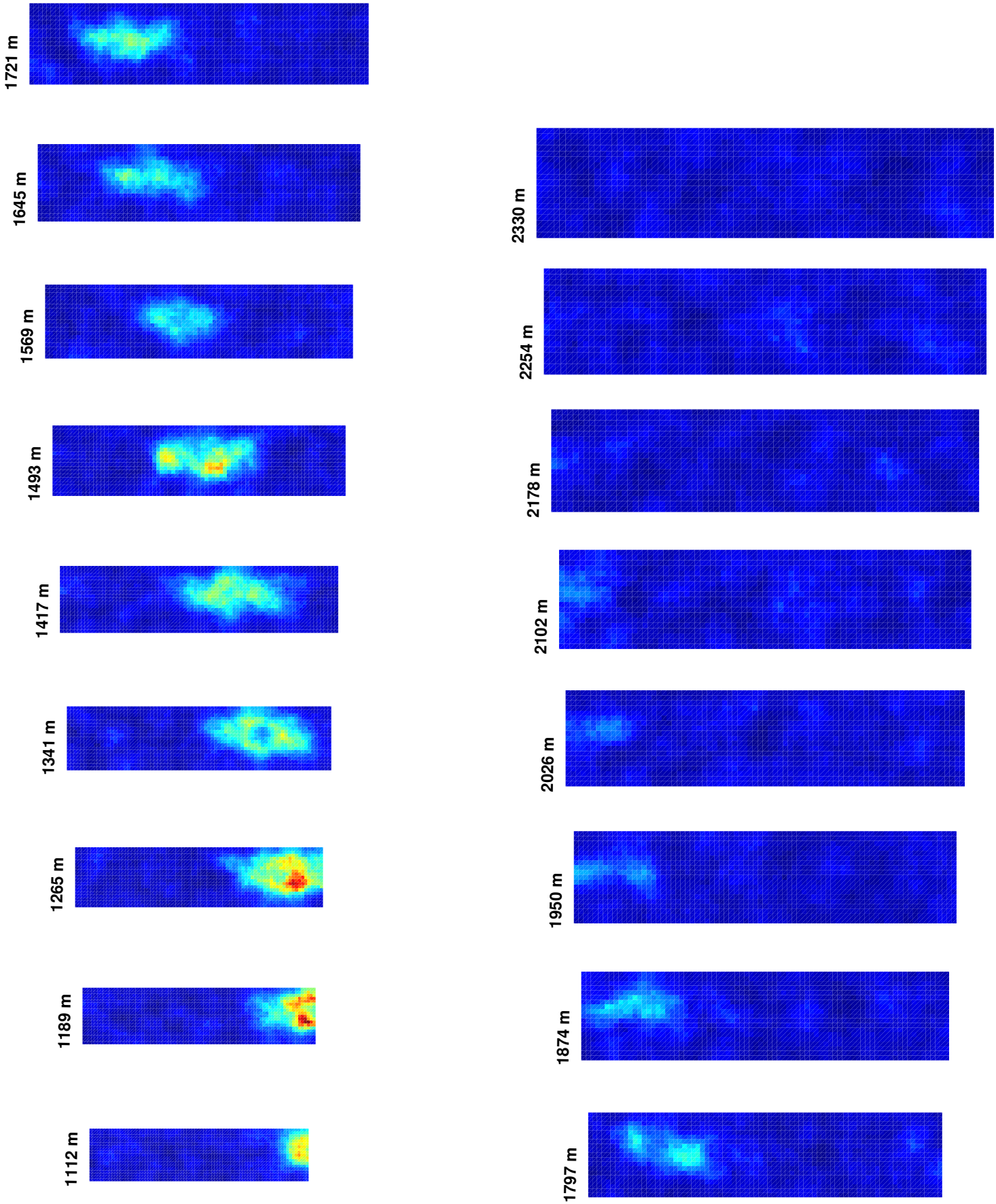

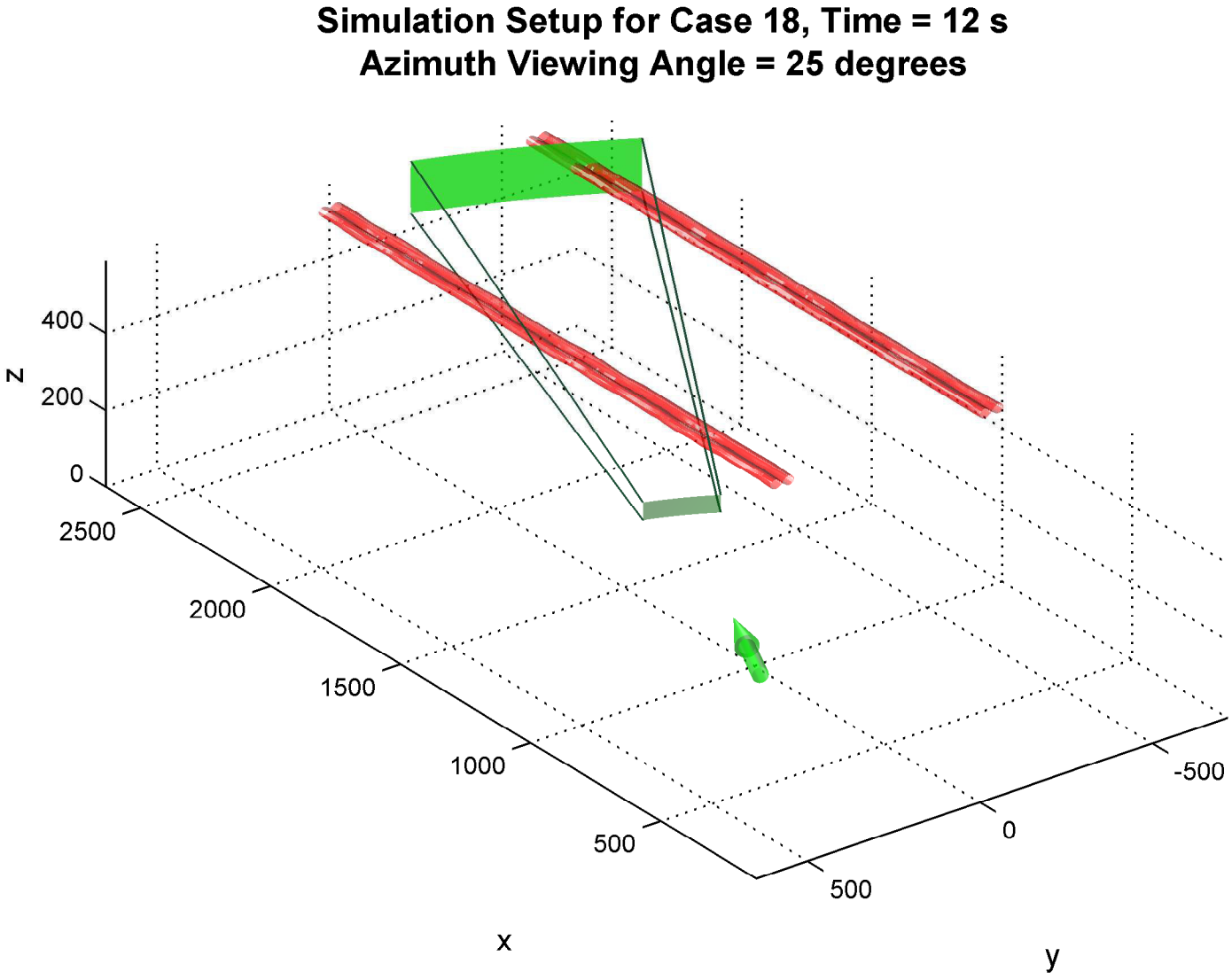
Simulation Setup for Case 18, Time = 12 s
Azimuth Viewing Angle = 25 degrees
z
400
200
0
2500
2000
1500
1000
500
x
500
0
-500
y

Simulation Results for Case 18, Time = 12 s
Azimuth Viewing Angle = 25 degrees

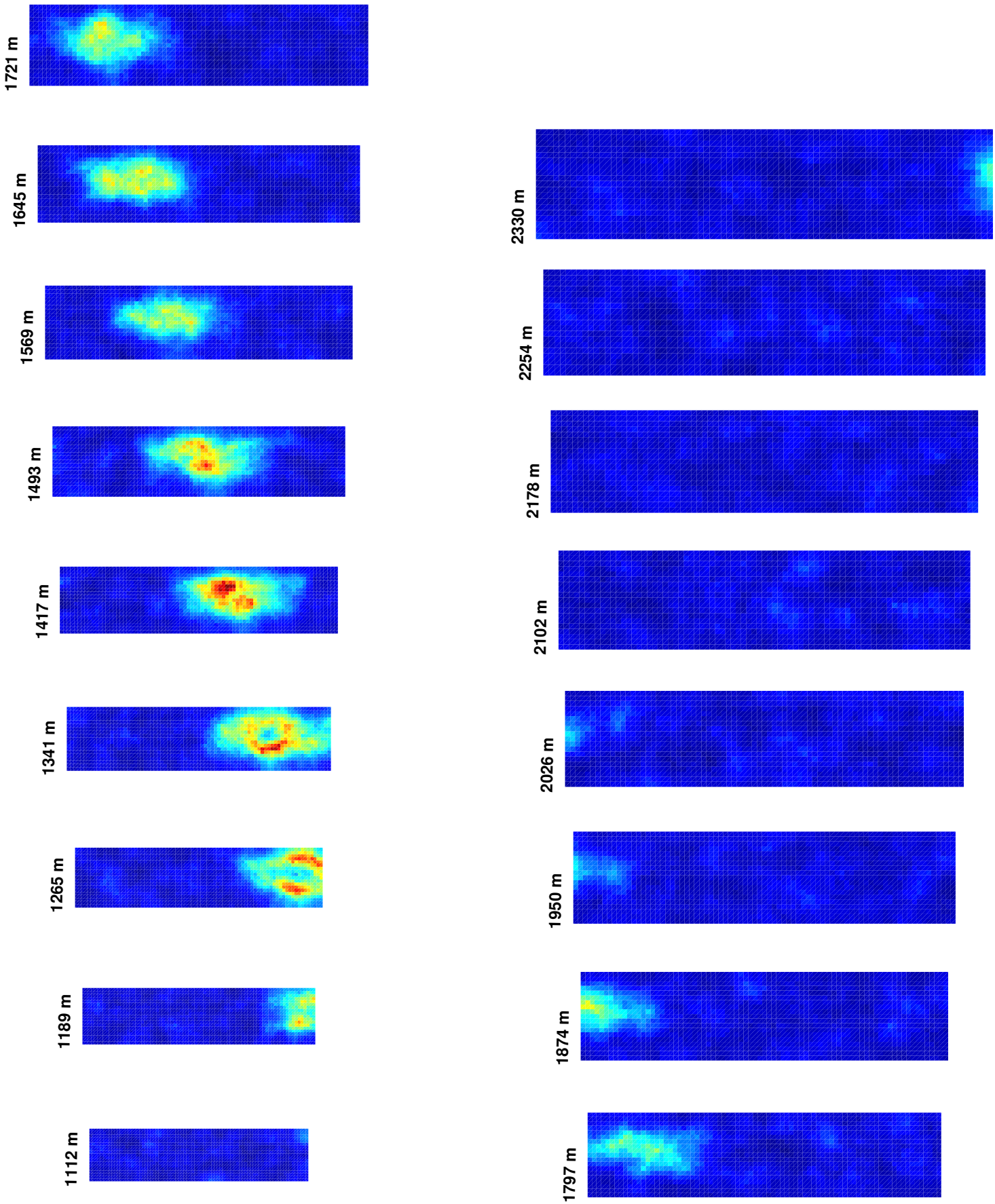

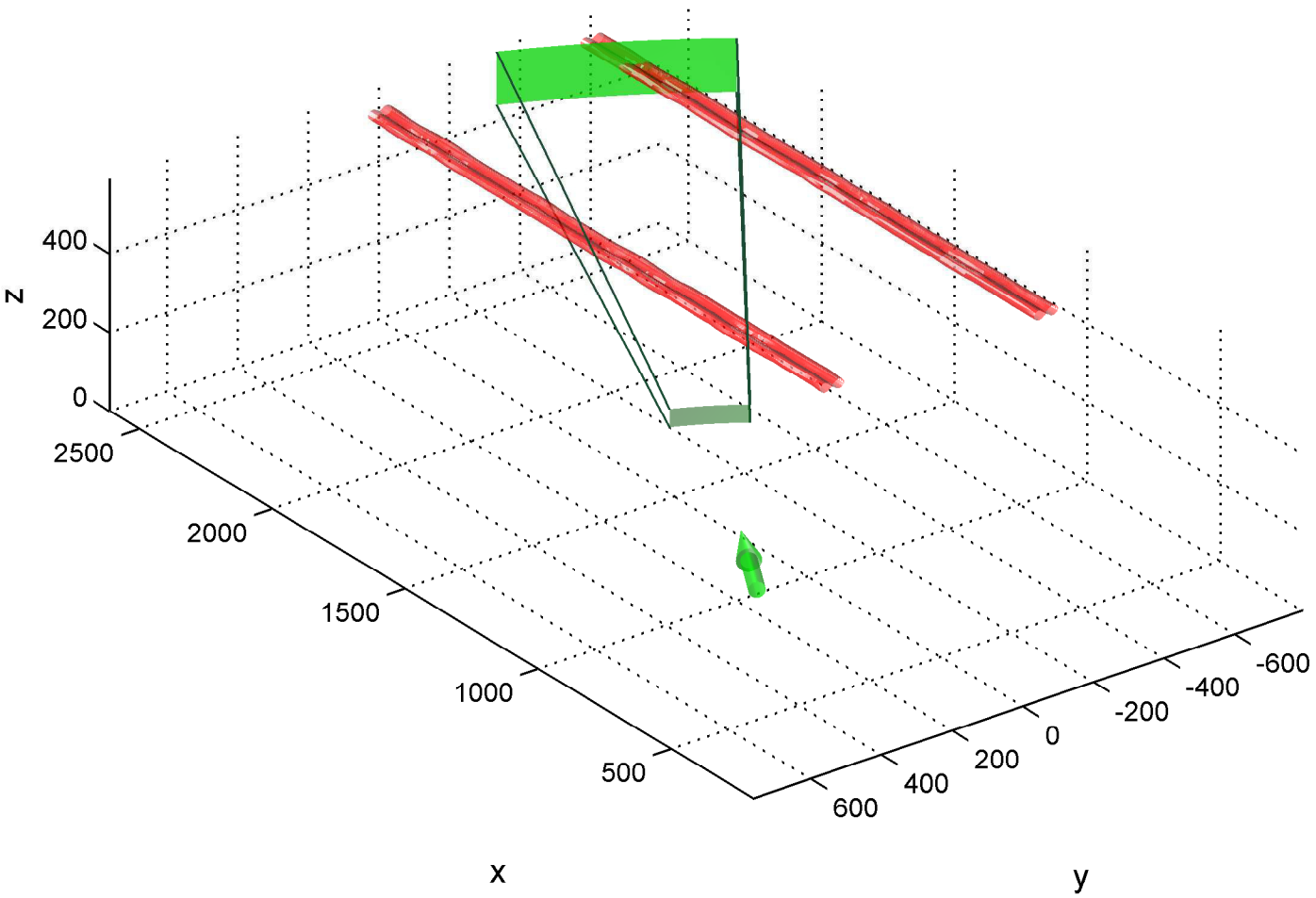
Simulation Setup for Case 18, Time = 12 s
Azimuth Viewing Angle = 30 degrees
z
400
200
0
2500
2000
1500
1000
500
x
600
400
200
0
-200
-400
-600
y

Simulation Results for Case 18, Time = 12 s
Azimuth Viewing Angle = 30 degrees

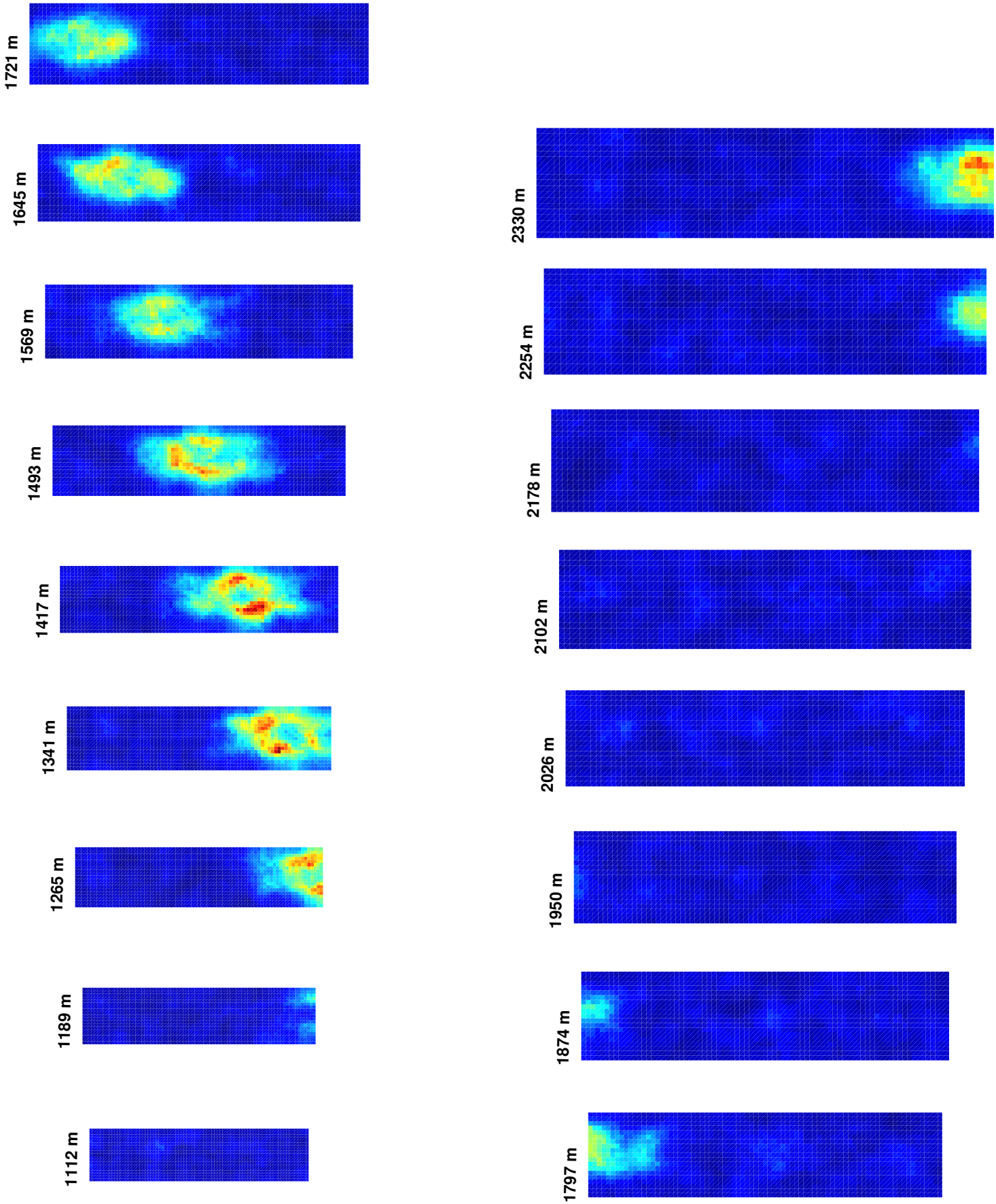

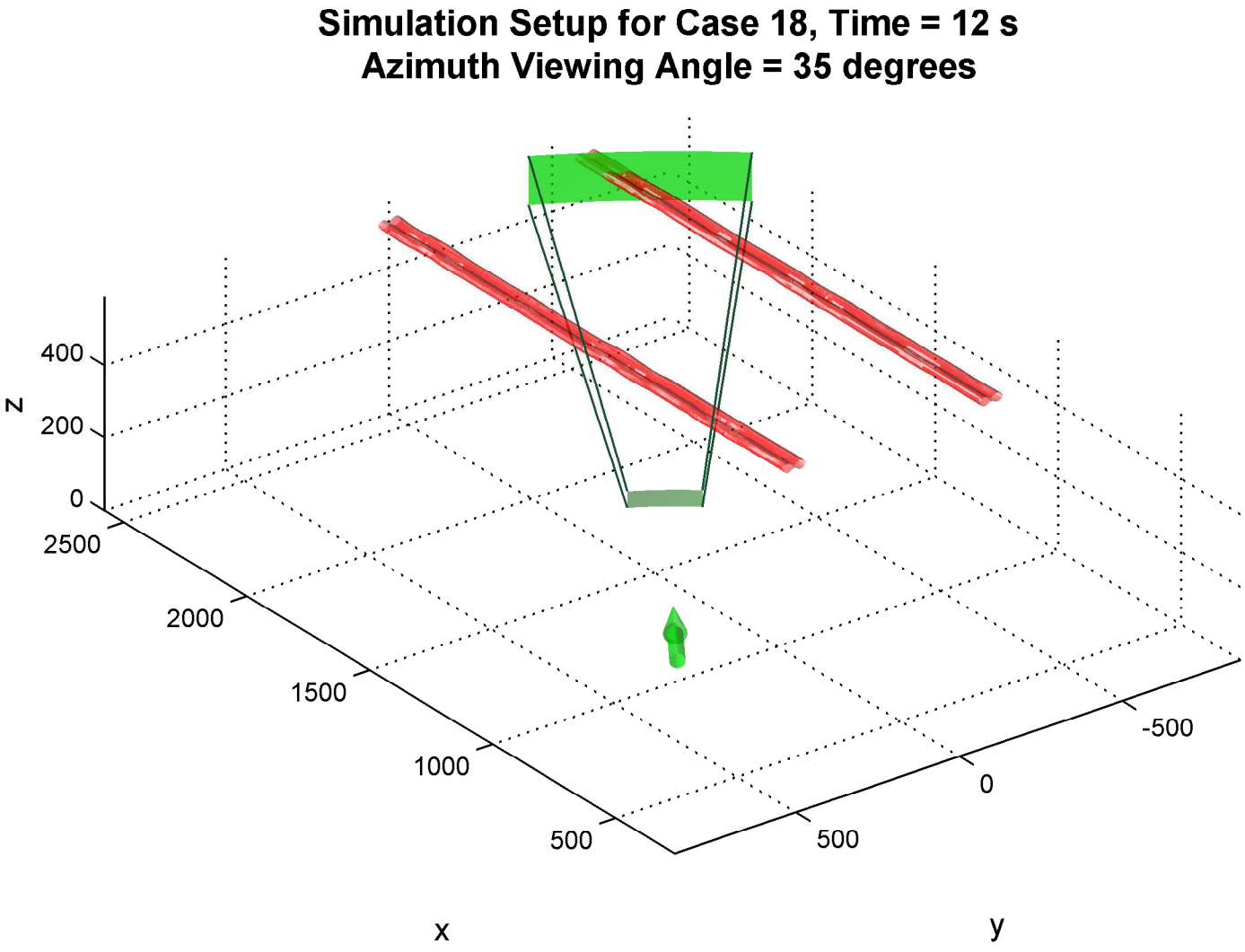
Simulation Setup for Case 18, Time = 12 s
Azimuth Viewing Angle = 35 degrees
z
400
200
0
2500
2000
1500
1000
500
x
500
0
-500
y

Simulation Results for Case 18, Time = 12 s
Azimuth Viewing Angle = 35 degrees

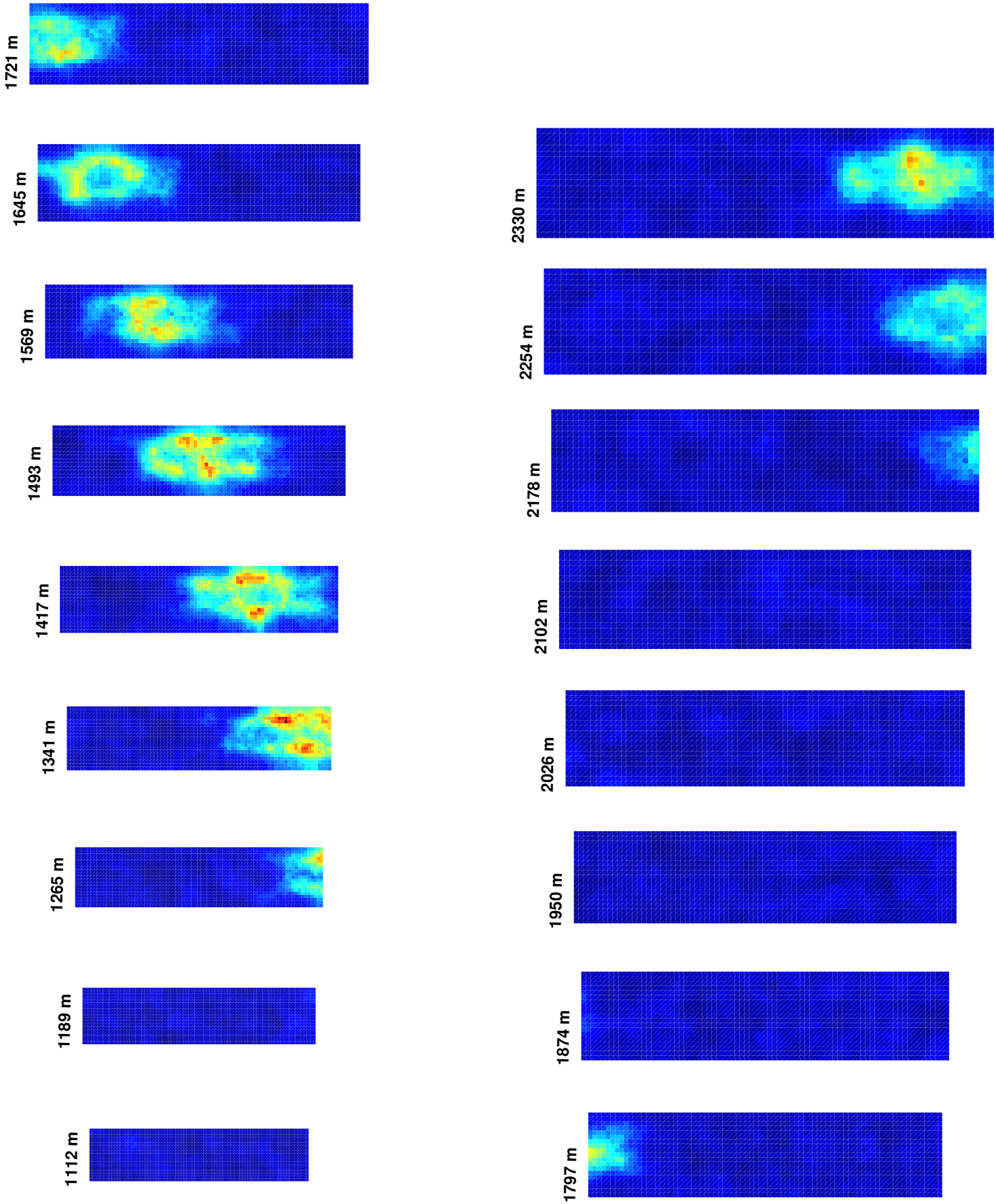

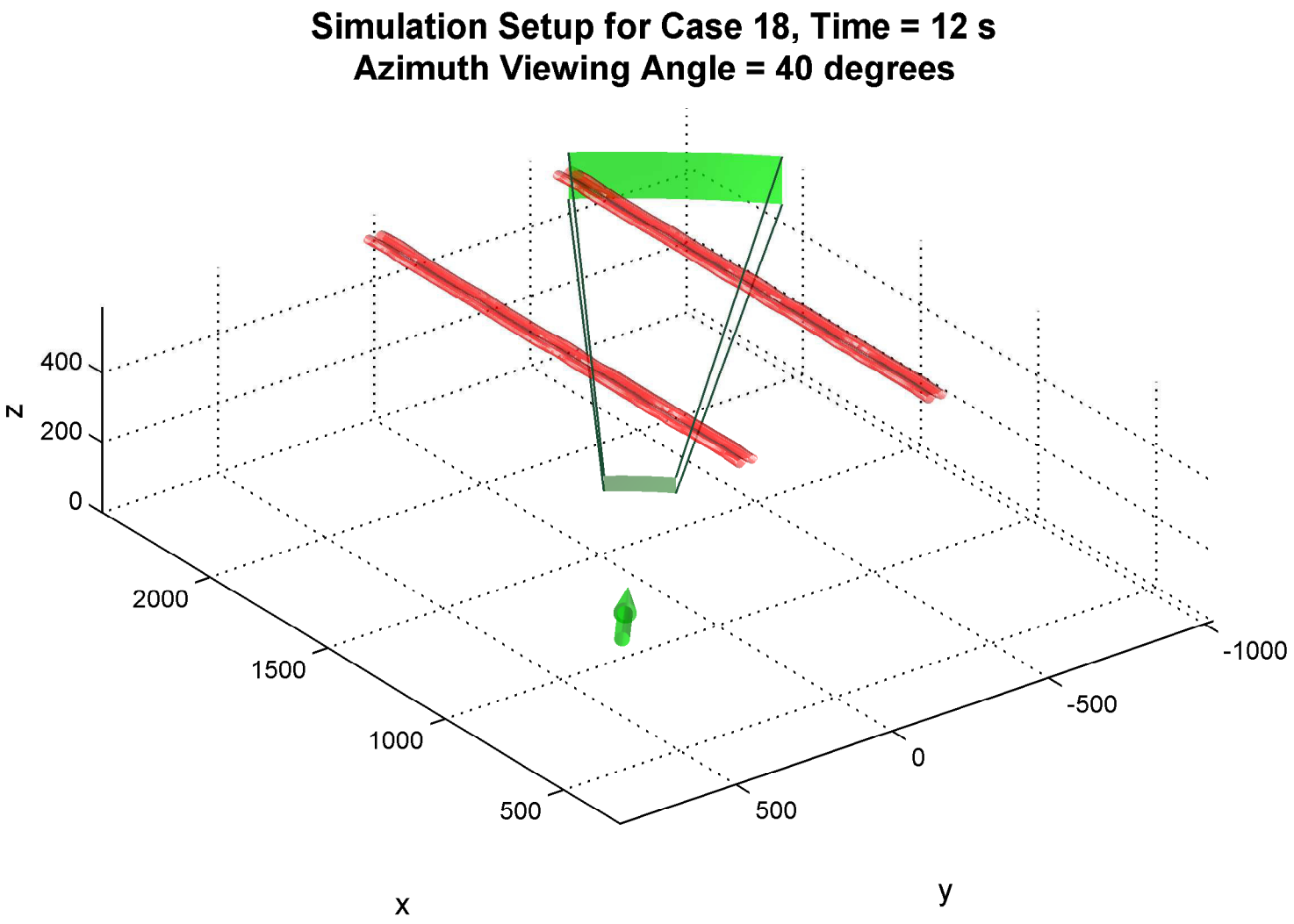
Simulation Setup for Case 18, Time = 12 s
Azimuth Viewing Angle = 40 degrees
z
400
200
0
2000
1500
1000
500
x
500
0
-500
-1000
y

Simulation Results for Case 18, Time = 12 s
Azimuth Viewing Angle = 40 degrees

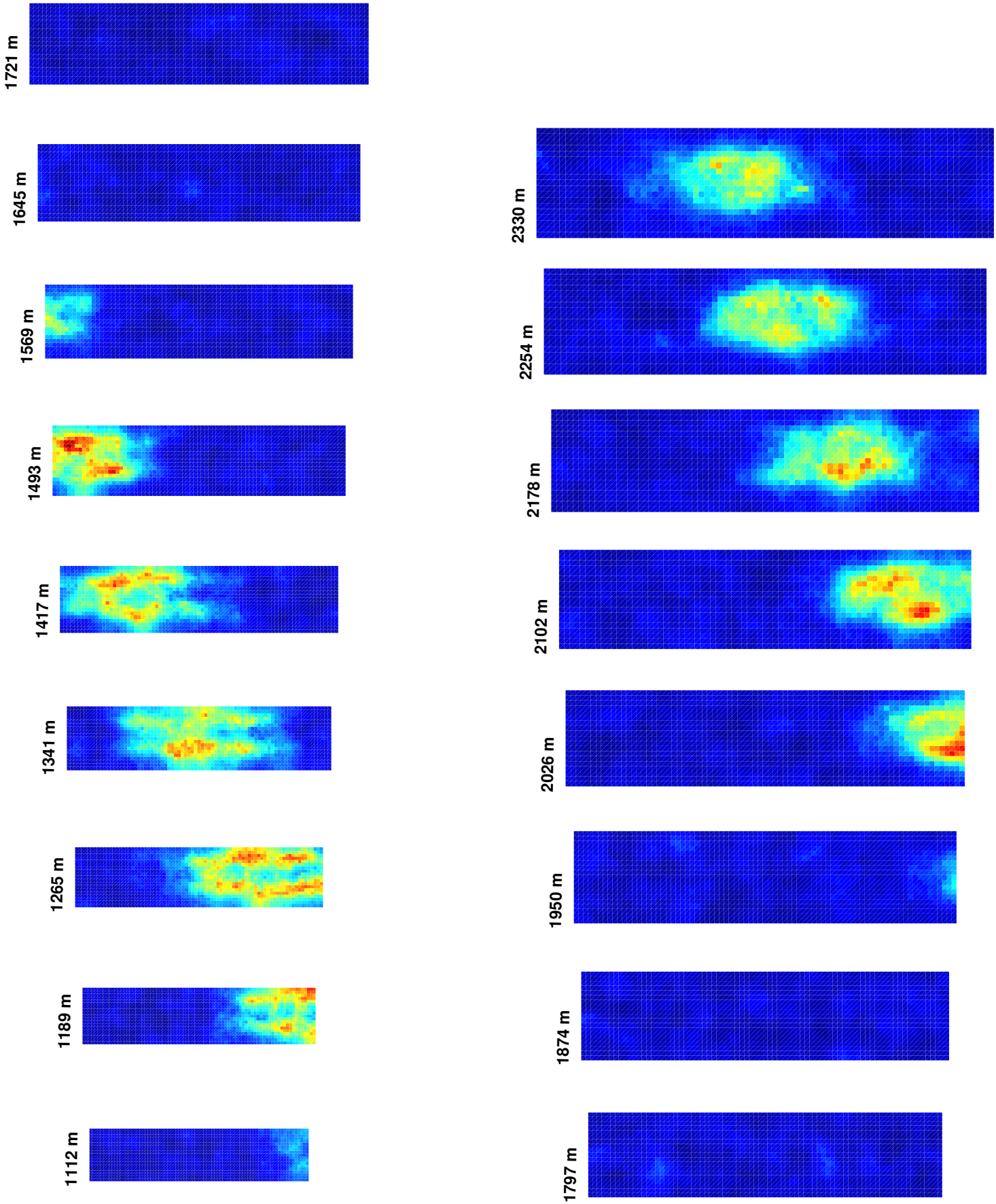

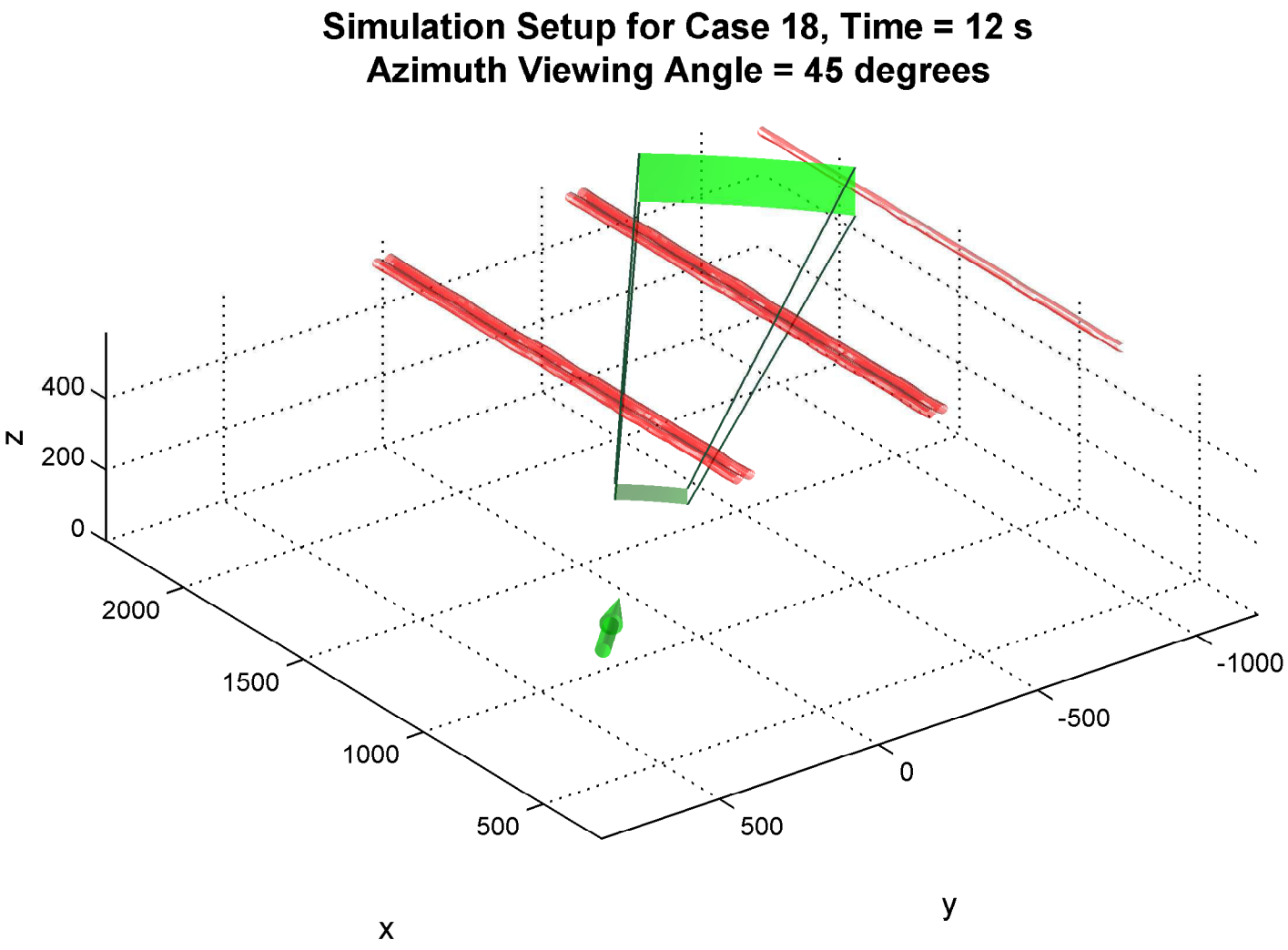
Simulation Setup for Case 18, Time = 12 s
Azimuth Viewing Angle = 45 degrees
z
400
200
0
2000
1500
1000
500
x
500
0
-500
-1000
y

Simulation Results for Case 18, Time = 12 s
Azimuth Viewing Angle = 45 degrees

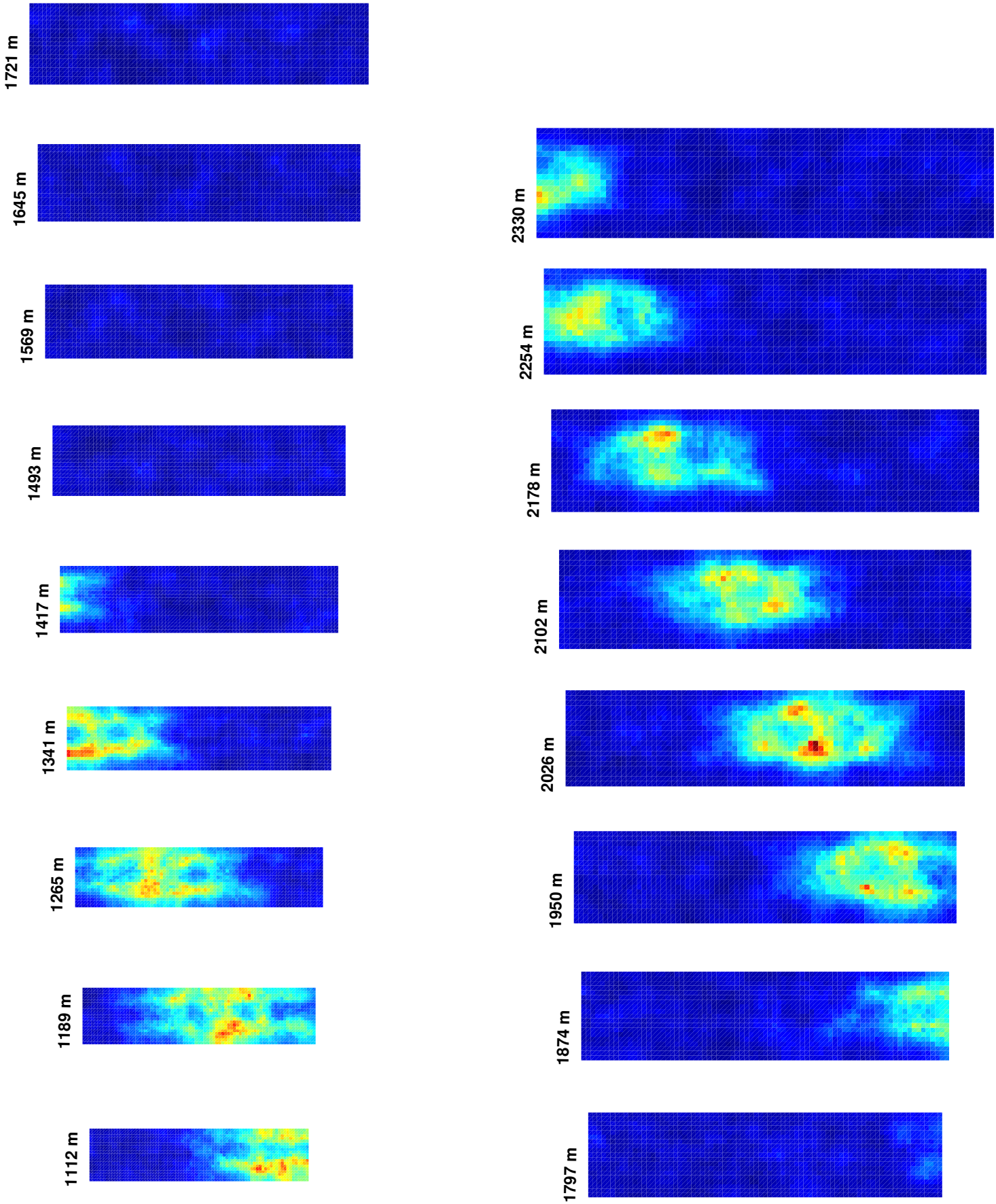

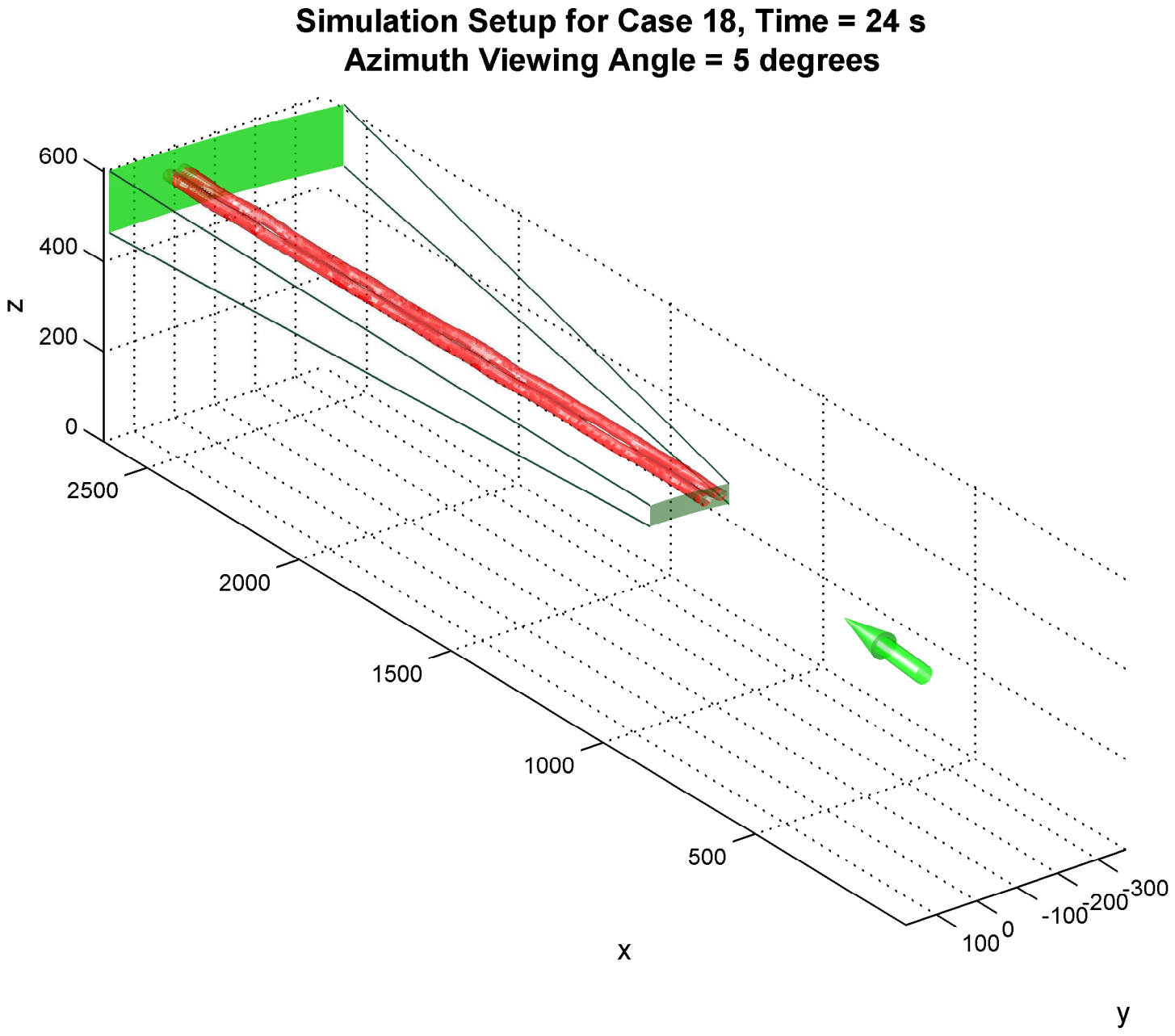
Simulation Setup for Case 18, Time = 24 s
Azimuth Viewing Angle = 5 degrees
600
400
200
0
z
2500
2000
1500
1000
500
x
100
0
-100
-200
-300
y

Simulation Results for Case 18, Time = 24 s
Azimuth Viewing Angle = 5 degrees

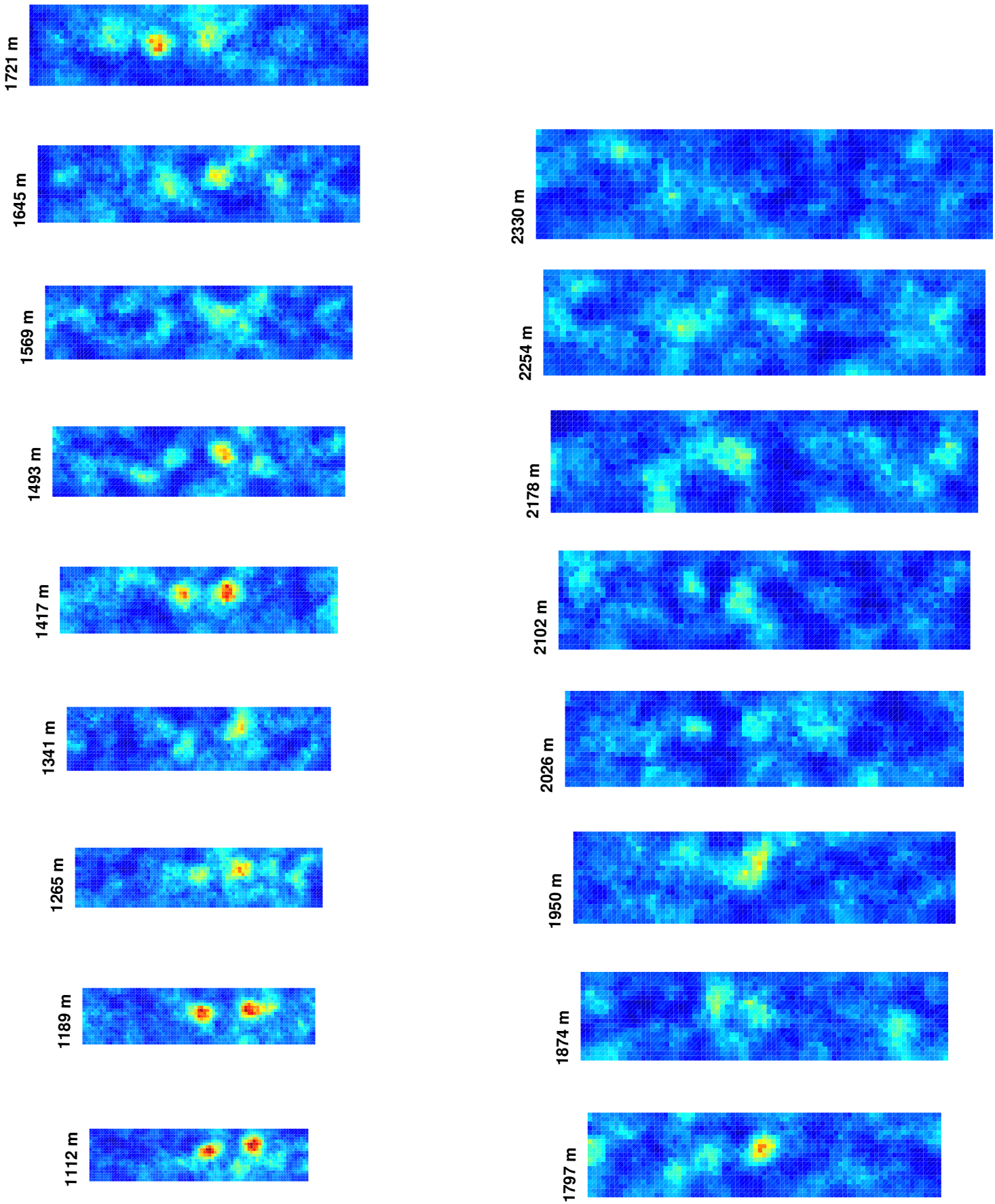

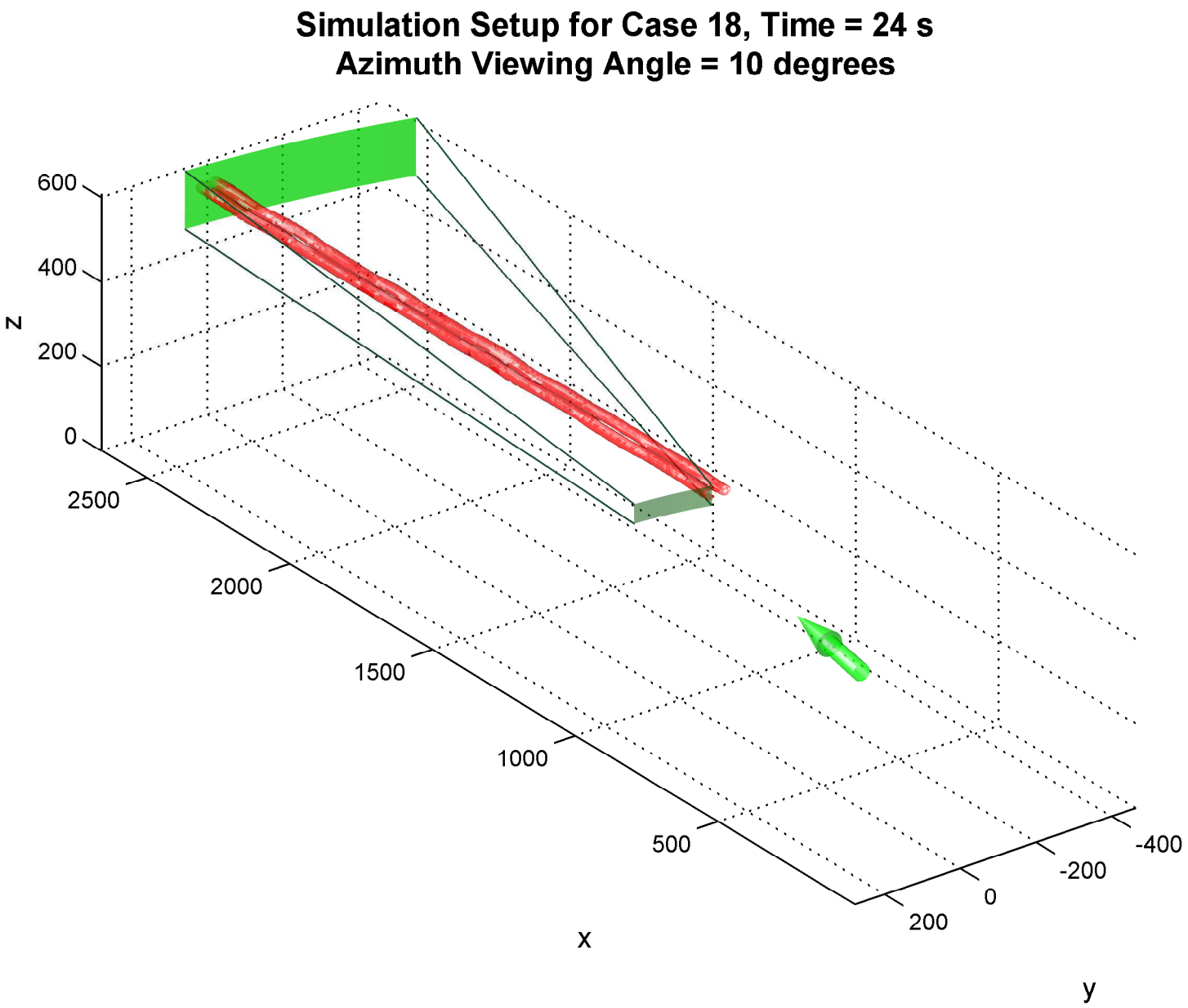
Simulation Setup for Case 18, Time = 24 s
Azimuth Viewing Angle = 10 degrees
600
400
200
0
z
2500
2000
1500
1000
500
x
200
0
-200
-400
y

Simulation Results for Case 18, Time = 24 s
Azimuth Viewing Angle = 10 degrees

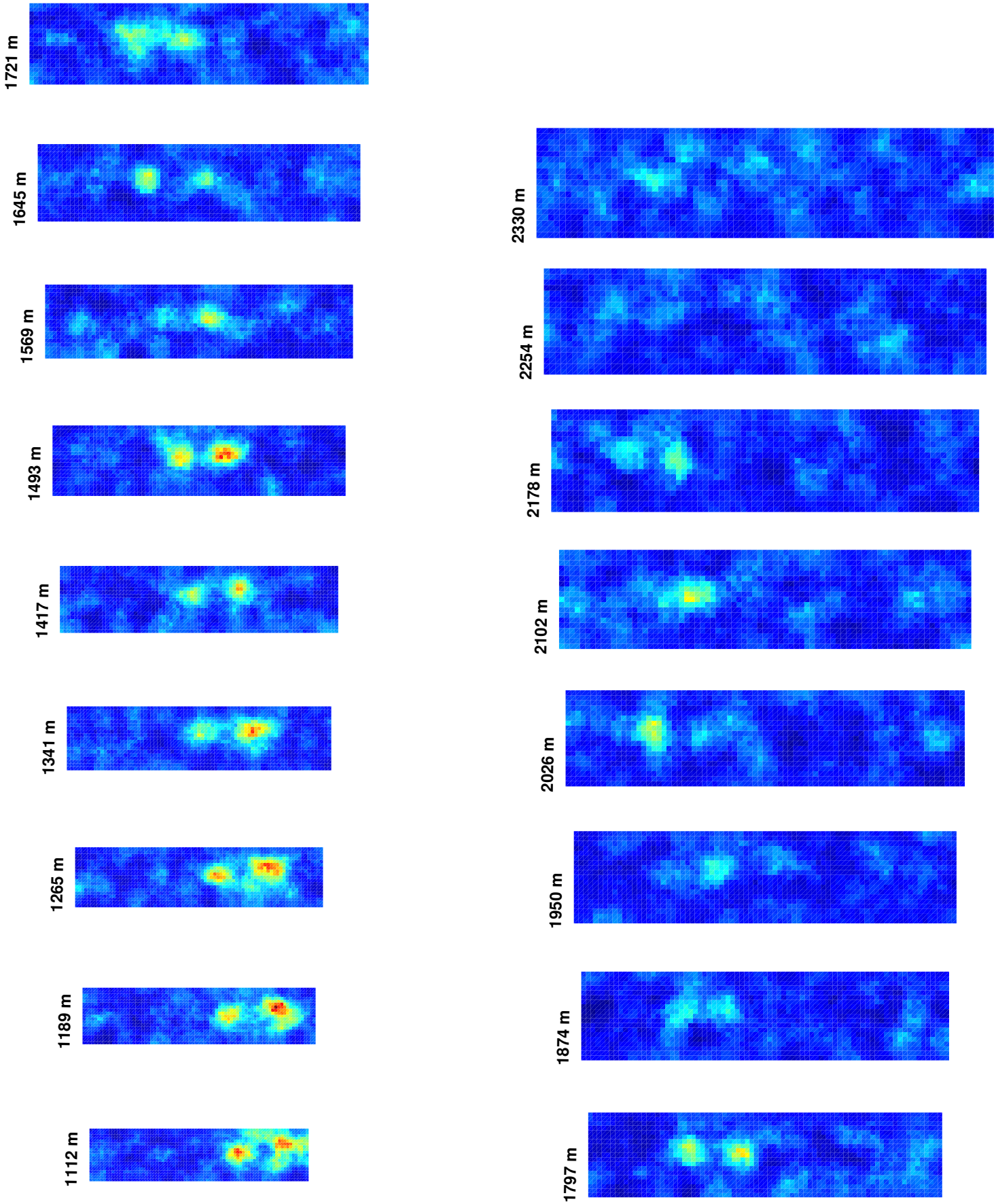

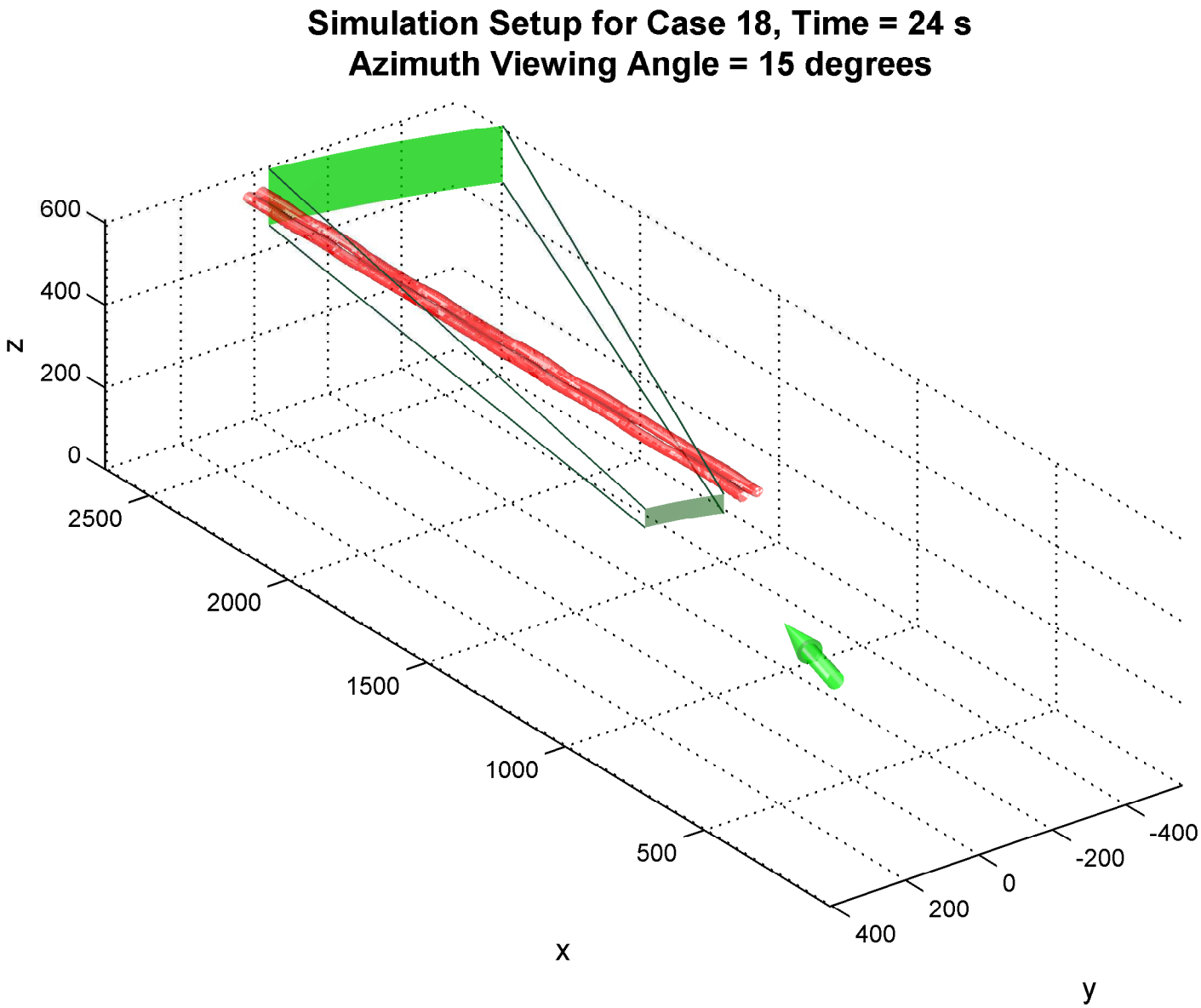
Simulation Setup for Case 18, Time = 24 s
Azimuth Viewing Angle = 15 degrees
600
400
200
0
z
2500
2000
1500
1000
500
x
400
200
0
-200
-400
y

Simulation Results for Case 18, Time = 24 s
Azimuth Viewing Angle = 15 degrees

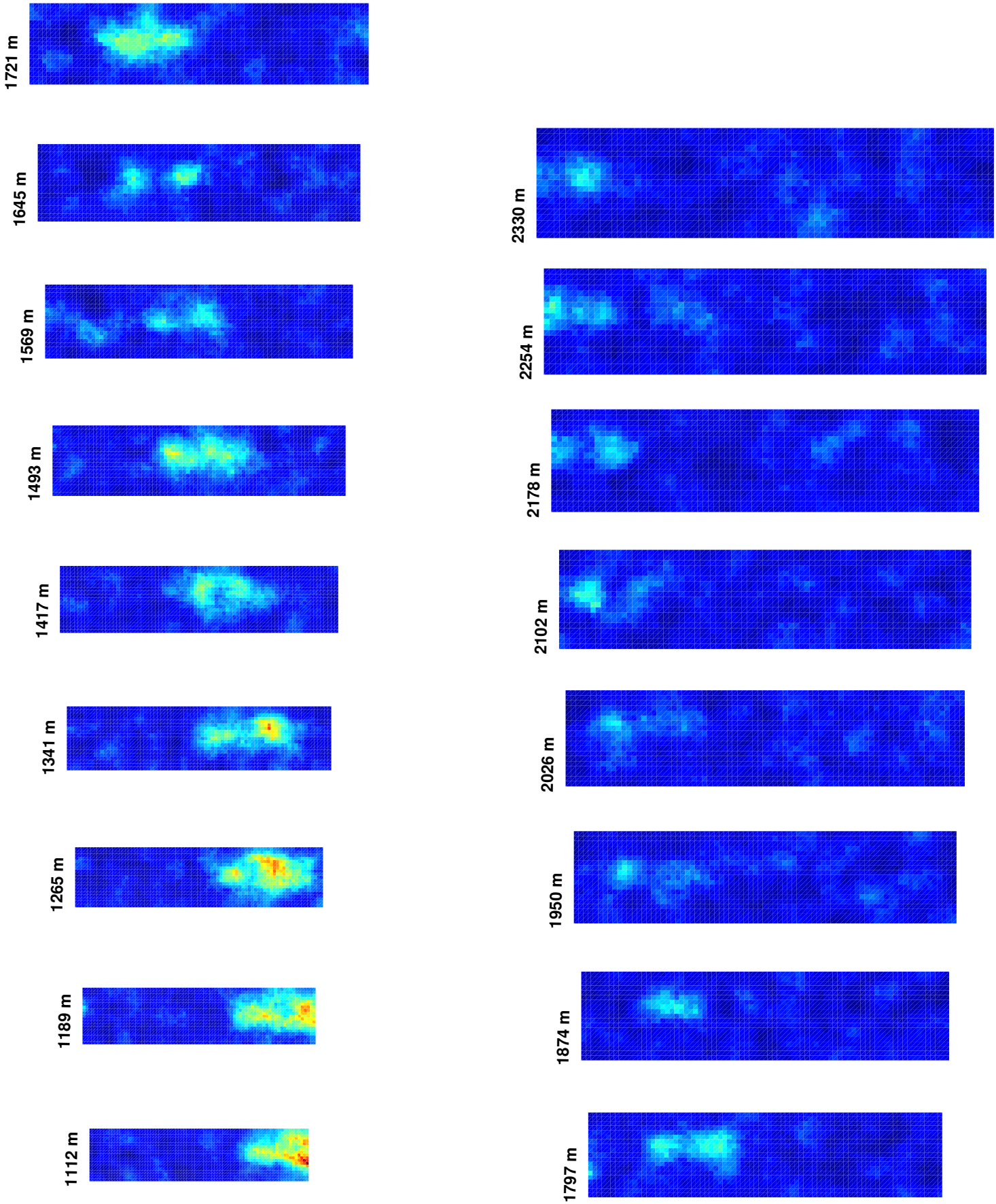

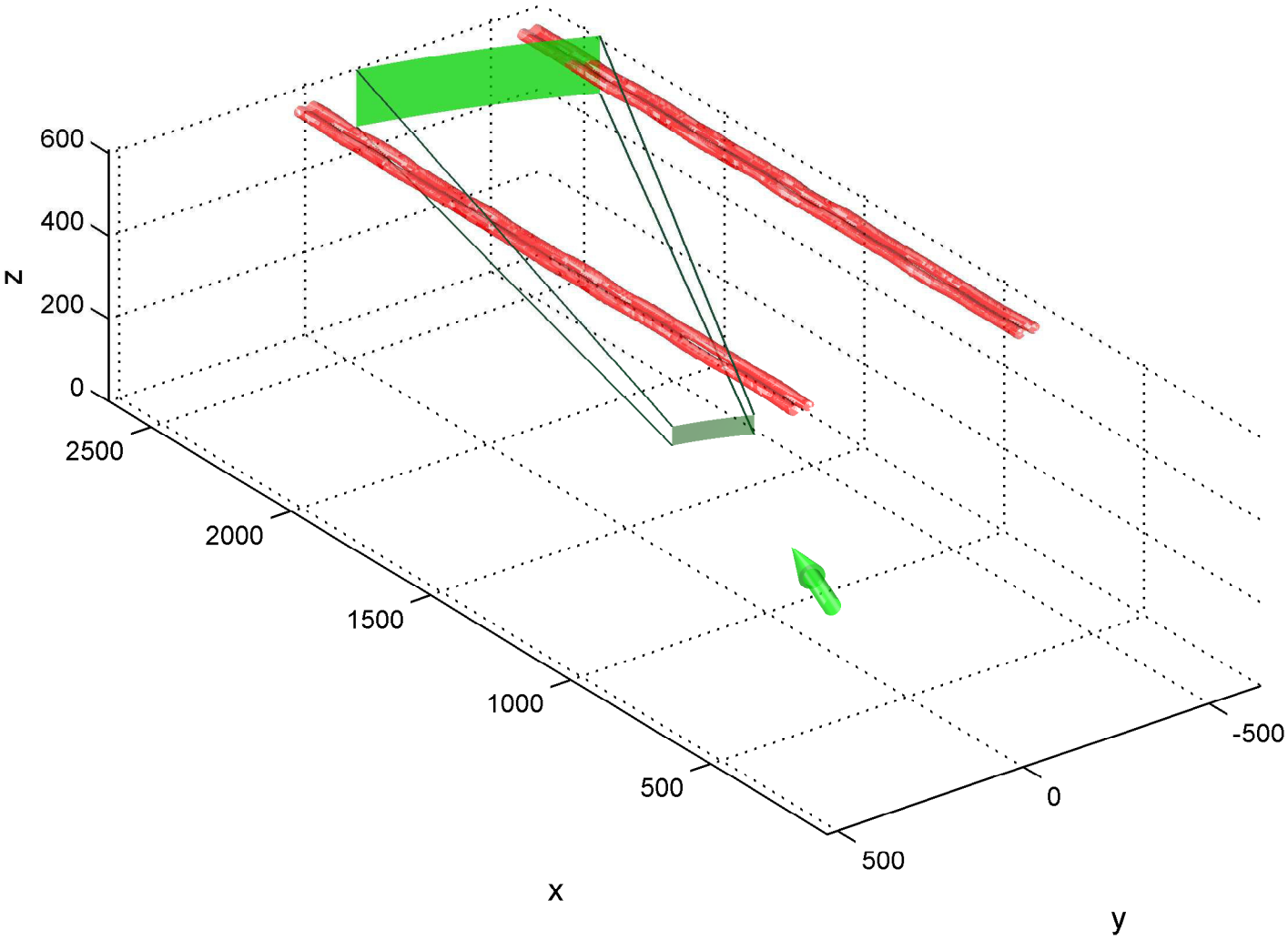
Simulation Setup for Case 18, Time = 24 s
Azimuth Viewing Angle = 20 degrees
600
400
200
0
z
2500
2000
1500
1000
500
x
500
0
-500
y

Simulation Results for Case 18, Time = 24 s
Azimuth Viewing Angle = 20 degrees

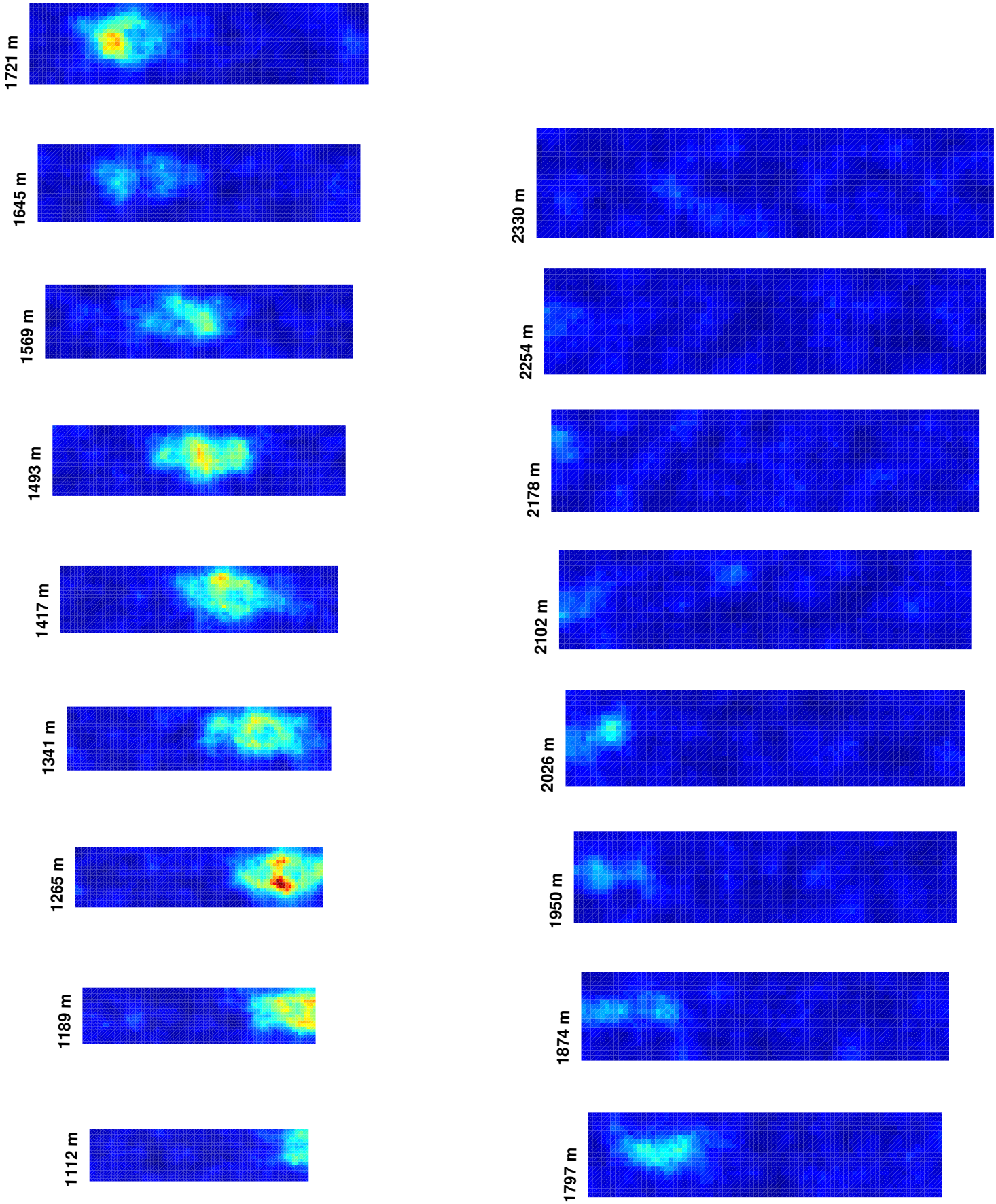

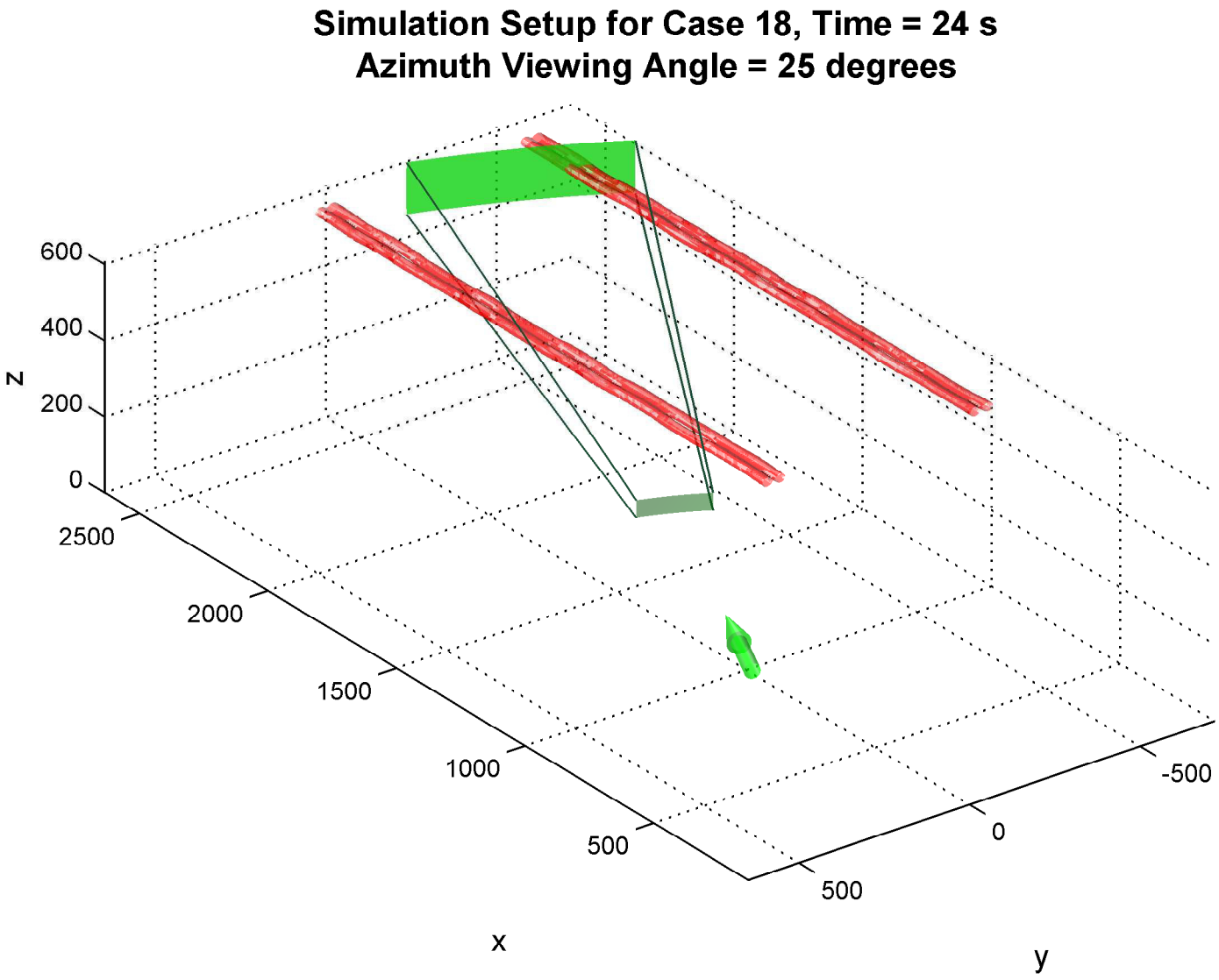
Simulation Setup for Case 18, Time = 24 s
Azimuth Viewing Angle = 25 degrees
600
400
200
0
z
2500
2000
1500
1000
500
x
500
0
-500
y

Simulation Results for Case 18, Time = 24 s
Azimuth Viewing Angle = 25 degrees

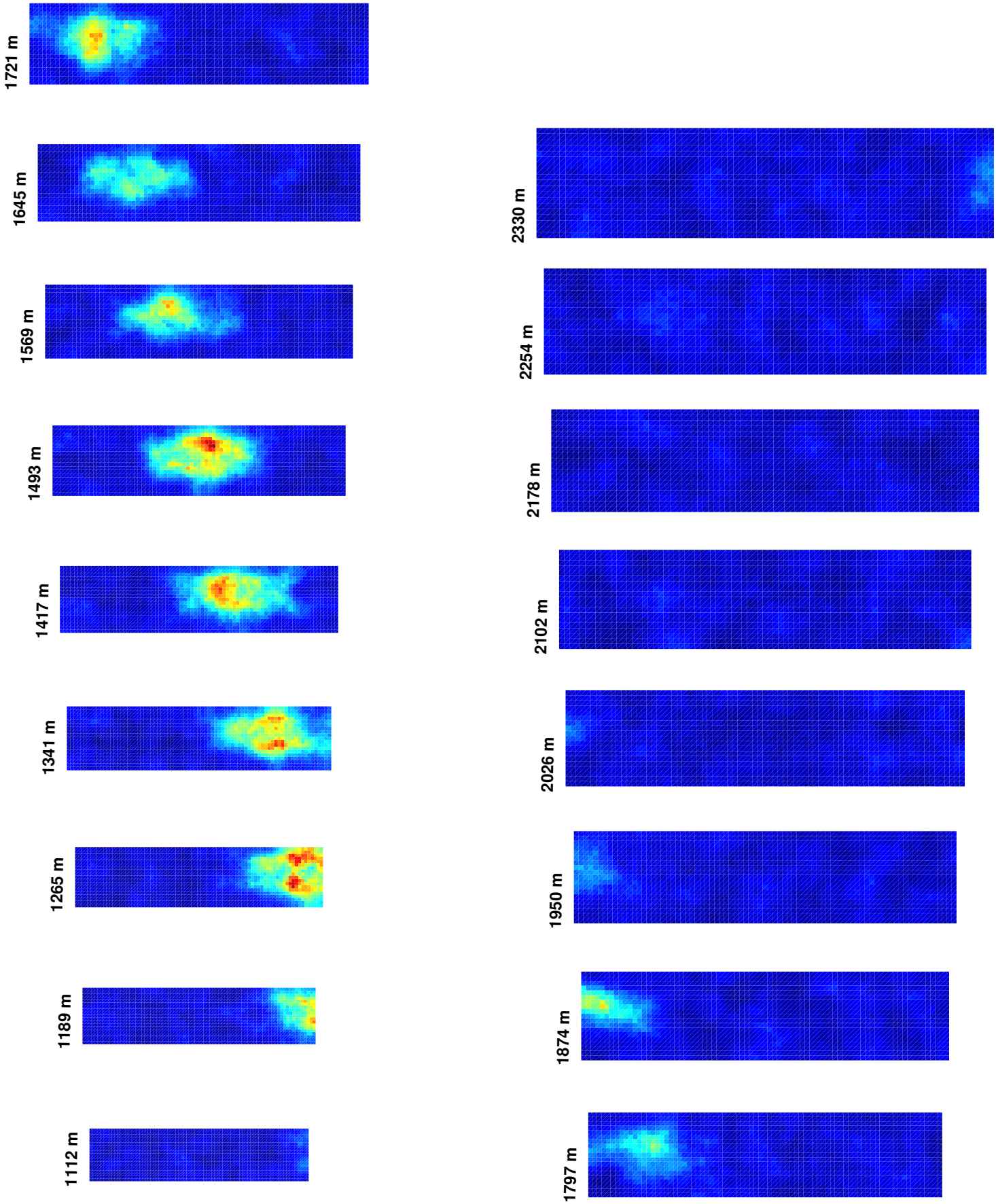

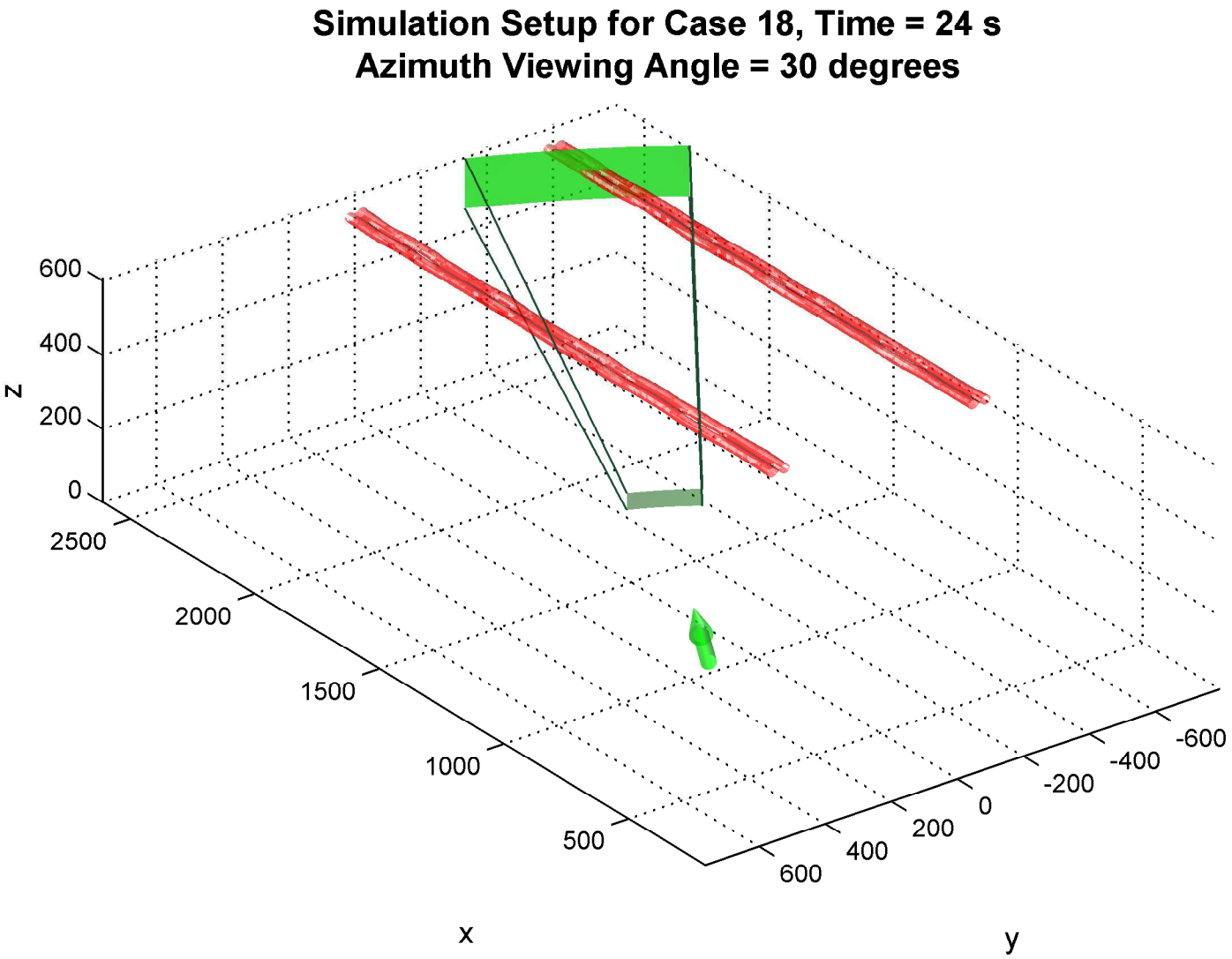
Simulation Setup for Case 18, Time = 24 s
Azimuth Viewing Angle = 30 degrees
z
600
400
200
0
2500
2000
1500
1000
500
x
600
400
200
0
-200
-400
-600
y

Simulation Results for Case 18, Time = 24 s
Azimuth Viewing Angle = 30 degrees

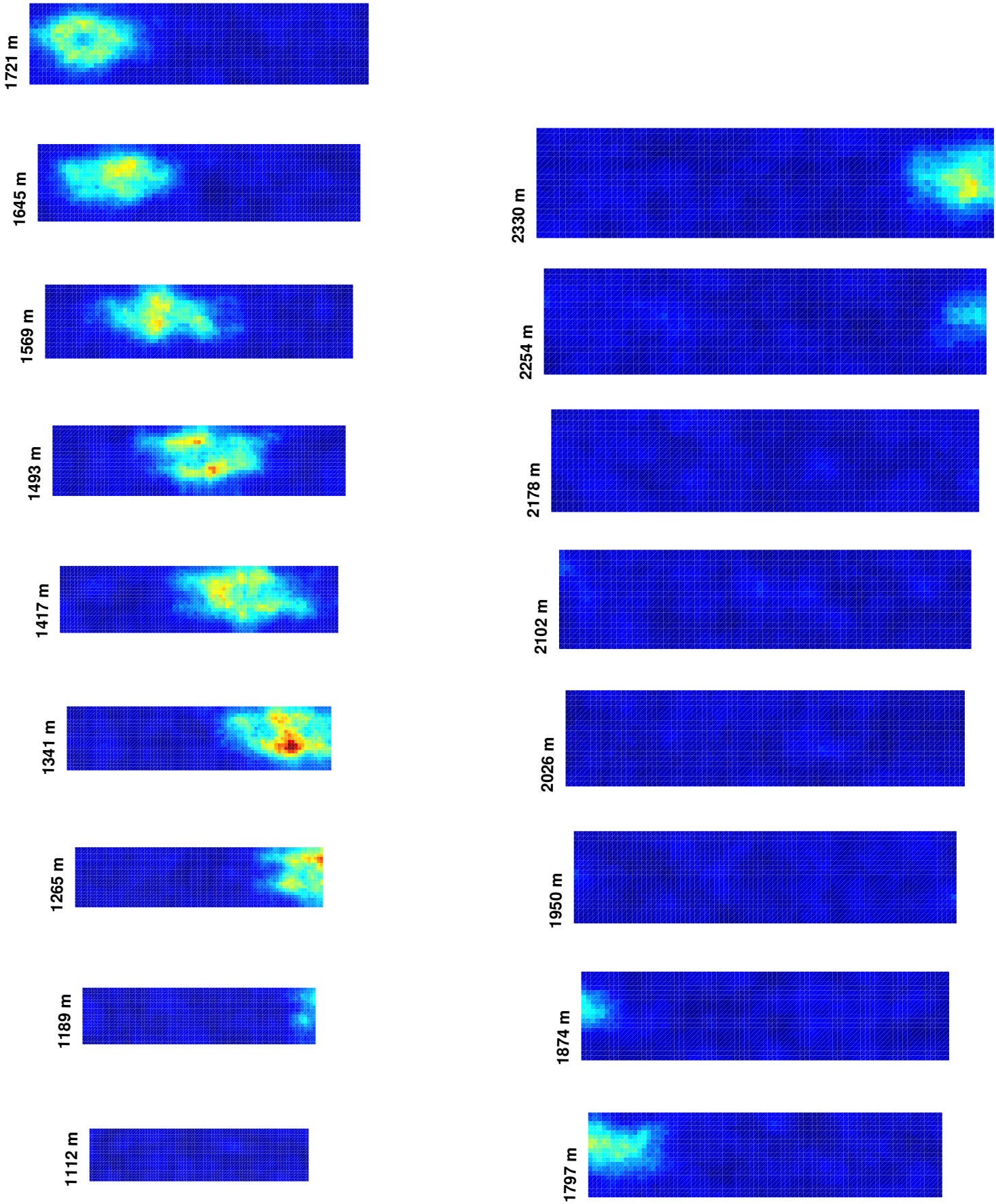

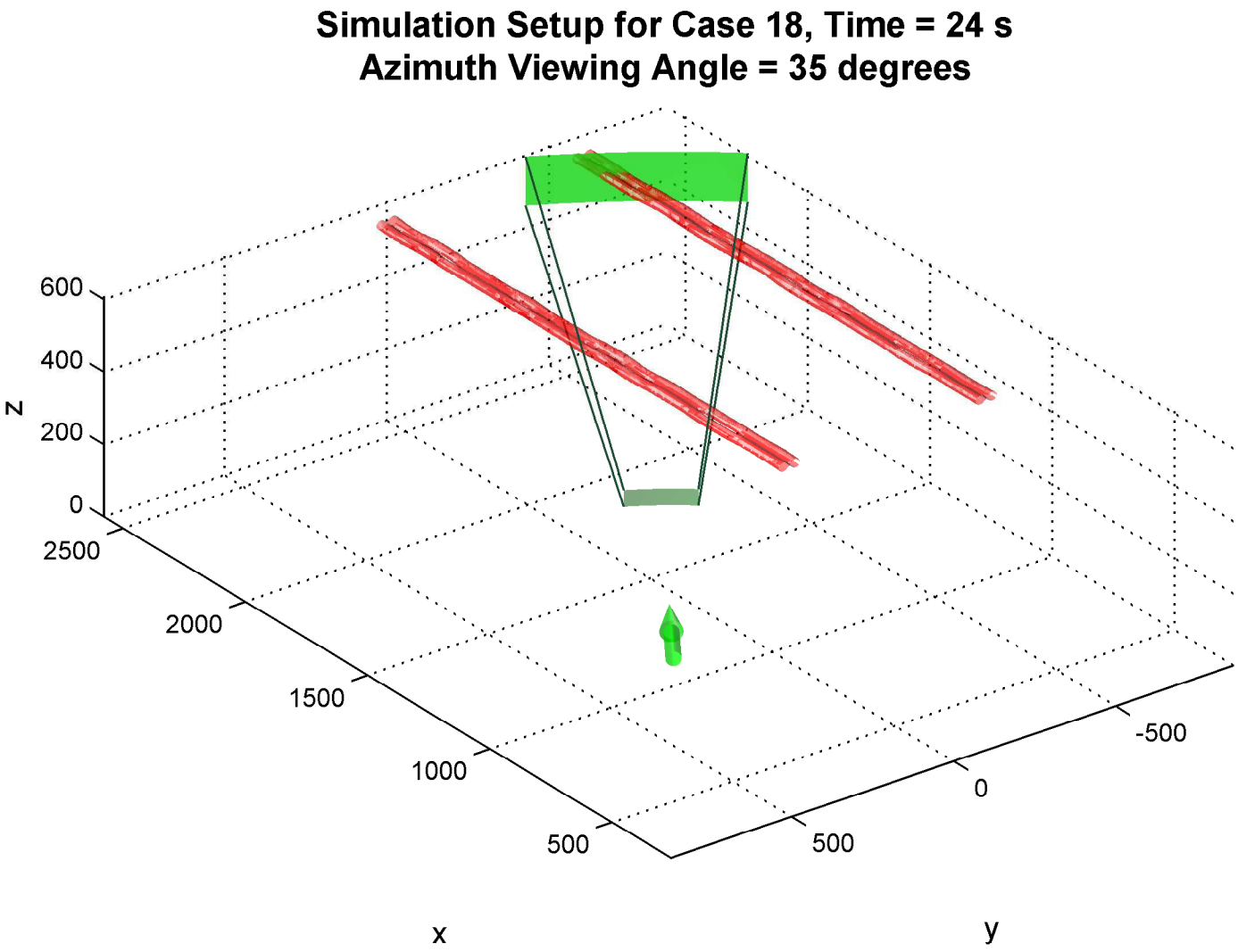
Simulation Setup for Case 18, Time = 24 s
Azimuth Viewing Angle = 35 degrees
600
400
200
0
z
2500
2000
1500
1000
500
x
500
0
-500
y

Simulation Results for Case 18, Time = 24 s
Azimuth Viewing Angle = 35 degrees

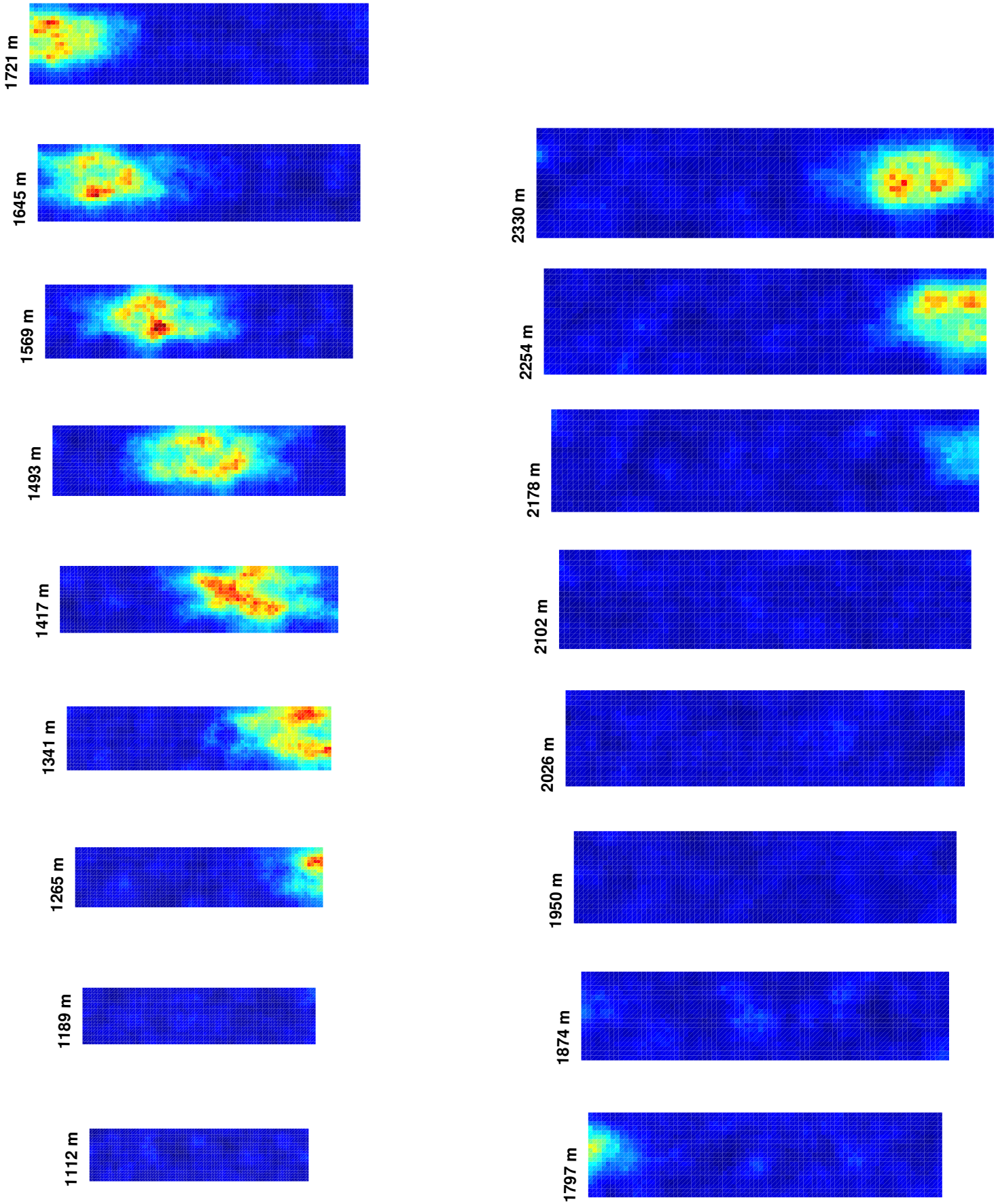

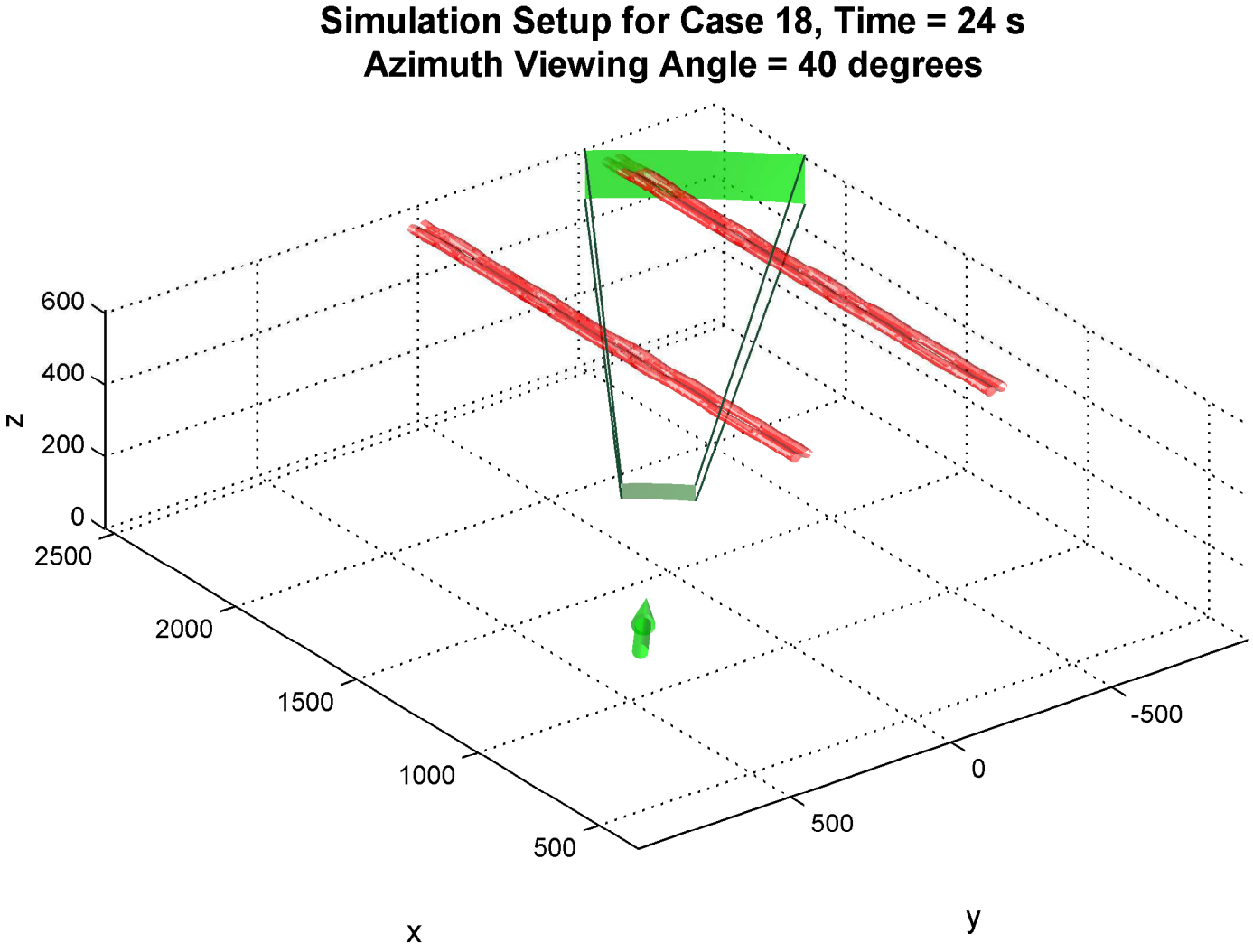
Simulation Setup for Case 18, Time = 24 s
Azimuth Viewing Angle = 40 degrees
600
400
200
0
z
2500
2000
1500
1000
500
x
-500
0
500
y

Simulation Results for Case 18, Time = 24 s
Azimuth Viewing Angle = 40 degrees

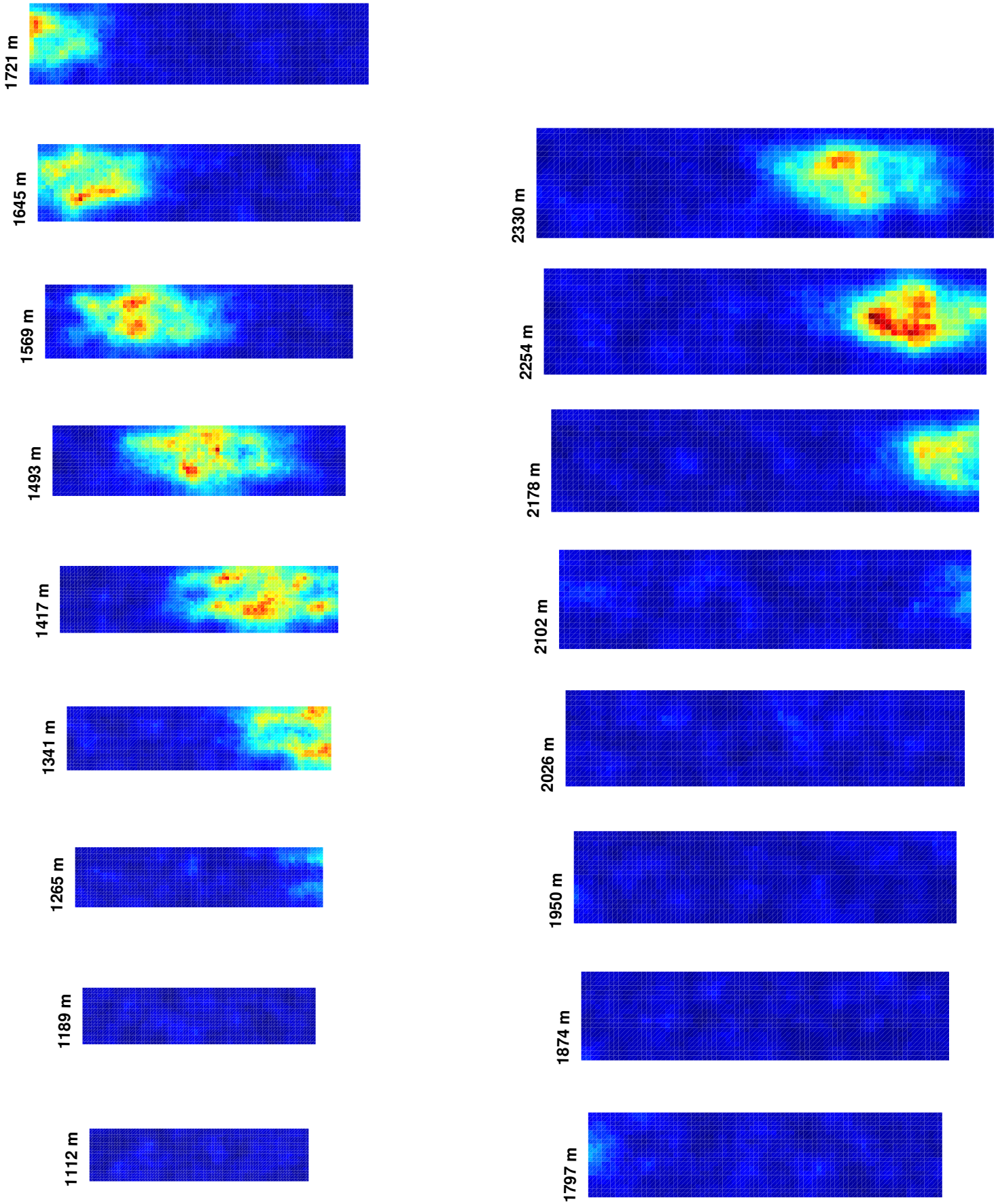

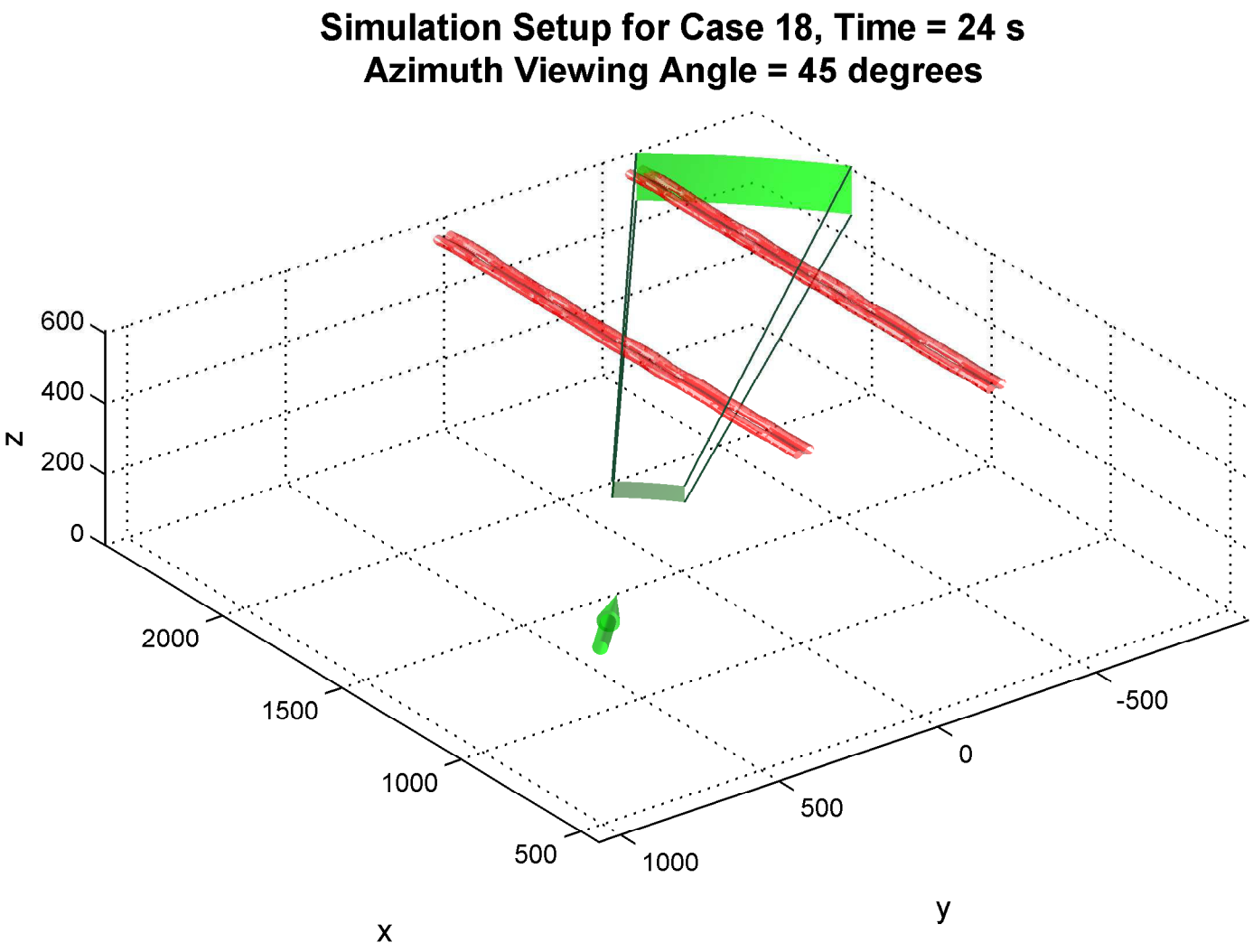
Simulation Setup for Case 18, Time = 24 s
Azimuth Viewing Angle = 45 degrees
600
400
200
0
z
2000
1500
1000
500
x
1000
500
0
-500
y

Simulation Results for Case 18, Time = 24 s
Azimuth Viewing Angle = 45 degrees

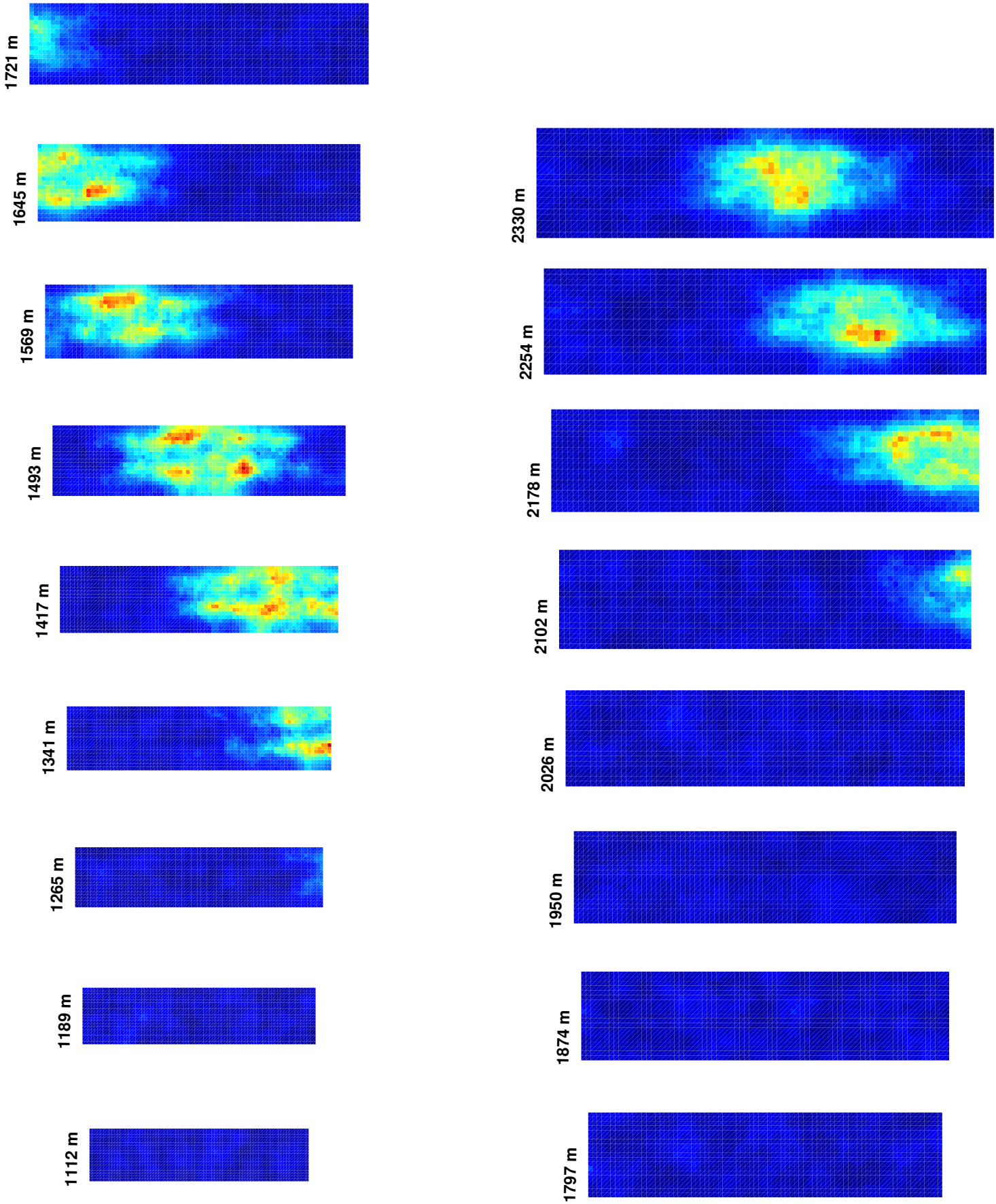

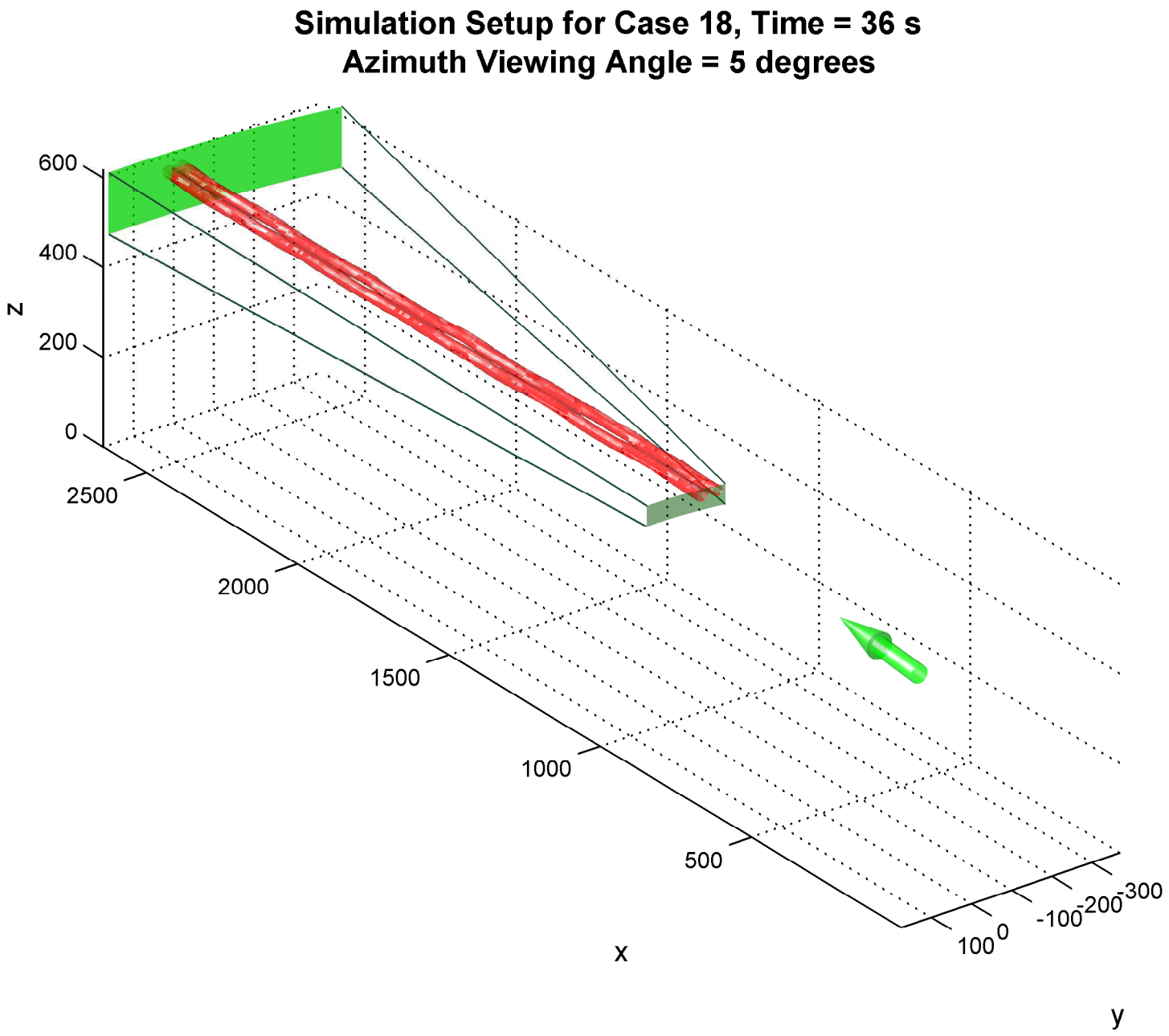
Simulation Setup for Case 18, Time = 36 s
Azimuth Viewing Angle = 5 degrees
600
400
200
0
z
2500
2000
1500
1000
500
x
100
0
-100
-200
-300
y

Simulation Results for Case 18, Time = 36 s
Azimuth Viewing Angle = 5 degrees

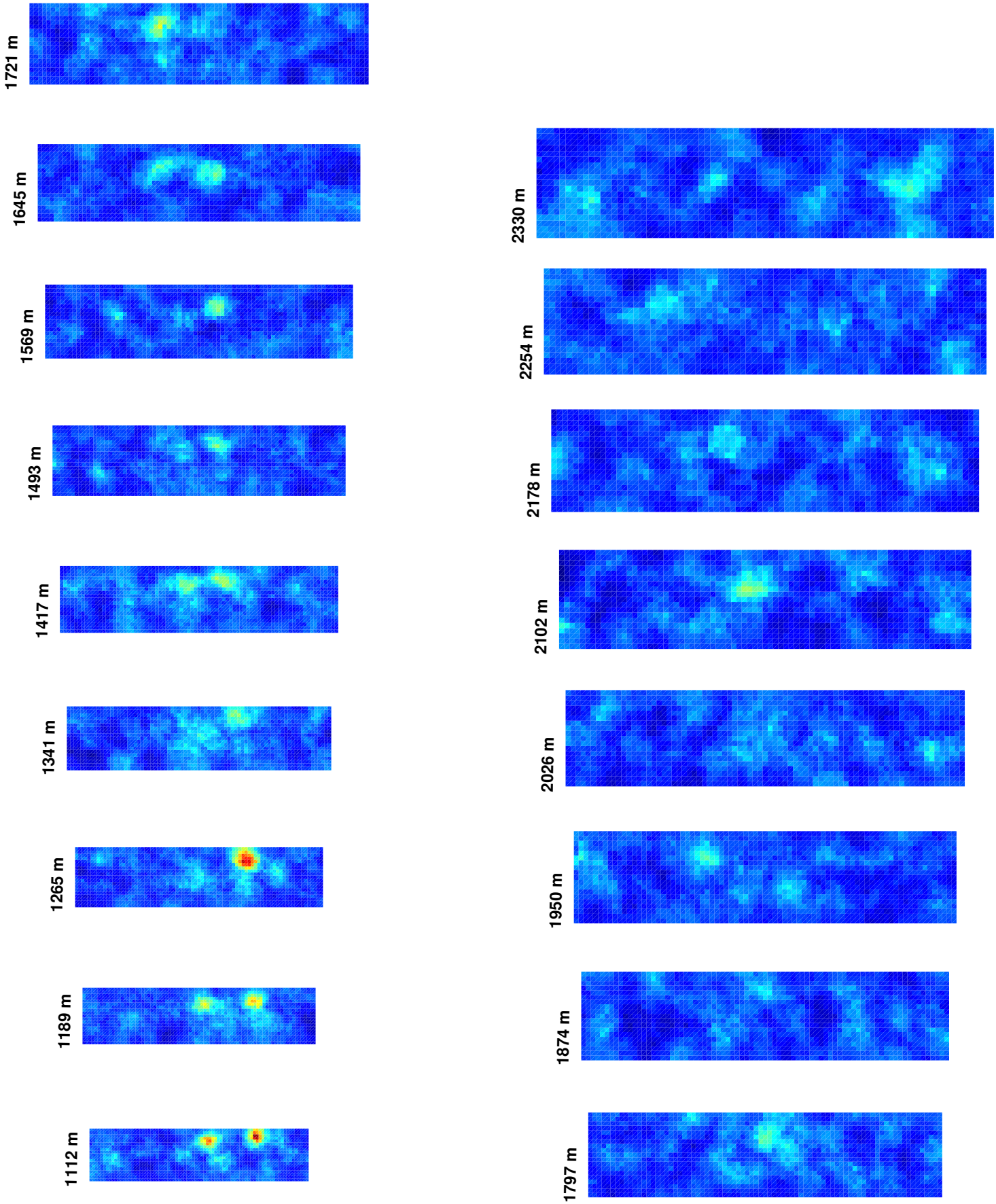

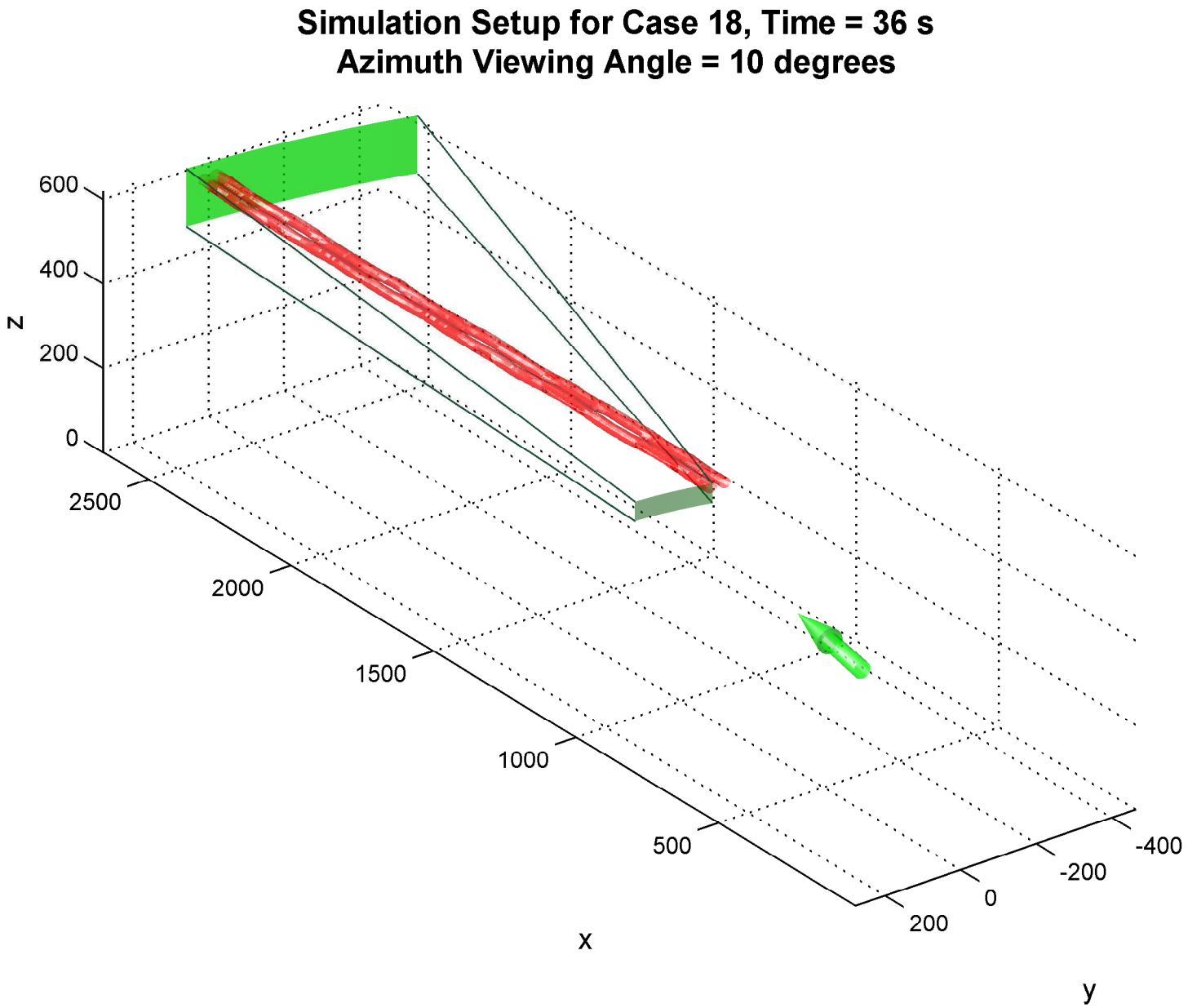
Simulation Setup for Case 18, Time = 36 s
Azimuth Viewing Angle = 10 degrees
600
400
200
0
z
2500
2000
1500
1000
500
x
200
0
-200
-400
y

Simulation Results for Case 18, Time = 36 s
Azimuth Viewing Angle = 10 degrees

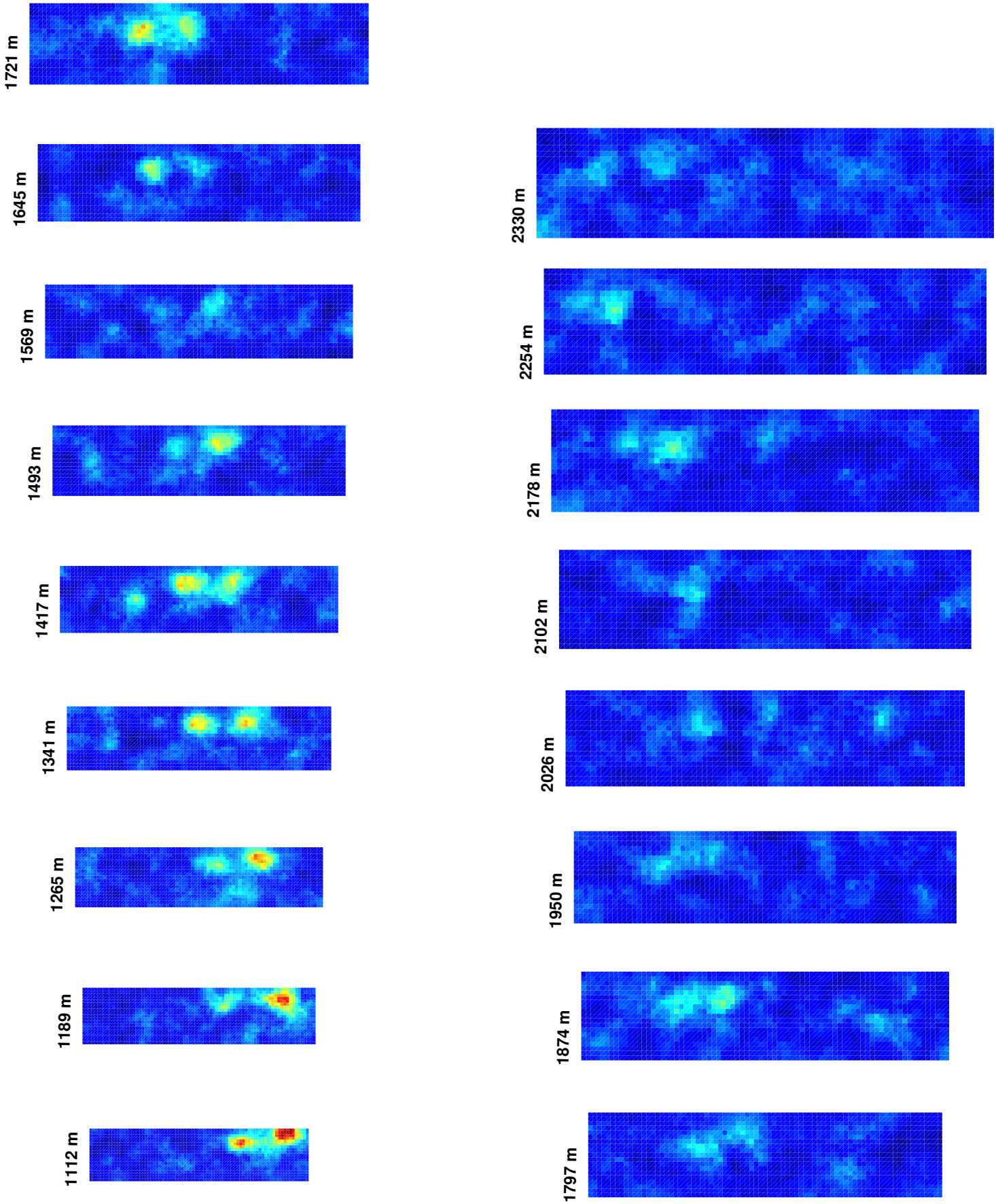

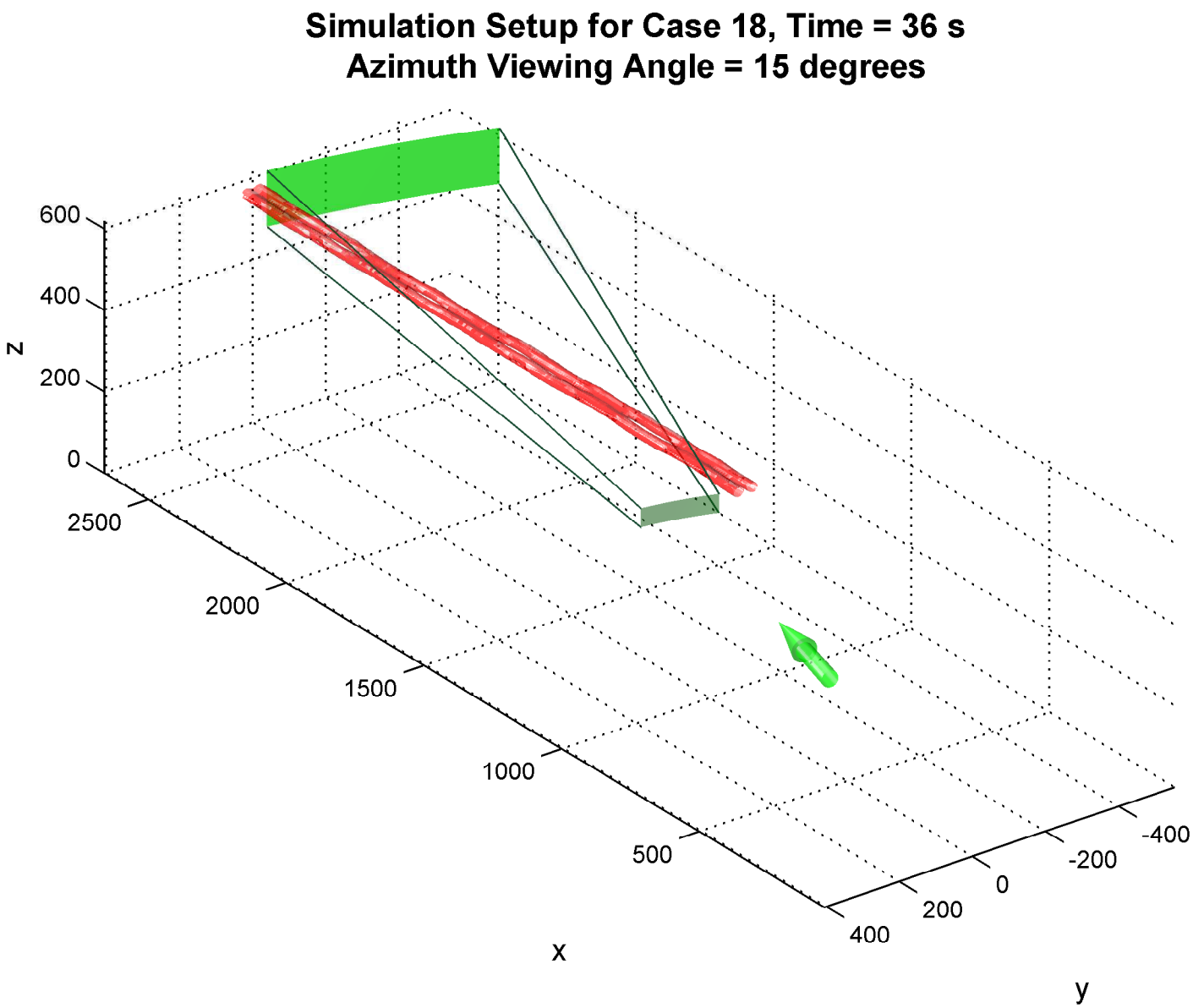
Simulation Setup for Case 18, Time = 36 s
Azimuth Viewing Angle = 15 degrees
600
400
200
0
z
2500
2000
1500
1000
500
x
400
200
0
-200
-400
y

Simulation Results for Case 18, Time = 36 s
Azimuth Viewing Angle = 15 degrees

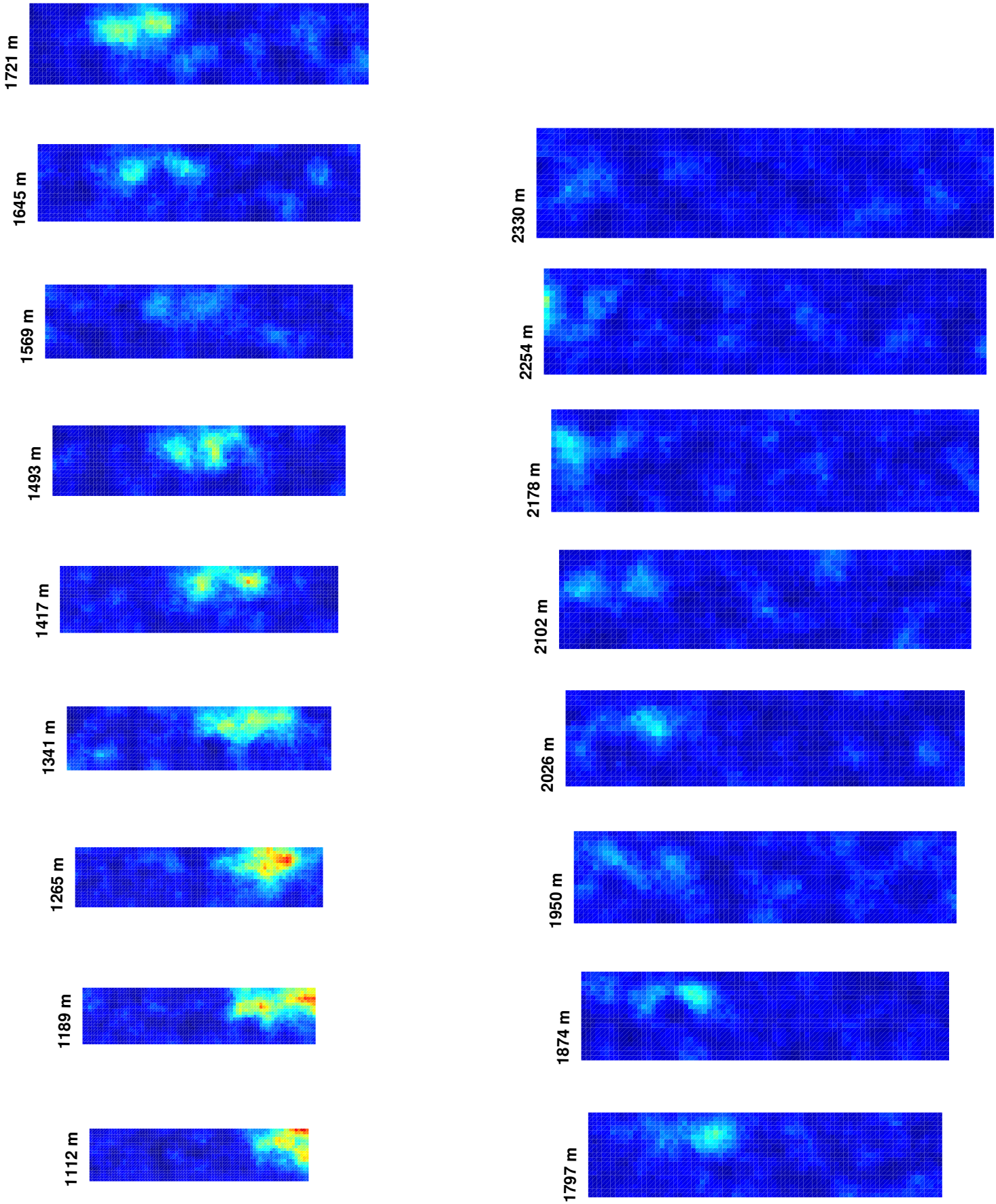

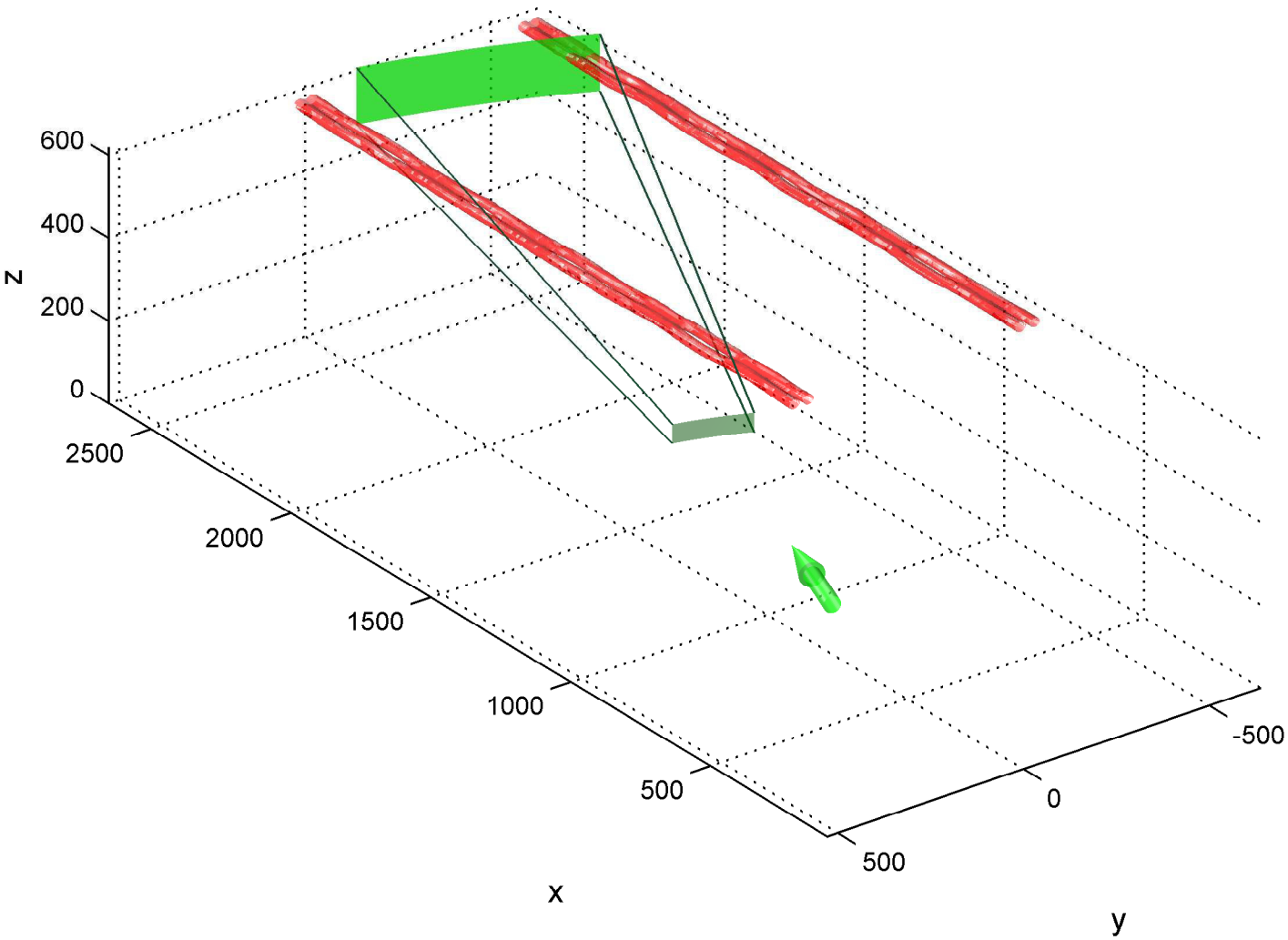
Simulation Setup for Case 18, Time = 36 s
Azimuth Viewing Angle = 20 degrees
600
400
200
0
z
2500
2000
1500
1000
500
x
500
0
-500
y

Simulation Results for Case 18, Time = 36 s
Azimuth Viewing Angle = 20 degrees

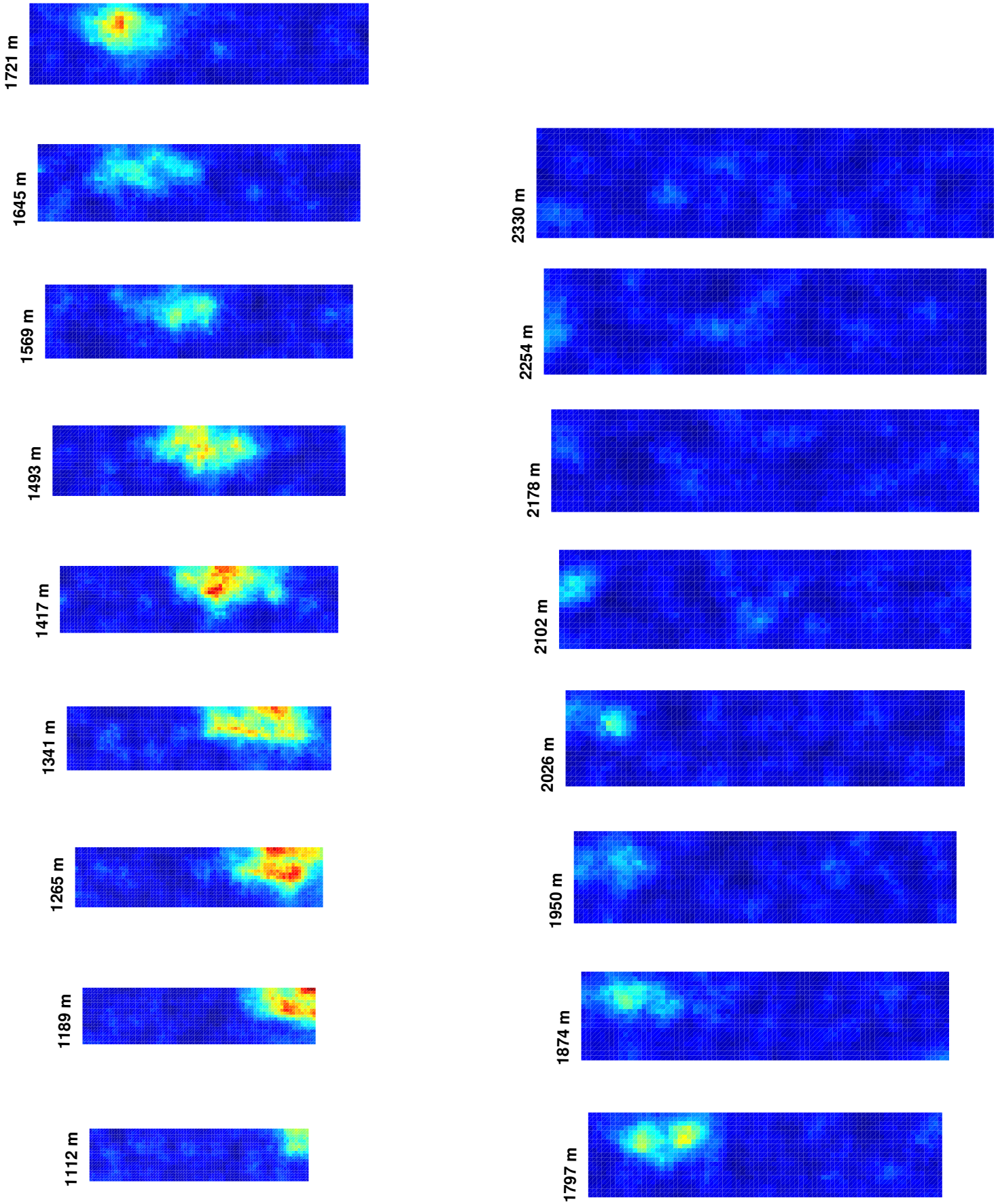

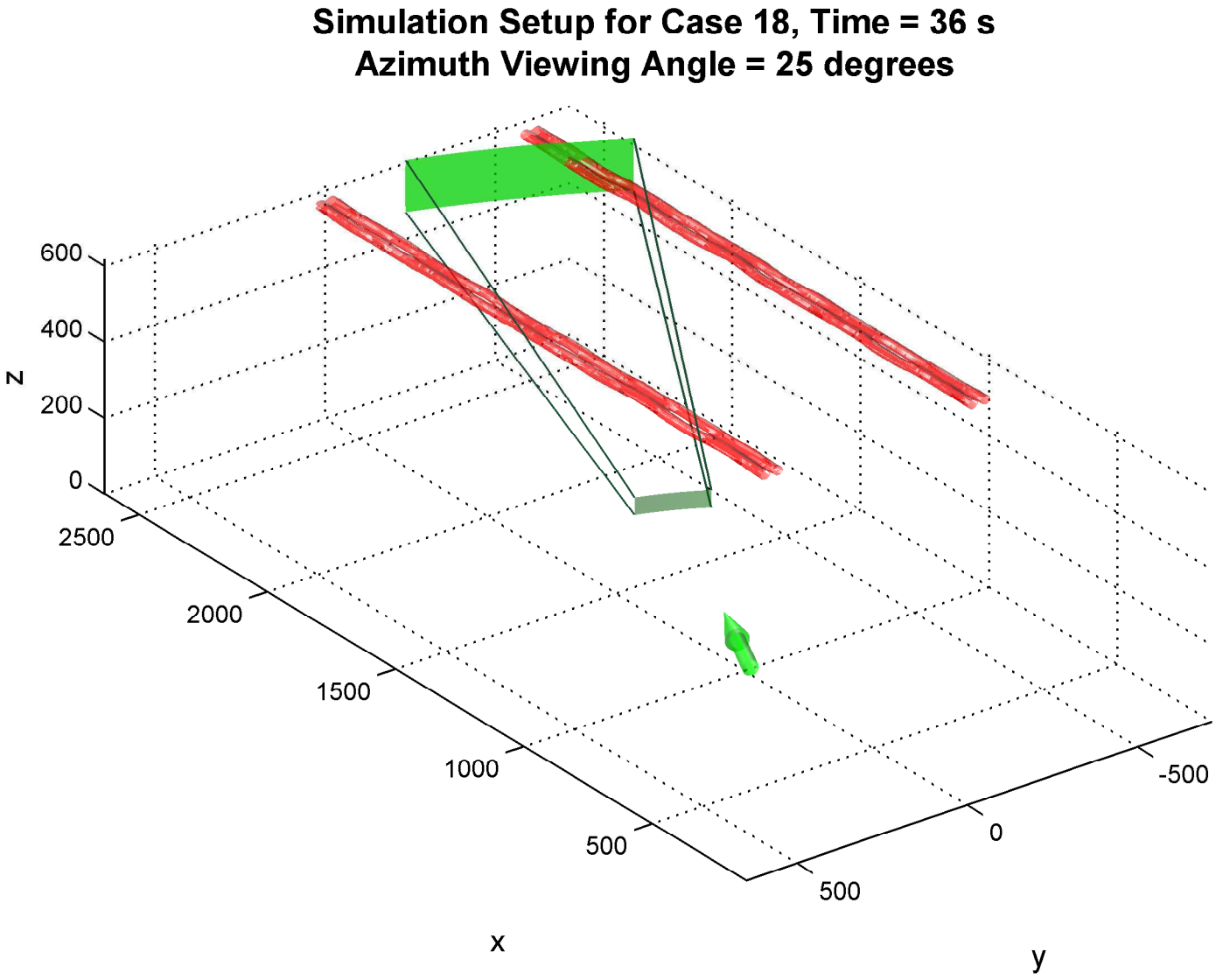
Simulation Setup for Case 18, Time = 36 s
Azimuth Viewing Angle = 25 degrees
600
400
200
0
z
2500
2000
1500
1000
500
x
500
0
-500
y

Simulation Results for Case 18, Time = 36 s
Azimuth Viewing Angle = 25 degrees

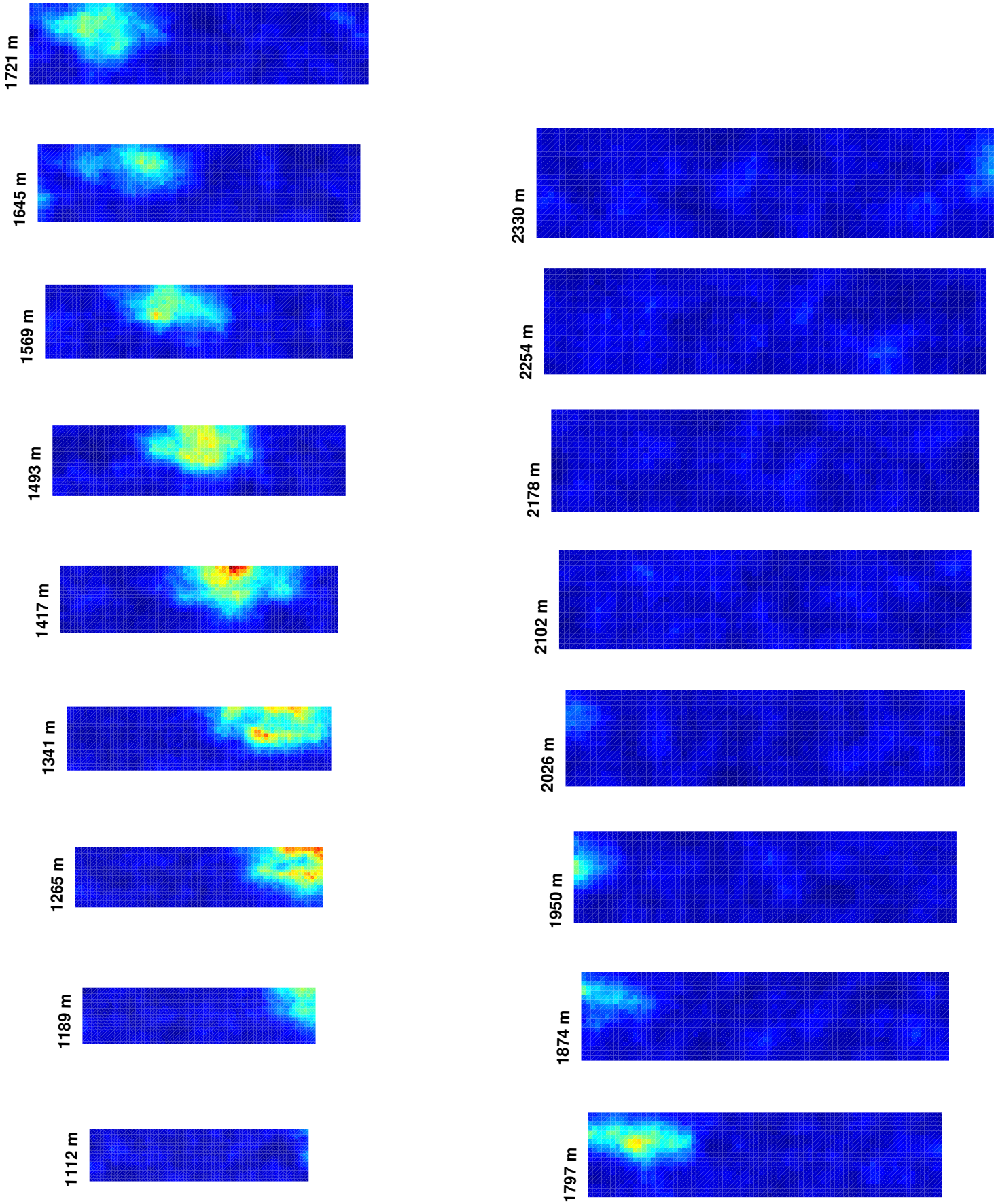

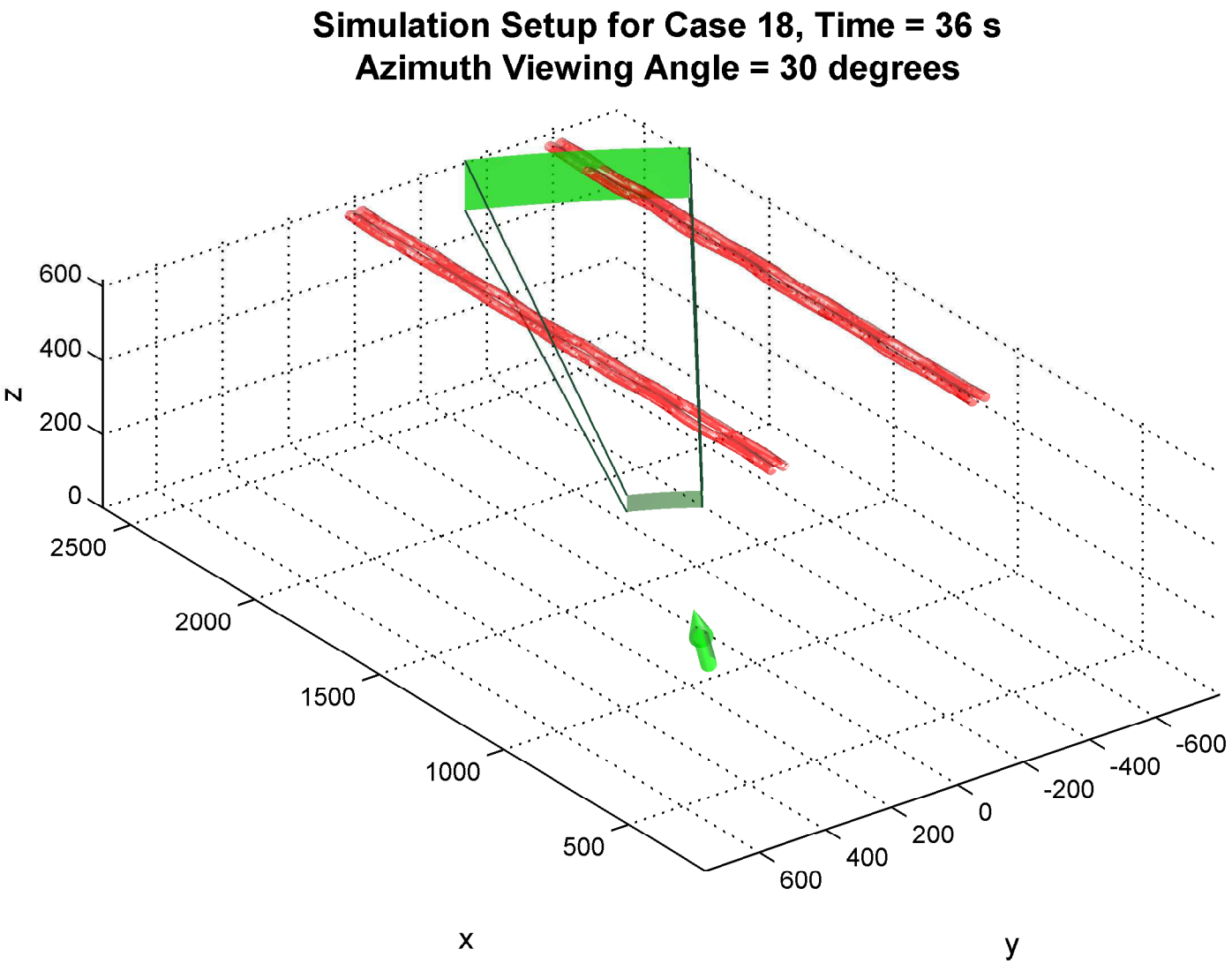
Simulation Setup for Case 18, Time = 36 s
Azimuth Viewing Angle = 30 degrees
z
600
400
200
0
2500
2000
1500
1000
500
x
600
400
200
0
-200
-400
-600
y

Simulation Results for Case 18, Time = 36 s
Azimuth Viewing Angle = 30 degrees

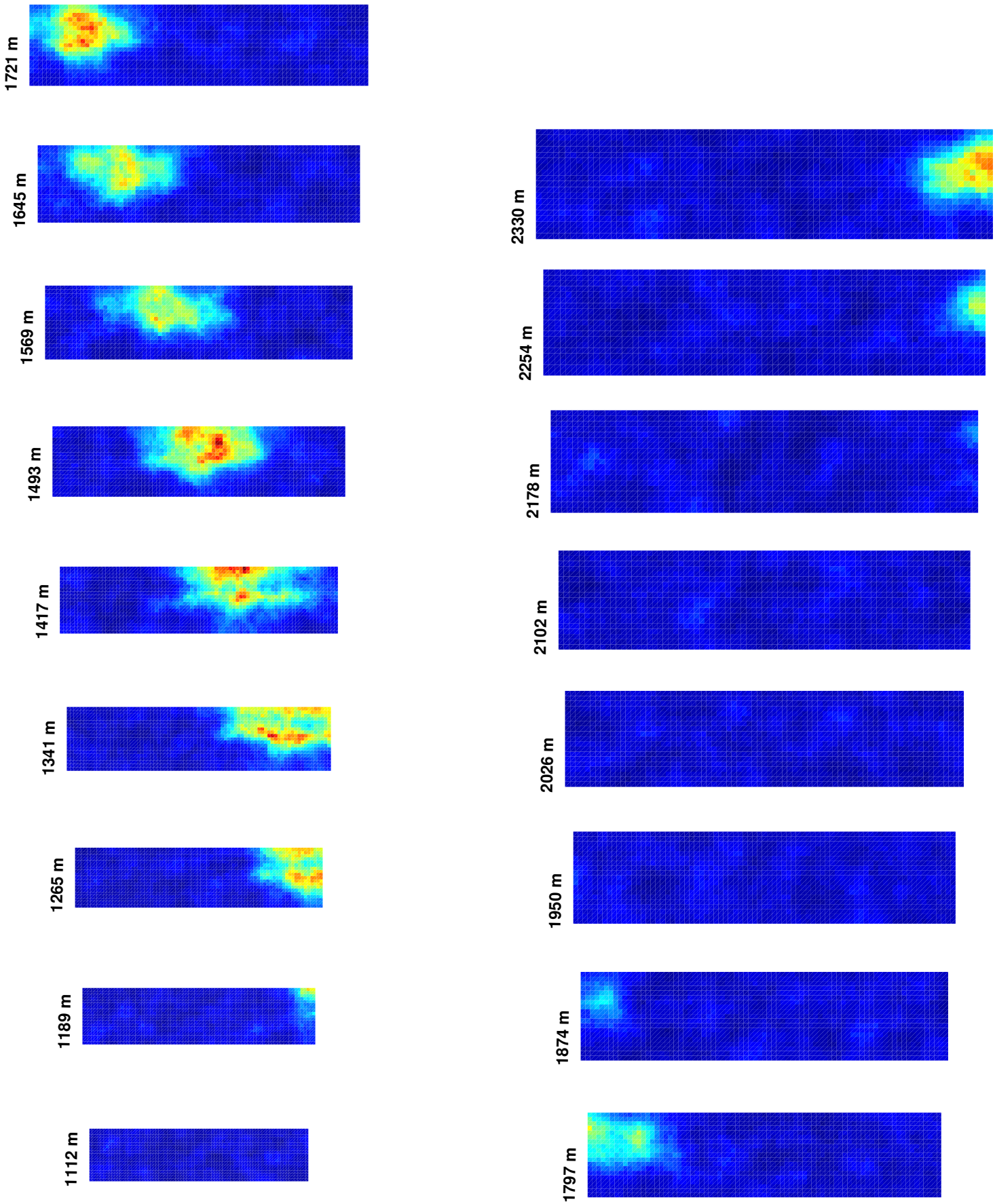

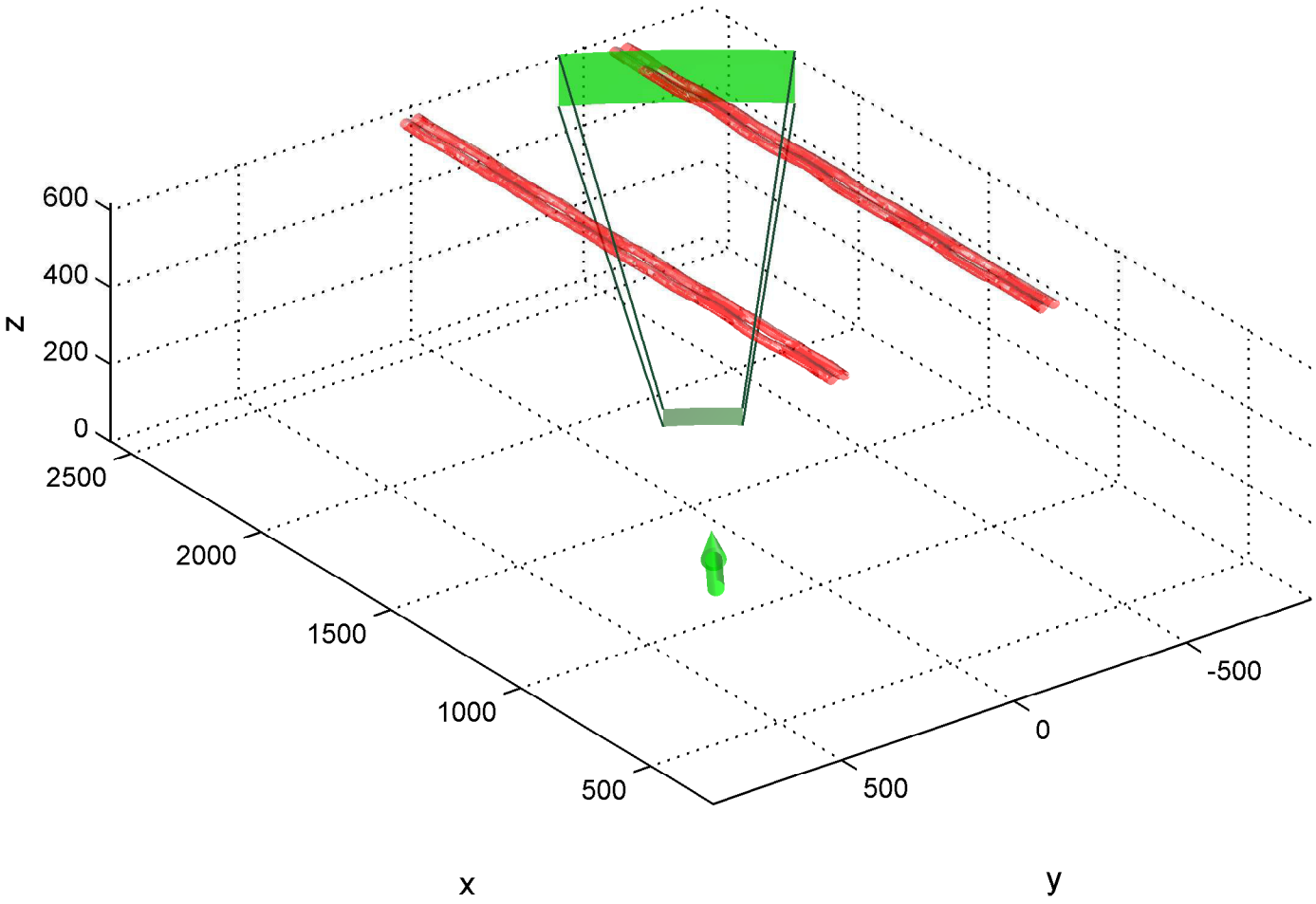
Simulation Setup for Case 18, Time = 36 s
Azimuth Viewing Angle = 35 degrees
600
400
200
0
z
2500
2000
1500
1000
500
x
500
0
-500
y

Simulation Results for Case 18, Time = 36 s
Azimuth Viewing Angle = 35 degrees

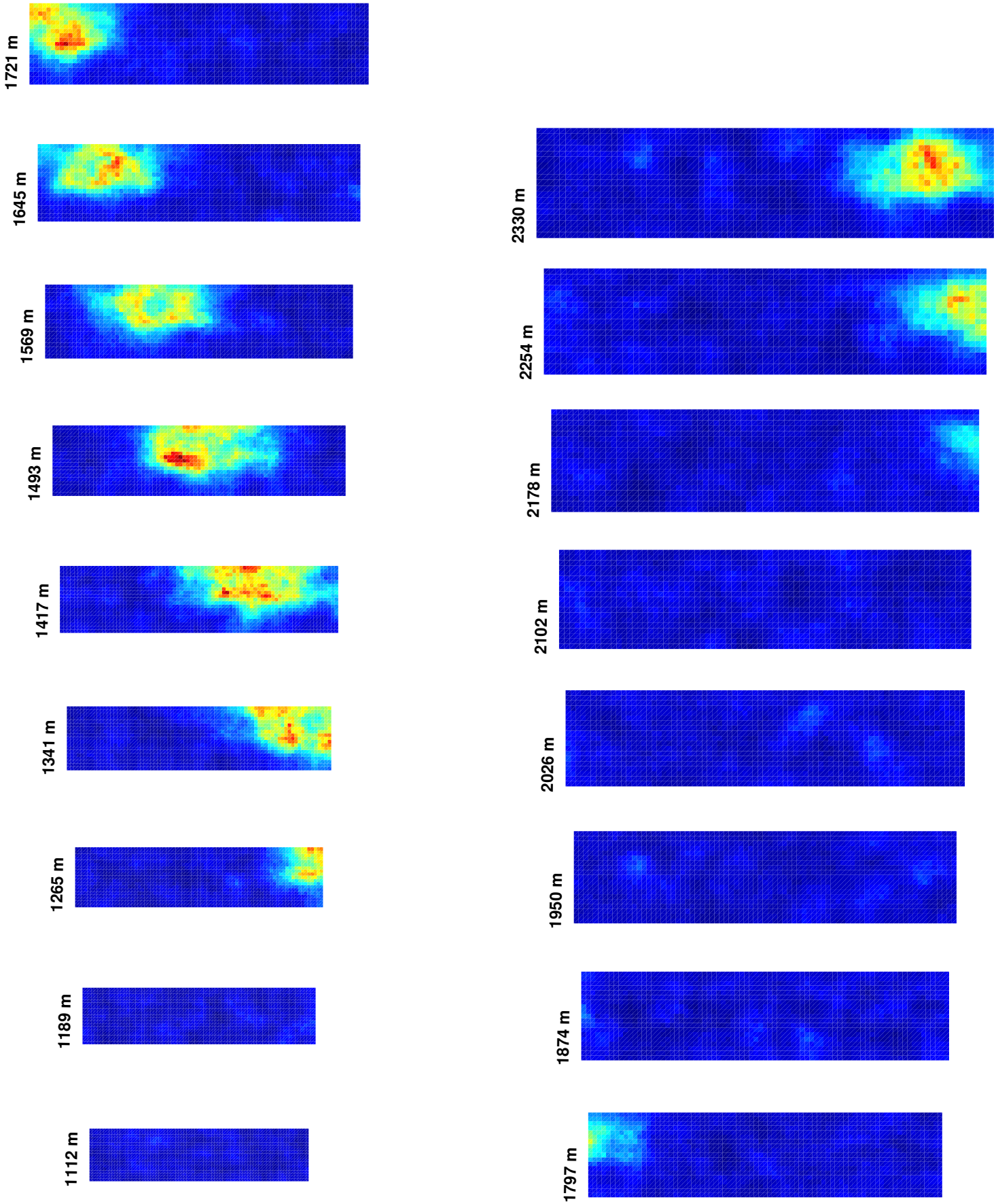

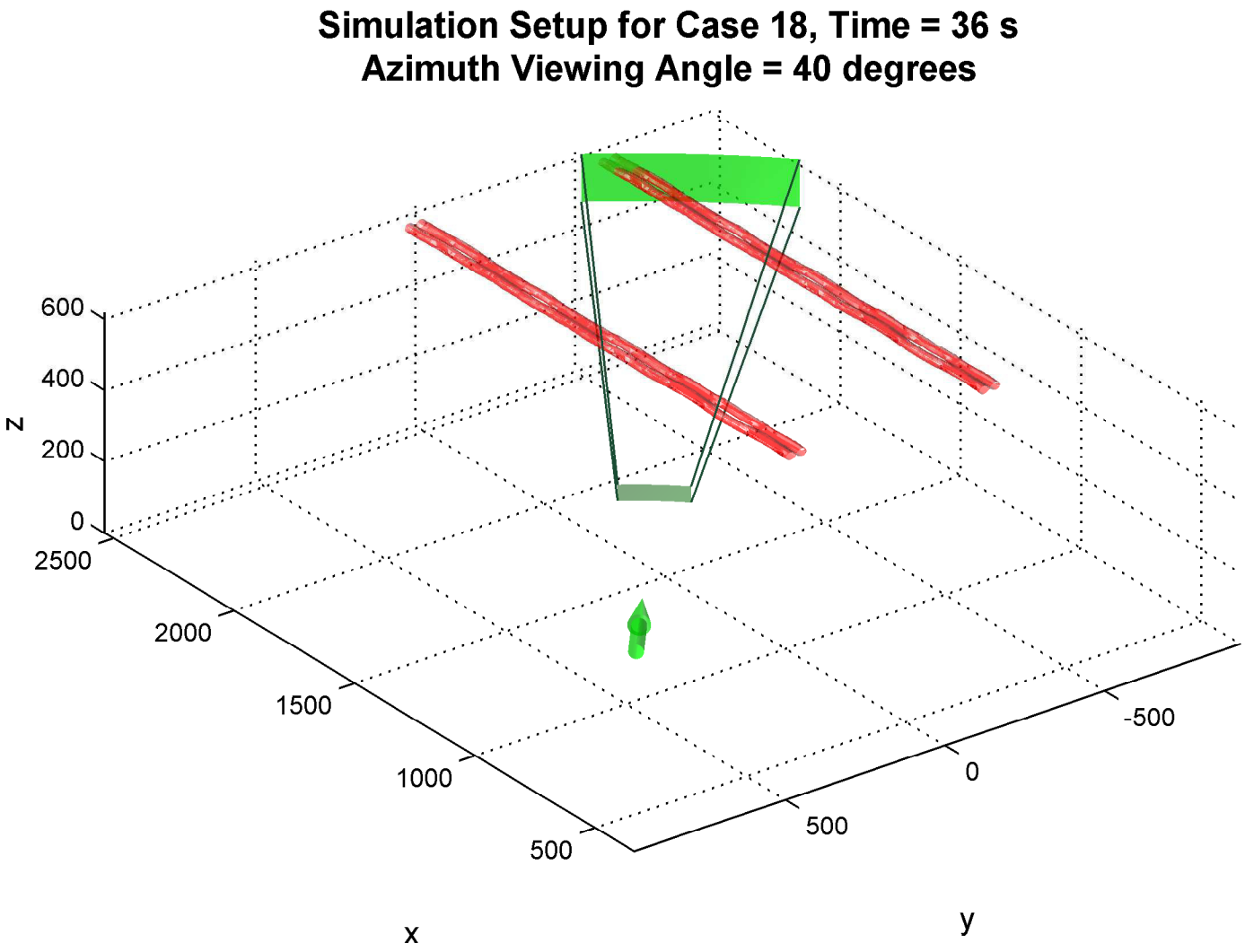
Simulation Setup for Case 18, Time = 36 s
Azimuth Viewing Angle = 40 degrees
600
400
200
0
z
2500
2000
1500
1000
500
x
-500
0
500
y

Simulation Results for Case 18, Time = 36 s
Azimuth Viewing Angle = 40 degrees

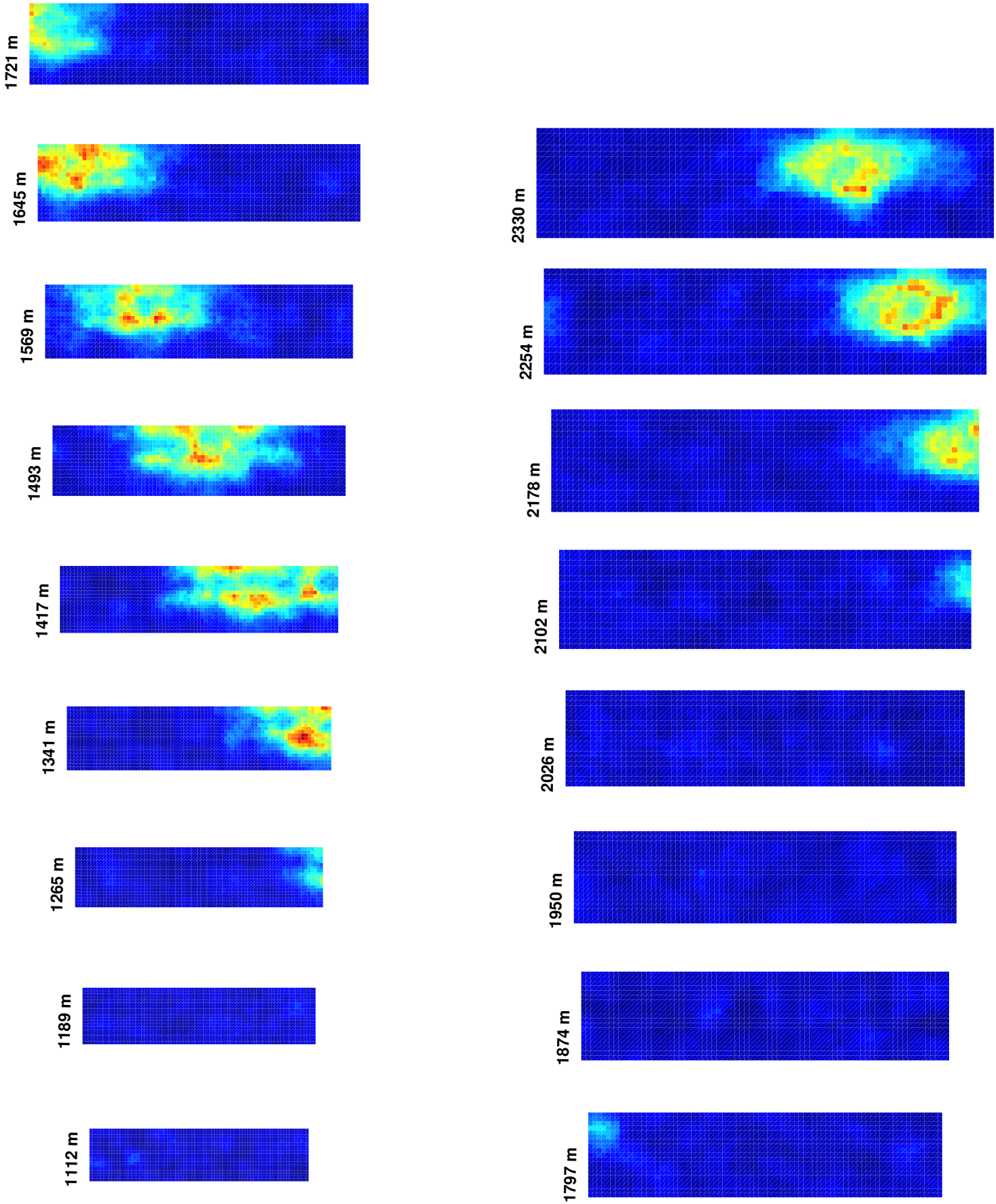

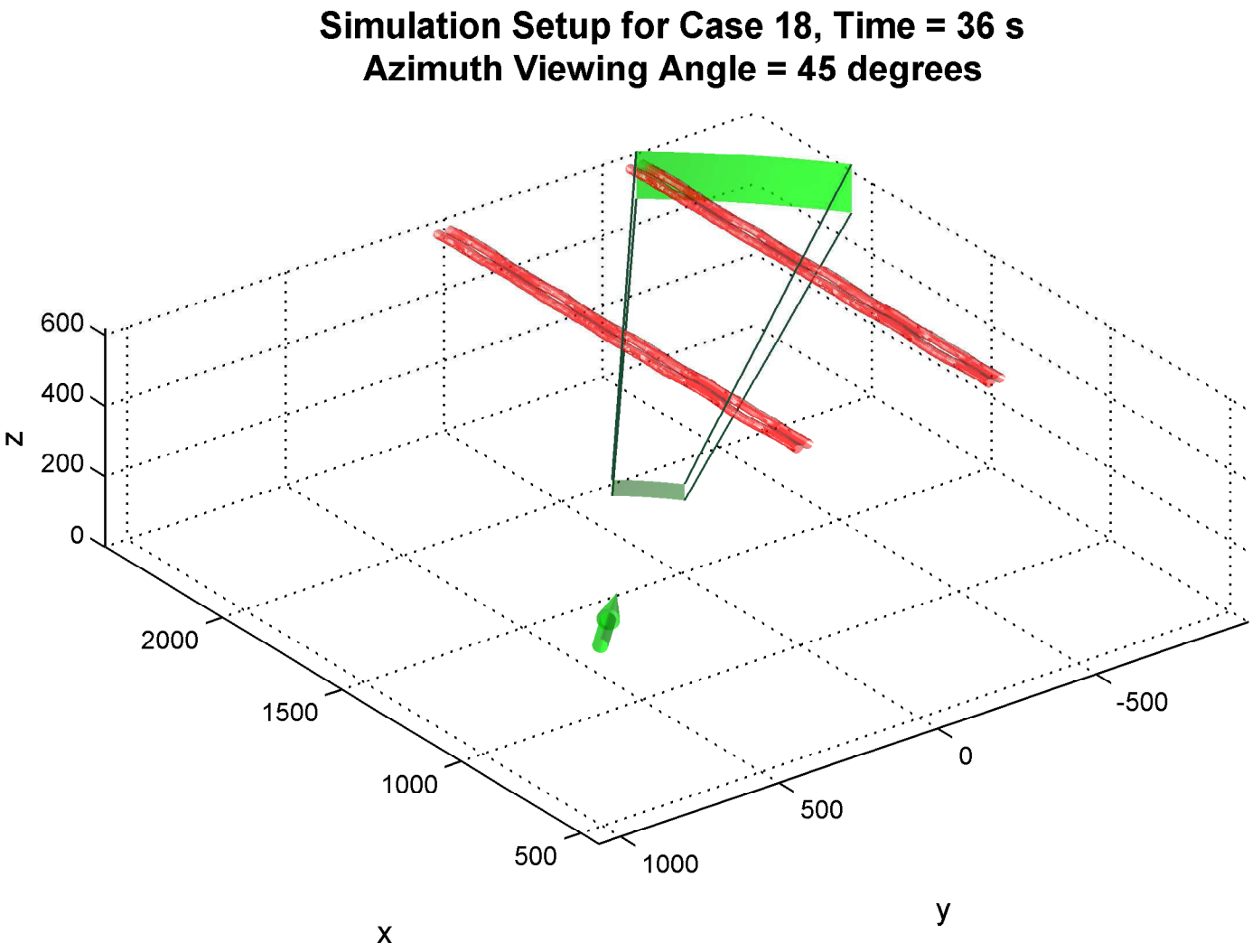
Simulation Setup for Case 18, Time = 36 s
Azimuth Viewing Angle = 45 degrees
600
400
200
0
z
2000
1500
1000
500
x
1000
500
0
-500
y

Simulation Results for Case 18, Time = 36 s
Azimuth Viewing Angle = 45 degrees

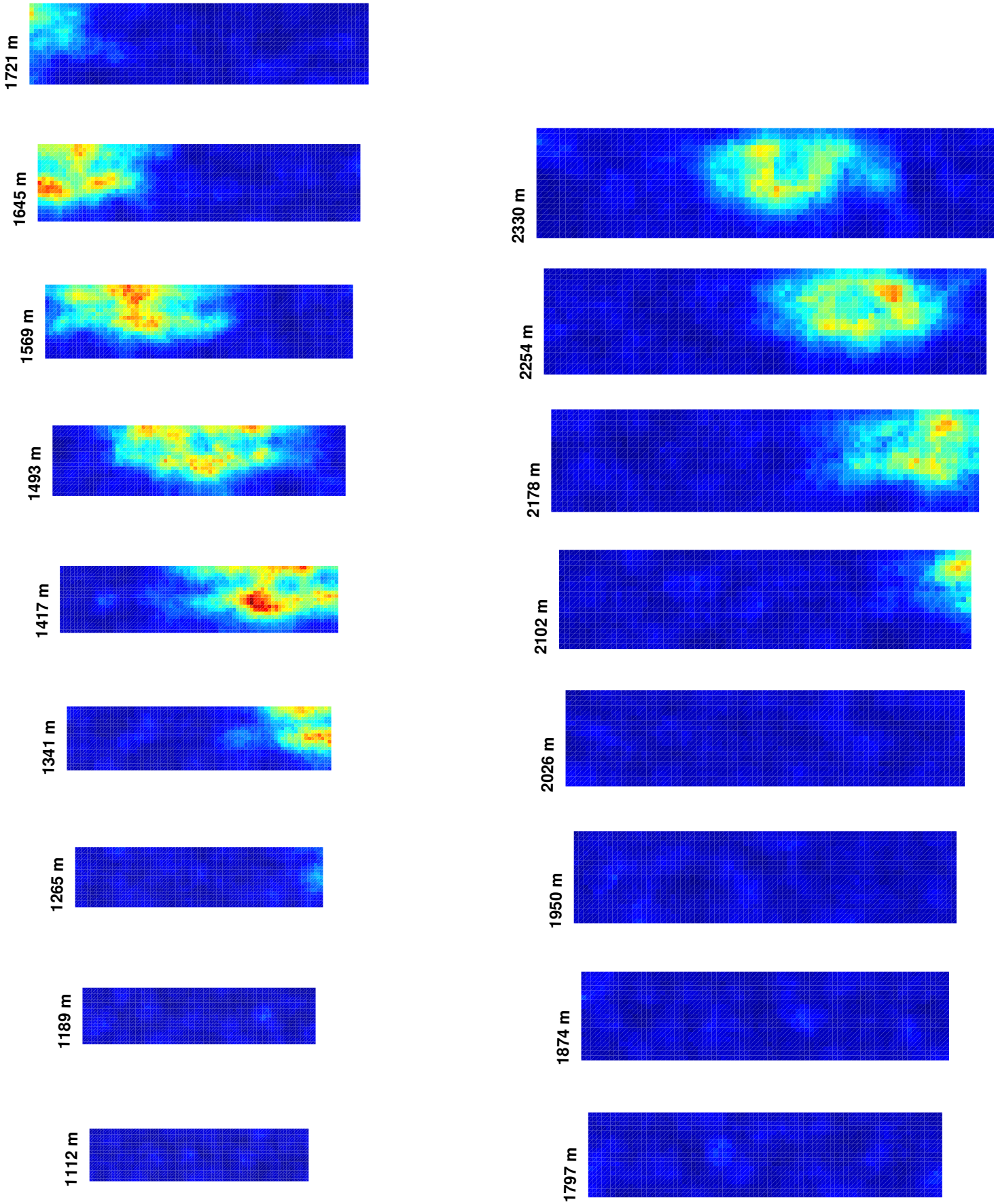

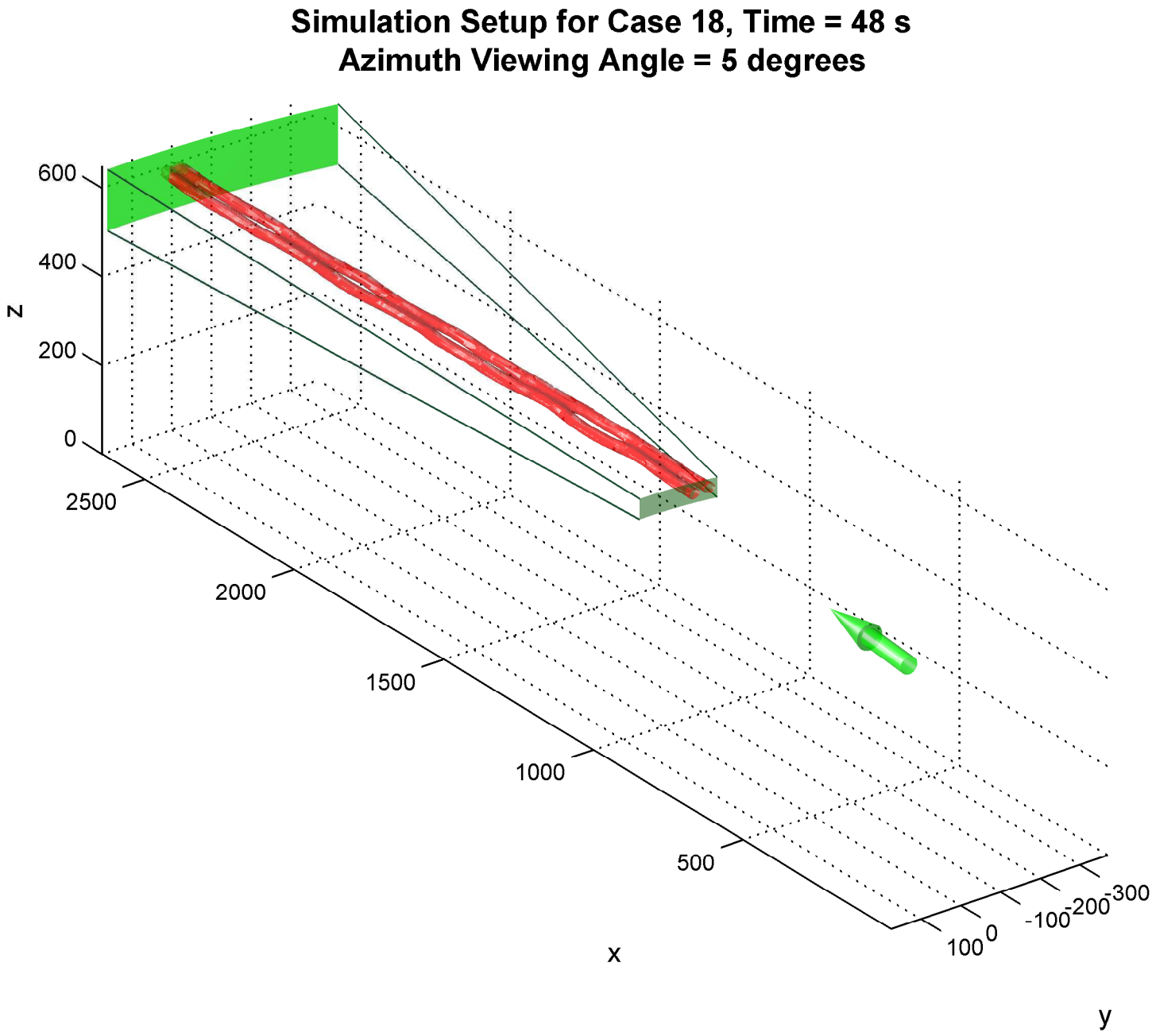
Simulation Setup for Case 18, Time = 48 s
Azimuth Viewing Angle = 5 degrees
600
400
200
0
z
2500
2000
1500
1000
500
x
100
0
-100
-200
-300
y

Simulation Results for Case 18, Time = 48 s
Azimuth Viewing Angle = 5 degrees

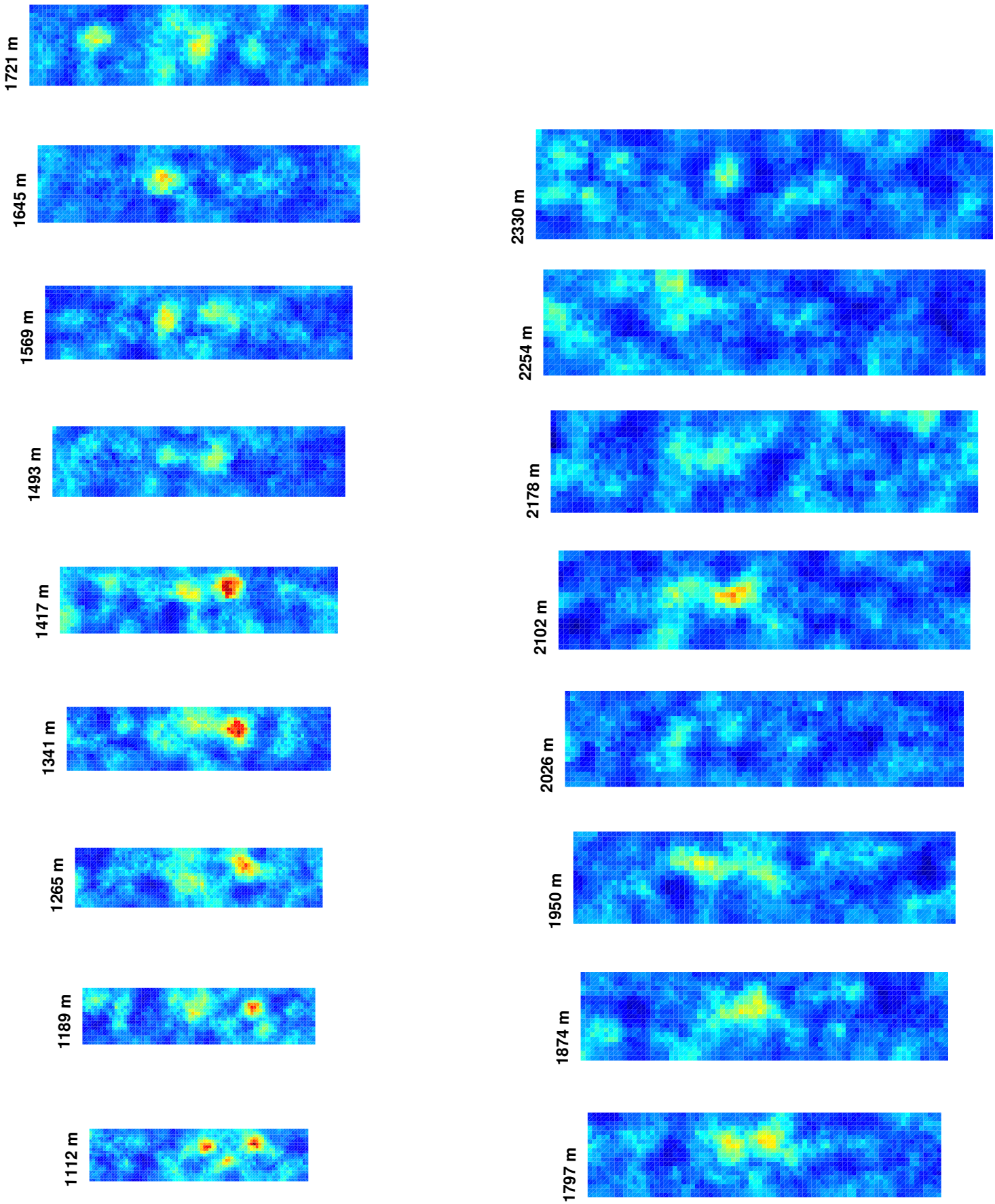

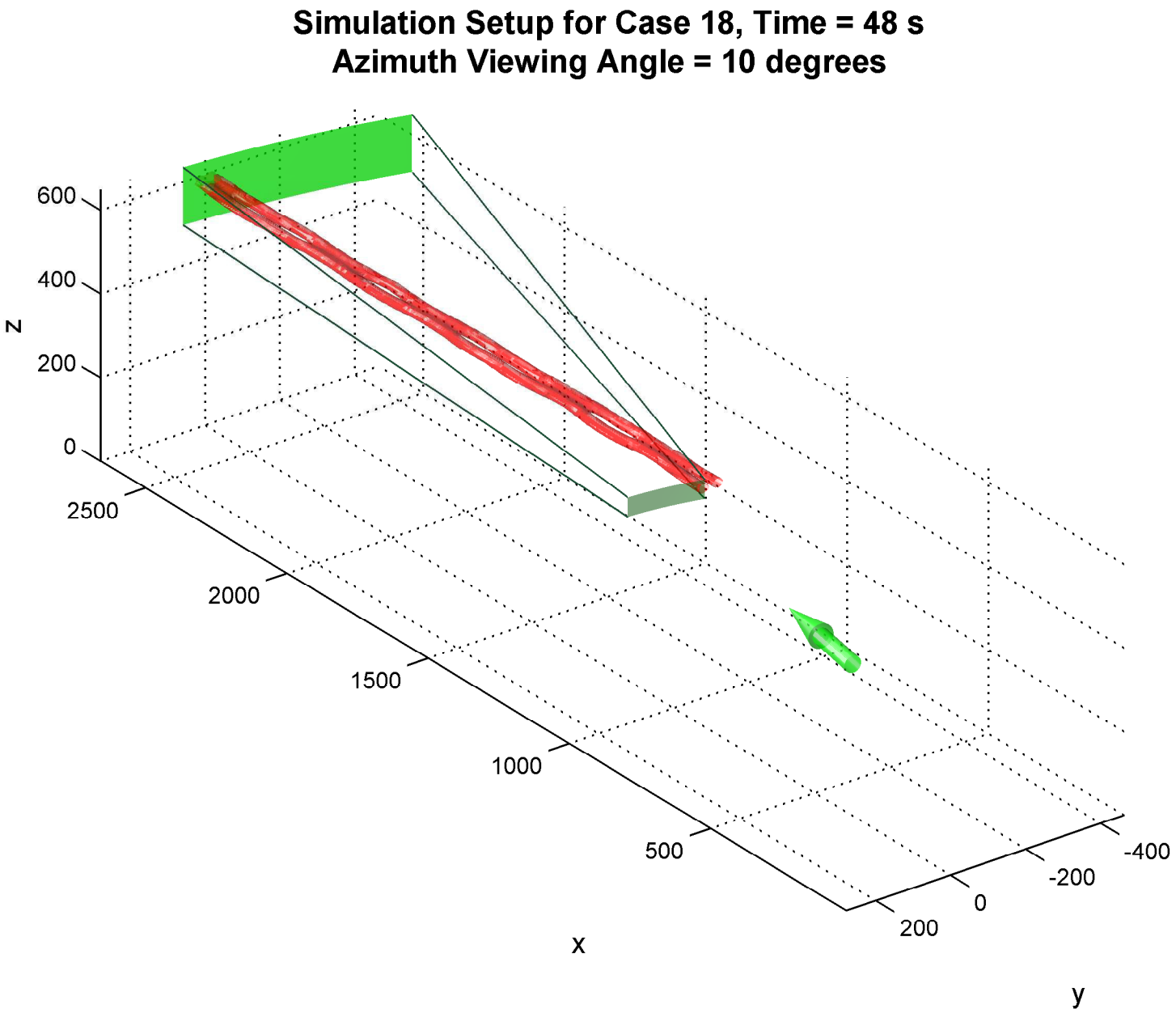
Simulation Setup for Case 18, Time = 48 s
Azimuth Viewing Angle = 10 degrees
600
400
200
0
z
2500
2000
1500
1000
500
x
200
0
-200
-400
y

Simulation Results for Case 18, Time = 48 s
Azimuth Viewing Angle = 10 degrees

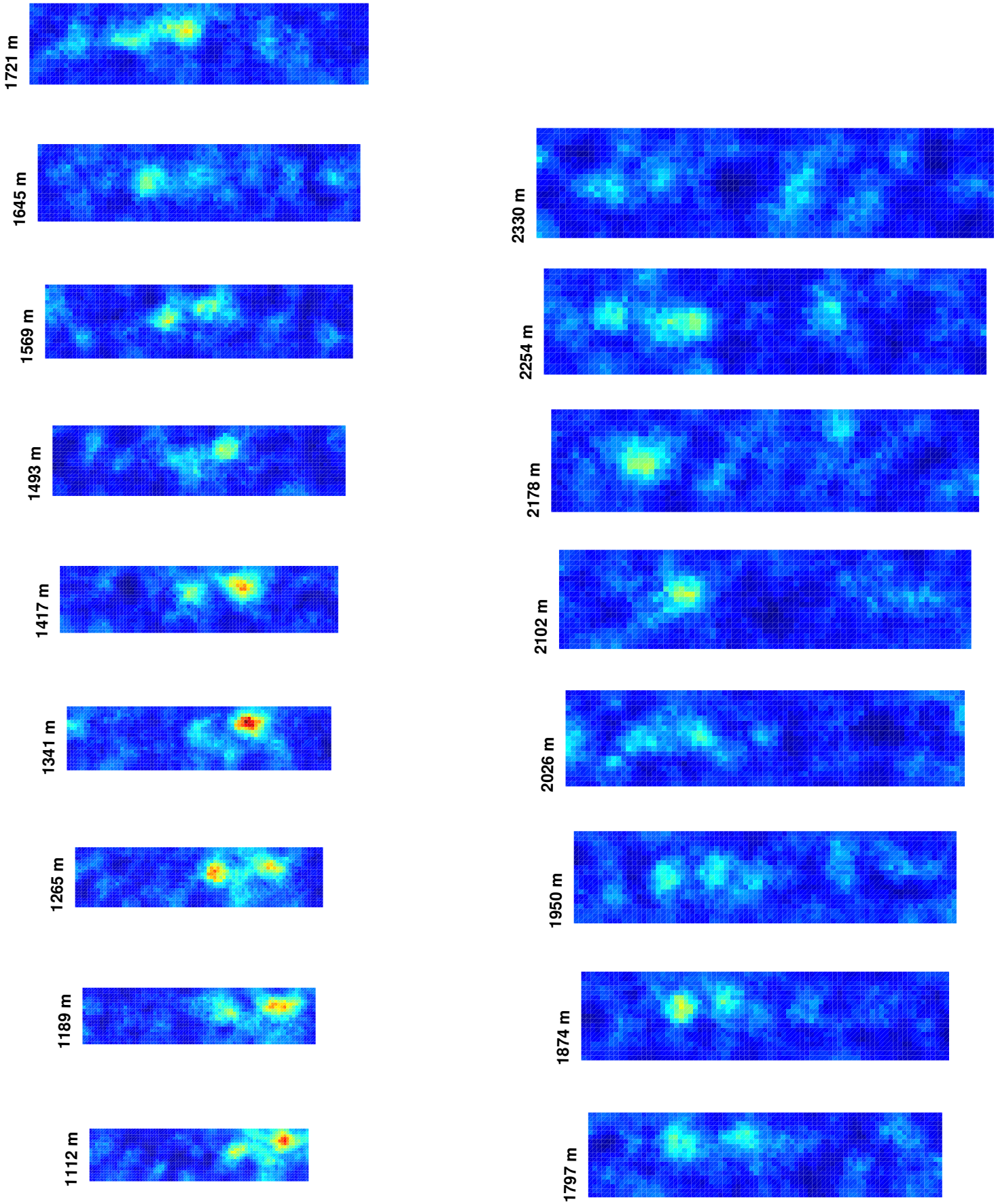

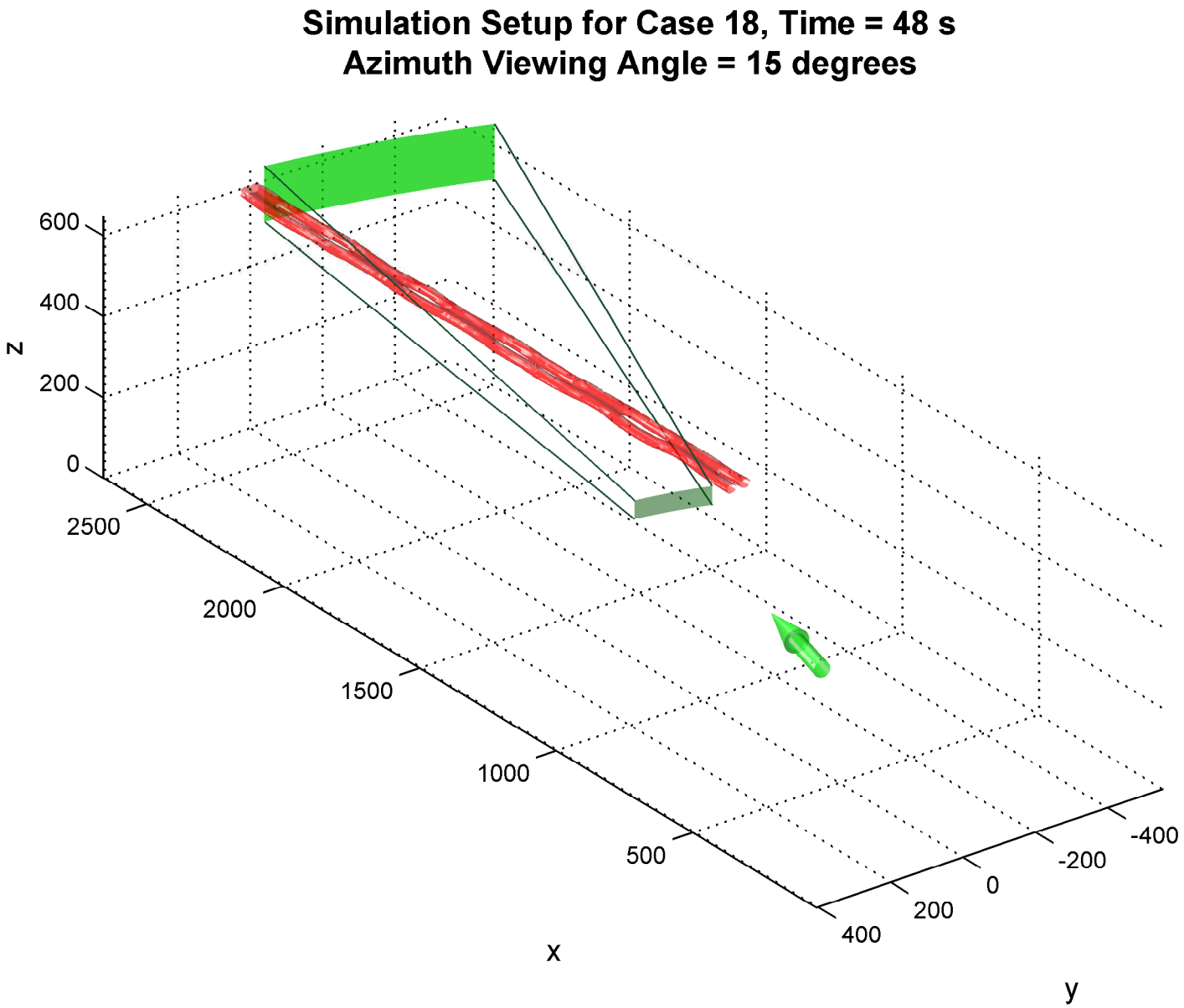
Simulation Setup for Case 18, Time = 48 s
Azimuth Viewing Angle = 15 degrees
z
600
400
200
0
2500
2000
1500
1000
500
x
400
200
0
-200
-400
y

Simulation Results for Case 18, Time = 48 s
Azimuth Viewing Angle = 15 degrees

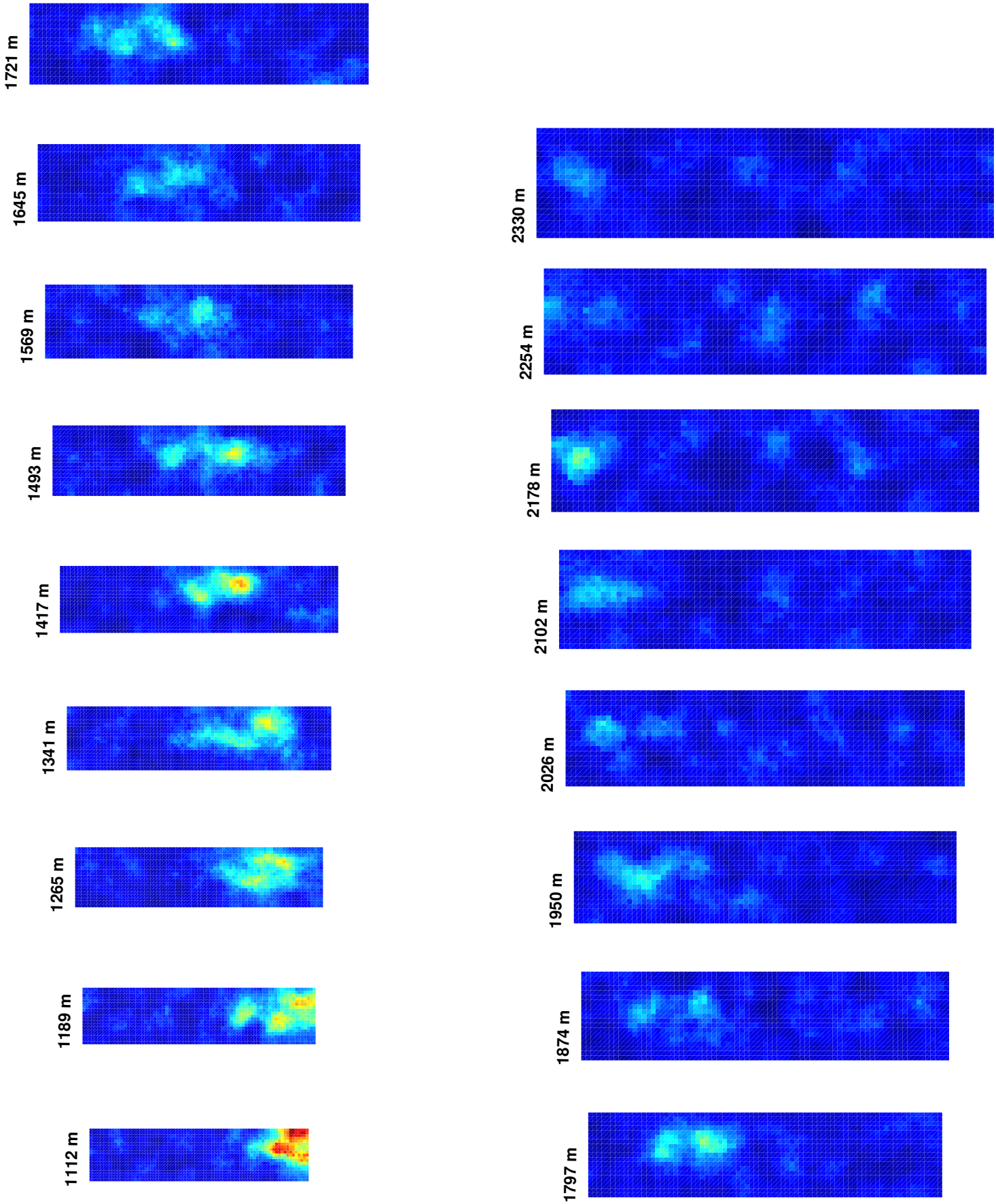

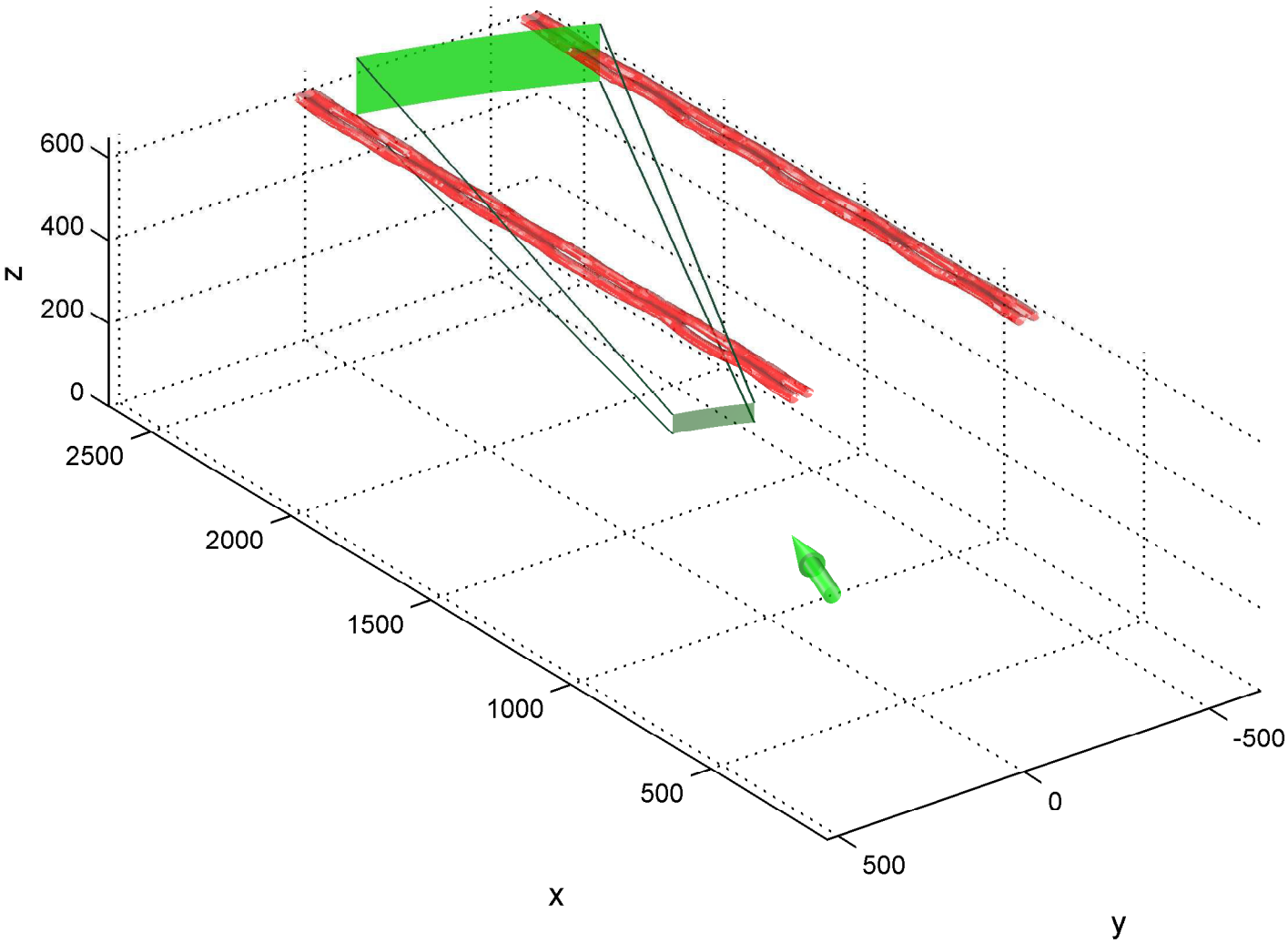
Simulation Setup for Case 18, Time = 48 s
Azimuth Viewing Angle = 20 degrees
600
400
200
0
z
2500
2000
1500
1000
500
x
500
0
-500
y

Simulation Results for Case 18, Time = 48 s
Azimuth Viewing Angle = 20 degrees

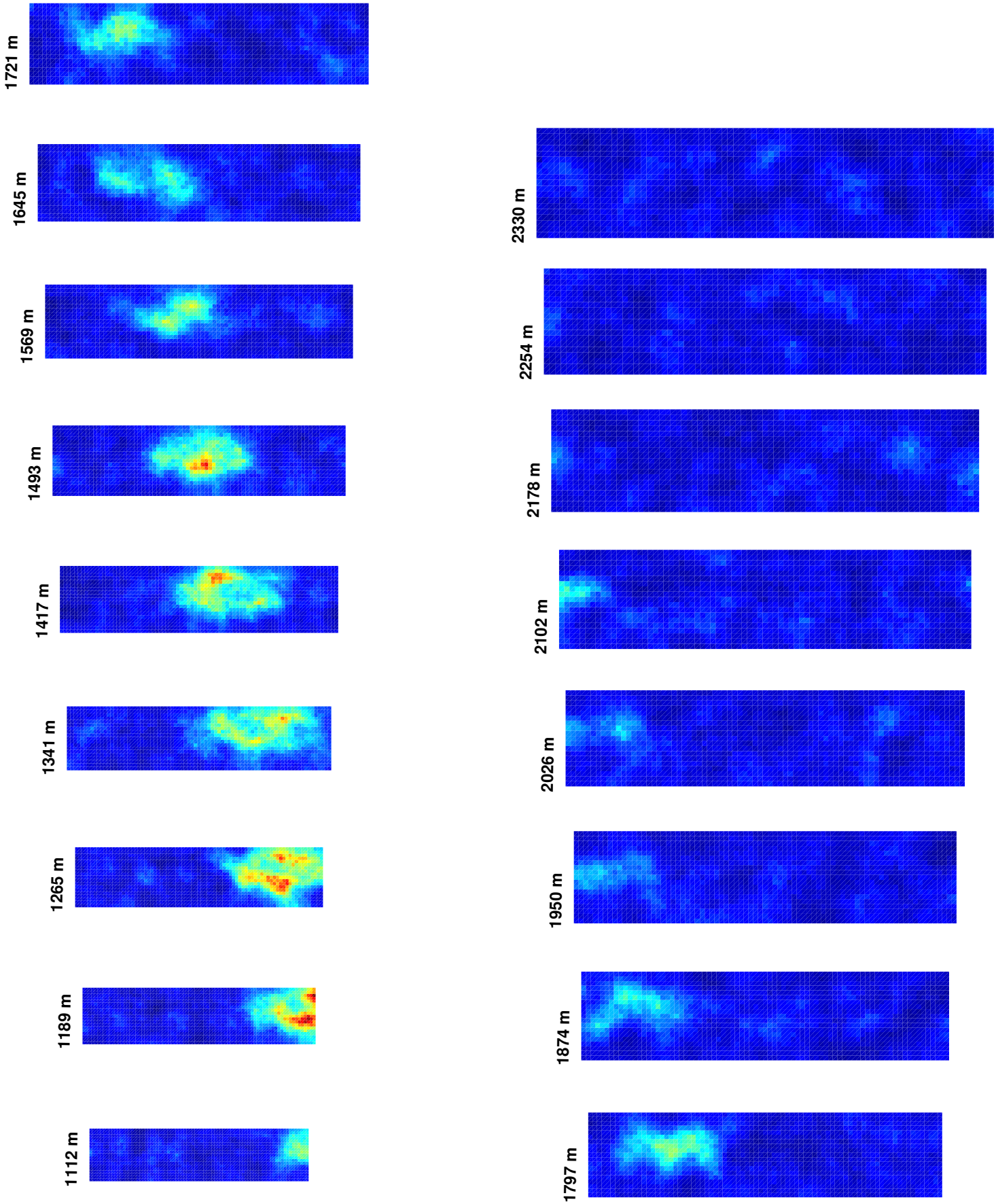

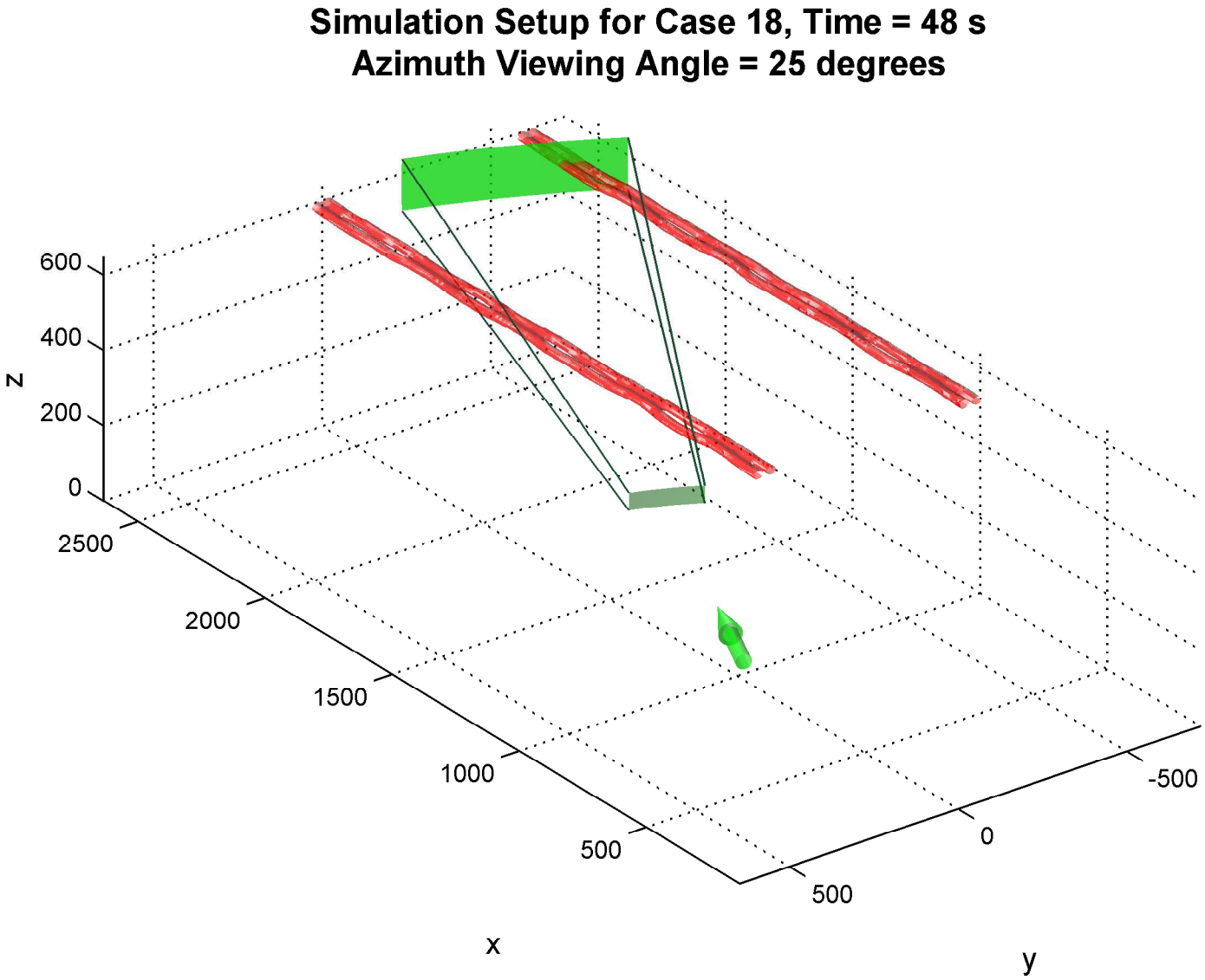
Simulation Setup for Case 18, Time = 48 s
Azimuth Viewing Angle = 25 degrees
600
400
200
0
z
2500
2000
1500
1000
500
x
500
0
-500
y

Simulation Results for Case 18, Time = 48 s
Azimuth Viewing Angle = 25 degrees

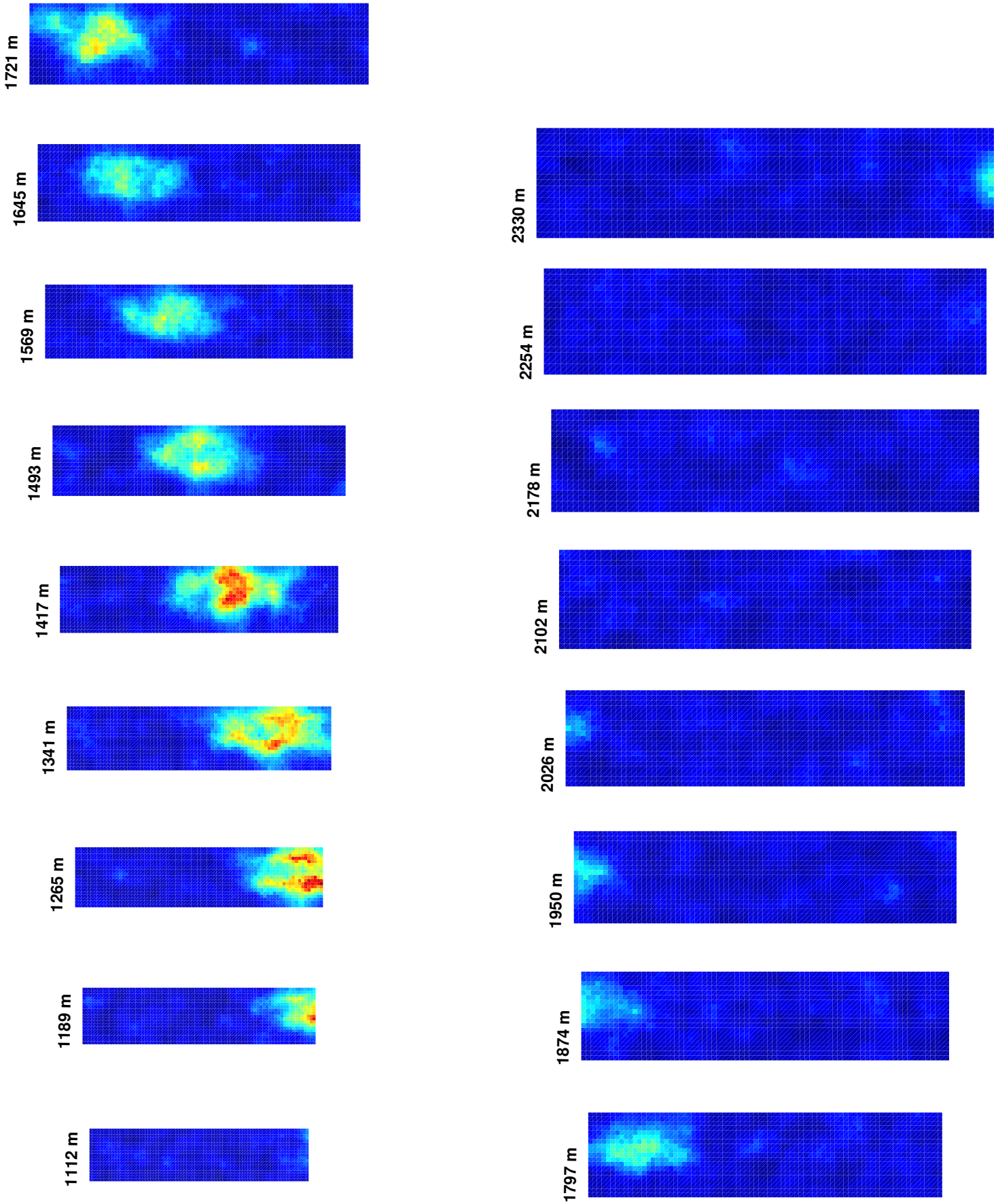

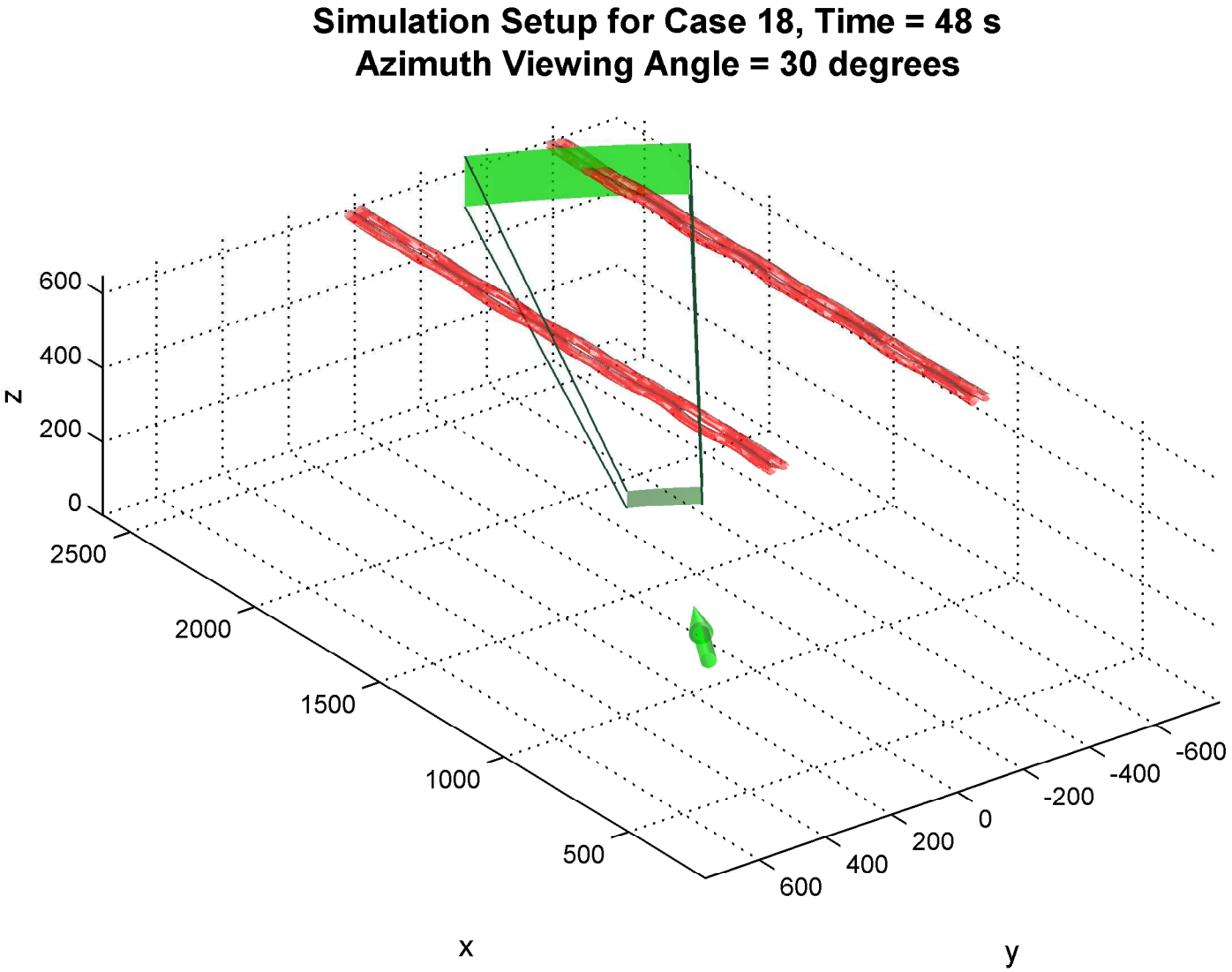
Simulation Setup for Case 18, Time = 48 s
Azimuth Viewing Angle = 30 degrees
z
600
400
200
0
x
2500
2000
1500
1000
500
y
600
400
200
0
-200
-400
-600

Simulation Results for Case 18, Time = 48 s
Azimuth Viewing Angle = 30 degrees

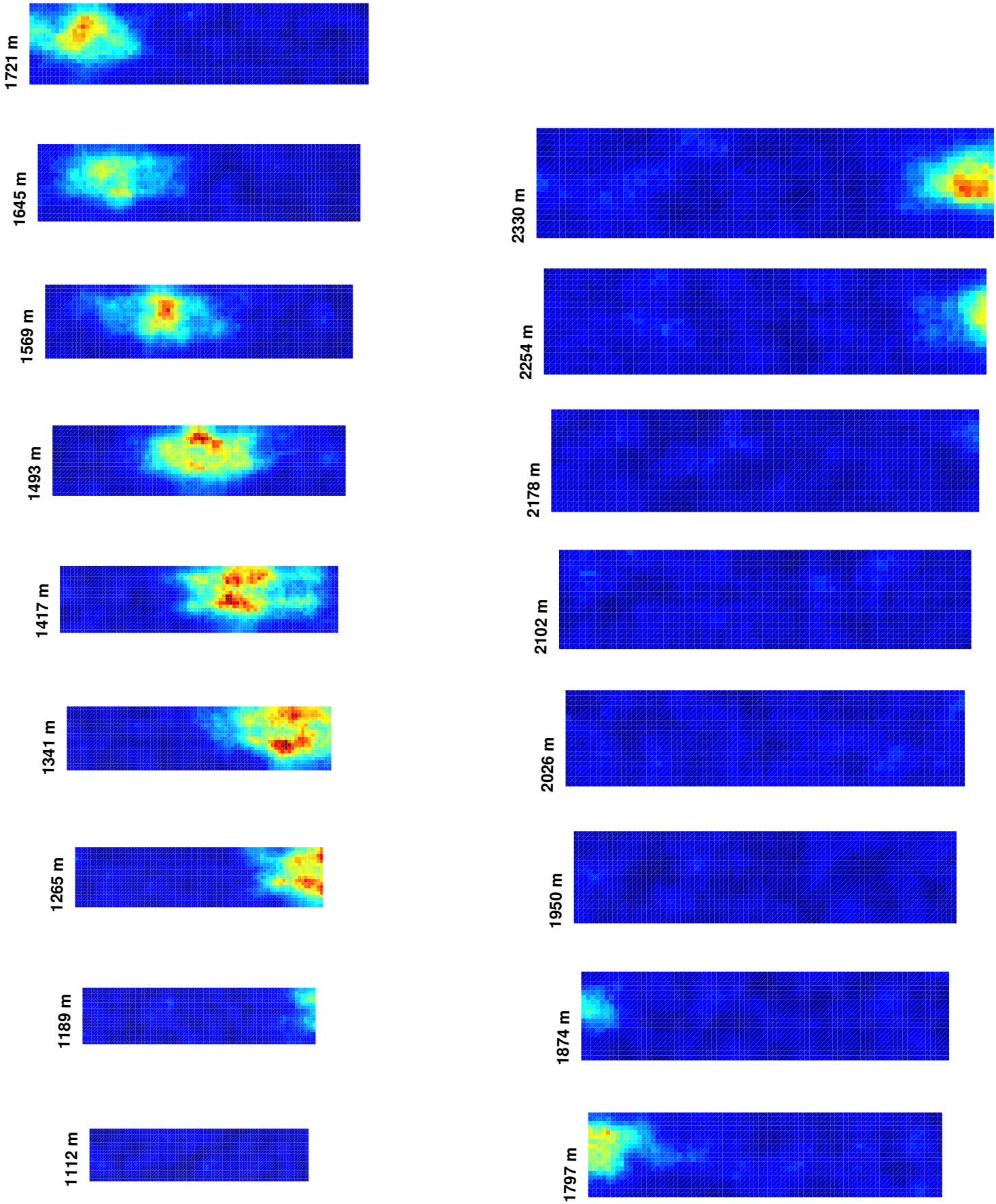

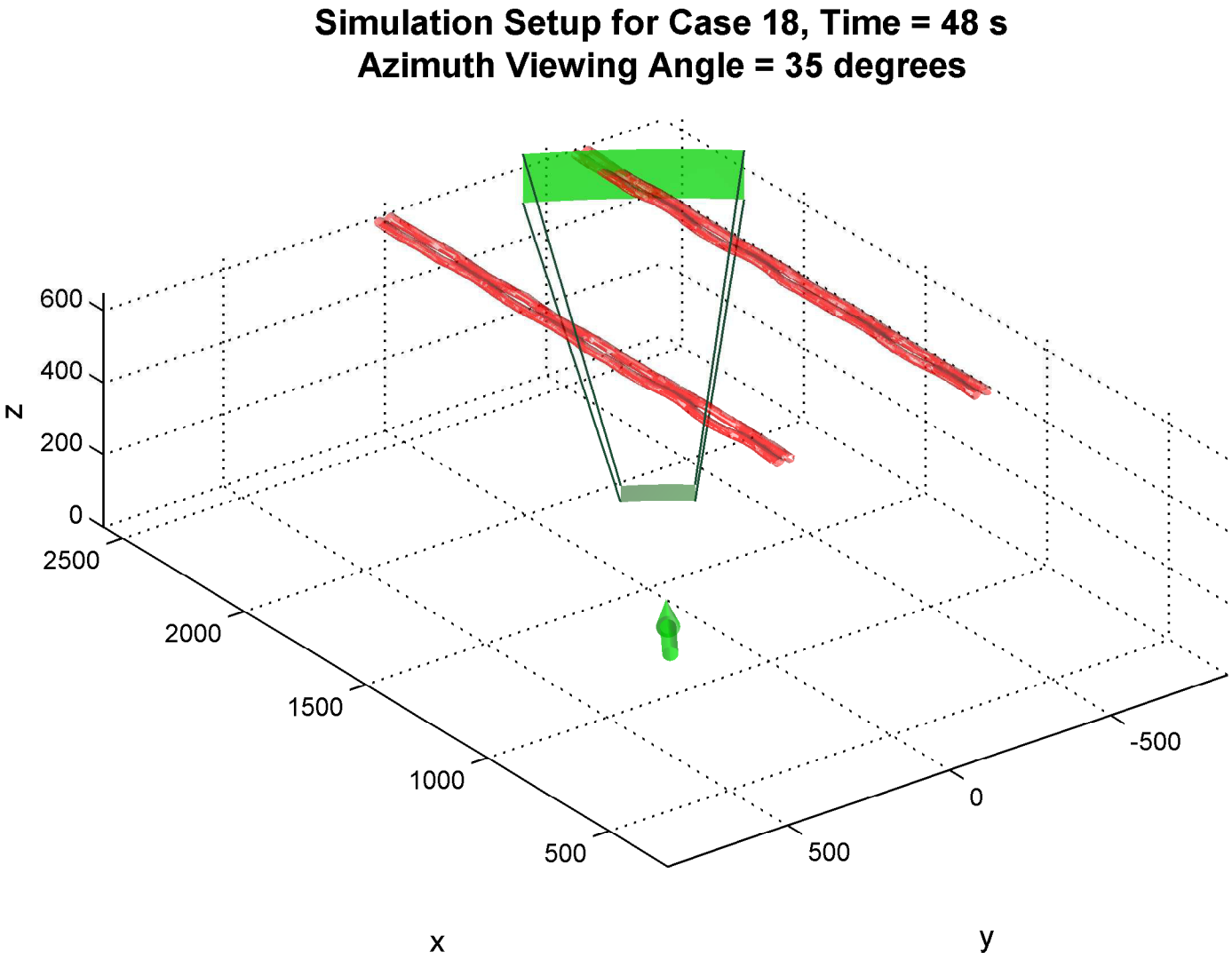
Simulation Setup for Case 18, Time = 48 s
Azimuth Viewing Angle = 35 degrees
600
400
200
0
z
2500
2000
1500
1000
500
x
500
0
-500
y

Simulation Results for Case 18, Time = 48 s
Azimuth Viewing Angle = 35 degrees

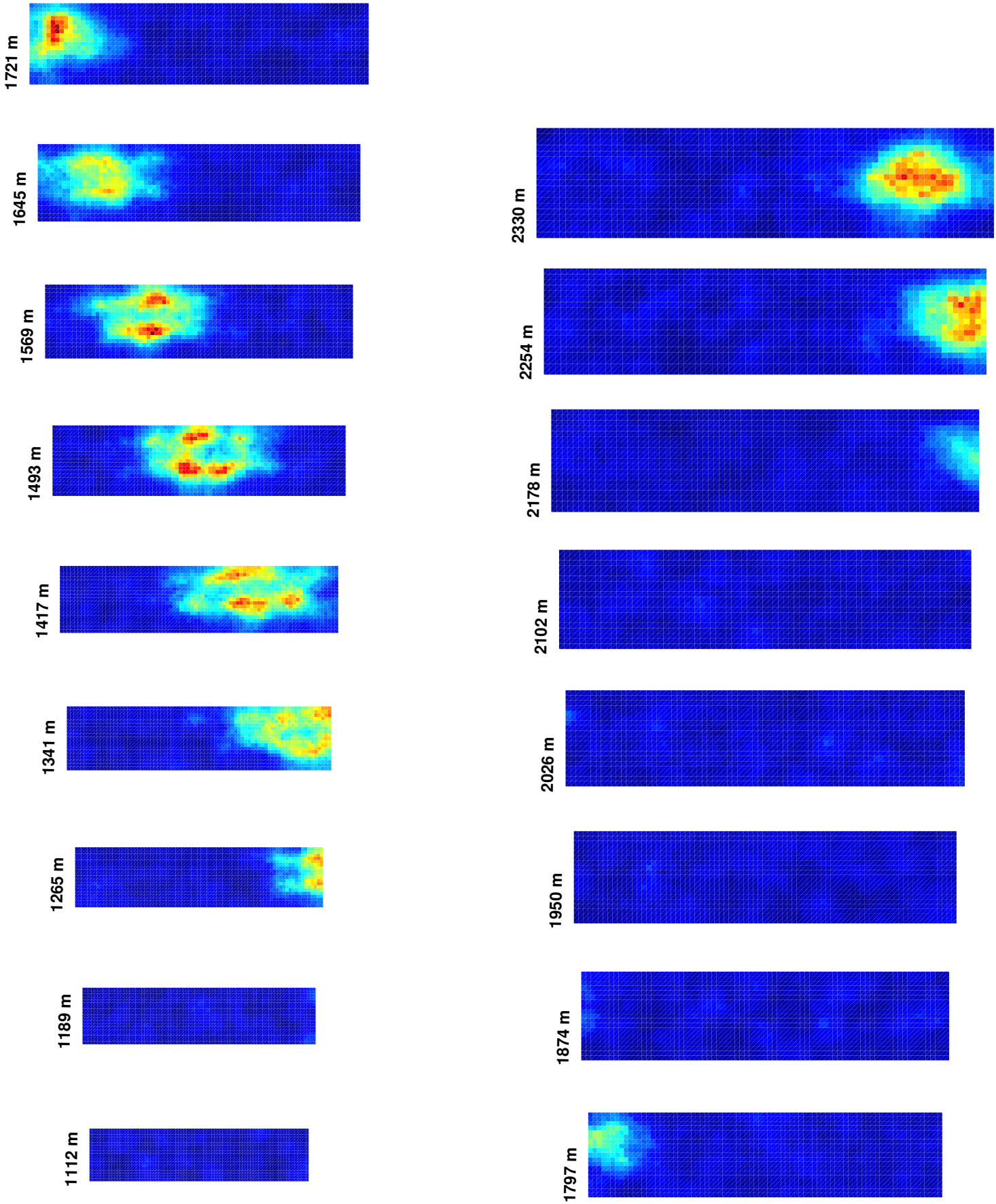

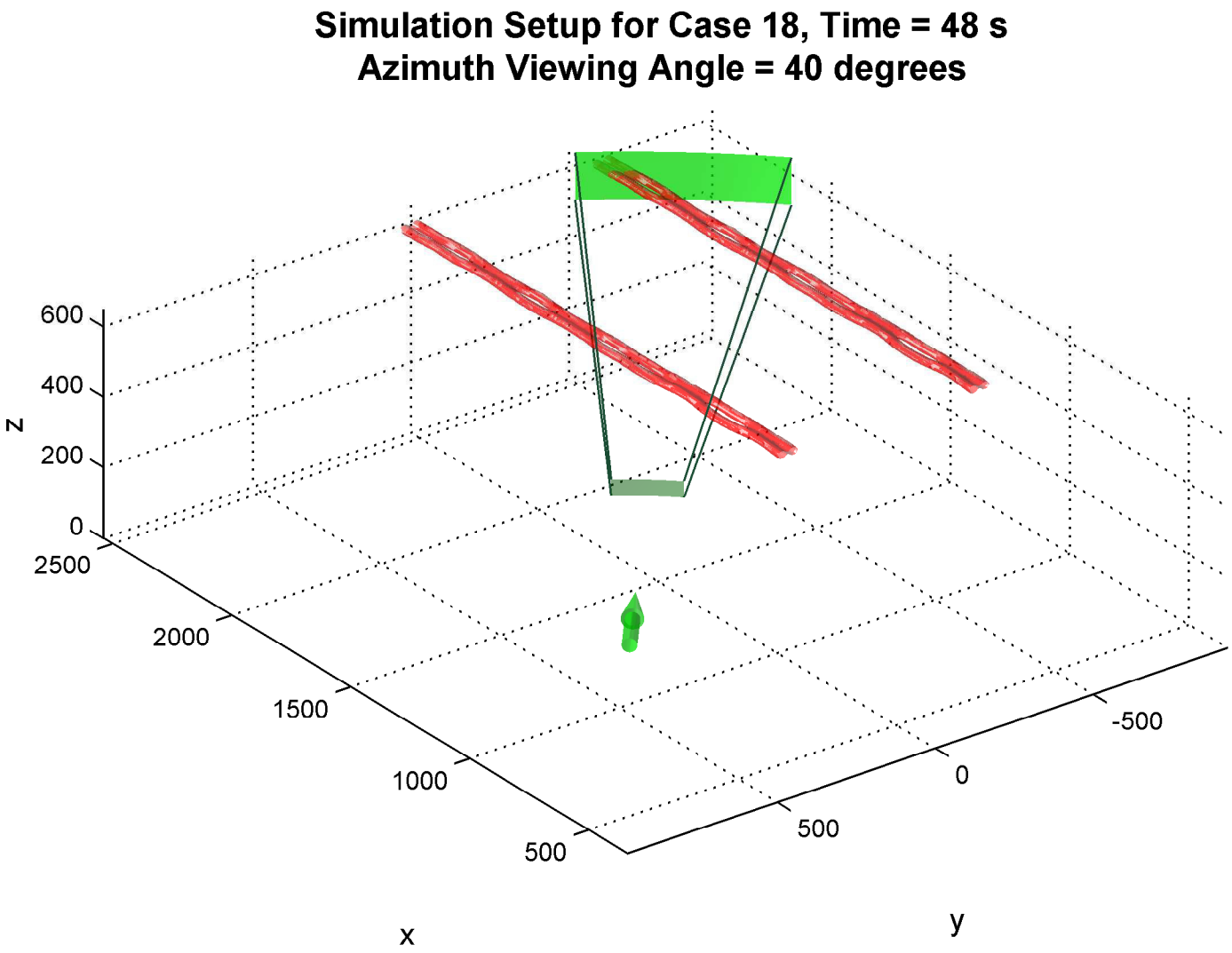
Simulation Setup for Case 18, Time = 48 s
Azimuth Viewing Angle = 40 degrees
600
400
200
0
z
2500
2000
1500
1000
500
x
-500
0
500
y

Simulation Results for Case 18, Time = 48 s
Azimuth Viewing Angle = 40 degrees

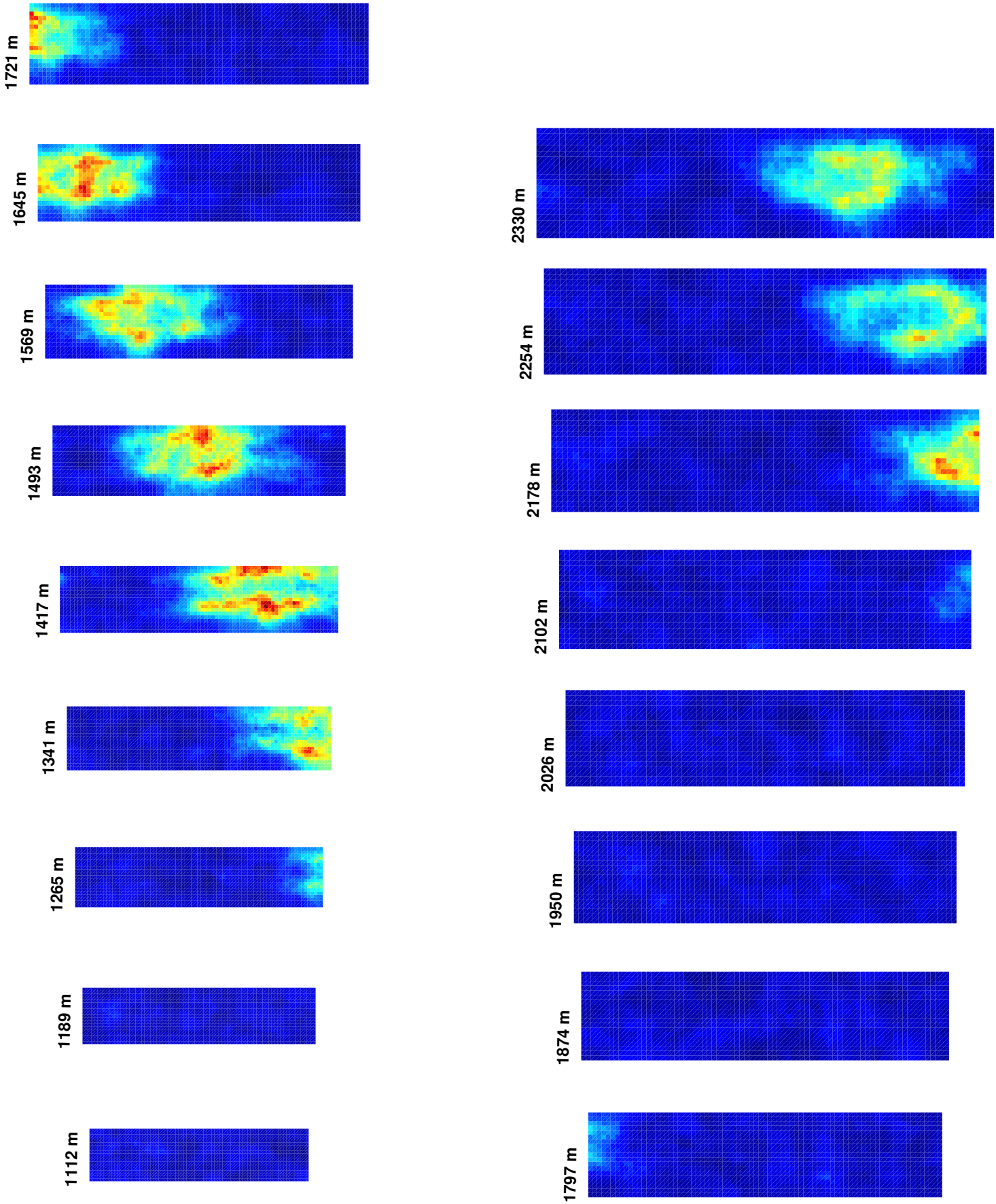

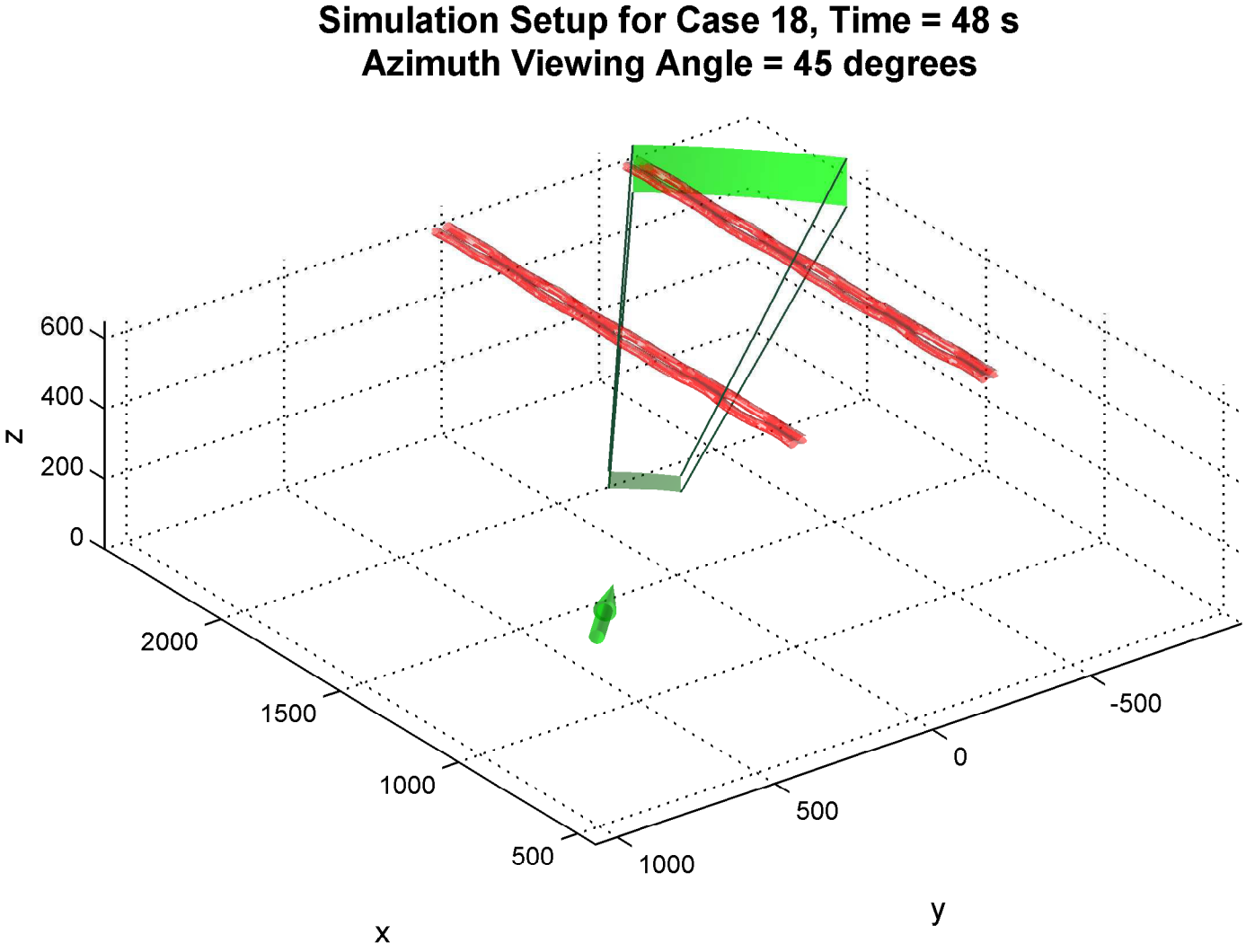
Simulation Setup for Case 18, Time = 48 s
Azimuth Viewing Angle = 45 degrees
600
400
200
0
z
2000
1500
1000
500
x
1000
500
0
-500
y

Simulation Results for Case 18, Time = 48 s
Azimuth Viewing Angle = 45 degrees

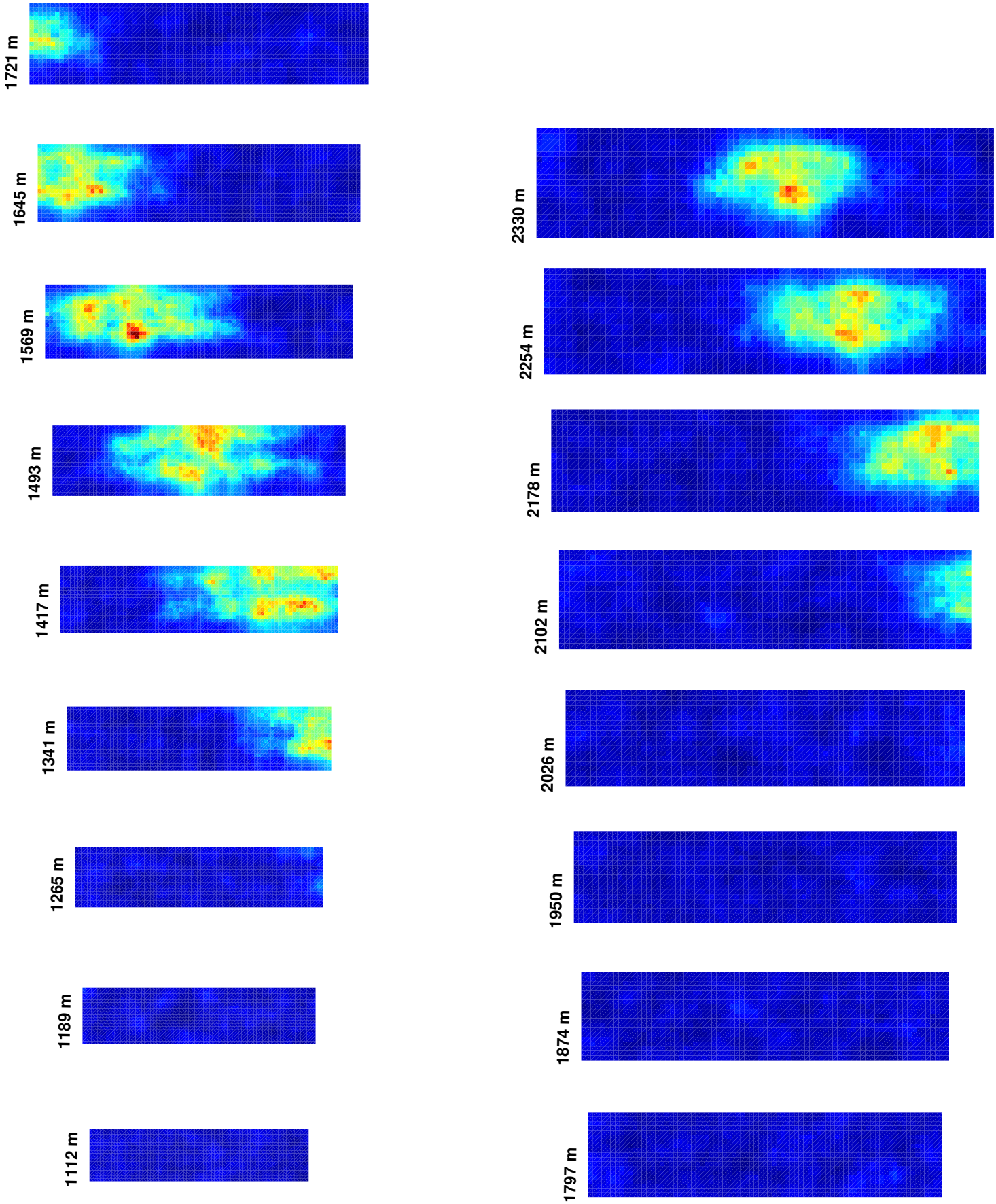

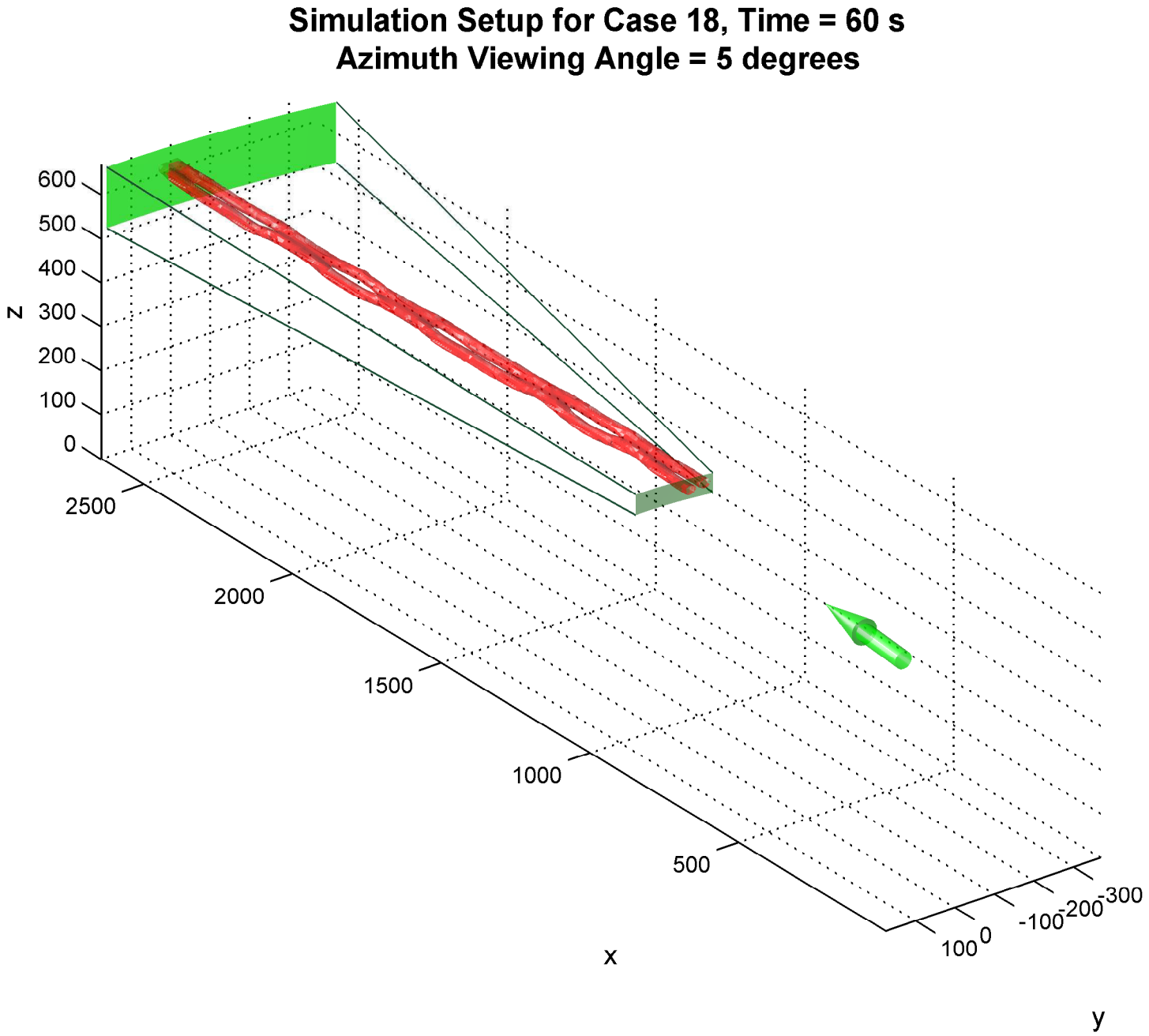
Simulation Setup for Case 18, Time = 60 s
Azimuth Viewing Angle = 5 degrees
z
600
500
400
300
200
100
0
2500
2000
1500
1000
500
x
100
0
-100
-200
-300
y

Simulation Results for Case 18, Time = 60 s
Azimuth Viewing Angle = 5 degrees

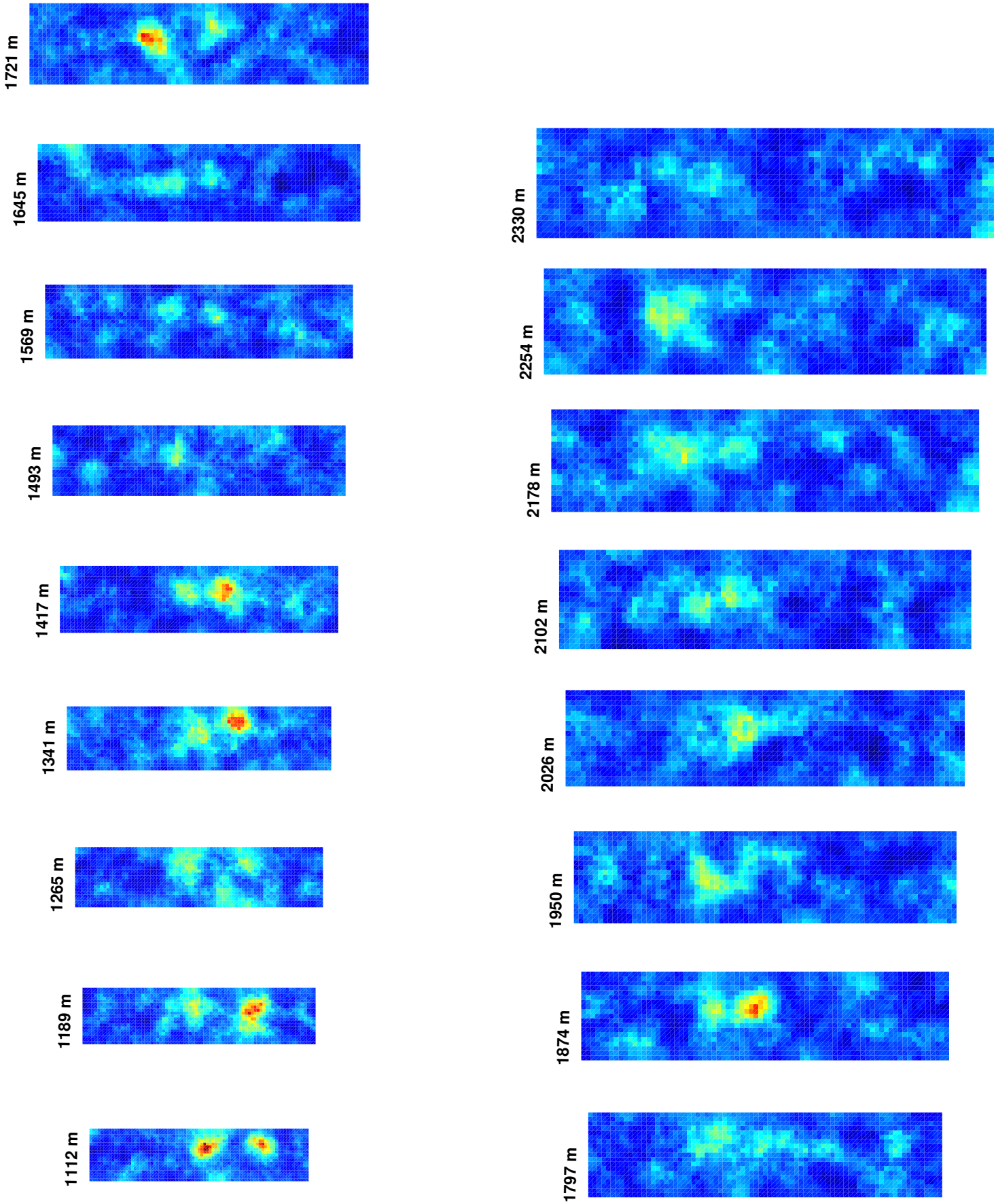

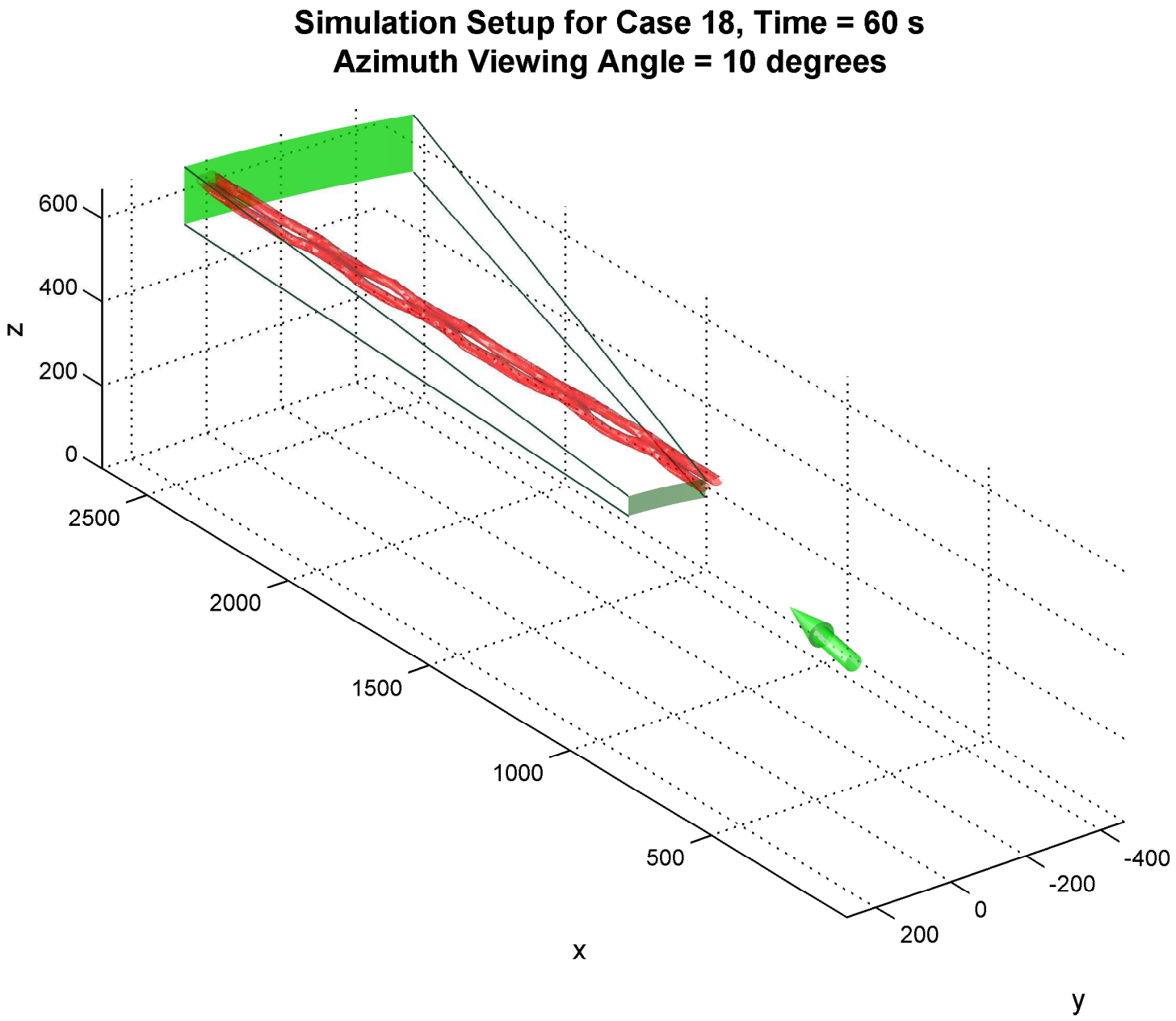
Simulation Setup for Case 18, Time = 60 s
Azimuth Viewing Angle = 10 degrees
600
400
200
0
z
2500
2000
1500
1000
500
x
200
0
-200
-400
y

Simulation Results for Case 18, Time = 60 s
Azimuth Viewing Angle = 10 degrees

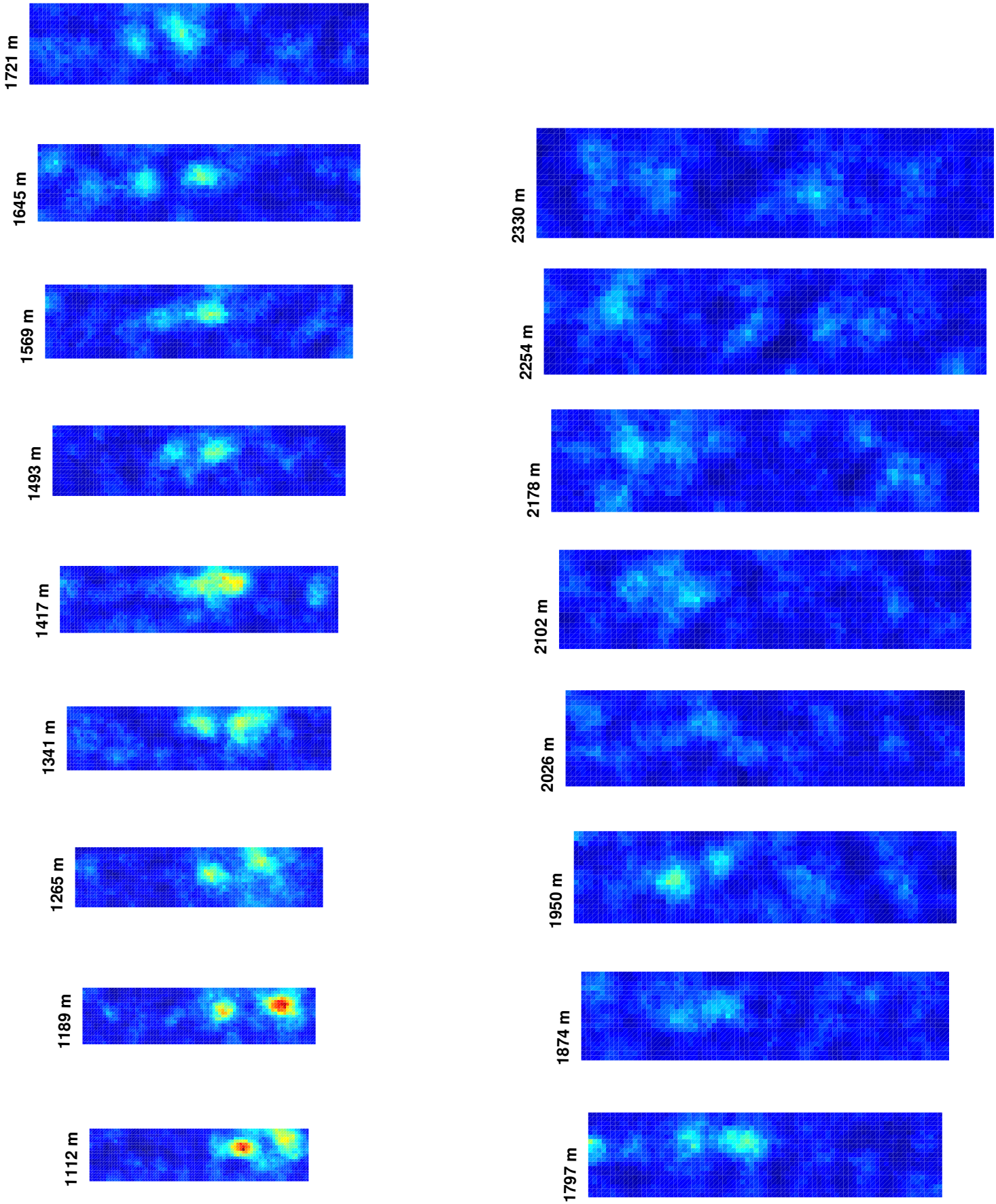

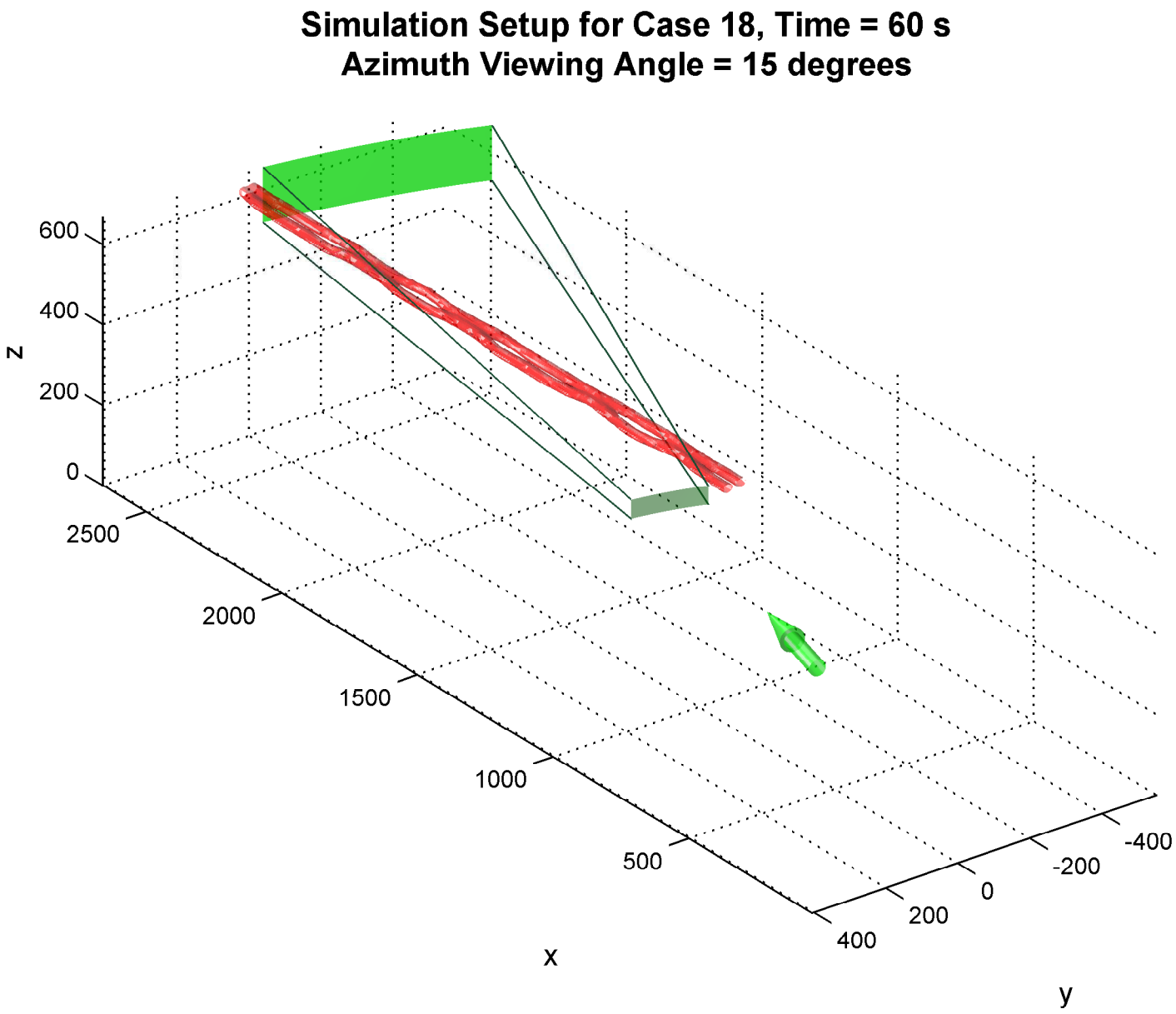
Simulation Setup for Case 18, Time = 60 s
Azimuth Viewing Angle = 15 degrees
600
400
200
0
z
2500
2000
1500
1000
500
x
400
200
0
-200
-400
y

Simulation Results for Case 18, Time = 60 s
Azimuth Viewing Angle = 15 degrees

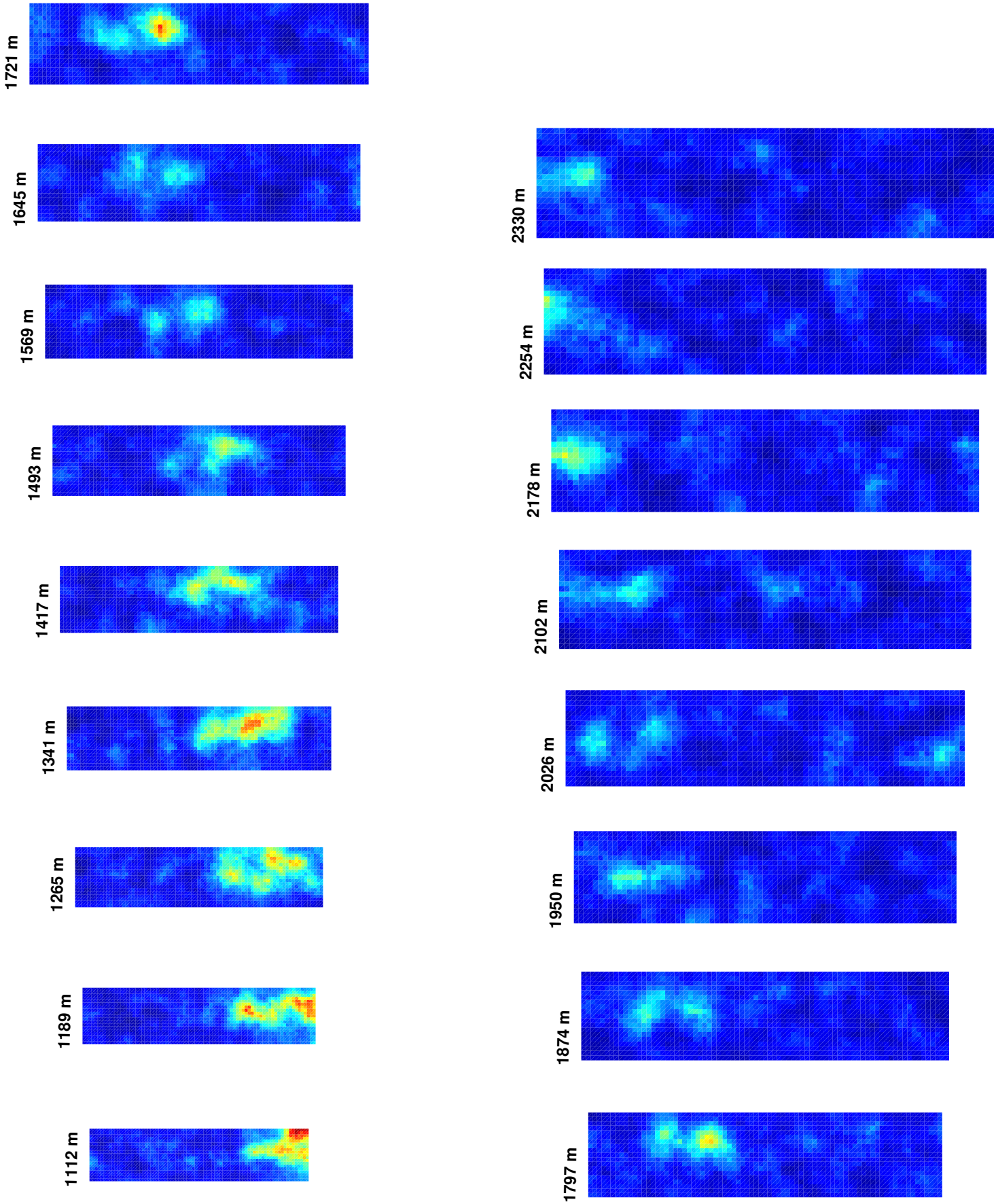

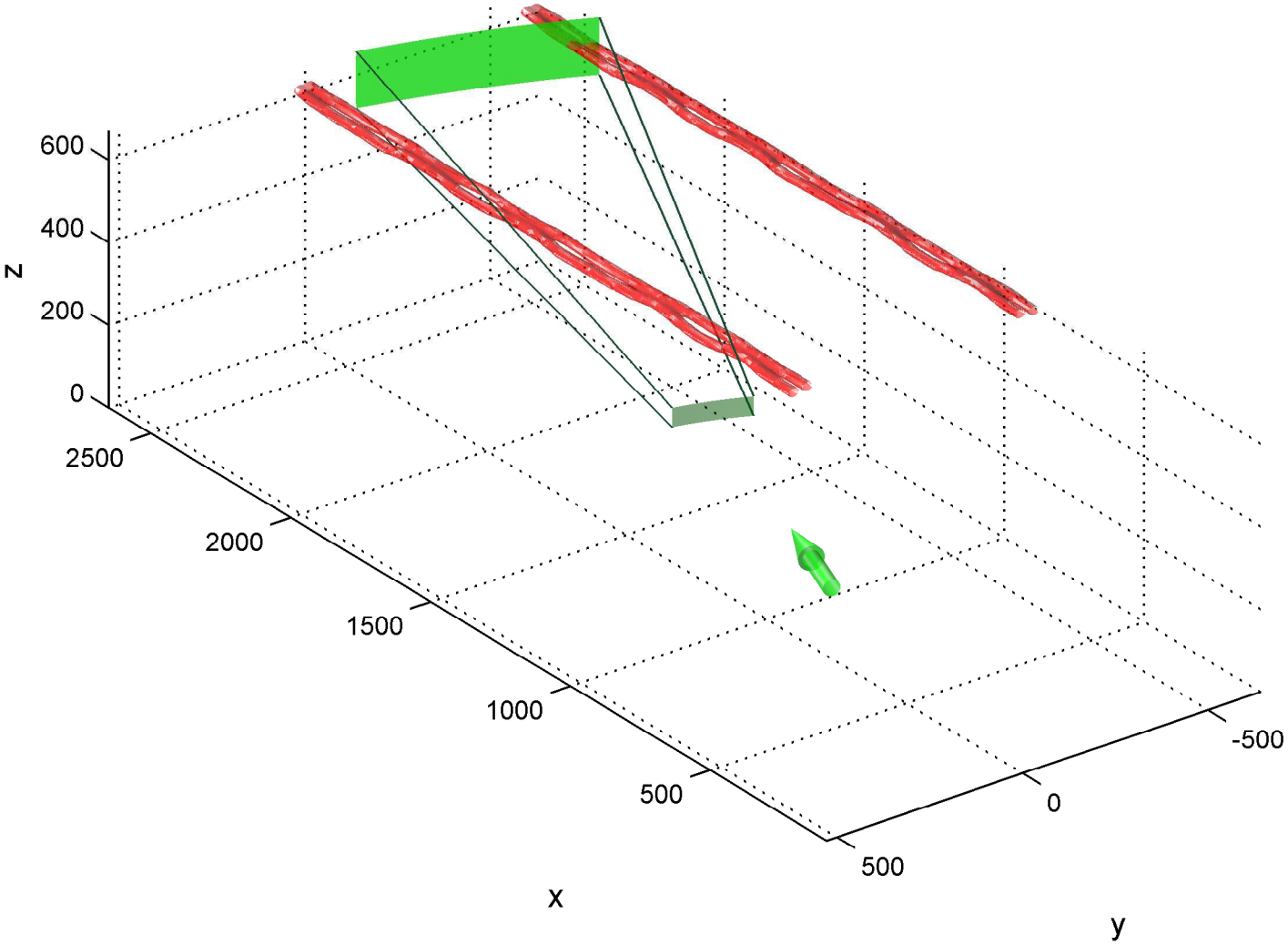
Simulation Setup for Case 18, Time = 60 s
Azimuth Viewing Angle = 20 degrees
600
400
200
0
z
2500
2000
1500
1000
500
x
500
0
-500
y

Simulation Results for Case 18, Time = 60 s
Azimuth Viewing Angle = 20 degrees

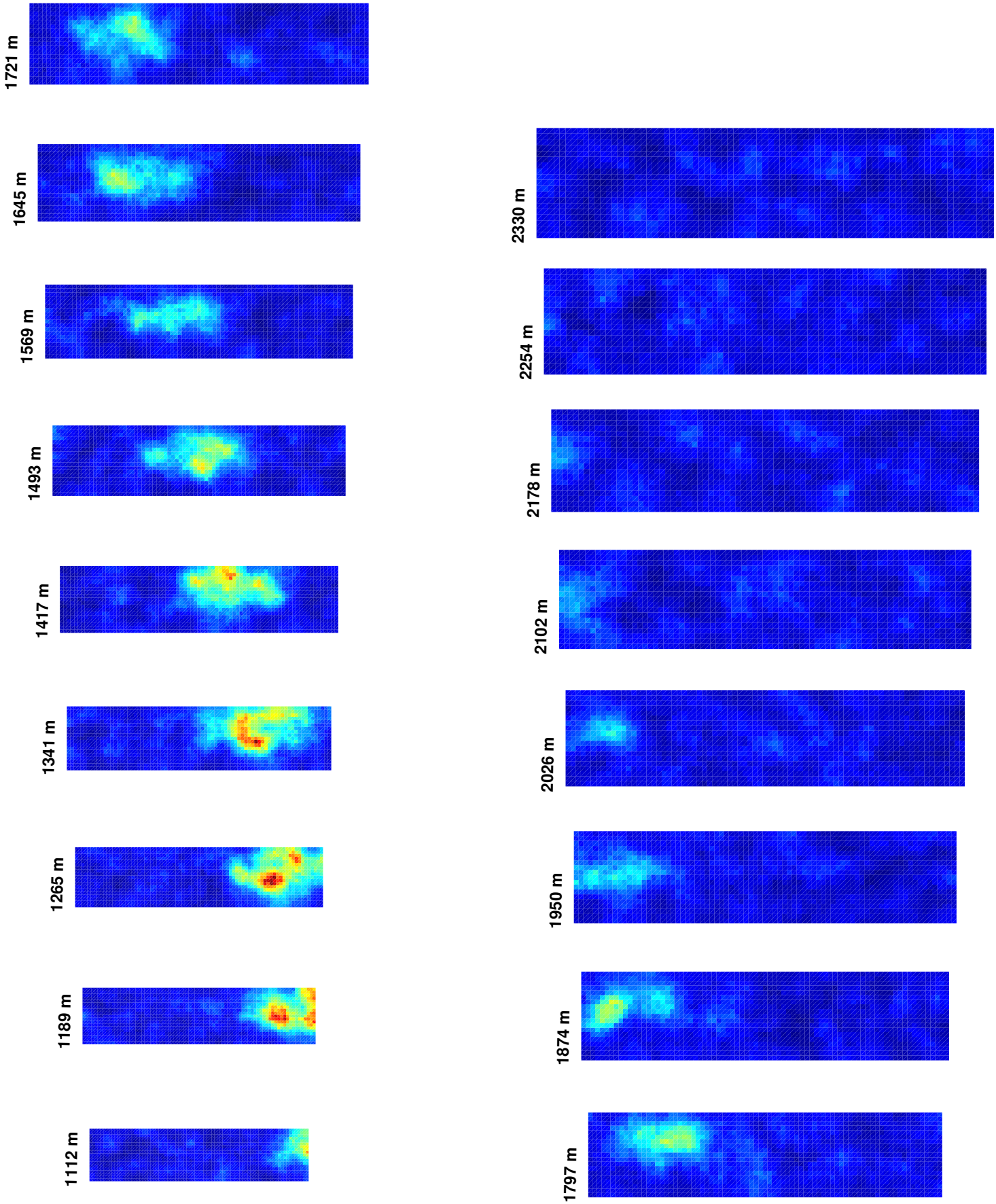

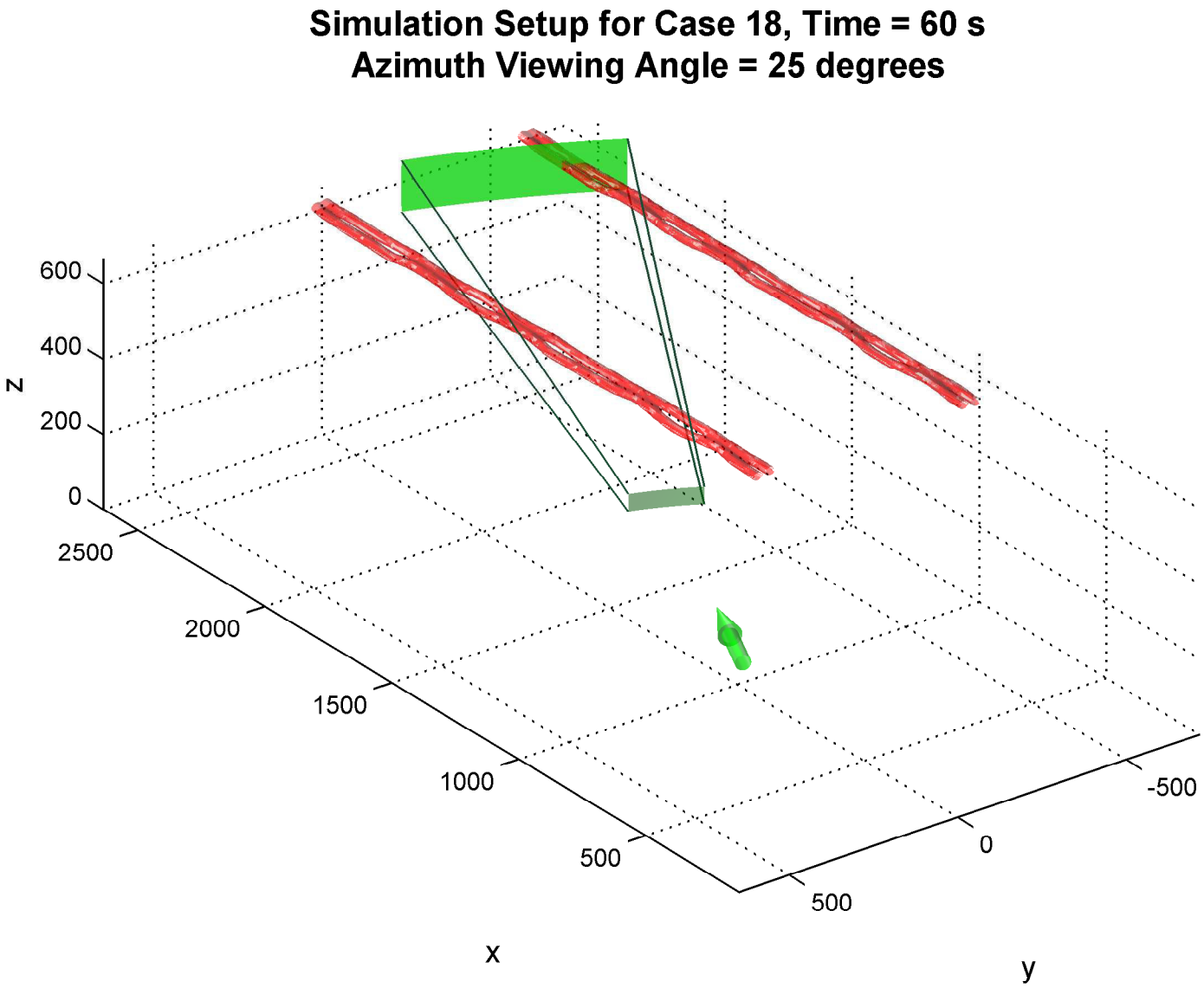
Simulation Setup for Case 18, Time = 60 s
Azimuth Viewing Angle = 25 degrees
600
400
200
0
z
2500
2000
1500
1000
500
x
500
0
-500
y

Simulation Results for Case 18, Time = 60 s
Azimuth Viewing Angle = 25 degrees

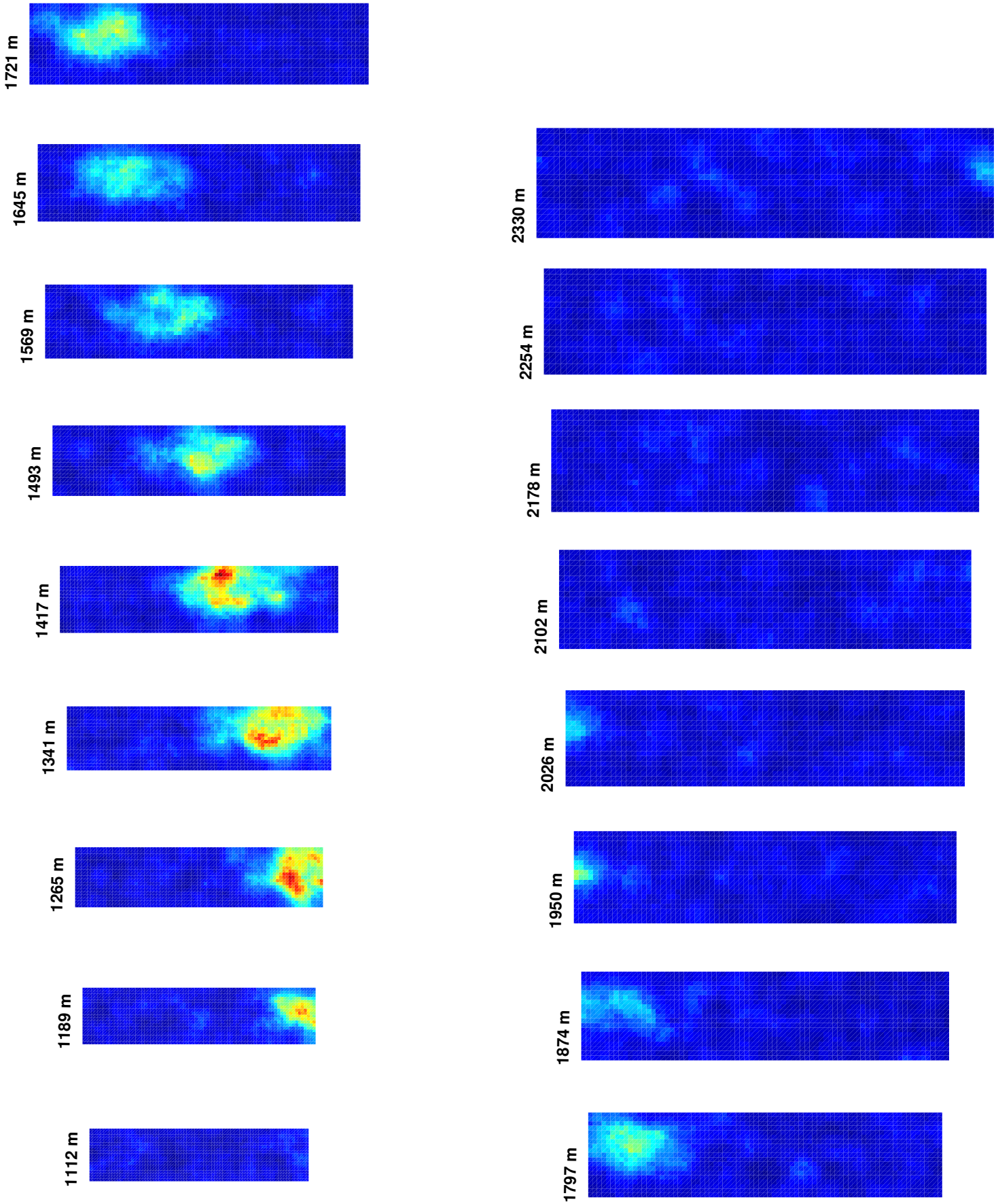

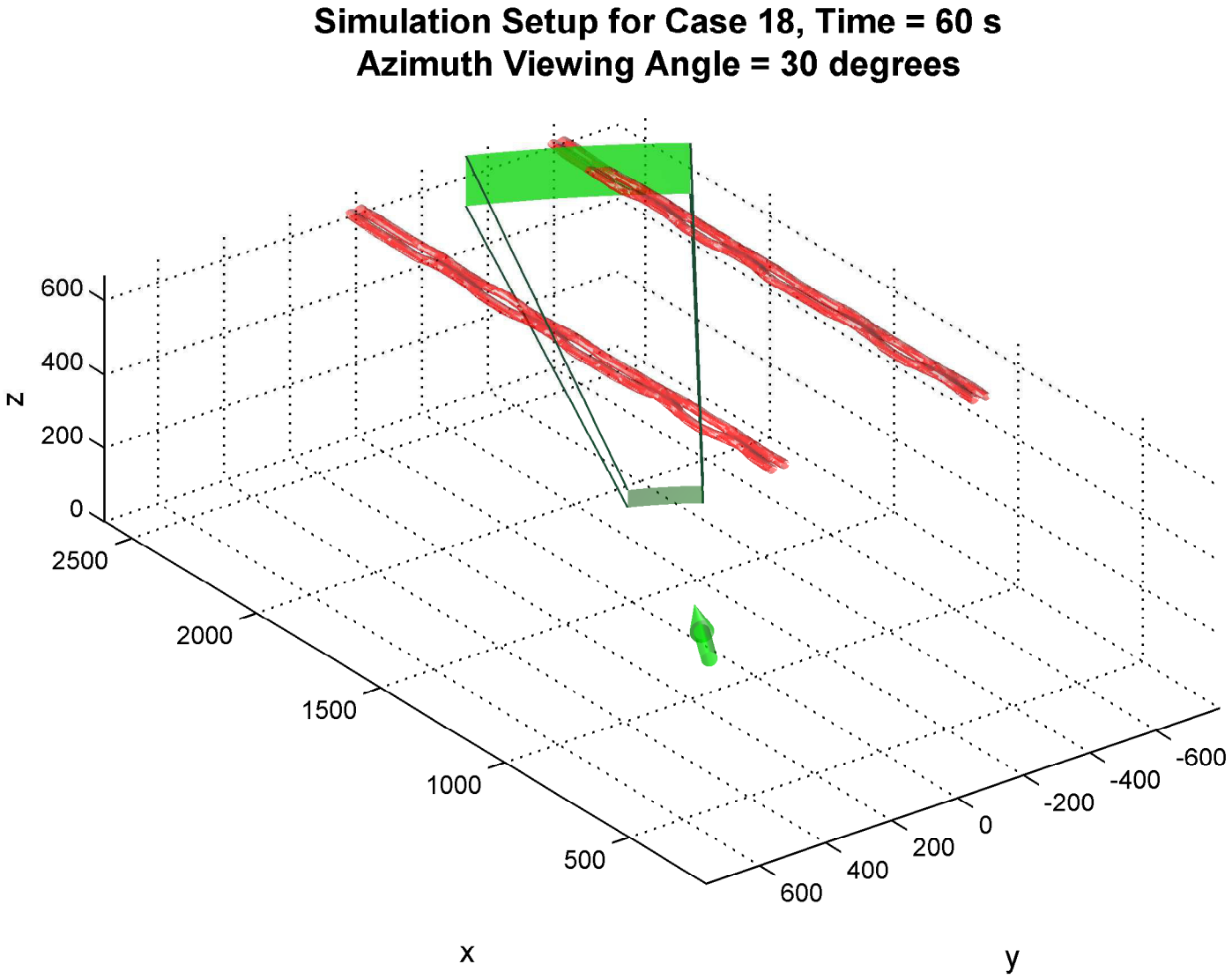
Simulation Setup for Case 18, Time = 60 s
Azimuth Viewing Angle = 30 degrees
z
600
400
200
0
2500
2000
1500
1000
500
x
-600
-400
-200
0
200
400
600
y

Simulation Results for Case 18, Time = 60 s
Azimuth Viewing Angle = 30 degrees

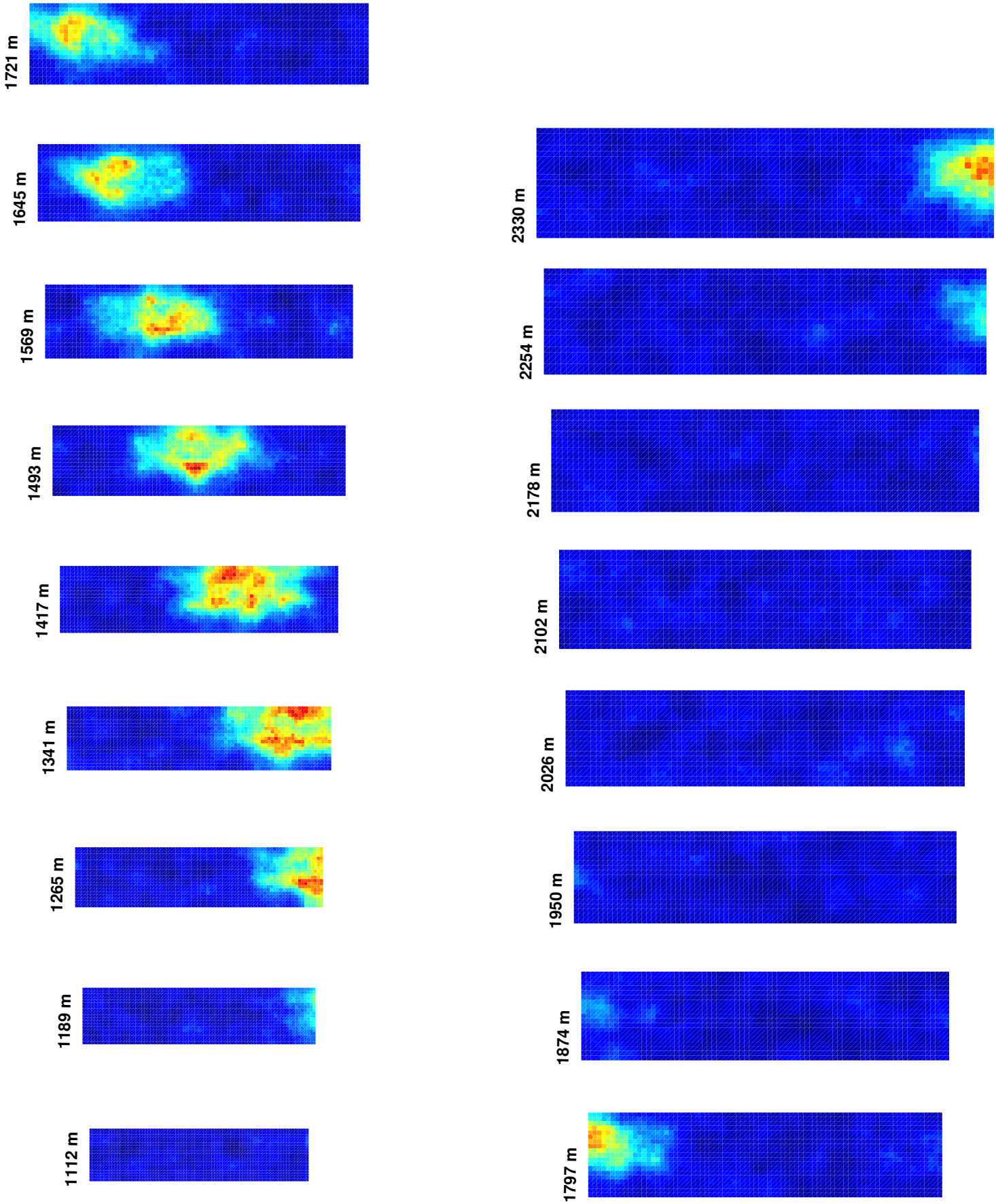

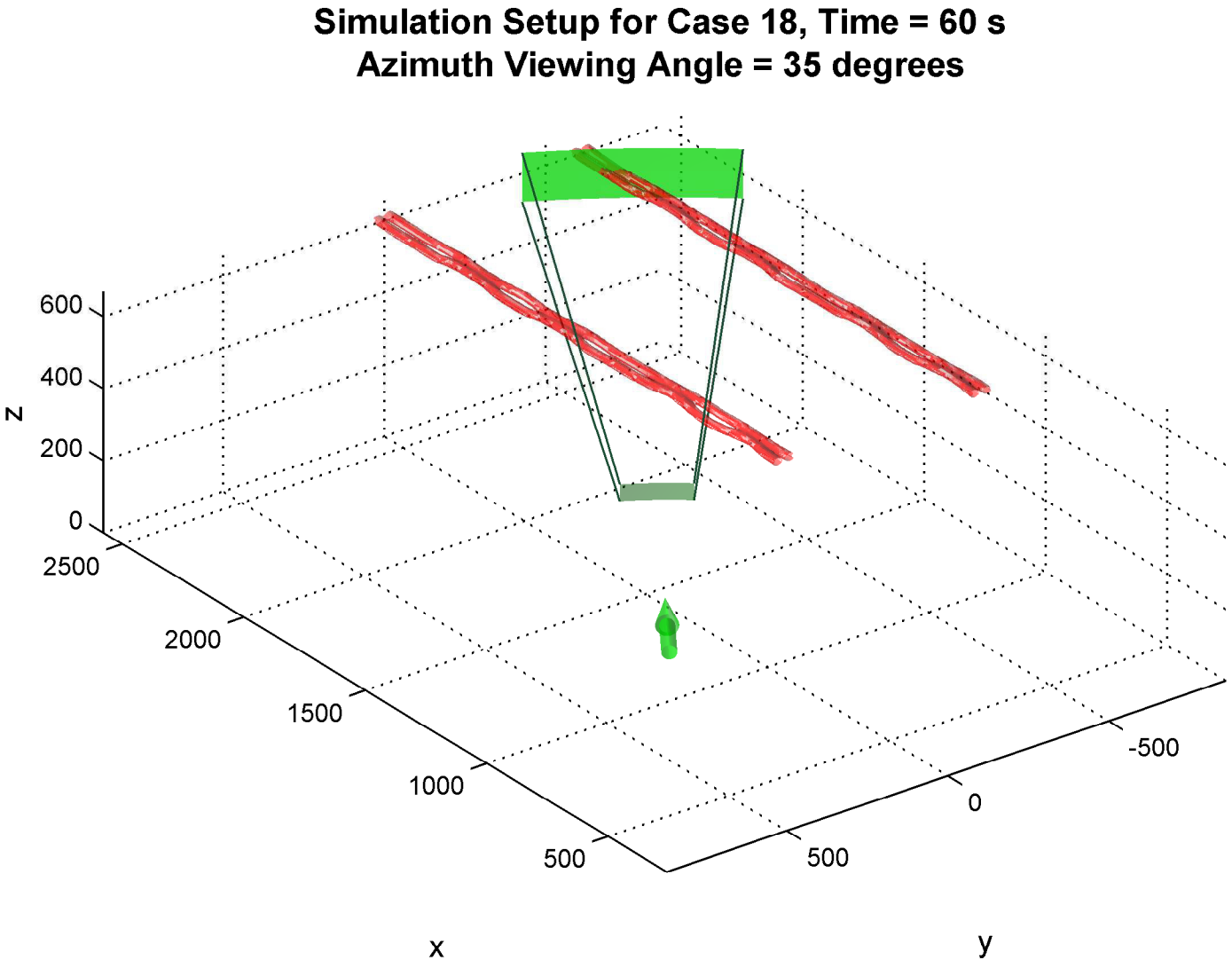
Simulation Setup for Case 18, Time = 60 s
Azimuth Viewing Angle = 35 degrees
600
400
200
0
z
2500
2000
1500
1000
500
x
500
0
-500
y

Simulation Results for Case 18, Time = 60 s
Azimuth Viewing Angle = 35 degrees

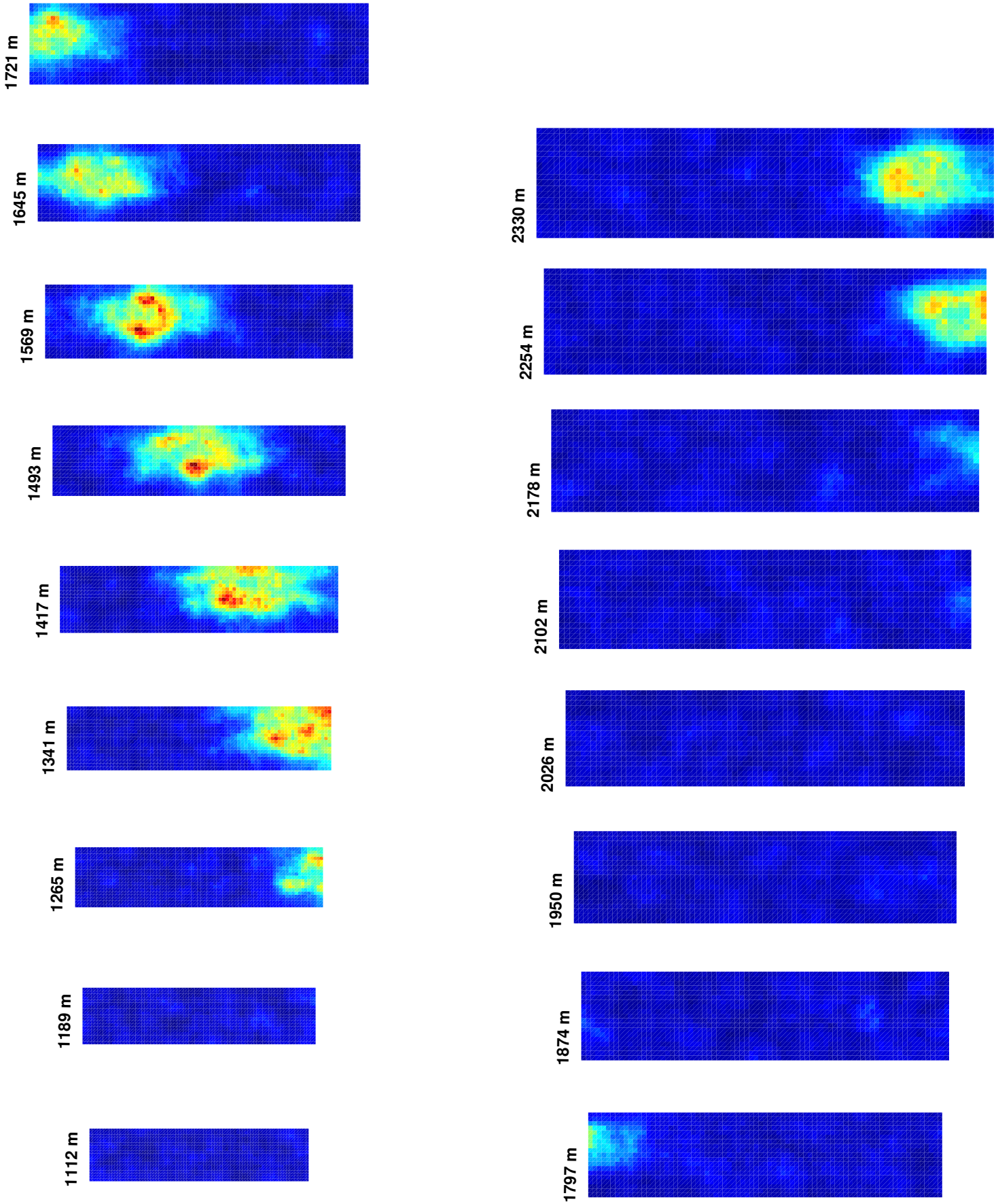

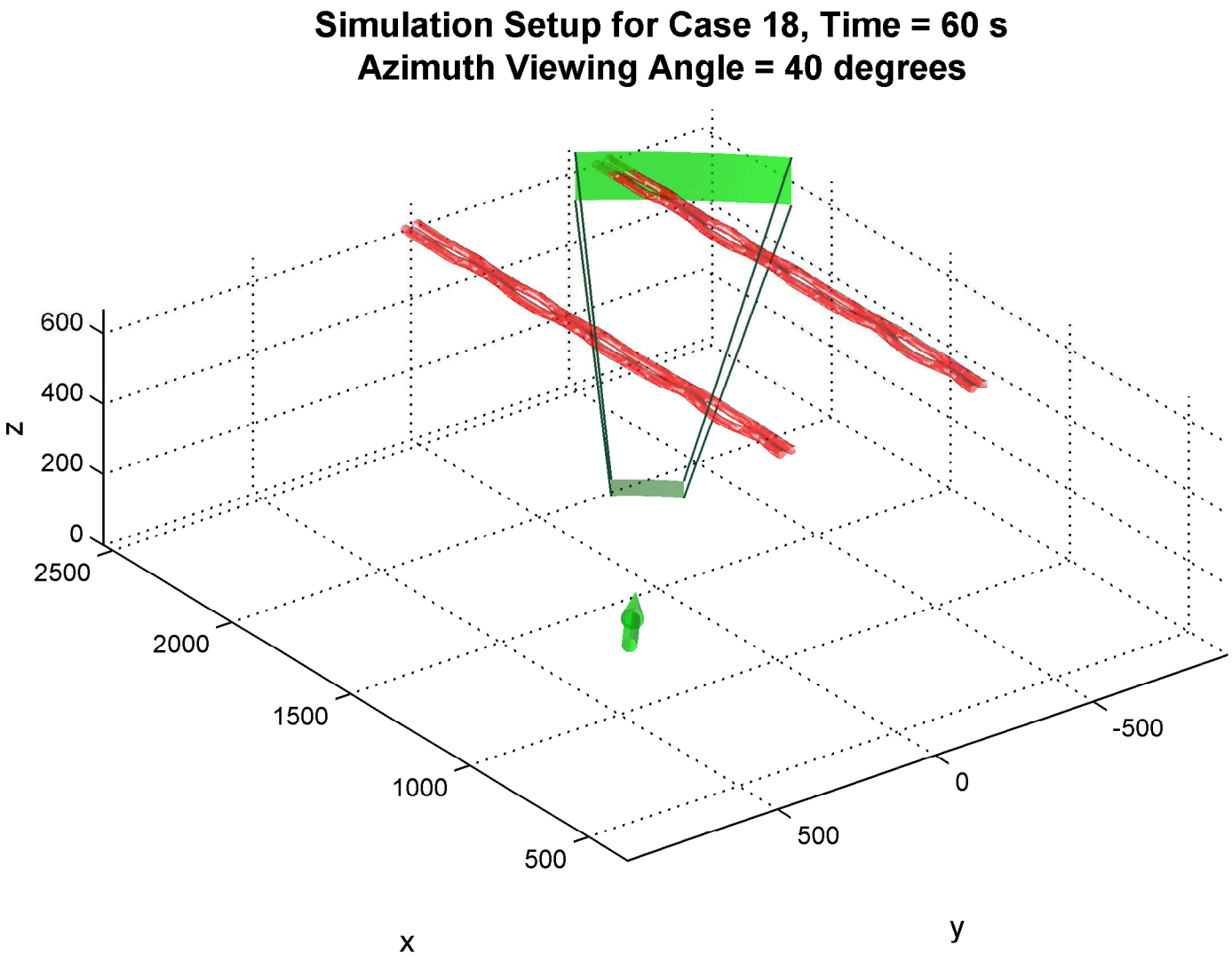
Simulation Setup for Case 18, Time = 60 s
Azimuth Viewing Angle = 40 degrees
600
400
200
0
z
2500
2000
1500
1000
500
x
-500
0
500
y

Simulation Results for Case 18, Time = 60 s
Azimuth Viewing Angle = 40 degrees

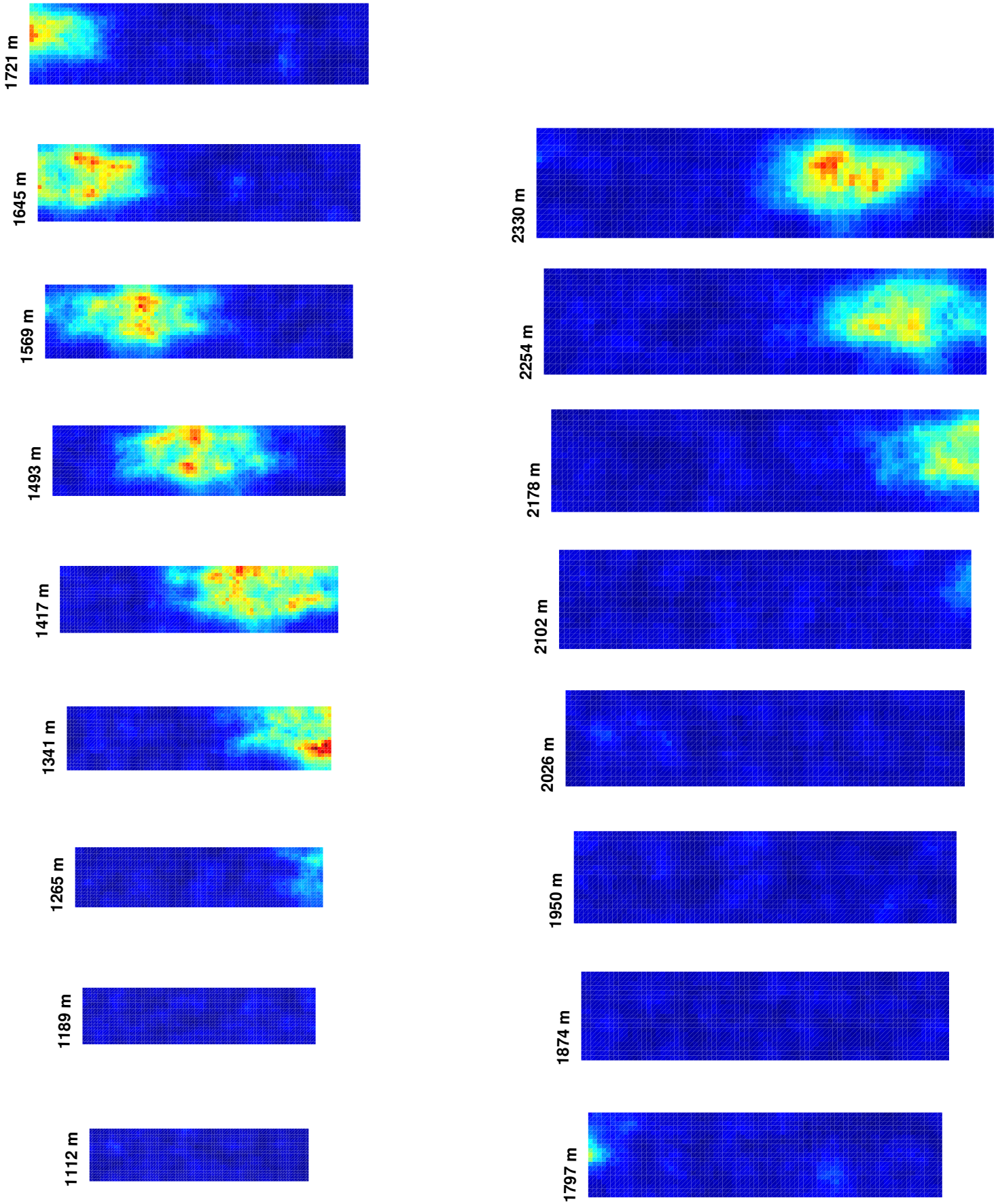

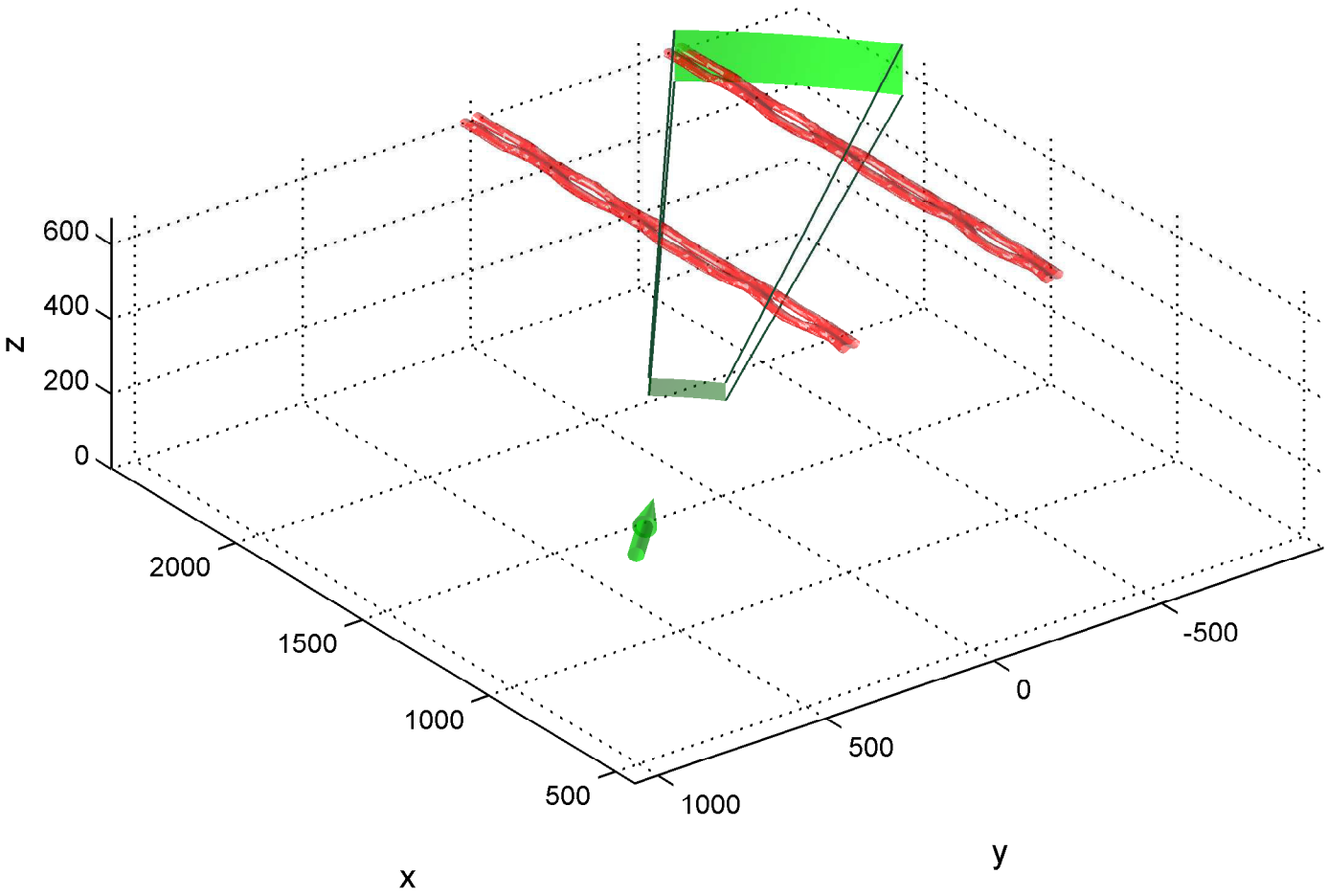
Simulation Setup for Case 18, Time = 60 s
Azimuth Viewing Angle = 45 degrees
600
400
200
0
z
2000
1500
1000
500
x
1000
500
0
-500
y

Simulation Results for Case 18, Time = 60 s
Azimuth Viewing Angle = 45 degrees

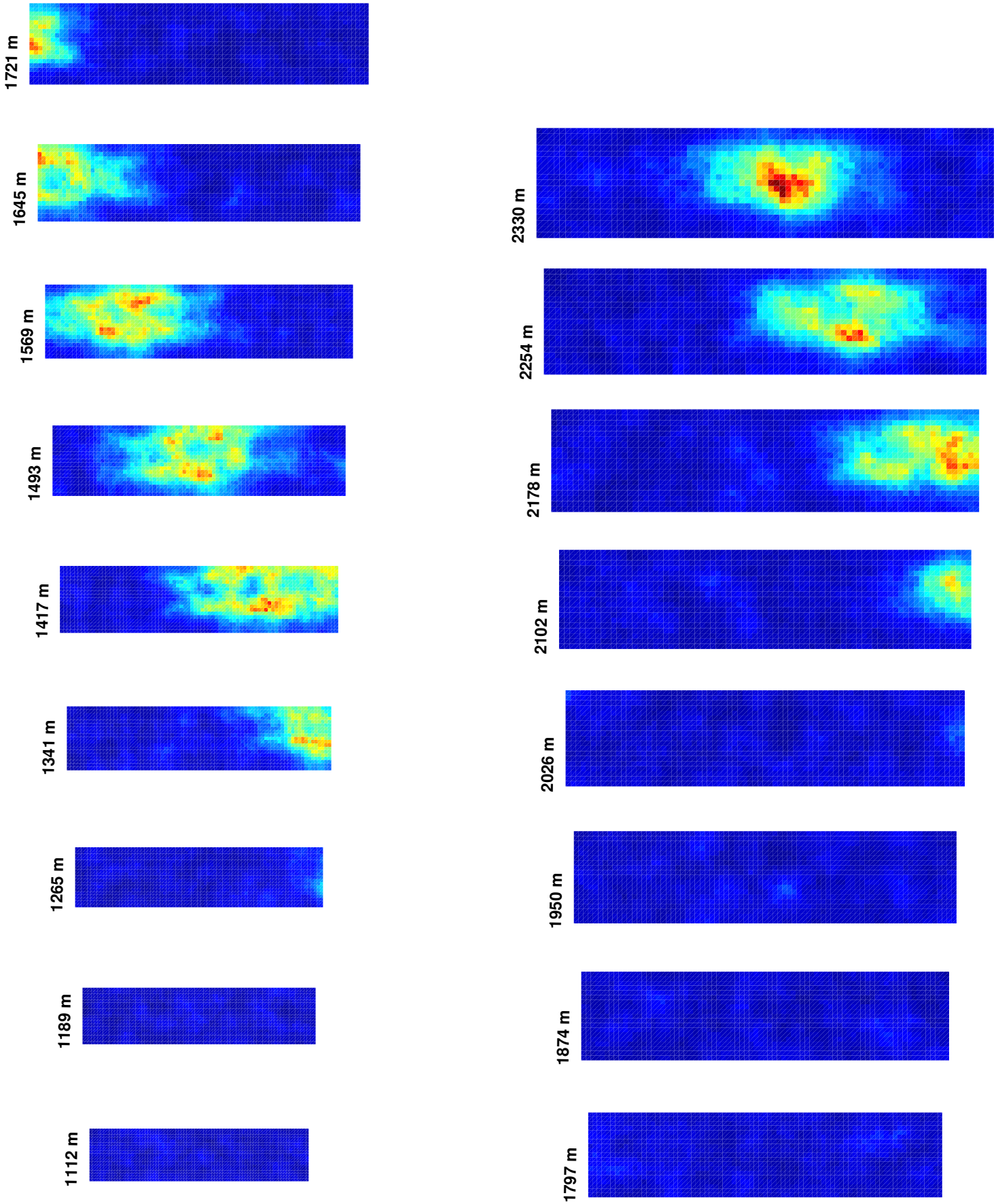

REPORT DOCUMENTATION PAGE

Form Approved
OMB No. 0704-0188

1. REPORT DATE *(DD-MM-YYYY)*	2. REPORT TYPE	3. DATES COVERED *(From - To)*
01- 06 - 2014	Contractor Report	

4. TITLE AND SUBTITLE

Simulating Wake Vortex Detection With the Sensivu Doppler Wind Lidar Simulator

5a. CONTRACT NUMBER

NNL12AA24C

5b. GRANT NUMBER

5c. PROGRAM ELEMENT NUMBER

6. AUTHOR(S)

Ramsey, Dan; Nguyen, Chi

5d. PROJECT NUMBER

5e. TASK NUMBER

5f. WORK UNIT NUMBER

648987.02.04.07.21

7. PERFORMING ORGANIZATION NAME(S) AND ADDRESS(ES)

NASA Langley Research Center
Hampton, Virginia 23681

8. PERFORMING ORGANIZATION REPORT NUMBER

9. SPONSORING/MONITORING AGENCY NAME(S) AND ADDRESS(ES)

National Aeronautics and Space Administration
Washington, DC 20546-0001

10. SPONSOR/MONITOR'S ACRONYM(S)

NASA

11. SPONSOR/MONITOR'S REPORT NUMBER(S)

NASA/CR-2014-218276

12. DISTRIBUTION/AVAILABILITY STATEMENT

Unclassified - Unlimited
Subject Category 06
Availability: NASA CASI (443) 757-5802

13. SUPPLEMENTARY NOTES

Langley Technical Monitor: Larry Goins

14. ABSTRACT

In support of NASA's Atmospheric Environment Safety Technologies NRA research topic on Wake Vortex Hazard Investigation, Aerospace Innovations(AI) investigated a set of techniques for detecting wake vortex hazards from arbitrary viewing angles, including axial perspectives. This technical report describes an approach to this problem and presents results from its implementation in a virtual lidar simulator developed at AI. Threedimensional data volumes from NASA's Terminal Area Simulation System (TASS) containing strong turbulent vortices were used as the atmospheric domain for these studies, in addition to an analytical vortex model in 3-D space. By incorporating a third-party radiative transfer code (BACKSCAT 4), user-defined aerosol layers can be incorporated into atmospheric models, simulating attenuation and backscatter in different environmental conditions and altitudes. A hazard detection algorithm is described that uses a twocomponent spectral model to identify vortex signatures observable from arbitrary angles.

15. SUBJECT TERMS

Atmospheric hazards; Atmospheric simulation; Avionics; Lidar; Remote sensing; Wake vortex

16. SECURITY CLASSIFICATION OF:			17. LIMITATION OF ABSTRACT	18. NUMBER OF PAGES	19a. NAME OF RESPONSIBLE PERSON
a. REPORT	b. ABSTRACT	c. THIS PAGE			STI Help Desk (email: help@sti.nasa.gov)
					19b. TELEPHONE NUMBER *(Include area code)*
U	U	U	UU	132	(443) 757-5802